DISSERTATION

OFF-RESONANT RF HEATING OF STRONGLY MAGNETIZED ELECTRONS IN ULTRACOLD NEUTRAL PLASMA

Submitted by

John M. Guthrie

Department of Physics

In partial fulfillment of the requirements

For the Degree of Doctor of Philosophy

Colorado State University

Fort Collins, Colorado

Spring 2021

Doctoral Committee:

Advisor: Jacob Roberts

William Fairbank Jr
Martin Gelfand
Jesse Wilson

ABSTRACT

OFF-RESONANT RF HEATING OF STRONGLY MAGNETIZED ELECTRONS IN ULTRACOLD NEUTRAL PLASMA

Magnetic fields are common in many plasma systems. Ultracold neutral plasmas (UCPs) are capable of not only accessing strong Coulomb coupling physics but also strong and extreme electron magnetization regimes, as well. These magnetization regimes, as defined by Baalrud and Daligault [S. Baalrud and J. Daligault, Phys. Rev. E, **96**, 043202 (2017)], are predicted to modify screening or binary collision properties as the electron cyclotron radius approaches or subceeds the relevant plasma length scales. UCPs provide an advantageous testing ground for measuring magnetized electron-ion interactions, such as collisional heating induced by applied off-resonant RF fields. The experiments described in this thesis are focused on observations of RF heating in a UCP made from a photoionized cloud of ultracold $^{85}\mathrm{Rb}$ at three electron magnetization strengths that span the weakly-strongly magnetized boundary to the strongly-extremely magnetized boundary. Relative comparisons between heating rates at different magnetic fields were measured with ~20% precision, and an absolute determination of the heating rate near the weak-strong magnetization boundary is determined with ~40% precision. The results from these experiments were compared to theoretical predictions we developed that account for the finite-RF amplitude conditions used in the UCP measurements. This finite-amplitude heating rate theory is shown to be an extension of low-amplitude magnetized AC conductivity treatments as well as unmagnetized nonlinear collisional radiation absorption treatments. Mixed agreement was discovered between our observations and the theory for the three magnetic fields investigated: 10.6, 65, and $134\,\mathrm{G}$. The measured absolute RF heating rate at $10.6\,\mathrm{G}$ and the relative rate between 134 and $10.6\,\mathrm{G}$ are in agreement with predictions within uncertainty; the relative rate between 65 and $10.6\,\mathrm{G}$ was observed to be a factor of ~3 lower than the predictions, with an absolute difference—in terms of the measurement

uncertainty—on the order of 10σ. The implications of this disagreement are discussed, and future measurements that can be conducted with this technique are presented.

ACKNOWLEDGEMENTS

Foremost, I want to thank my advisor Prof. Jake Roberts. Under his tutelage, he has served me as not only a role model physicist but also as an example of good character. His unrelenting forward-thinking attitude coupled with his patience provided an ideal environment for me to grow as a scientist. I feel that words do not do justice for the impact Jake has had on my life, and I am forever grateful for his advisorship.

I also want to acknowledge the help I received from fellow graduate students. In particular, Puchang Jiang has worked by my side throughout my time in the lab and assisted heavily with running and analyzing plasma simulations. I wish him well as he continues with his doctoral research. The student who preceded me on the experiment, Wei-ting Chen, was also extremely helpful. His guidance when I started working on the experiment apparatus was invaluable, and I appreciate the time he took transferring operational knowledge to me as the torch was passed, so to speak.

I feel compelled to acknowledge all of the institutional support I have received throughout my time in graduate school. I am grateful for the help and assistance provided by the Physics Department faculty and staff, such as those in the front office that graciously walked me through all the paperwork and bureaucracy. I also want to thank the Colorado State University staff, who provided a quality atmosphere, counseling, and amenities throughout my time as a student. I also acknowledge the funding support for my work from the Air Force Office of Scientific Research.

Last, but most certainly not least, I cannot begin to describe my gratitude for the support of my family and friends. I would not be able to achieve my goals without the unconditional encouragement I had from my Mom, Dad, and loved ones along the way. Finally, through the strength I gain from the love and support of my wife, Tessa, I have overcome incredible challenges.

DEDICATION

I would like to dedicate this dissertation to my daughter Rylie.

Keep asking questions, kiddo.

TABLE OF CONTENTS

LIST OF TABLES

LIST OF FIGURES

Chapter 1

Introduction

1.1 Motivation

Plasma is important. 99% of matter in the universe exists in a plasma state in a vast range of objects spanning things like accretion disks [1], stellar interiors and atmospheres [2], and solar wind [3]. Plasmas hold promise for clean energy production through nuclear fusion efforts [4–6]. They can be used for the study of physics in extreme conditions, such as high energy-density matter [7] or matter in accelerators with relativistic particles [8]. They also have numerous commercial and technological applications from microwave generation [9] to semiconductor fabrication [10] to new applications in water purification [11] and medical treatments [12]. Performing measurements in laboratory plasma systems well-suited for the measurements of interest can advance the field by testing current theoretical understanding and pushing the limits of theory. This dissertation is focused on measurements of off-resonant RF heating of strongly magnetized electrons in ultracold neutral plasma, which allows the investigation of electron-ion collision rates in magnetization conditions more commonly observed in astrophysical or extreme matter systems. In this introductory section, I outline the motivation for these measurements. I begin with an overview of our ultracold plasma properties and their relevance in the physics we are interested in measuring. This is followed by a list of summaries for the chapters as they have been organized in this thesis.

Ultracold neutral plasmas [13], or UCPs, were first reportedly created in Steve Rolston's lab in 1999 [14]. Many UCPs, like the one studied in this thesis, are formed by photoionizing a cloud of ultracold neutral atoms [15]. The resulting system of cold ions and electrons form a finite-sized, quasi-neutral, two-component plasma. The ions, if not confined by an external potential, are free to expand over a timescale determined by their mass [16]. The less massive electrons will experience a confining force due to the development of a positive space-charge potential generated by the inertially-localized ions. Measurements can be performed on these UCPs during their typical 10–

$100\,\mu\mathrm{s}$ finite lifetimes before expansion destroys the plasma. UCPs can reach electron temperatures on the order of $2\,\mathrm{K}$ and particle densities as low as $10^6\,\mathrm{cm}^{-3}$ [17].

The orders-of-magnitude lower temperatures of UCPs compared to other types of plasma give them access to interesting, exotic physics on laboratory scales. Furthermore, the lower charge densities of UCPs slow down many of the time and frequency scales that govern plasma dynamics to levels accessible by modern electronics [16]. UCPs are also relatively "clean" systems for plasma physics investigations with regard to their weak interactions with neutral species contaminates [14]. These qualities, in broad terms, show that UCPs are excellent systems for performing experiments to investigate basic plasma physics properties in a focused way.

One of the consequences of the temperature and density properties of UCPs is their accessibility to strong coupling physics [13, 18, 19]. The Coulomb coupling parameter, Γ, is a dimensionless ratio of average potential and kinetic energy scales in plasma. It compares the nearest-neighbor Coulomb potential energy to the average thermal energy,

$$\Gamma \equiv \frac{\langle \mathrm{nnPE} \rangle}{\langle \mathrm{KE} \rangle} = \frac{e^2}{4\pi\epsilon_0 k_\mathrm{B} T} \sqrt[3]{\frac{4\pi n}{3}}.$$

Most "ordinary" types of plasma exist in a weakly coupled regime when $\Gamma \ll 1$, but as plasma reduces in temperature or increases in density Γ increases. When Γ exceeds unity, strongly coupled physics will become considerable. One consequence of strong coupling is the development of spatial correlations among the charges in the plasma. There are many types of plasma, particularly those in high energy-density (HED) regimes like fusion and astrophysical systems, where strong coupling physics is important, and UCPs provide an efficient and accessible testbed for investigating this physics [7].

Strong coupling is not the only interesting physics accessible to UCPs. Magnetic fields are common in plasma systems. UCPs that rely on charge detection for measurements typically require magnetic fields to guide the charges toward a detector [15, 20]. As an example in HED systems, tokamak fusion reactors apply strong magnetic fields to control and confine the plasma [21, 22]. Considerable magnetic fields exist in many astrophysical plasma systems as well [23–25]. The

effect of a magnetic field on a plasma depends on how parameters like the cyclotron frequency and radius compare to other plasma frequency and length scales [26]. As the magnitude of the magnetic field increases from zero the cyclotron radius becomes smaller. Plasma transport, then Debye screening, then binary collision properties will be modified by the magnetic field as the cyclotron length shrinks [27].

Figure Figure 1.1 shows a temperature-density parameter space diagram of where several types

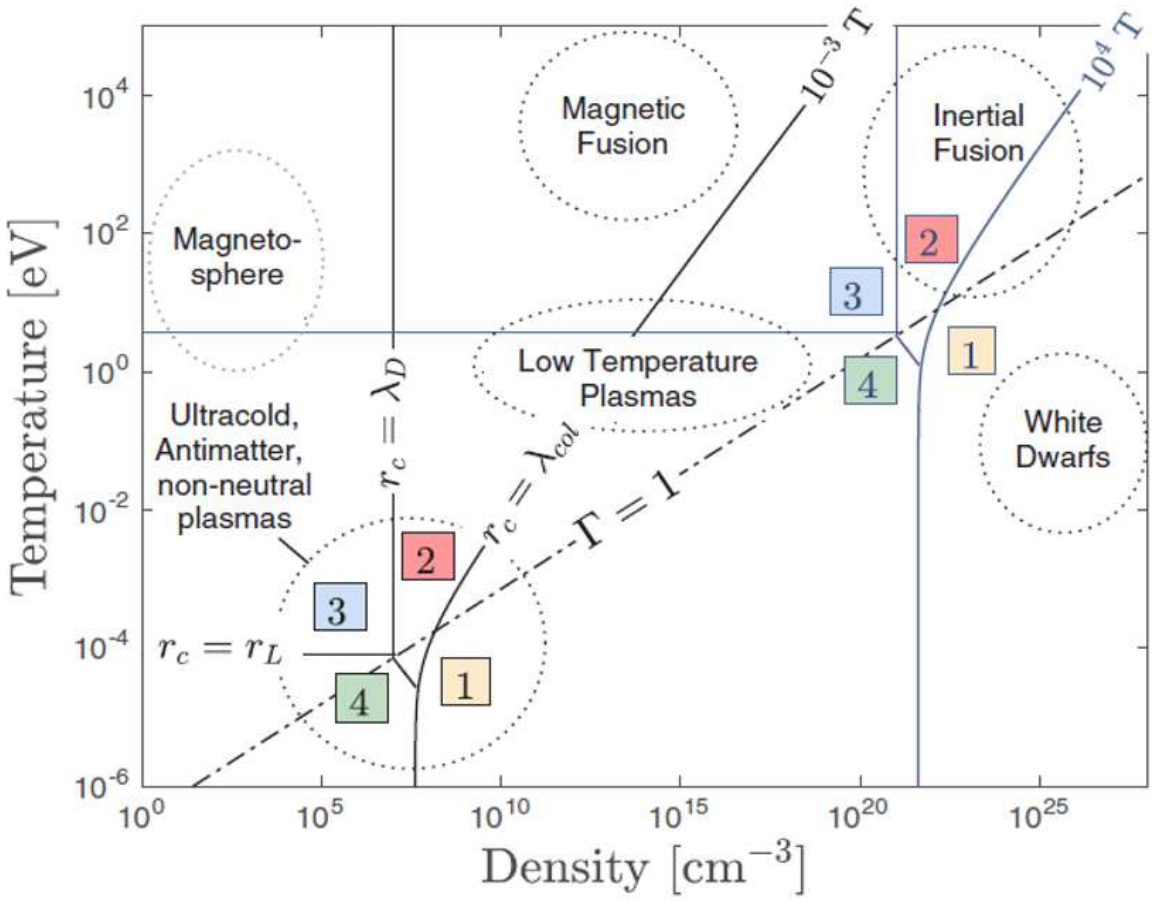

Figure 1.1: Temperature-density plasma parameter space diagram with magnetization regime boundaries, reproduced from Ref. [27]. The magnetization regimes are depicted for two magnetic field strengths $B = 10^{-3}$, 10^{4} T. The enumerated areas correspond to 1. Unmagnetized, 2. Weakly magnetized, 3. Strongly magnetized, and 4. Extremely magnetized electron regimes at the respective fields. See Section 2.5 for more info.

of plasma usually exist, reproduced from Ref. [27] "*Transport regimes spanning magnetization-coupling phase space*." The diagram shows how UCPs exist in a region that straddles the strongly

coupled regime boundary around $\Gamma = 1$. Overlayed with the temperature-density diagram are lines associated with boundaries that distinguish electron magnetization regimes. These regimes are defined in more detail in Chapter 2, but here I identify the numbered areas as 1. Unmagnetized, 2. Weakly magnetized, 3. Strongly magnetized, and 4. Extremely magnetized. The magnetization regime boundaries are depicted for two magnetic field magnitudes, $10^{-3}\,\mathrm{T}$ and $10^{4}\,\mathrm{T}$. This plot highlights the fact that plasma physics associated with non-negligible magnetization in HED or astrophysical systems with Tesla to mega-Tesla magnetic fields can be probed in UCPs with laboratory accessible fields. The mass disparity between electrons and atomic ions in UCPs means that the electron component is generally easier to magnetize than the ions. This is why we are studying strongly magnetized electron effects in ultracold plasma.

Plasma dynamics can be characterized by the hydrodynamic properties, such as expansion, and kinetic properties, like binary collisions [28]. The work presented in this thesis is focused on collisional processes. The primary types of binary collisions in neutral plasma can be classified into fundamental ion-ion, electron-electron, and electron-ion categories [26]. The ability to perform systematic surveys in UCPs also make them prime candidates for precisely determining electron-ion collision effects in parameter spaces that statistical theories struggle or fail to describe [7, 19].

Electron-ion collisions play an important role in evaluating neutral plasma kinetic theory coefficients for transport and diffusion [27, 29–31] as well as collisional relaxation and thermalization rates [32–38]. For example, experiments have been performed with the purpose of cooling heavy ion beams in a storage ring by interactions with injected electrons [33, 34]. These observations provide information about magnetized electron-ion collisions in some ways, but the properties of those experiments lead to plasmas with large temperature anisotropies and little control over the applied magnetic field strength. Electron-ion collisions are also relevant in many stopping power calculations, in which the energy loss of a projectile charge due to interactions with a plasma is evaluated [39–49]. Furthermore, electron-ion collisions play an important role in collisional AC conductivity [50–52] and inverse Bremsstrahlung processes [53–59] where kinetic energy is transferred to charges by absorbing radiation during binary Coulomb interactions. This physics is

utilized in certain laser-heated plasma and direct-drive fusion experiments [60–62], and in some ways it is comparable to off-resonant RF heating effects in magnetized UCPs.

The UCPs studied in this thesis have initial electron temperatures near $T_{\mathrm{e}} \approx 4\,\mathrm{K}$, densities around $n \approx 10^{7}\,\mathrm{cm}^{-3}$, and applied magnetic fields up to about $B \approx 140\,\mathrm{G}$. We can compare our UCP magnetization scales to other plasma systems by scaling up our temperature and densities with fixed coupling $\Gamma \sim n^{1/3}/T$ and scaling the magnetic field to match our cyclotron radius:screening length or cyclotron radius:binary collision length ratios. For instance, at temperatures and densities relevant for magnetized plasma jet formation at the OMEGA laser facility, the $33\,\mathrm{T}$ field in that system produces a magnetization much less than our UCP [61]. At those scales, MT-level fields would be required to match our UCP magnetization, like those proposed for MagLIF experiments [62]. The magnetically-confined fusion experiment ITER has design specifications that correspond to 1/10th of our UCP magnetization at $140\,\mathrm{G}$ with respect to the screening length ratio [22]. Magnetization scales comparable to our UCP exist in certain HED systems, like laser-heated nanorods [63], as well as astrophysical systems, such as the crust of white dwarf stars [23,24] and atmosphere of neutron stars [25]. It should be noted that while many of these example plasma systems have dynamics governed predominantly by magnetohydrodynamics, collisions can still be relevant in the underlying theories used in those treatments [64,65].

At the time that the work described in this thesis started, literature on systematic surveys of electron-ion interactions across magnetic field strengths backed by observations was practically nonexistent. Theories and measurements in general agreement for non-neutral magnetized collision rates have been developed [66], but the same is not true of magnetized electron-ion collisions. This is why we are interested in measurements of off-resonant RF heating of strongly magnetized electrons in ultracold neutral plasma—the subject of this thesis.

1.2 Chapter summary

In Chapter 1, I present the motivation and applicability for measurements of RF heating rates in magnetized ultracold neutral plasma. The Motivation section is followed by this one, the Chap-

ter summary section, where I outline the organization of information presented throughout this dissertation.

In Chapter 2, I define important plasma scales and parameters like the plasma oscillation frequency, Debye screening length, and Coulomb coupling parameter. A description of unmagnetized binary eletron-ion collisions in plasma is also provided. I reference the definitions of the magnetization regimes mentioned in the Motivation, and describe the challenges associated with evaluating magnetized binary collisions. This chapter concludes with a section summarizing key, distinctive properties that apply to our UCP. This sets up the basic foundation and background knowledge necessary to interpret the remainder of the dissertation.

The purpose of Chapter 3 is to develop a framework for understanding RF heating of magnetized plasma through theoretical approaches. I differentiate two independent treatments for plasma behavior, the binary collision treatment and the dielectric theory treatment. The range of validity of perturbative magnetized binary collision treatments is addressed, followed by a larger section focused on developing an applicable linear response dielectric theory treatment. I identify assumptions and limiting approximations in magnetized AC conductivity theories that may be violated in our experimental surveys. An alternative RF heating treatment based on stopping power-like energy transfer (SPLET) is formulated with the intention of providing theoretical predictions for magnetized RF heating rates that we can compared to our experimental observations. I evaluate the SPLET treatment across Coupling strengths, magnetization strengths, RF field amplitude, and RF frequency. The predicted effect of adding a collisional relaxation term to the dielectric function is characterized and shown to be relatively minor ~5% modification in the RF heating results for our conditions.

Chapter 4's goal is to lay out the relevant experimental aspects of our measurement and apparatus. The chapter begins with a general description of the chamber, lasers, and physics associated with the preparation and production of photoionized ultracold neutral plasma. These aspects are fairly ubiquitous among our group's UCP investigations, so many specific details concerning subjects in Section 4.1 can be found in previous student dissertations [15, 17]. I then go over in detail

several key modifications we made to the apparatus in order to conduct our magnetized RF heating experiments.

The second half of Chapter 4 concerns predicating measurements and calibration techniques we developed and executed in preparation for our ultimate determination of RF heating as presented in Chapter 5. Sections 4.3 and 4.4 describe the procedure and results for determining the charge number, DC field strength, electron center-of-mass oscillation frequency, and plasma density. Section 4.5 introduces the "partial extraction method" we developed for our measurements, as well as a technique for calibrating the extraction response to precisely determined energy differences via short electric field impulses, or "kicks." This is called the kick-temperature rise (or kick-ΔT) calibration, and it allows us to compare heating rates across applied magnetic field strengths. The following topic, the calibration technique we developed to determine the RF electric field amplitude, is split between Chapters 4 and 5. The principle associated with the calibration technique is introduced in Chapter 4, but the measurement procedure and final result ties directly into our determination of RF heating rates presented in Chapter 5.

In Chapter 5, I complete the discussion on the RF amplitude calibration technique. I explain how the procedure and results ultimately give us an evaluation of the absolute heating rate at $B \approx 11\,\mathrm{G}$. I show that the absolute heating rate we measured is burdened by uncertainties in the amplitude calibration factor that are not present in relative heating rate comparisons made using ratios. The primary experimental results for the absolute heating rate at $11\,\mathrm{G}$ and relative heating rates at 65 and $134\,\mathrm{G}$ as compared to that at $11\,\mathrm{G}$ are presented in Table 5.1. This is followed by a discussion on the mixed agreement observed between experimental measurements and theory predictions. Chapter 5 concludes with a section focused on exploring future research directions motivated by the work presented in this thesis.

Chapter 6 is a republishing of Ref. [67]. It can be considered supplemental to the primary UCP research presented in this thesis, as it is not directly related to the measurements of magnetized RF heating. In this chapter I detail work we did developing and demonstrating a scalable mean-field model for the electron component of a UCP. Accurately modeling charge particle dynamics

in finite-size plasma has challenges due to issues with inconsistent parameter scalings when one changes the total number of charges to reduce computational complexity, so we developed a scalable mean-field model that produces self-consistent electron thermal equilibrium distributions to address this problem. We demonstrate the model's usefulness by producing precise determinations of UCP potential depth as a function of applied DC field strength, for example.

Chapter 2

Basic plasma background

The purpose of this chapter is to introduce and define plasma parameters and properties necessary for understanding the theory and experiments detailed in the following chapters. Most topics covered can be found in additional detail in many introductory plasma textbooks. First, I identify important time, length, and dimensionless scales in the context of magnetic field-free plasmas from macro- and microscopic pictures. Then I go over in summary some of the differences and challenges that arise in treating plamas with strong uniform magnetic fields. Finally, I discuss key properties distinctive to ultracold neutral plasmas. These concepts provide the foundation for determining applicable physical models and interpreting experimental measurements as covered in the remainder of the dissertation.

2.1 Plasma oscillations

A number of important, general plasma parameters can be deduced from relatively straightforward configurations [26, 28, 68]. For example, the electron dynamic response timescale can be investigated using a simple slab model. Figure 2.1 shows a not-to-scale diagram of a plasma composed of heavy ions (with unit charge $Z_{\rm i} = +e$ and charge density $\rho_{\rm i} = Z_{\rm i} n$) and electrons with equal charge density $\rho_{\rm e} = -en$. If the slab is displaced an amount z then we can use Gauss's law to determine the electric field $\vec{\mathbf{E}}$ within the region of the plasma where the charge density is neutral. We assume the spatial extent of the plasma in the xy-plane is large compared to the z displacement so that $\vec{\mathbf{E}}$ is anti-parallel to the surface of a Gaussian pillbox $d\vec{A}$,

$$|\mathbf{E}| = enz/\epsilon_0. \tag{2.1}$$

This can be interpreted as a linear restoring force that causes the electrons to oscillate about the heavy ions with frequency ω. Newtonian mechanics predicts

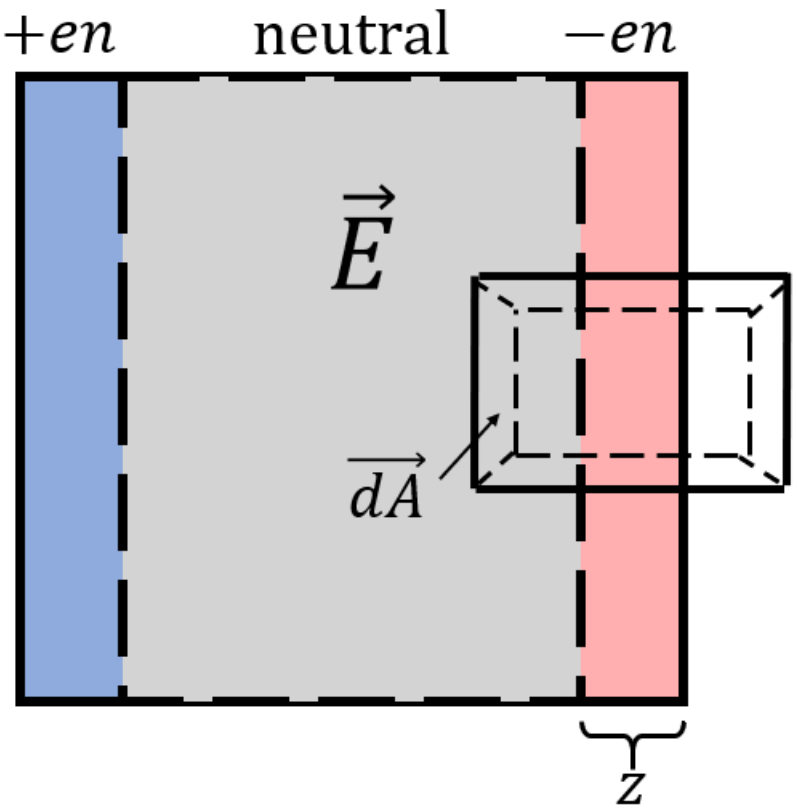

Figure 2.1: Slab model cartoon for exploring basic plasma properties.

$$
\begin{aligned}
m_{\mathrm{e}} z\omega^2 - e^2 n z/\epsilon_0 &= 0 \\
\omega_p &= \sqrt{\frac{e^2 n}{m_{\mathrm{e}}\epsilon_0}},
\end{aligned}
\tag{2.2}
$$

where we have identified the characteristic plasma frequency ω_p.

In the case of a finite ion mass, or other multicomponent considerations, the combined frequency is given by [68]

$$
\omega_p^2 = \sum_\nu \frac{q_\nu^2 n_\nu}{m_\nu \epsilon_0} = \sum_\nu \omega_{p\nu}^2, \tag{2.3}
$$

where ν represents the particle species. For our UCPs, the $^{85}\mathrm{Rb}$ ion mass is a factor of roughly 154,000 times larger than the electron [69]. Thus our plasma frequency is well approximated by the electron plasma frequency $\omega_p \approx \omega_{p\mathrm{e}}$.

2.2 Debye screening length

Alongside timescale ω_p^{-1} we also need to introduce an important characteristic length scale, the Debye screening length. The Debye screening length appears frequently in calculations for plasma collision parameters and dielectric response functions. It can also characterize how well the interior of the plasma is shielded from edge effects. In this section we derive expressions for the Debye length through different pictures that each provide context for this length scale's important role in plasma physics.

The derivation of the plasma frequency in Section 2.1 does not explicitly incorporate thermal effects for the particles. Imagine the same picture as Figure 2.1 with cold, motionless ions and electrons at temperature T_{e}. With a characteristic timescale ω_p^{-1} and thermal velocity $v_{\mathrm{th}} = \sqrt{k_{\mathrm{B}} T_{\mathrm{e}}/m_{\mathrm{e}}}$, we can define a characteristic length scale

$$
\lambda = \frac{v_{\mathrm{th}}}{\omega_p} = \sqrt{\frac{\epsilon_0 k_{\mathrm{B}} T_{\mathrm{e}}}{e^2 n_{\mathrm{e}}}}. \tag{2.4}
$$

In the context of the above slab configuration, we can identify the potential energy per electron $\Delta U(z)$. We find that a displacement $z = \lambda$ corresponds to a balance between thermal and potential

energy, [26]

$$\Delta U(\lambda) = \frac{e^2 n \lambda^2}{2\epsilon_0} = \frac{1}{2} k_{\mathrm{B}} T_{\mathrm{e}}. \tag{2.5}$$

These derivations demonstrate in a straightforward way the important relationships between plasma length scales, thermal properties, and dynamic timescales. A more formal derivation solves Poisson's equation for the electric potential response to a test charge q inside a plasma in thermal equilibrium with density n and temperature T [26, 28, 68]. The details of the derivation can be found in many introductory plasma textbooks, so I will simply quote that the end result finds a screened Coulomb response

$$\phi(r) = \frac{q}{4\pi\epsilon_0 r} e^{-r/\lambda_{\mathrm{D}}}, \tag{2.6}$$

where we've identified the characteristic lengthscale $\lambda \to \lambda_{\mathrm{D}}$ as the Debye screening length

$$\lambda_{\mathrm{D}} = \sqrt{\frac{\epsilon_0 k_{\mathrm{B}} T}{e^2 n}}. \tag{2.7}$$

A more detailed derivation produces the multicomponent form [68]

$$\frac{1}{\lambda_{\mathrm{D}}^2} = \sum_{\nu} \frac{q_\nu^2 n_\nu}{\epsilon_0 k_{\mathrm{B}} T_\nu} = \sum_{\nu} \frac{1}{\lambda_{\mathrm{D}\nu}^2}. \tag{2.8}$$

Even though this form suggests the ion contribution dominates the overall screening length when $T_{\mathrm{i}} \ll T_{\mathrm{e}}$, the UCP phenomena we are interested in occur on timescales fast enough that ion motion can be neglected. Therefore, we drop the ion contribution and revert to the form in (2.4) for λ_{D}.

2.3 Collisions & Coulomb Logarithm

The previous sections examined some macroscopic plasma behaviors by treating the electrons and ions as a continuous charge density. In addition, certain plasma properties can be deduced by analyzing the microscopic binary Coulomb interactions between individual charged particles. Here we consider the case of momentum transfer of a projectile electron due to ordinary binary

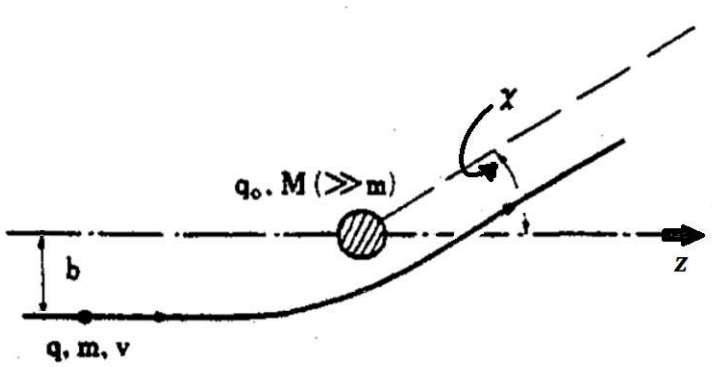

Figure 2.2: Coulomb collision between an electron and heavy ion, adapted from Ref. [68].

Rutherford scattering with a heavy ion $q_0 = +e$ as in Figure 2.2 [68]. The relationship between the projectile's velocity v, impact parameter b, and deflection angle χ is given by [26, 68]

$$b = \frac{e^2}{4\pi\epsilon_0 m_e v^2} \cot\frac{\chi}{2}. \tag{2.9}$$

For the special case where χ is a 90 degree deflection we have the characteristic impact parameter $b_\perp = e^2/4\pi\epsilon_0 m_e v^2$. Vector geometry tells us the momentum transfer from the initial z direction of travel is

$$\Delta p_z = -2|\mathbf{p}| \sin^2\frac{\chi}{2}. \tag{2.10}$$

Substituting the scattering angle from (2.9) into the above equation produces an expression for the momentum transfer of an unmagnetized binary Coulomb collision as a function of impact parameter and velocity.

Applying this in the case of an average rate of momentum transfer $\langle \dot{p}_z \rangle$ from multiple Coulomb collisions in an spatially uncorrelated cloud of charges with uniform density n and characteristic spatial extent σ yields

$$\langle \dot{p}_z \rangle = \int_0^\sigma \underbrace{\Delta p_z(b)}_{\frac{\text{Transfer}}{\text{Encounter}}} \underbrace{nv(2\pi b)\mathrm{d}b}_{\frac{\text{Encounters}}{\text{Time}}} \propto \int \frac{\zeta}{1+\zeta^2}\,\mathrm{d}\zeta \tag{2.11}$$

where $\zeta = b/b_\perp$. By inspection we see that this integral diverges logarithmically for large spatial extents. To correct for this unphysical result, a maximum impact parameter $b_{\max} \propto \lambda_{\mathrm{D}}$ is often used since this is the characteristic length scale over which plasma interactions decrease. This produces a textbook momentum transfer rate formula which contains the familiar Coulomb logarithm term,

$$\langle \dot{p_z} \rangle = -\frac{ne^4}{4\pi\epsilon_0^2 m_{\mathrm{e}} v^2} \ln \sqrt{1 + \frac{b_{\max}^2}{b_\perp^2}}. \tag{2.12}$$

Even though a maximum collision impact parameter is often utilized to correct for unphysical integral divergences, this particular solution using a hard, piecewise cutoff is itself unphysical. More detailed approaches seek to use screened, regularized, or effective potentials in place of bare Coulomb interactions [42, 70, 71]. Basically, the unmagnetized binary collision picture generally works well at describing shorter range interactions but fails when considering long range phenomena. This is in contrast to the dielectric linear response treatment, which will be discussed in more detail in Section 3.2, that can handle long range and collective effects well but formally diverges at small distances.

The $\ln \Lambda$ Coulomb logarithm term derived in (2.12) is $\ln \sqrt{1 + b_{\max}^2/b_\perp^2}$. Depending on the formalism and context of integration used in analyzing Coulomb collisions, other forms for $\ln \Lambda$ may appear like $\ln(b_{\max}/b_{\min})$ or $\ln(\lambda_{\mathrm{D}}/r_{\min})$ where $r_{\min}$ is the average classical distance of closest approach [26, 42, 72]. These forms produce divergent and unphysical results when the length scale ratios in the arguments approach unity or less. More detailed treatments that correct divergences in collision calculations self-consistently, such as the effective potential theory [70], can be used to find a generalized Coulomb logarithm. This generalized Coulomb logarithm can be approximated for many plasmas by the form $\ln\left(1 + C\lambda_{\mathrm{D}}/r_{\min}\right)$ where C is a constant of order unity [27, 70].

The regime where the Coulomb logarithm is well-approximated by the expression $\ln(\lambda_{\mathrm{D}}/r_{\min})$ is called the weakly coupled regime for reasons that will be explained in the following section [28]. Rewriting $r_{\min}$ in terms of the density n and λ_{D} yields

$$r_{\min} = \frac{e^2}{4\pi\epsilon_0 k_{\rm B} T_{\rm e}} = \frac{1}{4\pi n \lambda_{\rm D}^2}. \tag{2.13}$$

So when weakly coupled

$$\Lambda \approx \frac{\lambda_{\rm D}}{r_{\min}} = 4\pi n \lambda_{\rm D}^3 = 3N_{\rm D}, \tag{2.14}$$

where we have identified $N_{\rm D} = 4\pi n \lambda_{\rm D}^3/3$ as the average number of charges in the volume of a Debye sphere. Immediately we see that the weakly coupled limit corresponds to $N_{\rm D} \gg 1$, and conversely the strongly coupled limit implies $N_{\rm D} < 1$. The failure of basic plasma theory in the strong coupling regime is underscored by this unphysical, contradictory prediction that particle interactions are shielded by Debye screening over a distance $\lambda_{\rm D}$ even though there is on average fewer than one charge within that screening volume.

2.4 Coulomb coupling parameter

In the previous section we found that binary Coulomb interactions within plasma can be characterized using the "plasma parameter" $\Lambda \sim N_{\rm D}$. We showed how this parameter could be used to define a boundary between weakly and strongly coupled plasmas, and it can also be expressed as a ratio of characteristic length scales. In this section we gain additional insight in plasma parametrization by evaluating ratios of average particle energy scales.

Consider the average inter-particle potential energy between a pair of nearest-neighbor charges. For density n the nearest neighbor to a charge will on average be one Wigner-Seitz radius away, $a_{\rm WS} = (4\pi n/3)^{-1/3}$. Substituting $\langle|\mathbf{r}_1 - \mathbf{r}_2|\rangle \to a_{\rm WS}$ for the average inter-particle separation gives a nearest-neighbor potential energy (nnPE)

$$\langle {\rm nnPE} \rangle = \frac{e^2}{4\pi\epsilon_0 a_{\rm WS}}. \tag{2.15}$$

Taking $\langle {\rm KE} \rangle = k_{\rm B} T$ as proportional to the average kinetic energy per charge, we can define the dimensionless ratio of energies

$$\begin{aligned}\Gamma \equiv \frac{\langle \mathrm{nnPE} \rangle}{\langle \mathrm{KE} \rangle} &= \frac{e^2}{4\pi\epsilon_0 k_\mathrm{B} T} \sqrt[3]{\frac{4\pi n}{3}} \\ &\sim \frac{n^{1/3}}{T}.\end{aligned} \tag{2.16}$$

The defined quantity Γ is called the Coulomb coupling parameter [13].

From (2.16) we can identify another expression for Γ:

$$\begin{aligned}\Gamma &= \frac{1}{4\pi} \sqrt[3]{\frac{4\pi}{3}} n^{-2/3} \lambda_\mathrm{D}^{-2} \\ &= \frac{1}{3} N_\mathrm{D}^{-2/3} = \sqrt[3]{\frac{1}{3}} \Lambda^{-2/3}\end{aligned} \tag{2.17}$$

(2.17) demonstrates the relationship between the Coulomb coupling parameter Γ and the "plasma parameter" Λ. In the previous section we noted the relationship between Λ and the separation of weakly and strongly coupled plasma regimes. Here we identify $\Gamma \gtrapprox 1$ as the region where strong coupling effects are important. It coincides with $N_\mathrm{D} < 1$ as noted in Section 2.4. Furthermore, from the definition in (2.16), we see that the strongly coupled regime is characterized by nearest-neighbor interactions overtaking thermal effects. When this occurs, exotic plasma effects could become relevant such as the development of spatial correlations through caging or crystallization of charges [13].

Additionally, the Coulomb coupling parameter is useful for scaling plasma parameters. As mentioned in Chapter 1, Γ is important for translating the results from UCP research with their low-to-moderate densities and extremely low temperatures to hotter, denser plasmas like those involved in certain fusion experiments or found in some astrophysical systems. Direct links in relevant physics between systems can be established as long as the densities and temperatures are scaled to keep Γ fixed. To be more specific, UCPs can be directly compared to other plasmas at comparable Γ so long as classical mechanics approximations apply. Our relevant plasma length scales are orders of magnitude larger than the charges' de Broglie wavelengths. Therefore we

expect classical physics to dominate quantum effects[1]; this is not necessarily true of other strongly coupled systems [42, 74].

2.5 Magnetized plasma

Up until now in the chapter we have considered magnetic field-free cases for introducing plasma properties. Magnetic fields generate a Lorentz force term on plasma charges, and in this section we explore a number of important plasma scales and regimes that depend on the strength of the field. We begin by identifying parameters associated with individual magnetized charge trajectories and finish with a discussion on challenges facing treatments of magnetized binary Coulomb collisions.

2.5.1 Length scales and regimes

When a magnetic field is applied to a plasma the dynamics can change due to the additional force on the charges. First, let us examine the effect of the Lorentz force $\mathbf{F} = q\mathbf{v} \times \mathbf{B}$ on the trajectory of a single particle with charge q and velocity $\mathbf{v}$ moving in a uniform magnetic field $\mathbf{B}$. We define a coordinate system relative to the magnetic field so that $\hat{z}$ is parallel to $\mathbf{B}$. The motion of the particle is unaffected by the field in the parallel direction because the Lorentz force acts in the plane perpendicular to the magnetic field. The force is also perpendicular to the velocity, so the particle undergoes circular motion in the plane perpendicular to the magnetic field. The three dimensional trajectory is therefore in the shape of a helix. In terms of cylindrical coordinates where $r = 0$ is the central axis of the circular motion, the particle velocity can be expressed as $\mathbf{v} = 0\hat{r} + (\operatorname{sgn} q)v_\perp\hat{\phi} + v_z\hat{z}$. Figure 2.3 shows the helical trajectory of an electron moving in a region with $\mathbf{E} = 0$ and with speeds $v_z, v_\perp$ parallel and transverse to the direction of a magnetic field $\mathbf{B} = B\hat{\mathbf{z}}$.

[1]The main exception to this is the formation of Rydberg atoms via three-body recombination (TBR) (see Section 2.6.3). Even in the case of TBR in UCPs, semi-classical approximations describing dynamics of weakly bound, high quantum n-number Rydbergs are sometimes applicable [73].

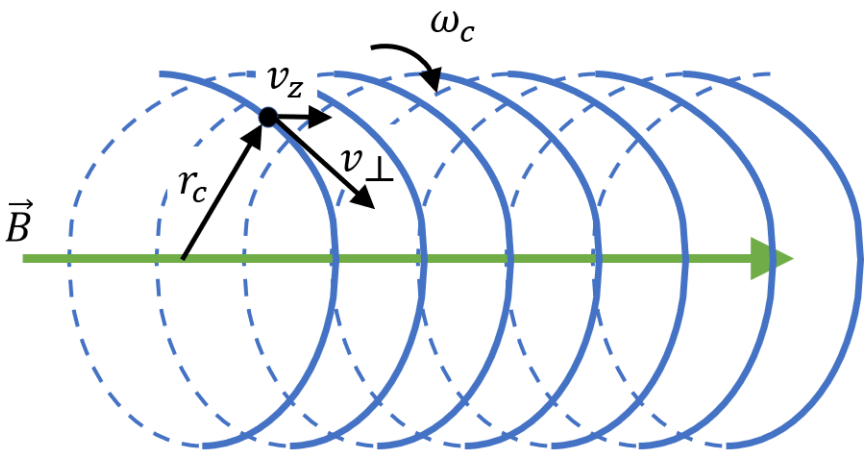

Figure 2.3: Helical trajectory of an electron in a uniform magnetic field.

The helical trajectory can be characterized using the cyclotron radius r_c (or Larmor radius, gyroradius) which is the radius of the circular path to the central axis (or guiding center) provided by the magnetic field. Newtonian mechanics finds

$$r_c = \frac{m_e v_\perp}{eB}. \tag{2.18}$$

Likewise, the cyclotron frequency (or Larmor frequency, gyrofrequency) is the angular frequency of the helical trajectory,

$$\omega_c = \frac{v_\perp}{r_c} = \frac{eB}{m_e}. \tag{2.19}$$

The plasma species' cyclotron frequencies can be compared to the plasma frequency. In particular, for the case of a UCP with $\omega_p \approx \omega_{pe}$ we find

$$\beta \equiv \frac{\omega_{ce}}{\omega_p} \gg \frac{\omega_{ci}}{\omega_p}, \tag{2.20}$$

due to the large mass ratio between species. In (2.20), we have defined the dimensionless magnetic field strength β. We see that this parameter depends linearly on the magnitude of the magnetic field, and we expect it to be an important scale factor for parameterizing magnetic field effects in

plasmas. Thus, for any magnitude of magnetic field applied to a UCP the magnetic field strength for electrons is effectively larger by the square root of the ~10^5 mass ratio compared to the ions.

Along with the frequency ratio β, magnetic field effects on a plasma can also be characterized by comparing length scales. In a typical weakly coupled plasma, each of the following length scales are distinguishable and form a hierarchy, from largest to smallest: the Coulomb mean-free-path λ_{col}, the Debye screening length λ_{D}, the inter-particle spacing a_{WS}, and the distance of closest approach (or Landau length) r_{min}. The effects of a magnetic field on a plasma depends on where the characteristic cyclotron radius $\bar{r}_c$ compares to this hierarchy of scales. Starting from (2.18), we can replace the projectile velocity assuming an isotropic Maxwell-Boltzmann distribution to define a characteristic electron cyclotron radius

$$\bar{r}_c \to r_c \equiv \sqrt{\frac{k_{\mathrm{B}} T_{\mathrm{e}}}{m_{\mathrm{e}}}} \frac{1}{\omega_c}. \tag{2.21}$$

We drop the bar over $\bar{r}_c$ in (2.21) assuming context determines whether r_c is for a single projectile with transverse speed $v_\perp$ or is a characteristic scale for a plasma with temperature T_{e}.

Ref. [27] investigates transport properties in the context of one-component plasma magnetization and identifies four regimes based on where r_c compares to the other plasma length scales. Since r_c depends on both the strength of the magnetic field in addition to the plasma temperature these regimes span a basis in the β-Γ parameter space. Figure 2.4 shows a diagram of the four magnetization regimes within this parameter space.[2] When $\Gamma \ll 1$ the four distinguishable regimes are, with increasing β, unmagnetized, weakly magnetized, strongly magnetized, and extremely magnetized plasmas. As Γ approaches and exceeds unity, strong coupling physics predicts a melding of length scales as the Debye length, inter-particle spacing (a in the figure), etc. become comparable to one another. As mentioned in Chapter 1, certain UCP experiments are capable of accessing and probing physics across these regimes.

[2]Reproduced from Ref. [27] with modifications as permitted by S Baalrud.

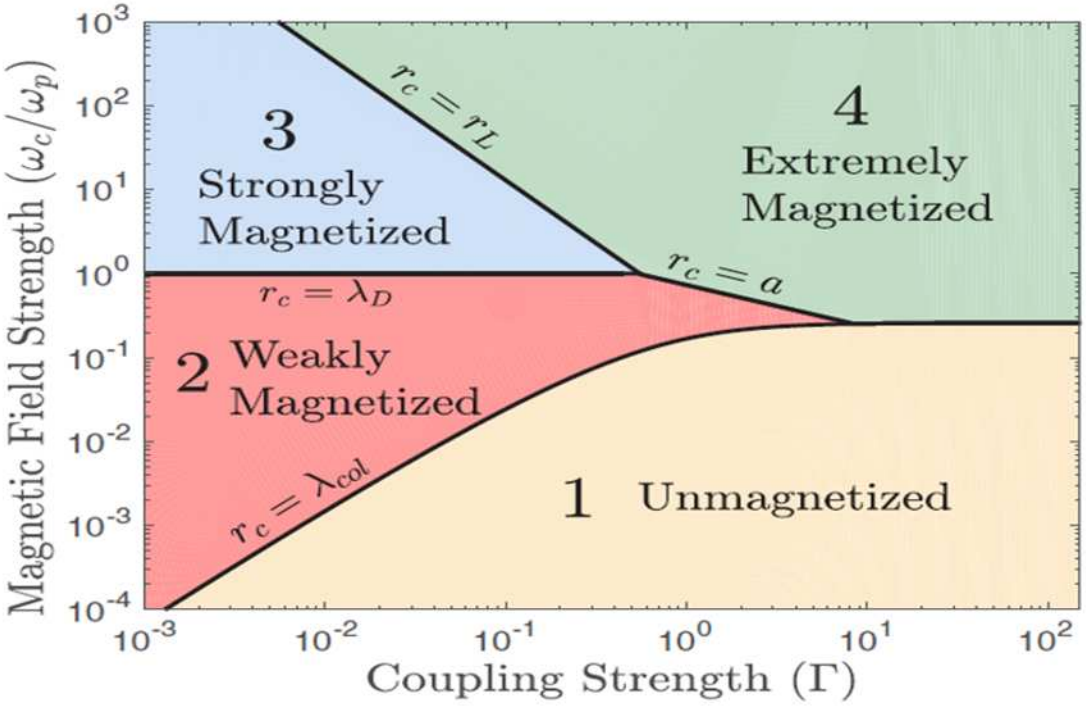

Figure 2.4: Transport regimes spanning magnetization-coupling phase space [27].

When $r_c > \lambda_{\text{col}}$, the plasma is considered unmagnetized. λ_{col} is the Coulomb collision "mean-free-path", v_{th}/ν where ν is the collision rate. I put the "mean-free-path" phrase in quotes because for weakly coupled plasma the charges undergo deflections due to the cumulative effect of *many* small-angle collisions over the length scale λ_{col}. If the cyclotron radius is larger than this length scale then the magnetic field has negligible effects on both the microscopic binary collisions as well as the average macroscopic transport properties as a whole.

If the cyclotron radius becomes comparable to λ_{col} but does not subceed the Debye screening length λ_{D}, then the magnetic field is expected to modify some macroscopic behavior while the microscopic collision dynamics remain largely unaffected. This is identified as the weakly magnetized regime [27].

For plasmas coupled weakly enough to have distinguishability between the Debye screening length and the classical distance of closest approach (or Landau length), we can identify a third regime: strongly magnetized. When $r_c < \lambda_{\text{D}}$ the dynamic screening properties of the plasma will be affected by electron magnetization. In terms of plasma kinetic theory (see Section 3.2), both the

distribution function and the collision operator become modified by the presence of the magnetic field.

The authors of Ref. [27] depict a boundary on strong magnetization given by $r_{\mathrm{L}} = \sqrt{2} r_{\mathrm{min}}$. If the magnetic field strength is large enough, then $r_c < r_{\mathrm{L}}$ and the cyclotron radius becomes the smallest relevant collisional length scale. In this "extremely magnetized" regime the plasma dynamics can be vastly different due to the confinement of electrons along magnetic field lines. Graphic simulations of particle behavior for the extremely magnetized OCP shows the charges oscillating with quasi-one dimensional trajectories [27, in Suppl. Materials]. The charge scattering angle distribution is greatly altered as the effects of cumulative, many low-angle collision interactions are suppressed while high-angle, 180° events dominate.

In principle, another regime boundary should exist when the charge cyclotron radius approaches the de Broglie wavelength. When this occurs, the cyclotron orbits become quantized into so-called Landau levels and a quantum description of plasma dynamics is prescribed [42, 74]. As mentioned previously, the de Broglie wavelength is orders of magnitude smaller than all relevant plasma length scales in our case, including the cyclotron radius, so a classical description is appropriate and the effects of quantum mechanics on plasma magnetization can be neglected.

2.5.2 Magnetized binary collisions

It is reasonable to desire an analytic approach to magnetized binary collisions as was utilized in Section 2.3 for the case of unmagnetized Coulomb interactions. However, the inclusion of the magnetic field in the equations of motion generates an inseparable coupled system that does not possess a general closed form solution [42]. The problem gets even more complex; the inclusion of a magnetic field breaks rotational symmetries without introducing compensatory invariants, therefore the Hamiltonian acquires additional degrees of freedom and becomes non-integrable [75–77]. This is also true in the case of bound, magnetized hydrogenic and Rydberg systems, which have been studied as diamagnetic Kepler problems [77–80]. The fact that the equations of motion

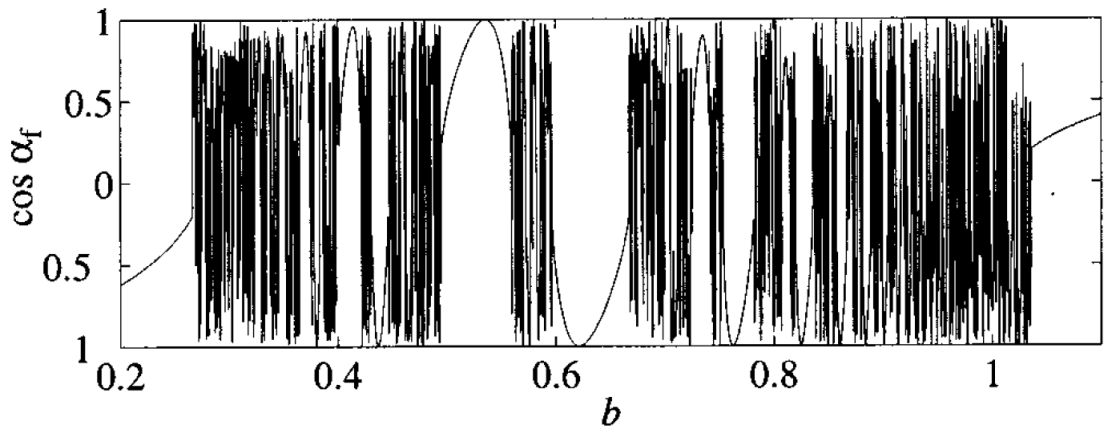

(a)

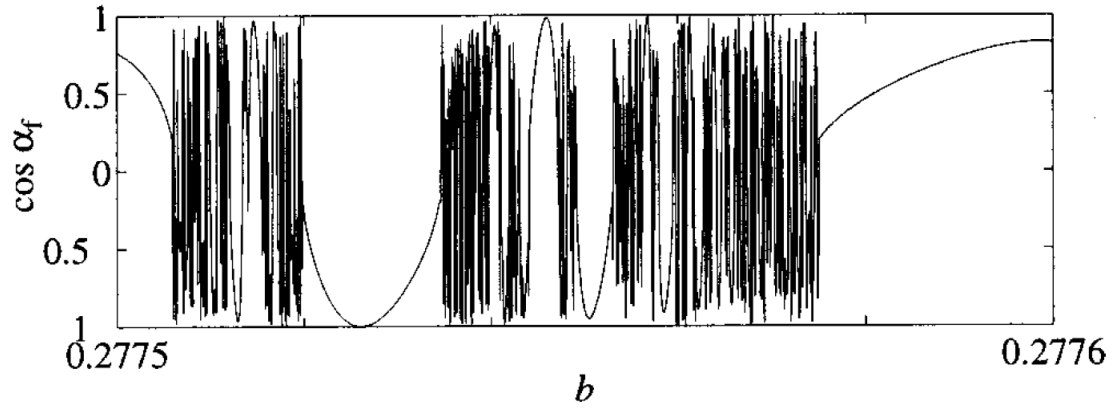

(b)

Figure 2.5: Magnetized Coulomb scattering angles as a function of scaled impact parameter exhibiting chaotic, fractal behavior [77].

are not integrable implies the possibility for regimes with chaotic behavior, and this is indeed observed to be the case.

Classical trajectory simulations of magnetized Coulomb interactions exhibit the chaos of the equations of motion. Figure 2.5 shows numerical results for the asymptotic final pitch angle $\cos\alpha_f = v_z/v$ for an electron scattering off an ion in a uniform magnetic field as a function of scaled impact parameter b [77]. Evaluation of a small subsection in b plotted in the lower panel Figure 2.5b reveals the fractal nature of the chaotic and nonchaotic windows [76]. The physical justification for the classical chaotic picture becomes less clear with the inclusion of quantum mechanical effects. While analogies can be made between closed, periodic orbits and quantum me-

chanical resonances through Einstein-Brillouin-Keller quantization and semiclassical eigenvalue solutions [78–80], the fractal nature of the sensitivity to initial conditions predicted in irregular classical trajectories unphysically infers variations over length scales shorter than the projectile de Broglie wavelength [42, 75–77].

Under certain circumstances, such as at high charge velocities, a perturbative treatment can be applied to the magnetized electron-ion scattering problem (see Chapter 3 of Ref. [42] and references therein). The validity of analyzing cold or low velocity magnetized binary collisions through perturbation theory is called into question in part due to the issues mentioned above. Further discussion of this treatment can be found in Section 3.1.

2.6 Ultracold plasmas

So far in this chapter I have introduced characteristic scales and parameters generally for any type of plasma. Ultracold plasma systems have distinctive properties that deserve differentiation from other plasma categories. In this section we continue to build on our introductory foundation by presenting these typical UCP properties; the specific details applicable to our laboratory's research plasma are discussed in Chapter 4.

2.6.1 Formation

Most UCPs are created from a finite-size, laser-cooled atomic sample generated in a particle trap [14,18,81–85] or from an atomic/molecular supersonic beam [86,87]. The cold neutral sample can be ionized using, e.g., resonant photoionization [14, 18, 82–84], ultrafast field ionization [85], or evolution from a Rydberg gas [81, 86, 87]. Under these circumstances the two charge species are heavy cations (atomic/molecular ions) and light anions (electrons). Conserving momentum and energy during the ionization process with such a large mass discrepancy between species implies the excess energy beyond the ionization threshold is almost entirely imparted to the lighter electrons. For a typical photoionized UCP beginning with a ~$100\,\mu$K neutral sample, this excess

energy (ΔE in temperature units) can range from many hundreds of Kelvin to below threshold [14, 19].

Immediately after ionization the system is charge-neutral. Assuming the formation region is mostly free of external fields (no Penning-type trap configurations for example), there is no force confining either particle species to the charge-neutral electron-ion "cloud", and the less massive, more energetic electrons are free to escape. Over a relatively short timescale, a positive space-charge potential develops as the most energetic electrons leave the region overlapping the cold ions. The no-longer-perfectly-neutral ionic potential becomes deep enough to confine the remaining electrons within the ion cloud once a large enough fraction of electrons have escaped. This lost fraction is often referred to as the charge imbalance. The resulting finite-sized, quasi-neutral system of electrons confined to the unbound, cold ions is what is identified as the ultracold plasma.

Depending on the conditions for formation, different total fractions of the initial neutral atomic/ molecular sample may be ionized. In our specific case of UCP formation through resonant photoionization with a saturating laser field, ionization fractions are typically between 10 and 50% [82]. Furthermore, the average initial atomic densities for our neutral cloud are on the order of $10^7\,\mathrm{cm}^{-3}$. These properties suggest interactions between the plasma species and neutral species can be ignored [14]. The mean free path for the Rb-e interactions is much larger than the plasma size since the cross-sections are so small [88, 89], and in our case there is not a large enough fractional concentration of neutrals to compensate. The gist here is after photoionization the remaining neutral Rb atoms have a negligible effect on the UCP, and the system can be treated as having only the two charged species.

This establishes three distinct UCP properties: a finite-sized, quasi-neutral, two-species system; a high mass ratio between the two species; and a significant temperature ratio between species immediately after formation. Even though the charge imbalance after formation can be upwards of 50% or more, screening effects will cause the remaining electron density distribution to roughly match the ion distribution in the center of the cloud where they overlap. This is why UCPs are classified as quasi-neutral; there can exist a significant imbalance in the total charge count as a

whole, but the plasma physics of interest occurs in an effectively charge-neutral region. This reasoning justifies the matching densities approximation $n_{\mathrm{e}} \approx n_{\mathrm{i}}$ wherever $n_{\mathrm{e}} \neq 0$.

At the very beginning of this chapter we introduced the plasma frequency $\omega_p = \sqrt{q^2 n/m\epsilon_0}$. Using the UCP properties we established, we can compare the ion and electron frequencies and find a combined effective plasma frequency using (2.3). Since the charge magnitude and densities of the two species are the same we have $\omega_{p\mathrm{e}}/\omega_{p\mathrm{i}} = \sqrt{m_{\mathrm{i}}/m_{\mathrm{e}}}$. For $^{85}\mathrm{Rb}$ this ratio is approximately 400, therefore $\omega_p \approx \omega_{p\mathrm{e}}$; sensically, the electrons dominate the timescale for a wide range of plasma dynamics.

Likewise, we can check the ramifications of UCP properties on the Debye screening length λ_{D}. Section 2.2 defines $\lambda_{\mathrm{D}} = \sqrt{\epsilon_0 k_{\mathrm{B}} T/q^2 n}$. For $T_{\mathrm{e}} \gg T_{\mathrm{i}}$ we have $\lambda_{\mathrm{De}}/\lambda_{\mathrm{Di}} = \sqrt{T_{\mathrm{e}}/T_{\mathrm{i}}} \gg 1$, so (2.8) would predict the effective plasma Debye length is predominantly ionic. This, however, is somewhat in contradiction with the statement made above that the electrons dominate the general plasma dynamics over the colder, heavier ions. This is rectified by simply neglecting the comparably small ion mobility and keeping only the electronic contribution [68], so the effective UCP Debye screening length is

$$\lambda_{\mathrm{D}} \approx \lambda_{\mathrm{De}} = \sqrt{\frac{\epsilon_0 k_{\mathrm{B}} T_{\mathrm{e}}}{e^2 n_{\mathrm{e}}}}. \tag{2.22}$$

Since the UCPs we study are finite-size systems we can characterize their spatial extent with a length scale σ, like the width of a spherical Gaussian distribution. It is essential that the UCP screening length be shorter than this width, $\lambda_{\mathrm{D}} < \sigma$, in order for there to be a plasma rather than just a collection of charges. Else, the screened, quasi-neutrality assumption would be broken, and the system as we have defined it in this chapter would not exist as a plasma.

2.6.2 Expansion

Up to this point we identified ultracold plasmas as finite-size, quasi-neutral systems of cold, heavy ions and comparable or hotter electrons. The charge imbalance that begins developing immediately after formation generates the confining potential for the electrons. This is illustrated in cartoon format in steps I and II of Figure 2.6a. The ions, unlike the UCP electrons, are unbound

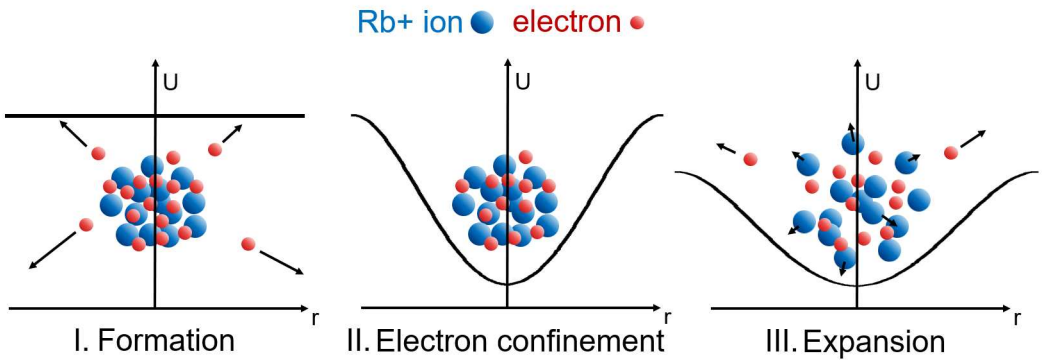

(a)

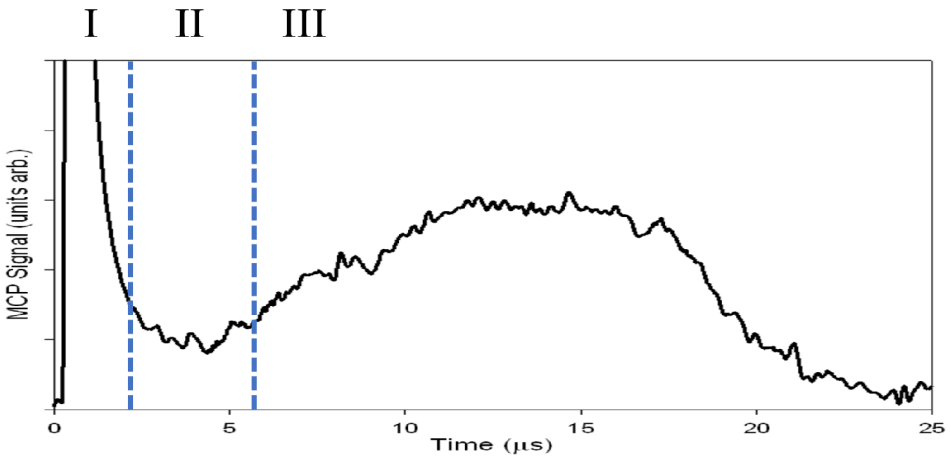

(b)

Figure 2.6: Diagram illustrating key steps in the formation and evolution of a UCP: (a) a cartoon depicting charge positions & velocities, and electric potential U as seen by electrons; (b) an example electron escape trace showing signatures of the prompt peak, confinement, and evaporation at the corresponding steps. Section 4.1.2 discusses the details for detecting UCP electron escape rates like that depicted here.

and free to expand, limiting the plasma lifetime. This final stage in the life of a UCP, where the ion expansion becomes significant, is illustrated in step III of Figure 2.6a. It depicts the diminishment of the ionic confining potential as the plasma expands, and this reduction in confining strength implies an increase in electron escape rate.

Before continuing, it is worth mentioning an observational challenge for UCP experiments. The ultracold nature of the plasma means any object near room temperature that becomes thermally coupled will destroy the UCP. Therefore *in situ* measurements using typical hot plasma diagnostic probes are impossible. This challenge can be overcome using other measurement techniques such

as spatial imaging of ions [90] or charge detection on a microchannel plate detector (MCP) [14,20]. Charge detection with MCPs can be split into two categories, time-resolved currents and spatially resolved distributions. Figure 2.6b shows an illustrative example of a time-resolved UCP electron escape current traced by an MCP from ~$300\,\mathrm{K}$ plasma electrons where the regions denoted I, II, and III roughly correspond to the steps depicted in Figure 2.6a.

With $t = 0$ as the moment of photoionization in Figure 2.6b, we see the early "off-the-charts" peak in escape rate associated with the development of the charge imbalance in interval I; this we call the prompt peak. Interval II, when the electrons are effectively well-confined, is characterized by the minimum escape rate detected. During the early part of this time the expansion of the plasma is practically negligible. While there are important early-time heating effects (see following section), the initial ion spatial and velocity distributions for the most part are determined by the ultracold neutral species' distributions at the time of ionization.[3]

Continuing along with this picture, the third and final interval begins when the ion expansion becomes significant. As the ions expand, the depth of the potential confining the electrons lessens. The signature for this behavior in Figure 2.6b can be seen as the later, broader maximum observed in electron escape rate. The escape current in interval III initially increases due to plasma expansion then decreases to zero as the plasma eventually becomes emptied of electrons.

There are two independent mechanisms that drive the plasma expansion: Coulomb explosions and thermal pressure. The Coulomb explosion mechanism is fairly straightforward: if an electron-confining space-charge develops then that same space-charge must anti-confine the oppositely-charged ions. The timescale associated with this ion-ion interaction process should be characterized by the ionic plasma frequency $t_{\mathrm{explosion}} \sim \omega_{p\mathrm{i}}^{-1} \gg \omega_{p\mathrm{e}}^{-1}$ and becomes less significant closer to neutrality. Numerical simulations of UCPs as a function of charge imbalance suggest the plasma interior is relatively unaffected due to screening. However, the enhanced ion expansion at larger charge imbalances can affect electron temperature [91]

[3]This approximation should hold true at least in cases when the ionization event (i.e. laser pulse) is shorter than ω_p^{-1}.

The expansion mechanism due to thermal pressure is only slightly more complicated. Immediately after formation, the ions have a characteristic thermal velocity comparable to the neutrals' velocity and much smaller than the electron thermal velocity $v_{\mathrm{i}} = \sqrt{k_{\mathrm{B}}T_{\mathrm{i}}/\mathrm{m_i}} \ll v_{\mathrm{e}}$. If the expansion is self-similar, as is predicted in the case with a Gaussian spatial distribution with size σ, then one would expect the size to behave like $\sigma(t)^2 = \sigma(0)^2 + v_{\mathrm{exp}}^2 t^2$ where naïvely the expansion velocity v_{exp} is the ions' thermal velocity v_{i} [92]. However, the coexistence of the electron species alters this behavior. In terms of a thermodynamic picture, the ionic potential forms a containing volume V that experiences a pressure P due to an electron gas with temperature T_{e}, $PV \propto T_{\mathrm{e}}$ [93]. Assuming a static volume (i.e. $v_{\mathrm{i}} = 0$) predicts the ion expansion will evolve according to the electron thermal velocity. A thorough analysis reveals the effective thermal expansion velocity is a weighted quadrature sum of species velocities, [92]

$$\begin{aligned} v_{\mathrm{th}}^2 &= v_{\mathrm{i}}^2 + \frac{m_{\mathrm{e}}}{m_{\mathrm{i}}} v_{\mathrm{e}}^2 \\ &= \frac{k_{\mathrm{B}}}{m_{\mathrm{i}}} \left(T_{\mathrm{i}} + T_{\mathrm{e}}\right) \approx \frac{k_{\mathrm{B}} T_{\mathrm{e}}}{m_{\mathrm{i}}}. \end{aligned} \tag{2.23}$$

For typical UCPs this electron thermal pressure is the dominant expansion mechanism [16, 20, 92]. The characteristic expansion time scales with the ion mass, in contrast to the plasma oscillation time ω_p^{-1}, and in certain cases may be considered slow compared to the electron-ion dynamics of interest.

2.6.3 Heating and cooling mechanisms

The objective of this thesis work is to investigate electron-ion collision rates across electron magnetization regimes through utilization of RF heating of ultracold plasma. With this plasma heating objective in mind, it is worth mentioning notable intrinsic heating mechanisms that exist for UCPs. Here I will make brief remarks on disorder induced heating, three-body recombination, and DC-field formation heating, among other temperature evolution effects.

One of the distinctive properties of photoionized UCPs mentioned in the previous section is that the initial ion phase-space distribution immediately after formation corresponds to the neutral

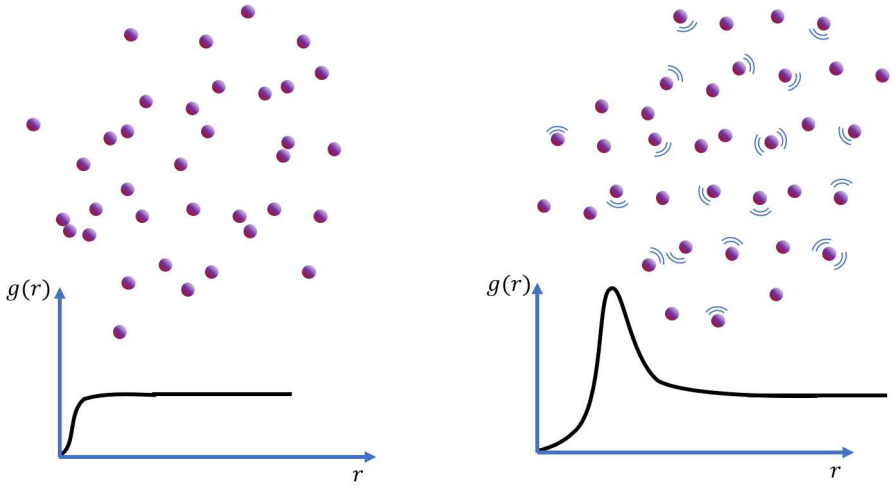

Figure 2.7: Sketch of the effect of disorder induced heating (DIH) on charge spacing and the pair correlation function $g(r)$: (a) immediately after formation the charges have uncorrelated positions with bunches and voids; (b) DIH creates more uniform particle spacings and converts correlation energy present in (a) into heat.

species distribution. Since the inter-molecular forces between the neutrals are predominantly close range with a range much smaller than the average interparticle spacing, then it is safe to assume the particle pairs are spatially uncorrelated to a good approximation. Once photoionized, if the charges' velocities do not change significantly, the uncorrelated initial pair positions imply that there will be a significant number of close repulsive neighbors and voids. A diagram illustrating these uncorrelated charges is shown in Figure 2.7a. The repulsion between close charges and relative attraction toward voids converts electrostatic potential energy into kinetic energy and eventually heat as the charges settle into spatially correlated potential wells, see Figure 2.7b. This is called disorder induced heating (DIH) [13, 94], and its observed effect is a rapid reduction in coupling strength as the charges approach a correlation temperature approximated by $T_{\mathrm{DIH}} = \frac{2}{3}\frac{e^2}{4\pi\epsilon_0 k_{\mathrm{B}} a_{\mathrm{WS}}}$ over a time $t \sim \omega_{p\nu}^{-1}$ where ν is an index indicating charge species [95]. The large ratio between electron and ion masses once again causes a timescale disparity such that DIH associated with the electrons occurs much faster than the ions.

The fact that UCPs are cold and quasi-neutral means there is a probability for ions and electrons to recombine into Rydberg atoms [96]. Electrons bound in Rydberg states with energies below the

kinetic bottleneck are statistically driven away from reionization and instead toward more deeply bound atomic states [73, 97]. These recombination and state-lowering interactions require a third particle be included to carry away the excess binding energy. In plasmas, these particles can be photons or charges. In the case of a photon it is called radiative recombination [26]. In the case of a charge, the light electrons have a higher likelihood of acting as an excess energy carrier than ions, so reactions with a secondary electron like

$$\mathrm{Rb}^{+} + 2\,\mathrm{e}^{-}(\mathrm{cold}) \rightarrow \mathrm{Rb}^{*} + \mathrm{e}^{-}(\mathrm{hot})$$

fall under the umbrella of three-body recombination (TBR) [96, 97].

Predictions for a weakly coupled UCP produce $T^{-0.63}$ and $T^{-9/2}$ temperature scalings for radiative and three-body recombination rates, respectively [98]. For ultracold temperatures radiative recombination is a much slower process compared to three-body recombination, and furthermore the product of a radiative reaction is two neutral particles that effectively cease to interact with the remaining plasma [26]. This is not true of three-body recombination. When a "bystander" third-body electron carries away excess energy from an electron binding to an ion or from an n level-lowering collision with a Rydberg, the bound neutral may effectively stop interacting with the plasma, however the free electron does not. The UCP will heat up from the accumulation of binding energy redistributed throughout the plasma as it gets transferred via third-body electrons. Figure 2.8 shows electron and ion temperatures from molecular dynamics simulations with initial conditions $T_{\mathrm{i}} = T_{\mathrm{e}} = 0$ and random uncorrelated particle positions [71]. It clearly illustrates the expected effects of disorder induced and three-body recombination heating.

Ultracold plasma experiments that rely on charge collection for observations, such as the one studied in this dissertation, necessarily require external DC fields to guide charges from the plasma toward the detector. Ref. [99] explores the influences of an electric field on plasma temperature during formation using numerical simulations with parameters that correspond to our experimental conditions. Unlike disorder induced heating and TBR, this electric field heating is predicted to be independent of initial plasma temperature for our conditions. For our experimental conditions, we

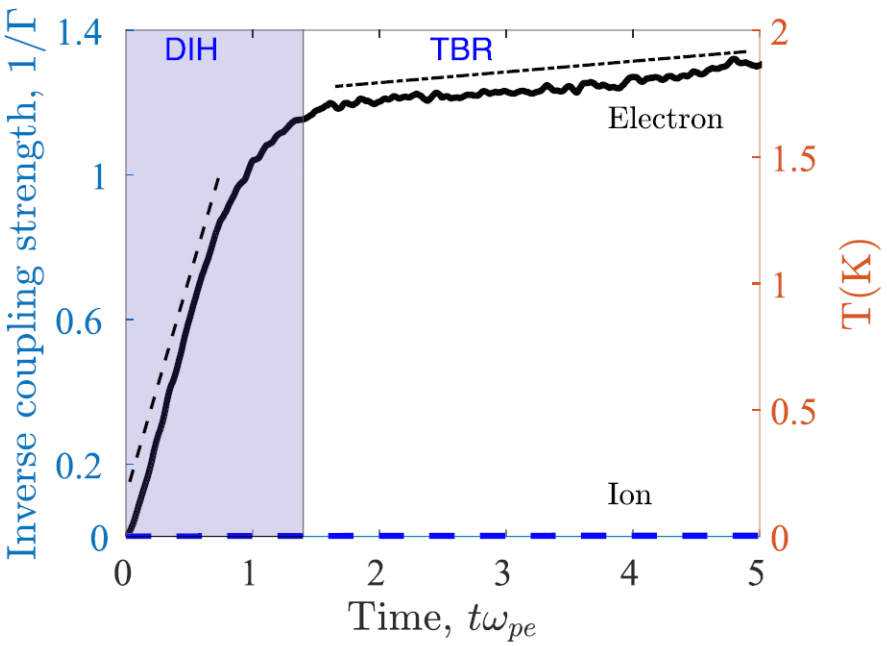

Figure 2.8: Simulated temperature evolution for electrons and ions starting with uncorrelated positions at $T_\mathrm{i} = T_\mathrm{e} = 0$ [71]. The electron temperature rise from disorder induced heating (DIH) and three-body recombination (TBR) is apparent.

can use small enough external DC fields at formation that the associated heating effect is less than 20% of the initial electron temperature.

In addition to the above heating mechanisms, there are also known cooling mechanisms that apply in UCPs. The two most obvious processes are adiabatic and evaporative cooling. In ideal thermodynamic terms, in the absence of heating mechanisms like those described above, an unbound ultracold plasma will expand freely into the vacuum according to adiabatic expansion with temperature evolution $T \propto V^{-2/3}$ [93, 100].

Since the electrons are bound by a finite potential the velocity distribution can be more accurately described as a truncated Maxwell-Boltzmann or a Michie-King distribution rather than a pure Boltzmann equilibrium distribution with a long "tail" of high velocity electrons [91, 101]. The cutoff on which velocity class of electrons that can escape the plasma moves to lower velocities when the ion expansion causes a reduction in depth of the electrons' confining potential. In principle, whether caused by expansion or an external field, the loss of electrons with statistically higher energies leads to a relative reduction in the temperature [102].

Heating and cooling effects in UCPs have been studied in great detail and often in the context of predicting limits on the achievability of strongly coupled conditions [13, 71]. Temperature increases of the electrons from disorder induced heating, TBR, DC-field formation heating, and even continuum lowering suggest an upper limit on electron coupling $\Gamma_{\rm e} \lessapprox 0.5$ just after formation [19]. The ion coupling typically ranges from $\Gamma_{\rm i} \approx 3$ and below, but in the context of laser cooling UCPs, the ion coupling parameter can be upwards of 10 or more [18].

In this chapter we identified and described key basic properties needed for understanding the physics in the rest of the thesis. We characterized a number of relevant physical scales and briefly discussed how magnetization parameters like the cyclotron radius and frequency can be used to define plasma magnetization regimes based on comparing these scales. We also concluded this chapter with a section summarizing typical UCP properties. All of these concepts introduced above will be referenced in some manner in the later chapters. The ultimate goal of this work is to report and interpret measurements of RF heating of magnetized electrons in a UCP, and this will be done in Chapter 5. In the next chapter we will explore and develop theoretical models in order to find an applicable scientific prediction for magnetized plasma RF heating.

Chapter 3

RF heating theory

The goal of this chapter is to develop a theory framework for understanding RF heating of magnetized plasma. We are motivated in part by the physics connection to RF heating of magnetically confined plasma like what is planned for ITER [21, 103, 104]. Through scaling relations in temperature and density, RF heating theory can also be mapped onto laser heating of plasma through inverse Bremsstrahlung effects such as what is used in direct-drive fusion designs [53, 54, 105]. There are a number of ways of approaching this problem, which includes various binary collision [30,42,45,106–109] and dielectric medium treatments [28,32,36,39,42–44,51,52,54,103,106]. In this chapter we briefly explore binary collision theories and develop in further detail two separate, yet related, dielectric linear response pictures: AC conductivity and stopping power-like energy transfer (SPLET).

3.1 Binary collisions

As shown in Section 2.3, in the absence of a magnetic field we could use a binary collision approach to determine an average momentum transfer rate for a projectile charge in a weakly coupled plasma. However, the inclusion of magnetic field effects in such a picture is nontrivial as even ordinary binary Rutherford scattering no longer has a general closed form solution for the trajectory. Remedies for this issue have arisen in an analytical form through perturbation theories [42, 45, 106, 109] or in a computational form through a modified collision operator [110].

The simple fact alone that a general analytic solution for magnetized collisions does not exist clearly makes their analysis a much more difficult beast, yet there are even more issues that arise in both the analytical and numerical realms. For example, classical trajectory and molecular dynamics-type simulations can require extraordinarily small timesteps to properly capture particle motion when ω_c is large or for hard scattering conditions when the impact parameter or velocity is small. Even when the solutions for these trajectories are computed with the proper timesteps the

picture is not simple. As mentioned in Section 2.5.2, there exist regions in parameter space where the trajectories are intrinsically chaotic. This amounts to considerable regimes where we expect perturbation theories to fail to apply.

Nevertheless, there are situations where a perturbative picture of magnetized binary collisions is appropriate. While the work presented in this thesis is not analyzed in the context of binary collisions where perturbative treatments are applicable, in the interest of inclusiveness, a brief summary of the principles of that treatment will be supplied; more in-depth discussion can be found in Refs. [42, 45, 109].

First, the many body interactions inherent in a plasma are approximated using a screened Coulomb potential as an effective two-body interaction. The authors of Refs. [42, 45, 106, 109] also "regularize" the interaction at the origin with a softening parameter to avoid issues that arise in pertubative treatments due to the singularity. Using a suitable potential for the collision, the interaction between the electron and target is treated as weak, i.e. the smallness parameter of the perturbative expansion is the electron-ion coupling strength $e^2/2\pi\epsilon_0\lambda m \langle v_0 \rangle^2 \sim \Gamma^{3/2} < 1$ where $\langle v_0 \rangle$ is the average initial relative velocity, λ the screening length, and m is the reduced mass which in our case of a heavy ion can be well-approximated by the electron mass. Analysis of the equations of motion in this picture yields a first-order approximation for the perturbed helical electron trajectory.

From the first-order perturbed trajectory of a single collision one can calculate the slowing force experienced by a charge traversing a plasma using a stopping power treatment. As demonstrated in Refs. [42, 45, 106, 109], calculating this slowing force using integrals based off the expansion of the $\exp i\mathbf{k} \cdot \mathbf{r}$ term in a Fourier transform can produce expressions for the first- and second-order energy transfer of the collision. They show the first-order term is zero (for the cases with and without magnetic field), and provide further discussion on the resulting non-zero second-order energy transfer. In Ref. [106] it is shown this binary collision picture agrees with an entirely alternate, yet complementary approach—the linear response treatment—in the weakly coupled

and fast projectile velocity regime assuming one chooses the correct cutoffs for integration in each treatment.

The wording used here is intentional; the solutions for charged particle energy transfer depend on the *user's choice* of cutoffs. There exists some physical justifications for cutoffs involving small impact parameters such as a quantum statistical potential [111] that approximates possible quantum diffraction effects [42]. Screening effects justify vanishing contributions from the largest impact parameters, but even this method often involves an unphysical hard cutoff. Similar arguments can be made for cutoffs used in divergent velocity integrals that appear within the treatments. Regardless, the relatively constrained region of validity in addition to the introduction of ad hoc cutoffs makes the applicability of this second-order perturbative energy transfer theory somewhat dubious in many cases. Even so, these perturbative treatments have been successfully used in establishing links to numerically evaluated magnetized collisions, even without proper handling of chaotic trajectories, albeit without precise agreement over arbitrary parameter ranges as well [42, 45, 106–109].

In light of these details we chose to approach an RF heating model using the complementary linear response treatment in lieu of the binary collision picture. In addition, development of an appropriate classical trajectory Monte Carlo simulation to predict charge energy transfer using binary collisions in the presence of an oscillating driving field has been an ongoing project happening in parallel to the work presented here. In principle, purely numerical analysis of RF heating in magnetized plasma using molecular dynamics (MD) simulations is also possible, but published results for magnetized UCP MD simulations omit time-dependent external electric fields and do not examine RF heating [71, 112]. In short, an appropriate treatment for RF heating of a magnetized UCP using the binary collision picture is presently an ongoing effort.

3.2 Linear response

Rather than treating plasmas as collections of discrete charged particles they can instead be treated as continuous, charged fluids. This fluid picture can be separated into two regimes based

on the product $\omega\tau$ where ω is a characteristic frequency of the studied phenomenon and τ is a relaxation time or characteristic timescale between particle collisions [28]. Using textbook estimates for the electron-ion thermal relaxation time [26], $1/\tau \sim \omega_p \Gamma^{3/2} \ln \Lambda$, we see that for moderate (finite, nonzero) ω_p the condition $\omega_p \tau \gg 1$ is satisfied when the Coulomb coupling is weak, i.e. $\Gamma < 1$. In this regime high-order correlation effects are negligible, and the plasma is well approximated using a microscopic description via particle distribution functions [28]. This is called the kinetic approach. In contrast, when $\omega_p \tau \ll 1$ either the collisionality is extremely high such that the mean free path length and τ become small or the sparseness is such that length scales of interest are much larger than the mean free path as is the case with collisionless space plasmas [28, 64]. In these limits higher order correlation effects become important and the microscopic treatment used in the kinetic approach can be replaced with a macroscopic approach. In such a case, instead of evaluating distribution functions, quantities of interest can be expressed in terms of thermodynamic state variables. This is called hydrodynamic behavior. The UCPs studied in this thesis work qualify for the former treatment, the kinetic description.

The kinetic approach starts by describing the plasma with an N particle phase-space distribution function $f^{(N)}(\mathbf{r}, \mathbf{v}, t)$ which obeys Maxwell's equations and the Boltzmann equation

$$\frac{\mathrm{d}f^{(N)}}{\mathrm{d}t} \equiv \frac{\partial f^{(N)}}{\partial t} + \frac{\partial \mathbf{r}}{\partial t} \cdot \frac{\partial f^{(N)}}{\partial \mathbf{r}} + \frac{\partial \mathbf{v}}{\partial t} \cdot \frac{\partial f^{(N)}}{\partial \mathbf{v}} = \left(\frac{\partial f^{(N)}}{\partial t} \right)_{\text{coll}} . \tag{3.1}$$

In certain cases the collisional term on the right-hand-side can be neglected, and the system reduces to what is typically called the collisionless Vlasov-Poisson equations. The linear response treatment is born from the practice of approximating the distribution function as a small departure from the equilibrium distribution, $f^{(N)} = f_0^{(N)} + f_1^{(N)}$, and solving the subsequently linearized kinetic equations.

The AC conductivity and ion slowing models discussed in the following sections approximate solutions to the kinetic equations using the Bogolyubov-Born-Green-Kirkwood-Yvon (BBGKY) hierarchy [113–116] and first order Vlasov linearization [117], respectively. The BBGKY hierar-

chy is a formally equivalent decomposition of $\frac{\mathrm{d}f^{(N)}}{\mathrm{d}t} = 0$ into a chain of equations that describe the i particle distribution $f^{(i)}$ in terms of the $i+1$ particle distribution $f^{(i+1)}$ and lower order terms [28]. With the proper closure relation, this system can be truncated into a solvable system to approximate the Boltzmann equation. The smallness parameter justifying the truncation is essentially the same coupling strength parameter used to justify the kinetic description, $\Gamma^{3/2}$.

Oberman *et al* calculated the plasma high-frequency conductivity using this kinetic BBGKY approach [50]. The equation is linearized assuming the perturbed one-particle and two-particle distribution functions, $f_1^{(1)} = f_1$ and $f_1^{(2)} = g_1$, are small departures from the equilibrium one-particle and two-particle distribution functions, $f_0^{(1)} = f_0$ and $f_0^{(2)} = g_0$, where we now drop the superscripts out of convenience (including $f^{(N)} = f$). They truncate the BBGKY hierarchy assuming the three-particle correlation function is of negligible order and solve for g_1 in terms of f_1 and f_0. Then, by substitution, the first order BBGKY equation describing f_1 becomes a solvable linear integral equation. The resulting calculations from this treatment will be discussed in additional detail in Section 3.4.1.

In the interest of completeness, we also note the kinetic description formulated independently by Lenard [118] and Balescu [119]. Rather than approaching the kinetic equations assuming a binary collision approximation with long-range interactions handled *ex post facto*, Lenard-Balescu treatments describe weakly coupled plasma dynamics from the solutions of the BBGKY particle correlation equations assuming screening has been already built-in [72, 120]. Regardless, both the Lenard-Balescu and linearized Vlasov pictures express plasma dynamics through the so-called dielectric response function $\epsilon(k, \omega)$.

3.2.1 Dielectric response function

The kinetic description of a plasma involves solving the Boltzmann equation in conjunction with Maxwell's equations for a polarizable medium. In the linear response treatment the polarization field $\mathbf{P}$ is assumed to be a linear function of the external field $\mathbf{E}$, that is

$$\begin{aligned}\mathbf{D} &= \epsilon_0(\mathbf{E}+\mathbf{P}) \approx \epsilon_0(\mathbf{E}+\chi\mathbf{E}) = \epsilon_0(1+\chi)\mathbf{E} \\ \mathbf{D} &\approx \epsilon_0\epsilon\mathbf{E},\end{aligned} \tag{3.2}$$

where $\mathbf{D}$ is the dielectric displacement, χ is the susceptibility, and ϵ is the dielectric response [121]. Here we adopt a notation where ϵ is unitless so it may be straightforwardly compared with formulæ expressed in Gaussian-cgs units, but we otherwise continue to use the SI unit system. In general for anisotropic media such as magnetized UCPs the dielectric response is a tensor $D_i \approx \epsilon_0 \sum_j \epsilon_{ij} E_j$ [28].

Proper handling of anisotropic, time-dependent phenomena requires careful treatment of the dielectric response. Foremost, a finite response time can be accounted for with the convolution of the electric field with the retarded dielectric response $\epsilon_{ij}(\mathbf{r}-\mathbf{r}', t-t')$. We adopt here the formulation as presented in Ref. [74]:

$$\frac{D_i(\mathbf{r},t)}{\epsilon_0} = E_i(\mathbf{r},t) + \sum_j \int_{-\infty}^{t} \mathrm{d}t'\mathrm{d}\mathbf{r}' \epsilon_{ij}(\mathbf{r}-\mathbf{r}', t-t') E_j(\mathbf{r}', t') + \mathcal{O}(E^2). \tag{3.3}$$

Assuming a homogeneous linear medium, performing the typical Fourier transforms in position-momentum ($\mathbf{r} \leftrightarrow \mathbf{k}$) and time-frequency ($t \leftrightarrow \omega$), and utilizing the convolution theorem produces the expression

$$D_i(\mathbf{k},\omega) = \epsilon_0 \sum_j \epsilon_{ij}(\mathbf{k},\omega) E_j(\mathbf{k},\omega). \tag{3.4}$$

It should be noted that while the inhomogeneous, time dependent dielectric tensor $\epsilon_{ij}(\mathbf{r},t)$ is related to the quantity $\epsilon_{ij}(\mathbf{k},\omega)$ they are not simply Fourier transforms of one another [122].

If there is no substantial temperature anisotropy then this dielectric response tensor can be broken up into longitudinal and transverse parts,

$$\epsilon_{ij}(\mathbf{k},\omega) = \frac{k_i k_j}{k^2}\epsilon^L(\mathbf{k},\omega) + \left(\delta_{ij} - \frac{k_i k_j}{k^2}\right)\epsilon^T(\mathbf{k},\omega), \tag{3.5}$$

where $k_i k_j / k^2$ is the tensor product of unit vectors, δ_{ij} is the Kronecker delta tensor, and ϵ^L (ϵ^T) is the longitudinal (transverse) dielectric response function. The aim of this work primarily concerns the longitudinal behavior so we drop the affixed qualifier and superscript to write $\epsilon^L(\mathbf{k}, \omega) = \epsilon(\mathbf{k}, \omega)$ as simply the dielectric response function.

Depending on the nature of the plasma, such as the existence of a magnetic field, different dielectric functions may be appropriate. For the typical collisionless case of infinite mass ions with Maxwellian, unmagnetized electrons with thermal velocity v_{th} one obtains [42]

$$\begin{gathered} \epsilon(\mathbf{k}, \omega) = 1 + \frac{1}{k^2 \lambda_{\text{D}}^2} (\tilde{g} + i\tilde{f}), \\ \text{where } \tilde{g} = 1 - 2\zeta e^{-\zeta^2} \int_0^\zeta \mathrm{d}t \, e^{t^2}, \; \tilde{f} = \sqrt{\pi} \zeta e^{-\zeta^2}, \text{ and } \zeta = \frac{\omega}{\sqrt{2} k v_{\text{th}}}. \end{gathered} \tag{3.6}$$

In Ref. [36] the authors derive a dielectric function for the collisional, magnetized case with electron cyclotron frequency ω_c and collision frequency γ. The authors relate this collision frequency to the electron-electron and electron-ion collision frequencies, γ_{ee} and γ_{ei}. Starting from

$$\frac{\partial f}{\partial t} + \mathbf{v} \cdot \vec{\nabla} f + \mathbf{F}_{\text{EM}} \cdot \vec{\nabla}_{\mathbf{p}} f = \left(\frac{\partial f}{\partial t} \right)_{\text{coll}}, \tag{3.7}$$

they treat the collisional term using a standard BGK-type relaxation time approximation [123]

$$\left(\frac{\partial f}{\partial t} \right)_{\text{coll}} = -\gamma [f - \frac{n}{n_0} f_0], \tag{3.8}$$

where $n = \int \mathrm{d}^3 v \, f(\mathbf{r}, \mathbf{v}, t)$ is the spatial charge density and the 0 subscripts denote equilibria functions.

Assuming a Maxwellian distribution for the equilibrium function f_0, they arrive at the following solution for the dielectric response function of a collisional plasma with magnetized electrons:

$$\epsilon(\mathbf{k}, \omega, \gamma) = 1 + \frac{1}{k^2 \lambda_{\text{D}}^2} \left[F_1(\mathbf{k}, \omega) + i F_2(\mathbf{k}, \omega) \right] \tag{3.9}$$

with

$$
\begin{aligned}
F_1(\mathbf{k},\omega) &= 1 + \sum_{m=-\infty}^{\infty} \frac{1}{\omega + m\omega_c} e^{-\beta_k} I_m(\beta_k)[\omega \mathcal{G}(x_m, y) - \gamma \mathcal{F}(x_m, y)] \\
F_2(\mathbf{k},\omega) &= \sum_{m=-\infty}^{\infty} \frac{1}{\omega + m\omega_c} e^{-\beta_k} I_m(\beta_k)[\omega \mathcal{F}(x_m, y) + \gamma \mathcal{G}(x_m, y)]
\end{aligned}
\tag{3.10}
$$

Here I_m is the m^{th} order modified Bessel function of the first kind, $x_m = \dfrac{\omega + m\omega_c}{|k_\parallel| v_{\text{th}}}$, $y = \dfrac{\gamma}{|k_\parallel| v_{\text{th}}}$, $\beta_k = \dfrac{k_\perp^2 v_{\text{th}}^2}{\omega_c^2}$, and

$$
\begin{aligned}
\mathcal{G}(x, y) &= \frac{x}{\sqrt{2\pi}} \int_{-\infty}^{\infty} \mathrm{d}t \frac{(t - x) e^{-t^2/2}}{(t - x)^2 + y^2} \\
\mathcal{F}(x, y) &= \frac{xy}{\sqrt{2\pi}} \int_{-\infty}^{\infty} \mathrm{d}t \frac{e^{-t^2/2}}{(t - x)^2 + y^2},
\end{aligned}
\tag{3.11}
$$

where the parallel and perpendicular subscripts refer to the orientation with respect to the magnetic field vector.

Computing $\mathcal{F}$ and $\mathcal{G}$ numerically from their definitions in (3.11) can be computationally inefficient. Instead we recognize them as Voigt functions [124, § 7.19] and reduce them to

$$
\begin{Bmatrix} \mathcal{G}(x, y) \\ \mathcal{F}(x, y) \end{Bmatrix} = \sqrt{\frac{\pi}{2}} x \begin{Bmatrix} -\mathrm{Im} \\ \mathrm{Re} \end{Bmatrix} \left[\exp \frac{(y - ix)^2}{2} \mathrm{erfc} \left(\frac{y - ix}{\sqrt{2}} \right) \right] \tag{3.12}
$$

for which there are standard numerical libraries that can be used to calculate complex error functions and the related Faddeeva function [125]. This form is also useful for identifying the real and imaginary parts of these functions. From (3.12) we immediately see $\mathcal{G}$ and $\mathcal{F}$ are strictly real; this implies F_1 and F_2 in (3.10) are strictly real. The form for $\epsilon(\mathbf{k}, \omega, \gamma)$ given in (3.9) can therefore be used to effortlessly split the dielectric response function into its real and imaginary parts. In the next section we show how this is helpful and expand on other properties useful in calculations that incorporate the function.

3.3 Properties of the dielectric response function

Before continuing it is prudent to identify certain important properties of $\epsilon(\mathbf{k},\omega,\gamma)$ in (3.9) that are useful when using the function in calculations. In particular, symmetries, parities, and limiting forms will be explored. In Section 3.4 we will be analyzing integrals with terms of the form $\mathrm{Im}[-1/\epsilon]$, the energy loss function (ELF) [36], so we begin here by rewriting the ELF using (3.9) with our knowledge of its real and imaginary parts

$$\mathrm{ELF} = \mathrm{Im}\frac{-1}{\epsilon(\mathbf{k},\omega,\gamma)} = \frac{k^2\lambda_{\mathrm{D}}^2 F_2}{(k^2\lambda_{\mathrm{D}}^2+F_1)^2+F_2^2} \tag{3.13}$$

Furthermore, in our calculations we encounter evaluations of the ELF at frequencies $\omega = n\omega_0$ where n here is an integer summation index not to be confused with the density. In such cases we write $x_{m,n} = \dfrac{n\omega_0 + m\omega_c}{|k_\parallel| v_{\mathrm{th}}}$.

3.3.1 Parity

We can evaluate the parity of our summations and functions under the substitutions $m \to -m$ and $n \to -n$. By inspection we see $x_{-m,-n} = -x_{m,n}$. Thus

$$\begin{aligned}
\mathcal{G}(x_{-n,-m},y) &= \frac{-x_{n,m}}{\sqrt{2\pi}}\int_{-\infty}^{\infty}\mathrm{d}t\frac{(t+x_{n,m})e^{-t^2/2}}{(t+x_{n,m})^2+y^2} \\
\mathcal{F}(x_{-n,-m},y) &= \frac{-x_{n,m}y}{\sqrt{2\pi}}\int_{-\infty}^{\infty}\mathrm{d}t\frac{e^{-t^2/2}}{(t+x_{n,m})^2+y^2}.
\end{aligned} \tag{3.14}$$

Substituting $t' = -t$ produces

$$\begin{aligned}
\mathcal{G}(x_{-n,-m},y) &= \frac{-x_{n,m}}{\sqrt{2\pi}}\int_{\infty}^{-\infty}(-\mathrm{d}t')\frac{(-t'+x_{n,m})e^{-t'^2/2}}{(-t'+x_{n,m})^2+y^2} = \mathcal{G}(x_{n,m},y) \\
\mathcal{F}(x_{-n,-m},y) &= \frac{-x_{n,m}y}{\sqrt{2\pi}}\int_{\infty}^{-\infty}(-\mathrm{d}t')\frac{e^{-t'^2/2}}{(-t'+x_{n,m})^2+y^2} = -\mathcal{F}(x_{n,m},y)
\end{aligned} \tag{3.15}$$

Therefore, under the same n and m substitutions,

$$
\begin{aligned}
F_1(\mathbf{k}, -n\omega_0) &= 1 + \sum_{m=\infty}^{-\infty} \frac{1}{-n\omega_0 - m\omega_c} e^{-\beta_k} I_{-m}(\beta_k)[-n\omega_0 \mathcal{G}(x_{-n,-m}, y) - \gamma \mathcal{F}(x_{-n,-m}, y)] \\
&= 1 + \sum_{m=-\infty}^{\infty} \frac{(-1)}{n\omega_0 + m\omega_c} e^{-\beta_k} I_m(\beta_k)[-n\omega_0 \mathcal{G}(x_{n,m}, y) + \gamma \mathcal{F}(x_{n,m}, y)] \\
&= F_1(\mathbf{k}, n\omega_0)
\end{aligned}
\tag{3.16}
$$

and

$$
\begin{aligned}
F_2(\mathbf{k}, -n\omega_0) &= \sum_{m=\infty}^{-\infty} \frac{1}{-n\omega_0 - m\omega_c} e^{-\beta_k} I_{-m}(\beta_k)[-n\omega_0 \mathcal{F}(x_{-n,-m}, y) + \gamma \mathcal{G}(x_{-n,-m}, y)] \\
&= \sum_{m=-\infty}^{\infty} \frac{(-1)}{n\omega_0 + m\omega_c} e^{-\beta_k} I_m(\beta_k)[n\omega_0 \mathcal{F}(x_{n,m}, y) + \gamma \mathcal{G}(x_{n,m}, y)] \\
&= -F_2(\mathbf{k}, n\omega_0).
\end{aligned}
\tag{3.17}
$$

Since we know F_2 is odd and F_1 is even under these transformations it's trivial to show the ELF is ultimately odd for $m \to -m$ and $n \to -n$ as well.

3.3.2 Symmetry

While it's assumed there is cylindrical symmetry about the azimuthal direction, the dependence of the ELF on the polar angle θ between $\mathbf{k}$ and $\mathbf{B}$ can be evaluated. Under the substitution $\theta \to \pi - \theta$ we find that the arguments x_m, y, β_k are unchanged. Thus F_1, F_2, and the ELF all have even symmetry about the $\theta = \pi/2$ plane.

3.3.3 Limiting forms

Lastly, we can examine the form of the dielectric response function in the limit of no collisions and no magnetic field. In the collisionless limit when $\gamma \to 0$, Ref. [36] shows the functions $\mathcal{G}$ and $\mathcal{F}$ reduce to the Fried-Conte dispersion functions [126]

$$\begin{aligned}\mathcal{G}(x,0) &= \frac{x}{\sqrt{2\pi}}\mathcal{P}\int_{-\infty}^{\infty}\mathrm{d}t\frac{e^{-t^2/2}}{t-x}\\ \mathcal{F}(x,0) &= \sqrt{\frac{\pi}{2}}xe^{-x^2/2}\end{aligned} \tag{3.18}$$

where $\mathcal{P}$ denotes the Cauchy principle value to account for the singularity at $x = t$. F_1 and F_2 become

$$\begin{aligned}F_1(\mathbf{k},\omega,\gamma\to 0) &= 1+\sum_{m=-\infty}^{\infty}\frac{1}{\omega+m\omega_c}e^{-\beta_k}I_m(\beta_k)[\omega\mathcal{G}(x_m,0)]\\ &= 1+\frac{\omega}{\sqrt{2}|k_\parallel|v_{\mathrm{th}}}\sum_{m=-\infty}^{\infty}e^{-\beta_k}I_m(\beta_k)\pi^{-\frac{1}{2}}\mathcal{P}\int_{-\infty}^{\infty}\mathrm{d}t\frac{e^{-t^2}}{t-\frac{x_m}{\sqrt{2}}}\end{aligned} \tag{3.19}$$

and

$$\begin{aligned}F_2(\mathbf{k},\omega,\gamma\to 0) &= \sum_{m=-\infty}^{\infty}\frac{1}{\omega+m\omega_c}e^{-\beta_k}I_m(\beta_k)[\omega\mathcal{F}(x_m,0)]\\ &= \frac{\omega}{\sqrt{2}|k_\parallel|v_{\mathrm{th}}}\sum_{m=-\infty}^{\infty}e^{-\beta_k}I_m(\beta_k)\pi^{\frac{1}{2}}e^{-\frac{x_m^2}{2}}\end{aligned} \tag{3.20}$$

Substitution into (3.9) gives

$$\begin{aligned}\epsilon(\mathbf{k},\omega,\gamma\to 0) &= 1+\frac{1}{k^2\lambda_{\mathrm{D}}^2}\left\{1+\frac{\omega}{\sqrt{2}|k_\parallel|v_{\mathrm{th}}}\right.\\ &\quad\left.\times\sum_{m=-\infty}^{\infty}e^{-\beta_k}I_m(\beta_k)\left[\pi^{-\frac{1}{2}}\mathcal{P}\int_{-\infty}^{\infty}\mathrm{d}t\frac{e^{-t^2}}{t-\frac{x_m}{\sqrt{2}}}+i\pi^{\frac{1}{2}}e^{-\frac{x_m^2}{2}}\right]\right\}\\ &= 1+\frac{1}{k^2\lambda_{\mathrm{D}}^2}\left[1+\frac{\omega}{\sqrt{2}|k_\parallel|v_{\mathrm{th}}}\sum_{m=-\infty}^{\infty}e^{-\beta_k}I_m(\beta_k)Z\left(\frac{x_m}{\sqrt{2}}\right)\right]\end{aligned} \tag{3.21}$$

where $Z(x)$ is the plasma dispersion function for the special case $\mathrm{Im}\,x = 0$ [126]. This is precisely the dielectric function used in e.g. Matsuda's treatment of collisionless, magnetized plasma AC conductivity [52].

Finally, we should expect this collisionless dielectric function to reduce to the standard form used in (3.6) in the limit of zero magnetic field. To quote the authors of Ref. [36], "the limit of the

vanishing magnetic field in [terms in (3.21)] is not trivial." Thankfully, in an appendix, the authors derive an equivalent integral representation of the collisional, magnetized dielectric function that more readily shows the recovery of the field-free limit (see Eq. (A7) in Ref. [36]).

We are interested in the collisionless ($\gamma = 0$) case and can therefore simplify the aforementioned integral representation to

$$\epsilon(\mathbf{k}, \omega, \gamma = 0) = 1 + \frac{1}{k^2 \lambda_{\mathrm{D}}^2} \left[1 + is \int_0^\infty \mathrm{d}t \, e^{-X(t) + ist} \right] \tag{3.22}$$

where $s = \omega / k v_{\mathrm{th}}$ and

$$X(t) = \frac{t^2}{2} \frac{k_\parallel^2}{k^2} + \frac{k_\perp^2 v_{\mathrm{th}}^2}{\omega_c^2} \left[1 - \cos\left(\frac{t \omega_c}{k v_{\mathrm{th}}} \right) \right]. \tag{3.23}$$

In the $B = 0$ limit we can Taylor expand the $\cos$ term in $X(t)$ to find $\lim_{\omega_c \to 0} X(t) = t^2/2$, thus

$$\lim_{\gamma, \omega_c \to 0} \epsilon(\mathbf{k}, \omega) = 1 + \frac{1}{k^2 \lambda_{\mathrm{D}}^2} \left[1 + is \int_0^\infty \mathrm{d}t \, e^{-\frac{t^2}{2} + ist} \right]. \tag{3.24}$$

We can re-express the integral in (3.24) using Cauchy's theorem where the contour C is the rectangle in the lower-half plane formed by the vertices $0 + 0i, 0 - is, L - is, L + 0i$,

$$\begin{aligned} &\oint_C e^{-z^2/2} \, \mathrm{d}z = 0 \\ &= \int_0^L \mathrm{d}x \, e^{-(x - is)^2/2} + i \int_{-s}^0 \mathrm{d}y \, e^{-(L + iy)^2/2} + \int_L^0 \mathrm{d}x \, e^{-x^2/2} + i \int_0^{-s} \mathrm{d}y \, e^{y^2/2} \end{aligned} \tag{3.25}$$

Taking $L \to \infty$ and reorganizing terms yields

$$\begin{aligned} \int_0^\infty \mathrm{d}t \, e^{-\frac{t^2}{2} + ist} &= e^{-s^2/2} \int_0^\infty \mathrm{d}x \, e^{-(x - is)^2/2} = \frac{e^{-s^2/2}}{\sqrt{2} i} \left(i\sqrt{\pi} - 2 \int_0^{s/\sqrt{2}} \mathrm{d}t \, e^{t^2} \right) \\ &= \frac{1}{\sqrt{2} i} Z\left(\frac{s}{\sqrt{2}} \right), \end{aligned} \tag{3.26}$$

where we have identified the plasma dispersion function [126]

$$Z(u) = e^{-u^2}\left(i\sqrt{\pi} - 2\int_0^u \mathrm{d}t\, e^{t^2}\right).$$

This produces the well-known expression for the isotropic, Maxwell-Boltzmann dielectric function

$$\lim_{\omega_c,\gamma\to 0}\epsilon(\mathbf{k},\omega) = 1 + \frac{1}{k^2\lambda_{\mathrm{D}}^2}\left[1 + \frac{\omega}{\sqrt{2}kv_{\mathrm{th}}}Z\left(\frac{\omega}{\sqrt{2}kv_{\mathrm{th}}}\right)\right] \tag{3.27}$$

which may alternatively be expressed as

$$\lim_{\omega_c,\gamma\to 0}\epsilon(\mathbf{k},\omega) = 1 + \frac{1}{k^2\lambda_{\mathrm{D}}^2}(\tilde{g} + i\tilde{f}) \tag{3.28}$$

where $\tilde{g}$ and $\tilde{f}$ are exactly what we expect from (3.6).

For the case of the infinite magnetic field we find $\lim_{\omega_c\to\infty} X(t) = t^2\cos^2\theta/2$. Substitution into (3.22) produces an expression much like (3.24), which may be re-expressed using techniques similar to what we used in the vanishing-field limit above.

3.4 RF heating

Our goal is to find a suitable model for the average thermal energy acquired by plasma electrons due to interactions with the ions in the presence of a radiofrequency driving electric field. In this section we explore two treatments using the linear response method: Ohmic heating determined by the magnetized AC conductivity in the small oscillation amplitude regime, and a stopping power-like model adapted to calculate the kinetic energy transfer between oscillating electrons and infinite mass ions.

Let us consider a model where the change in electron thermal energy due to center of mass (CM) oscillations driven with velocity $v(t)$ at frequency ω_0 is approximated by a heating rate η,

$$\frac{\mathrm{d}E}{\mathrm{d}t} = \eta m v(t)^2. \tag{3.29}$$

Taking $v(t) = a\omega_0 sin(\omega_0 t + \phi)$ where a is the CM oscillation amplitude and ϕ an arbitrary phase then time averaging over a single oscillation cycle gives us the average one-cycle energy change $\Delta E^{(1)} = \pi\eta m a^2 \omega_0$. If this change in energy is instantaneously thermalized we can write

$$\Delta E^{(1)} = \frac{3}{2} k_{\mathrm{B}} \Delta T = \pi \eta m a^2 \omega_0 \tag{3.30}$$

and express the heating rate η in terms of the electron temperature change ΔT and oscillation amplitude. Thus, we can compare predicted heating rates for different energy transfer models as long as we are able to estimate a change in thermal energy for a given driving field strength.

3.4.1 AC conductivity

One direct way of calculating the electron temperature increase due to plasma interactions with a driving RF field is through Ohmic heating. In the absence of significant nonlinear effects, we can assume Ohm's law, $\mathbf{J} = \sigma \mathbf{E}$, to find the power of the fields doing work on the charge density $\mathbf{J}$. This power density p can be calculated from $p = \mathbf{J} \cdot \mathbf{E} = \sigma E^2$ where σ is the plasma conductivity. From p the energy-change rate for a single electron (the charge carrier for the current density in the lab frame) can be averaged over a single oscillation cycle and compared to (3.30) to determine the RF heating rate.

In general, both the dielectric response and conductivity are tensors, ϵ_{ij} and σ_{ij}. The well-known relationship between the dielectric and conductivity tensors is [28, 121]

$$\epsilon_{ij} = \delta_{ij} + \frac{i}{\epsilon_0 \omega} \sigma_{ij}. \tag{3.31}$$

Just as the dielectric tensor may be expressed in terms of $\mathbf{k}$ and ω the same is true of the conductivity. Similarly, the conductivity can also be separated into longitudinal and transverse parts $\sigma_{\parallel}$ and $\sigma_{\pm}$, where the transverse conductivity is further decomposed into right- and left-circular polarization components. Once again, we are most interested in the longitudinal behavior and focus our efforts on the parallel AC conductivity $\sigma_{\parallel}(\mathbf{k}, \omega)$.

Oberman and Shure derived a formula for the conductivity tensor of a magnetized plasma with correlated, infinite mass ions [51]. Kyoko Matsuda extended the derivation for uncorrelated ions using a test particle method and provides expressions to calculate $\mathrm{Re}\ \sigma_{ij}(\mathbf{k},\omega)$ which are needed for treating wave absorption [52]. Matsuda reports the longitudinal conductivity assuming infinite mass, uncorrelated ions as

$$\sigma_{\parallel}(\omega) = i\frac{\epsilon_0}{4\pi}\frac{\omega_p^2}{\omega}\left[1 - \frac{e^2}{\epsilon_0 m\omega^2}\frac{I_{\parallel}(\omega)}{(2\pi)^2}\right] \tag{3.32}$$

where

$$I_{\parallel}(\omega) = 2\iiint \mathrm{d}k_{\parallel}k_{\perp}\mathrm{d}k_{\perp}\mathrm{d}\phi\frac{k_{\parallel}^2}{k^2}\left[\frac{1}{\epsilon(\mathbf{k},0)} - \frac{1}{\epsilon(\mathbf{k},\omega)}\right]. \tag{3.33}$$

The real part is given by the following, after switching to polar coordinates,

$$\mathrm{Re}\,\sigma_{\parallel}(\omega) = \frac{e^4 n_{\mathrm{e}}}{2\pi^2\epsilon_0 m^2\omega^3}\int_0^{k_{\max}}\mathrm{d}k\int_0^{\pi/2}\mathrm{d}\theta\,k^2\sin\theta\cos^2\theta\left[\mathrm{Im}\,\frac{-1}{\epsilon(\mathbf{k},\omega)}\right]. \tag{3.34}$$

The one-cycle RF heat is then

$$\Delta E_{\mathrm{AC}}^{(1)} = \frac{\pi E^2}{n_{\mathrm{e}}\omega_0}\mathrm{Re}\,\sigma_{\parallel}(\omega_0). \tag{3.35}$$

The $k_{\max}$ parameter is introduced to avoid logarithmic divergences of the integral. It effectively represents the failure of the linear response treatment in the case of small impact parameter collisions between charges. The value of $k_{\max}$ is typically taken to be $1/r_{\min}$ where $r_{\min} = e^2/4\pi\epsilon_0 k_{\mathrm{B}}T$ is a characteristic collisional length scale related to the average distance of closest approach in a thermal charge distribution. So, the $k_{\max}$ parameter signifies the neglect of small-impact parameter, large-angle collision effects within the linear response framework unless otherwise corrected for.

The formulæ presented here were derived under the following assumptions: the product $\omega\tau$ mentioned in the beginning of Section 3.2 is understood here to be a comparison of the driving frequency $\omega \to \omega_0$ and the cumulative 90° deflection time, $\tau \to t_{90}$. Oberman *et al* cite the Spitzer formula to find this characteristic collision time [26, 50],

$$t_{90} = \frac{2\pi\epsilon_0^2\sqrt{m}(3k_{\mathrm{B}}T)^{3/2}}{n_{\mathrm{e}}e^4 \ln\Lambda}. \tag{3.36}$$

It is assumed that the driving frequency is high enough that $\omega_0 t_{90} \gg 1$. This is called the reactive approximation; essentially, the driving field is changing much faster than the charge's trajectory changes due to collisions. In Ref. [51] it is explained that the reactive approximation also fails when the driving frequency approaches the cyclotron frequency, $\omega_0 \approx \omega_c$. In this case the circularly polarized components of the transverse driving field rotate at the same frequency as the electron gyrofrequency, so in the rest frame of the electron the electric field appears to be static and should be treated with a resistive limit. Lastly, in Ref. [52] Matsuda expresses a limiting field amplitude in terms of the distance of closest approach $eE/m\omega_0^2 < r_{\min}$ which yields

$$E < E_{\mathrm{lim}} = \frac{em\omega_0^2}{4\pi\epsilon_0 k_{\mathrm{B}}T}. \tag{3.37}$$

We can estimate these limiting assumptions for conditions in general correspondence with our UCP experiment parameters. That is, for electron density and temperature $n_{\mathrm{e}} = 1.2{\cdot}10^7\,\mathrm{cm}^{-3}$, $T = 4.5\,\mathrm{K}$ we get $t_{90} = 43\,\mathrm{ns}$ which corresponds to a limiting driving frequency $1/t_{90} = 2\pi \cdot 3.7\,\mathrm{MHz}$ [26]. In our RF heating measurements we drove the electric field with a frequency $60\,\mathrm{MHz}$ which satisfies the reactive approximation outside the cyclotron resonance at $B = 21\,\mathrm{G}$. From (3.37) this driving frequency gives us a limiting amplitude $E_{\mathrm{lim}} = 3.00\,\mathrm{V/m}$.

In this thesis work we report on measurements of UCPs that can exceed these limiting conditions. Motivated by the quest for an applicable magnetized plasma RF heating model, we also developed a stopping power-like energy transfer model (SPLET) in an effort to estimate heating beyond the limiting conditions enforced by the AC conductivity treatment.

3.4.2 Stopping power-like energy transfer (SPLET)

Since the AC conductivity formulation has limiting conditions on, e.g., the driving oscillation amplitude, we explored other methods for calculating the energy transfer. The definition of stopping power is $S = -\mathrm{d}E/\mathrm{d}l$, the loss of energy per unit path length of a projectile. This can be

regarded as the slowing force associated with a charged particle's motion [42, 45]

$$S = \hat{\mathbf{v}} \cdot (e\vec{\nabla}\Phi). \tag{3.38}$$

Here $\hat{\mathbf{v}}$ is the particle velocity unit vector and Φ is the self-consistent electric potential associated with the superposition of the particle's potential and the magnetized electron plasma potential. An approximate solution for Φ can be calculated using first-order linearization of the Vlasov-Poisson equations [28, 42, 117, 122].

Ref. [42, § 2.4] uses this method to formulate an expression for the stopping power of an ion with mass M, charge $q = Ze$, traveling with velocity $\mathbf{v}_i(t) = \dot{\mathbf{r}}_i(t)$ through a magnetized electron-ion plasma with densities n_ν, and axially symmetric temperatures $\frac{1}{3}T_{\parallel\nu} + \frac{2}{3}T_{\perp\nu} = T_\nu$, where $\nu \to (e \text{ or } i)$ is an index for particle species. The details of the derivation are not important in and of themselves, so I will simply quote the starting point and results.

Using the Nersisyan *et al* notation for the distribution functions $f_\nu = n_\nu f_{0\nu} + n_\nu f_{1\nu}$, where $f_{0\nu}$ is the anisotropic Maxwell-Boltzmann distribution

$$f_{0\nu}(v_\parallel, v_\perp) = \frac{1}{(2\pi)^{3/2} v_{\mathrm{th}\perp\nu}^2 v_{\mathrm{th}\parallel\nu}} \exp\left(-\frac{v_\perp^2}{2v_{\mathrm{th}\perp\nu}^2}\right) \exp\left(-\frac{v_\parallel^2}{2v_{\mathrm{th}\parallel\nu}^2}\right), \tag{3.39}$$

$v_{\mathrm{th}\{\parallel,\perp\}\nu}^2 = k_\mathrm{B} T_{\{\parallel,\perp\}\nu}/m_\nu$, and $f_{1\nu}$ is the perturbed part of the distribution function, we write the linearized Vlasov-Poisson equations as

$$\frac{\partial f_{1\nu}}{\partial t} + \mathbf{v} \cdot \frac{\partial f_{1\nu}}{\partial \mathbf{r}} \pm \omega_{c\nu}(\mathbf{v} \times \hat{\mathbf{B}}) \cdot \frac{\partial f_{1\nu}}{\partial \mathbf{v}} - \frac{q_\nu}{m_\nu} \frac{\partial \Phi}{\partial \mathbf{r}} \cdot \frac{\partial f_{0\nu}}{\partial \mathbf{v}} = 0 \tag{3.40}$$

and

$$\epsilon_0 \nabla^2 \Phi = -\rho_i(\mathbf{r}, t) - \sum_\nu n_\nu q_\nu \int \mathbf{d}^3 v \, f_{1\nu}(\mathbf{r}, \mathbf{v}, t). \tag{3.41}$$

The projectile ion charge density $\rho_i(\mathrm{r}, t)$ can be replaced with that of a point charge delta function $q\delta(\mathrm{r} - \mathrm{r}_i(t))$.

The authors solve (3.40) and (3.41) for the potential Φ [42, Eq. 2.46]. Plugging this into (3.38) produces the following expression for the stopping power in terms of the magnetized dielectric response function $\epsilon(\mathbf{k}, \omega)$

$$S = \frac{2ie^2}{4\pi\epsilon_0(2\pi)^3 v_i(t)} \int \mathrm{d}^3\mathbf{k} \int_{-\infty}^{\infty} \mathrm{d}\omega \frac{\mathbf{k}\cdot\mathbf{v}_i(t)}{k^2\,\epsilon(\mathbf{k},\omega)} \Xi_i(\mathbf{k},\omega,t) \int_{-\infty}^{\infty} \mathrm{d}t' \Xi^{\star}(\mathbf{k},\omega,t') \tag{3.42}$$

where $\Xi_i(\mathbf{k}, \omega, t) = \exp[i\mathbf{k}\cdot\mathbf{r}_i(t) - i\omega t]$ [42, Eq. 2.52]. They then simplify the expression for special cases such as the case of a heavy, unmagnetized ($r_c \gg \lambda_{\mathrm{D}}$) ion moving in a trajectory with constant velocity, $\mathbf{r}_i(t) = \mathbf{v}_i t$. Here we consider an alternate situation where the projectile is a heavy ion oscillating coaxial with the magnetic field with frequency ω_0 at an amplitude $\mathbf{a}$ in a plasma with negligible temperature anisotropy.

The connection between this oscillating-ion stopping power-like model and the magnetized off-resonant RF heating we wish to calculate becomes plainly evident with a reference frame transformation. In the lab frame the light, magnetized electrons have a distribution of velocities with a characteristic magnitude set by the thermal velocity v_{th}. In the absence of e-i interactions, an external off-resonant AC electric field parallel to the magnetic field will cause the electrons to oscillate at the driving frequency with an average center of mass amplitude and without alteration to their relative velocities. The heavy, cold, unmagnetized ions remain effectively stationary since their oscillation amplitude is smaller than the electrons' by the mass ratio factor of roughly 10^5.

Now consider the noninertial frame of reference that oscillates in-phase with and at the same frequency and amplitude as the electron center of mass motion. In this frame the average electron motion associated with the driving electric field is exactly canceled by a fictitious force; conversely, these forces would cause a heavy stationary ion to appear to oscillate in the noninertial frame at the electron amplitude and frequency. This is the same picture described by the oscillating-ion stopping power-like model. Even though this argument relies on fictitious forces, it does not matter; the relative velocities of the heavy ion and plasma are the same between the two pictures. The work done by electrons with a stationary center of mass on an oscillating ion is equivalent to the work done by oscillating electrons on a stationary ion.

This motivates us to develop a stopping power-like model using the formulation presented with (3.42) under the following substitutions for the projectile ion equation of motion: $\mathbf{r}_i(t) = \mathbf{a}\sin(\omega_0 t)$, and $\mathbf{v}_i(t) = \mathbf{a}\omega_0\cos(\omega_0 t)$. While the stopping power-like force is useful to know, we actually want the energy change $\Delta E = \mathrm{Re}\int S(t)v_i(t)dt$.

$$\begin{aligned} S(t)v_i(t) = \frac{2ie^2}{4\pi\epsilon_0(2\pi)^3}\int \mathrm{d}^3\mathbf{k}\int_{-\infty}^{\infty}\mathrm{d}\omega\frac{\mathbf{k}\cdot\mathbf{a}\omega_0\cos(\omega_0 t)}{k^2\,\epsilon(\mathbf{k},\omega)}\exp[i\mathbf{k}\cdot\mathbf{a}\sin(\omega_0 t) - i\omega t] \\ \times\int_{-\infty}^{\infty}\mathrm{d}t'\exp[-i\mathbf{k}\cdot\mathbf{a}\sin(\omega_0 t') + i\omega t']. \end{aligned} \tag{3.43}$$

Derived from the Bessel generating function, we can use the expression

$$\exp[-i\mathbf{k}\cdot\mathbf{a}\sin(\omega_0 t)] = \sum_{n=-\infty}^{\infty} J_n(\mathbf{k}\cdot\mathbf{a})e^{-in\omega_0 t} \tag{3.44}$$

and perform the $\mathrm{d}t'$ integral.

$$\int_{-\infty}^{\infty}\mathrm{d}t'\exp[i(\omega - n\omega_0)t'] = 2\pi\delta(\omega - n\omega_0) \tag{3.45}$$

so the $\mathrm{d}\omega$ integral becomes trivial and our expression in (3.43) reduces to

$$S(t)v_i(t) = \frac{2ie^2}{4\pi\epsilon_0(2\pi)^2}\int \mathrm{d}^3\mathbf{k}\sum_{n=-\infty}^{\infty}\sum_{m=-\infty}^{\infty}\frac{\mathbf{k}\cdot\mathbf{a}\omega_0\cos(\omega_0 t)}{k^2\,\epsilon(\mathbf{k},n\omega_0)}J_n(\mathbf{k}\cdot\mathbf{a})J_m(\mathbf{k}\cdot\mathbf{a})e^{-i(n-m)\omega_0 t}. \tag{3.46}$$

Expanding the $\cos(\omega_0 t)$ term and integrating over one RF period $2\pi/\omega_0$ lets us simplify with

$$\begin{aligned} &\int_0^{2\pi/\omega_0}\mathrm{d}t\left\{\exp[i(m-n+1)\omega_0 t] + \exp[i(m-n-1)\omega_0 t]\right\} \\ =&\frac{e^{2i\pi(m-n+1)}-1}{i(m-n+1)\omega_0} + \frac{e^{2i\pi(m-n-1)}-1}{i(m-n-1)\omega_0} \\ =&\frac{2\pi}{\omega_0}\left(\delta_{m(n-1)} + \delta_{m(n+1)}\right) \end{aligned} \tag{3.47}$$

to get

$$\int_0^{2\pi/\omega_0} \mathrm{d}t\, S(t) v_i(t) = \frac{ie^2}{4\pi\epsilon_0(2\pi)} \int \mathrm{d}^3\mathbf{k} \sum_{n=-\infty}^{\infty} \frac{\mathbf{k}\cdot\mathbf{a}}{k^2\,\epsilon(\mathbf{k}, n\omega_0)} J_n(\mathbf{k}\cdot\mathbf{a}) \times \left[J_{n-1}(\mathbf{k}\cdot\mathbf{a}) + J_{n+1}(\mathbf{k}\cdot\mathbf{a})\right] \tag{3.48}$$

Using the Bessel recurrence relation $J_{\nu-1}(z) + J_{\nu+1}(z) = \frac{2\nu}{z} J_\nu(z)$ and changing to spherical coordinates reduces the expression on the right-hand side of (3.48) to

$$\frac{ie^2}{4\pi\epsilon_0} \int_0^{\infty} \mathrm{d}k \int_0^{\pi} \mathrm{d}\theta \sum_{n=-\infty}^{\infty} \frac{2n\sin\theta}{\epsilon(\mathbf{k}, n\omega_0)} J_n(ka\cos\theta)^2 \tag{3.49}$$

the real part of which gives the one-cycle energy transfer

$$\Delta E_{\mathrm{SP}}^{(1)} = \frac{e^2}{2\pi\epsilon_0} \sum_{n=-\infty}^{\infty} \int_0^{\infty} \mathrm{d}k \int_0^{\pi} \mathrm{d}\theta\, n\sin\theta J_n(ka\cos\theta)^2 \left[\mathrm{Im}\frac{-1}{\epsilon(\mathbf{k}, n\omega_0)}\right]. \tag{3.50}$$

Up to this point we have not designated any functional form for $\epsilon(\mathbf{k}, \omega)$. We can now use the properties illustrated in Section 3.3 for the dielectric response function—collisional, magnetized, or otherwise—and ELF to further simplify (3.50). We know the ELF is odd with respect to negation of the index n and likewise J_n^2 is even. Due to the leading n in the integrand we readily see the summation is overall even with a vanishing $n = 0$ term and may thus be written $\sum_{n=-\infty}^{\infty} \to 2\sum_{n=1}^{\infty}$. Furthermore, $\sin\theta$, J_n^2, and the ELF all have even symmetry with respect to $\theta = \pi/2$ so the $\mathrm{d}\theta$ integration may be rewritten from $\int_0^{\pi}$ to $2\int_0^{\pi/2}$. The infinite upper boundary on the $\mathrm{d}k$ integration leads to divergences just like the AC conductivity treatment and therefore is cutoff at $k_{\max} = 1/r_{\min}$. This yields our final expression for the one-cycle energy change

$$\Delta E_{\mathrm{SP}}^{(1)} = \frac{2e^2}{\pi\epsilon_0} \int_0^{k_{\max}} \mathrm{d}k \int_0^{\pi/2} \mathrm{d}\theta \sin\theta \sum_{n=1}^{\infty} n\, J_n(ka\cos\theta)^2 \left[\mathrm{Im}\frac{-1}{\epsilon(\mathbf{k}, n\omega_0)}\right]. \tag{3.51}$$

At this point we note the similarity of the above result to the one derived in Ref. [54], however in their case the derivation is done assuming no external magnetic field. The formula as written in (3.51) includes magnetization effects assuming one uses the proper, magnetized dielectric function.

3.4.3 Low amplitude, high frequency limit

Now we evaluate (3.51) for the low amplitude, collisionless case and show exact correspondence with the expression calculated for the one-cycle heating using AC conductivity in Section 3.4.1. We consider the driven-damped harmonic oscillation amplitude

$$a = \frac{eE/m_{\mathrm{e}}}{\sqrt{(\omega_0^2 - \omega_{CM}^2)^2 + (\xi\omega_0)^2}} \tag{3.52}$$

in the high frequency limit $(\omega_0/\omega_{CM})^2 \gg 1$ where $\omega_{CM} \sim \omega_p$ is the electron center of mass oscillation frequency. Here ξ is an oscillation damping rate related to—not necessarily equivalent to—the collision rate γ. Starting from (3.51), substituting $a \approx eE/m_{\mathrm{e}}\omega_0^2$, neglecting contributions from $n > 1$ order Bessel functions, and using the small argument approximation $J_1(z) \approx z/2$ yields

$$\begin{aligned}
\lim_{a,\gamma\to 0} \Delta E_{\mathrm{SP}}^{(1)} &= \frac{2e^2}{\pi\epsilon_0} \int_0^{k_{\max}} \mathrm{d}k \int_0^{\pi/2} \sin\theta \mathrm{d}\theta \left(\frac{eEk\cos\theta}{2m_{\mathrm{e}}\omega_0^2}\right)^2 \left[\mathrm{Im}\frac{-1}{\epsilon(\mathbf{k},\omega_0)}\right] \\
&= \frac{\pi E^2}{n_{\mathrm{e}}\omega_0} \mathrm{Re}\,\sigma_{\parallel}(\omega_0) \\
&= \Delta E_{\mathrm{AC}}^{(1)}.
\end{aligned} \tag{3.53}$$

Equation (3.53) demonstrates how we recover the magnetized AC conductivity from SPLET in the low amplitude, high frequency limit.

3.4.4 Scaling and extension beyond UCPs

Even though our main focus is on predictions in reference to UCPs, the results shown here can be extended to plasmas with different temperatures and densities through scaling relationships. This can be seen most clearly by transforming the expressions into dimensionless forms using natural, characteristic units. We apply the transformations $k\lambda_{\mathrm{D}} \to k'$, $\omega/\omega_p \to \omega'$, $\omega_c/\omega_p \to \beta$ to the collisionless, magnetized dielectric function (3.21), for example. It can thus be rewritten

$$\epsilon(\mathbf{k}',\omega') = 1 + \frac{1}{k'^2}\left[1 + \frac{\omega'}{\sqrt{2}|k'_\parallel|}\sum_{m=-\infty}^{\infty}\exp\left(-\frac{k'^2_\perp}{\beta^2}\right) I_m\left(\frac{k'^2_\perp}{\beta^2}\right) Z\left(\frac{\omega' + m\beta}{\sqrt{2}|k'_\parallel|}\right)\right] \tag{3.54}$$

A similar expression follows in the collisional case, (3.9), by naturally scaling the collision rate with γ/ω_p.

In the context of RF heating we examine the scaled form for the heating rate $\eta/\omega_p \to H$. This can be expressed with the above dimensionless parameters $k',\ \omega',\ \beta$, in addition to the coupling parameter Γ, as well as a properly scaled amplitude.

In the stopping power treatment, the amplitude gets scaled by the screening length, $a/\lambda_{\rm D} \to a'$. With this transformation we rewrite (3.51)

$$\Delta E^{(1)}_{\rm SP} = \frac{2e^2}{\pi\epsilon_0\lambda_{\rm D}}\int_0^{k'_{\rm max}} {\rm d}k' \int_0^{\pi/2} {\rm d}\theta \sin\theta \sum_{n=1}^{\infty} n\, J_n(k'_\parallel a')^2 \left[{\rm Im}\frac{-1}{\epsilon(\mathbf{k}', n\omega'_0)}\right]. \tag{3.55}$$

From our expression for η in (3.30) we get

$$\begin{aligned} H_{\rm SP} &= \frac{\eta_{\rm SP}}{\omega_p} = \frac{\Delta E^{(1)}_{\rm SP}}{\pi m a^2 \omega_0 \omega_p} \\ &= \frac{8\sqrt{3}}{\pi}\frac{\Gamma^{3/2}}{\omega' a'^2}\int_0^{k'_{\rm max}} {\rm d}k' \int_0^{\pi/2} {\rm d}\theta \sin\theta \sum_{n=1}^{\infty} n\, J_n(k'_\parallel a')^2 \left[{\rm Im}\frac{-1}{\epsilon(\mathbf{k}', n\omega'_0)}\right]. \end{aligned} \tag{3.56}$$

For the AC conductivity treatment we start by naturally scaling (3.34).

$$\frac{{\rm Re}\,\sigma_\parallel(\omega')}{\epsilon_0\omega_p} = \frac{2\sqrt{3}}{\pi}\frac{\Gamma^{3/2}}{\omega'^3}\int_0^{k'_{\rm max}} {\rm d}k' \int_0^{\pi/2} {\rm d}\theta\, k'^2_\parallel \sin\theta \left[{\rm Im}\,\frac{-1}{\epsilon(\mathbf{k}', \omega')}\right]. \tag{3.57}$$

From (3.30) and (3.35) we get

$$H_{\rm AC} = \frac{\eta_{\rm AC}}{\omega_p} = 3\frac{\Gamma^3\omega'^2}{a'^2}\left(\frac{E}{E_{\rm lim}}\right)^2 \frac{{\rm Re}\,\sigma_\parallel(\omega')}{\epsilon_0\omega_p} \tag{3.58}$$

where $E_{\rm lim}$ is the characteristic electric field amplitude defined in (3.37). This field amplitude can be expressed as a relationship between the high frequency-limit amplitude $a \approx eE/m\omega_0^2$ and the distance of closest approach $r_{\rm min} = e^2/4\pi\epsilon_0 k_{\rm B}T$ [52]. With this notation the scaled heating rate

can be reduced to

$$H_{\mathrm{AC}} = \omega'^2 \frac{\mathrm{Re}\,\sigma_{\parallel}(\omega')}{\epsilon_0 \omega_p}. \tag{3.59}$$

Both H_{SP} and H_{AC} show similar scaling relationships. This is not necessarily surprising given we previously showed agreement between models in the appropriate low amplitude limit. In the next section we evaluate the above expressions from the SPLET and AC conductivity treatments and characterize some of their differences.

3.4.5 Model evaluations vs. applied magnetic field and RF amplitude for UCP conditions

We wish to compare the SPLET and AC conductivity models within a parameter space spanning the magnetic field strength $\beta = \omega_c/\omega_p$, the Coulomb coupling strength Γ, and the driving amplitude E/E_{lim}. In Section 3.4.3 we found that SPLET converges to the AC conductivity treatment in the high frequency, low amplitude limit when the amplitude is well-approximated by $a \approx eE/m\omega_0^2$. Unless specified otherwise, the function evaluations in this section use this form for the oscillation amplitude—as opposed to (3.52)—so that differences that arise between the models can be observed directly.

Before continuing further, I should note a disclaimer statement for the evaluations presented in this chapter: the linearization approximation for the electron distribution in the Vlasov equation should begin breaking down when the electron oscillation velocity due to the RF, $v_{RF} = a\omega_{RF}$, exceeds the thermal velocity v_{th}. This restriction is violated for some ranges of conditions in some of the plots presented below, and this occurs in plots where the RF amplitude and/or frequency become very large. The SPLET equations were evaluated under these conditions not with the illogical intention of producing strong predictions where the theory is invalid but rather to establish general behavior and trends. In more casual language, I evaluated the theory we developed in regions it should breakdown out of curiosity to see how things breakdown. I show whole ranges of parameter spaces for comparisons, but it is important to note the theoretical breakdown expected around $v_{RF} > v_{\mathrm{th}}$.

I evaluated the expressions to produce the following results using an assortment of computational packages. A one-dimensional adaptive quadrature integration algorithm and certain special functions were taken from the ALGLIB free C++ numerical analysis library [127]. The results presented here were all calculated using an n-dimensional quadrature integration algorithm, Cubature, provided by the Joannopolous *ab initio* Research Group at MIT [128]. Terms related to the complex error function and Faddeeva function, such as those in (3.12), were calculated using the open-source Faddeeva Package also provided by the Joannopolous *ab initio* Group [125]. I found that for comparable numerical tolerances the 2-D Cubature and two nested 1-D ALGLIB integrators produced practically identical results, however the Cubature implementation was one to two orders of magnitude faster in time to converge. The relative tolerance was set between 1×10^{-3} and 1×10^{-4}; this is more than precise enough for the predictions we are interested in.

For the parameter space of interest, we found numerical convergence to within the integrator tolerance using $n_{\max}, m_{\max}$ ranging from 80 to over 1000 for the maximum indices in the sums involving the J_n and I_m Bessel functions. Due to numerical instabilities, the large argument asymptotic form for the $e^{-\beta_k} I_m(\beta_k)$ terms was used when the $\beta_k = k_\perp'^2/\beta^2$ argument is greater than 50, such as when β approaches zero [124, § 10.40(i)]. This asymptotic expression diverges when $m^2 \gg \beta_k$, so in such cases I used the large argument, large order double-asymptotic expression provided by [124, § 10.41(iv)] and references therein. Along the same lines, when $\beta = 0$ the models used the unmagnetized dielectric function (3.6) to avoid computational divergences. The collisionless, magnetized dielectric function (3.21) was otherwise used for all $\beta \neq 0$. Long numerical integration times disincentivized me from densely evaluating regions where the electron temperature was high, magnetic field was low, and/or the driving amplitude was high.

We performed a series of calculations using these theories with several goals in mind. We wanted to determine the predicted effect of an applied magnetic field on heating rates associated with geometries and dimensionless parameters accessible to UCP experiments. This includes quantifying variations in H as a function of β from weak to extreme magnetization and investigating the dependence on applied RF amplitude and frequency scales. Lastly, we wanted to see if includ-

ing a collision term in the SPLET theory resulted in significant changes in the heating rate for our conditions. These predictions establish a baseline for expectations associated with our parameters and help us consider how important different effects might be.

Figures 3.1 and 3.2 show the scaled heating rates H_{SP} and H_{AC} as a function of magnetic field strength β and driving amplitude E/E_{lim} for coupling parameters $\Gamma = 0.137, 0.0456, 0.0137$ and scaled driving frequency $\omega' = 1.93$. These correspond to the following UCP experimental parameters: $n_{\mathrm{e}} = 1.2 \cdot 10^7\ \mathrm{cm}^{-3}$, $T_{\mathrm{e}} = 4.5, 13.5, 45\ \mathrm{K}$, and $\omega_0 = 2\pi \cdot 60\ \mathrm{MHz}$. At this driving frequency and these three temperatures the characteristic electric field amplitudes are $E_{\mathrm{lim}} = 3.0, 1.0, 0.3\ \mathrm{V/m}$, respectively. The three non-zero magnetic field strengths evaluated in Figure 3.2, $\beta = 0.962, 5.85, 12.1$, correspond to $B = 10.6, 65.0, 134\ \mathrm{G}$. For the most strongly coupled condition presented here ($\Gamma = 0.137$), the magnetic field strength associated with the onset of the extremely magnetized regime—when $r_c < r_{\mathrm{min}}$—is $\beta = 11.4$.

In Section 3.4.4 we found that H_{SP} and H_{AC} both scale with coupling strength in terms of the product of $\Gamma^{3/2}$ with an integral that diverges logarithmically in its upper bound as $k'_{\mathrm{max}} = \lambda_{\mathrm{D}}/r_{\mathrm{min}} \sim \Gamma^{-3/2}$. Combined, the scaling with coupling strength will be between $\Gamma^{1/2}$ and $\Gamma^{3/2}$. This is corroborated by comparing the vertical scale of each panel in Figures 3.1 and 3.2.

The variation in heating rate as a function of magnetic field strength at the scales we are interested in appears to be relatively small as is illustrated in Figure 3.1. There is little variation at low fields near $\beta = 0$, and near $\beta = \omega'$ we see a local maximum. For $\beta > \omega'$ we see a local minimum followed by a gradually increasing heating rate, but this all occurs within a few percent of the average value over the plotted region. The heating rate predicted by SPLET depends on oscillation amplitude and decreases relative to the AC conductivity prediction with increasing driving field strength. The qualitative structure of the heating rate as a function of magnetization does not significantly change with coupling strength or driving strength over the region of interest.

Plotting the heating rate versus driving field amplitude, like in Figure 3.2, we can clearly see that for small amplitudes the SPLET heating rate exhibits the same linear dependence on the square driving amplitude as predicted by the AC conductivity's Ohmic heating. As the amplitude E/E_{lim}

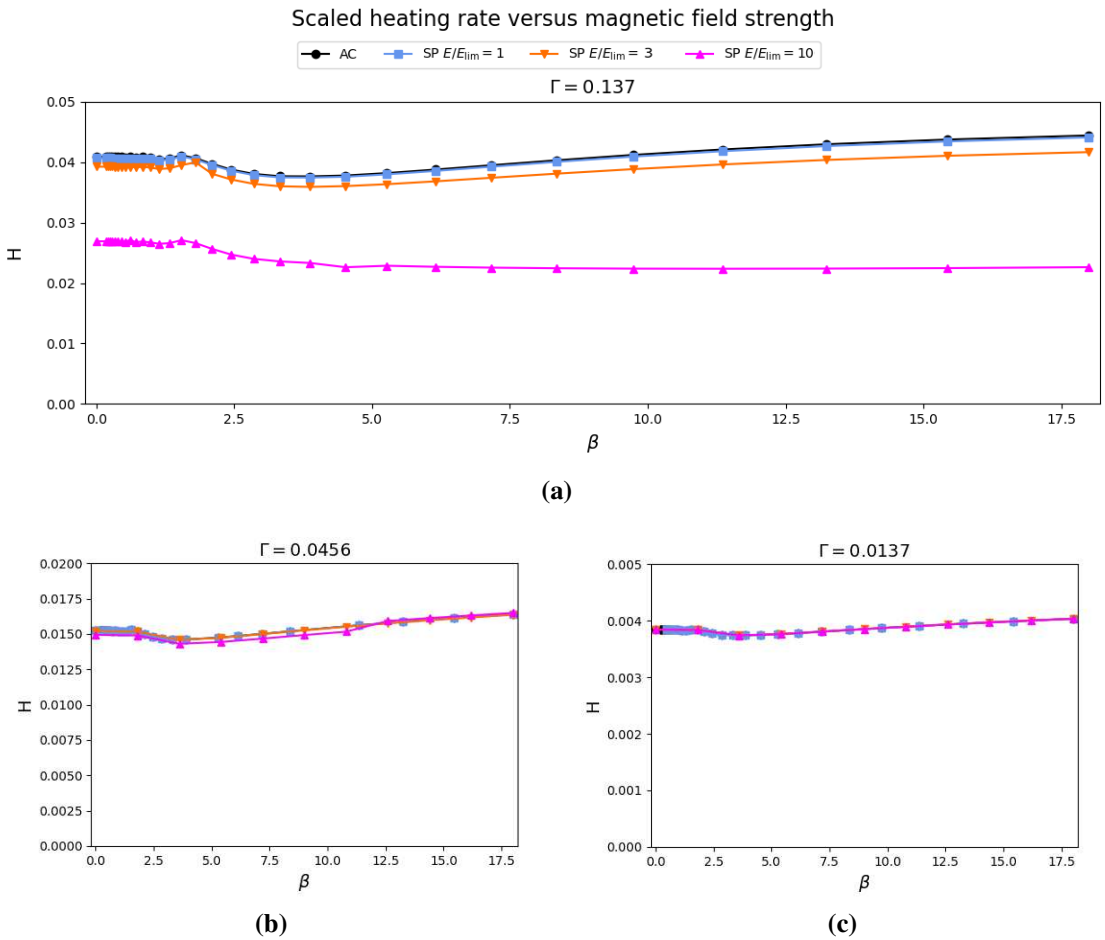

Figure 3.1: Scaled heating rates H_{SP} and H_{AC} as defined in (3.56) and (3.59) versus magnetic field strength $\beta = \omega_c/\omega_p$ at density $n = 1.2 \cdot 10^7\ \mathrm{cm}^{-3}$ and RF driving frequency $\omega' = \omega_{RF}/\omega_p = 1.93$. In each panel H_{SP} is plotted for three driving amplitudes scaled by the temperature-dependent characteristic field E_{lim} defined in (3.37). The coupling strengths across the panels work out to the following electron temperatures and E_{lim}: (a) $\Gamma = 0.137$, $T_{\mathrm{e}} = 4.5\,\mathrm{K}$, $E_{\mathrm{lim}} = 3.0\,\mathrm{V/m}$; (b) $\Gamma = 0.0456$, $T_{\mathrm{e}} = 13.5\,\mathrm{K}$, $E_{\mathrm{lim}} = 1.0\,\mathrm{V/m}$; (c) $\Gamma = 0.0137$, $T_{\mathrm{e}} = 45\,\mathrm{K}$, $E_{\mathrm{lim}} = 0.3\,\mathrm{V/m}$.

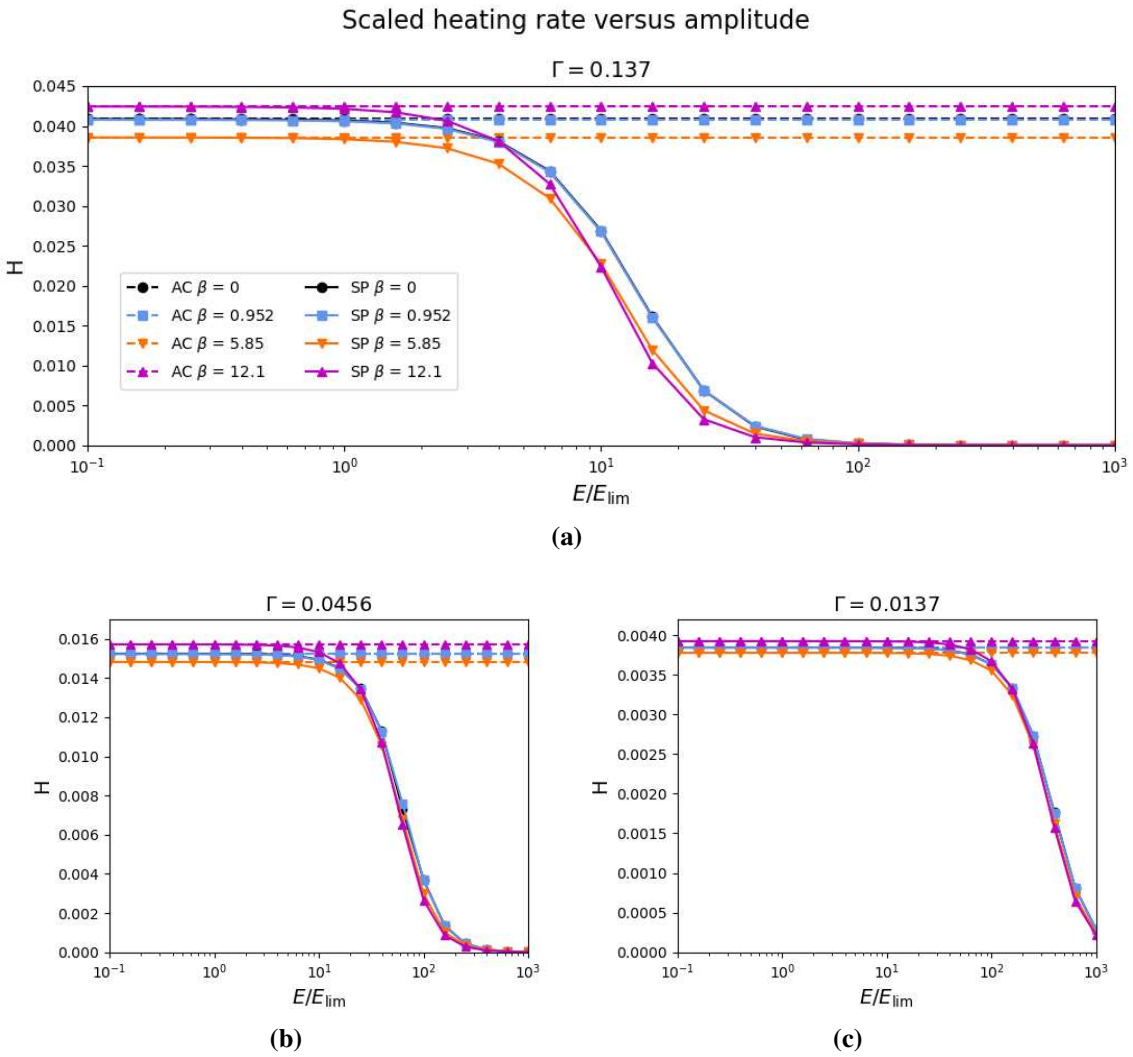

Figure 3.2: Scaled heating rates H_{SP} and H_{AC} as defined in (3.56) and (3.59) versus scaled driving electric field amplitude E/E_{lim} at density $n = 1.2 \cdot 10^7\ \mathrm{cm}^{-3}$ and RF driving frequency $\omega' = \omega_{RF}/\omega_p = 1.93$. E_{lim}, defined in (3.37), is a temperature-dependent characteristic electric field amplitude. In each panel both H_{SP} and H_{AC} are plotted for four magnetic field strengths $\beta = \omega_c/\omega_p$. The three non-zero β correspond to the following magnetic fields $B = 10.6, 65, 134\,\mathrm{G}$. The coupling strengths across the panels work out to the following electron temperatures and E_{lim}: (a) $\Gamma = 0.137$, $T_{\mathrm{e}} = 4.5\,\mathrm{K}$, $E_{\mathrm{lim}} = 3.0\,\mathrm{V/m}$; (b) $\Gamma = 0.0456$, $T_{\mathrm{e}} = 13.5\,\mathrm{K}$, $E_{\mathrm{lim}} = 1.0\,\mathrm{V/m}$; (c) $\Gamma = 0.0137$, $T_{\mathrm{e}} = 45\,\mathrm{K}$, $E_{\mathrm{lim}} = 0.3\,\mathrm{V/m}$.

increases, the nonlinear terms in the SPLET cause the predicted heating rate to deviate from the linear approximation. This deviation generally becomes significant when the oscillation velocity $a\omega_{RF}$ approaches or exceeds the electron thermal velocity $v_{\rm th}$ [54]. This condition for the onset of nonlinearity can be expressed as $v' \equiv a\omega_{RF}/v_{\rm th} > 1$; in terms of our scaled driving parameters $E/E_{\rm lim}$ and $\omega' = \omega_{RF}/\omega_p$ we have

$$\frac{E}{E_{\rm lim}} > \frac{1}{\sqrt{3}\,\omega'\,\Gamma^{3/2}} \quad \Leftrightarrow \quad v' > 1. \tag{3.60}$$

One way we can characterize this deviation in the models is by finding the amplitude at which there is a 10% difference between predictions as a function of magnetization. That is, we solve $1 - H_{\rm SP}(E/E_{\rm lim})/H_{\rm AC} = 0.1$ for $E/E_{\rm lim}$ and define the solutions as the 10%-deviation amplitude. Figure 3.3 plots the 10%-deviation amplitude in terms of $E/E_{\rm lim}$ as a function of β for the lower temperature $\Gamma = 0.137$ condition and two RF driving frequencies, $\omega' = 1.93, 5.79$. Figures 3.2(b) and (c) show the same curves as (a) with rescaled vertical axes to highlight the relative features. The red vertical lines in (b) and (c) denote the magnetic field strengths where the cyclotron frequency equals the RF frequency, $\omega_c = \omega_{RF}$.

For the most part, the amplitude for a constant fractional deviation between models gradually decreases with higher magnetic field strength with the exception of features in the shape of the curve associated with cyclotron frequencies near harmonics of the RF frequency. This mild behavior in the predicted onset of RF heating nonlinearity as a function of magnetic field has been similarly observed in magnetized stopping power theory [46].

3.4.6 Modeled heating rate dependence on driving frequency

Even though the RF heating experiments performed for this thesis used a single value for the driving frequency, as part of a broader review of H [129], we looked at its dependence on ω_{RF}. Doing so allows us to establish baseline expectations and predictions for trends. This is potentially useful for guiding planned parameter spaces in future experimental explorations.

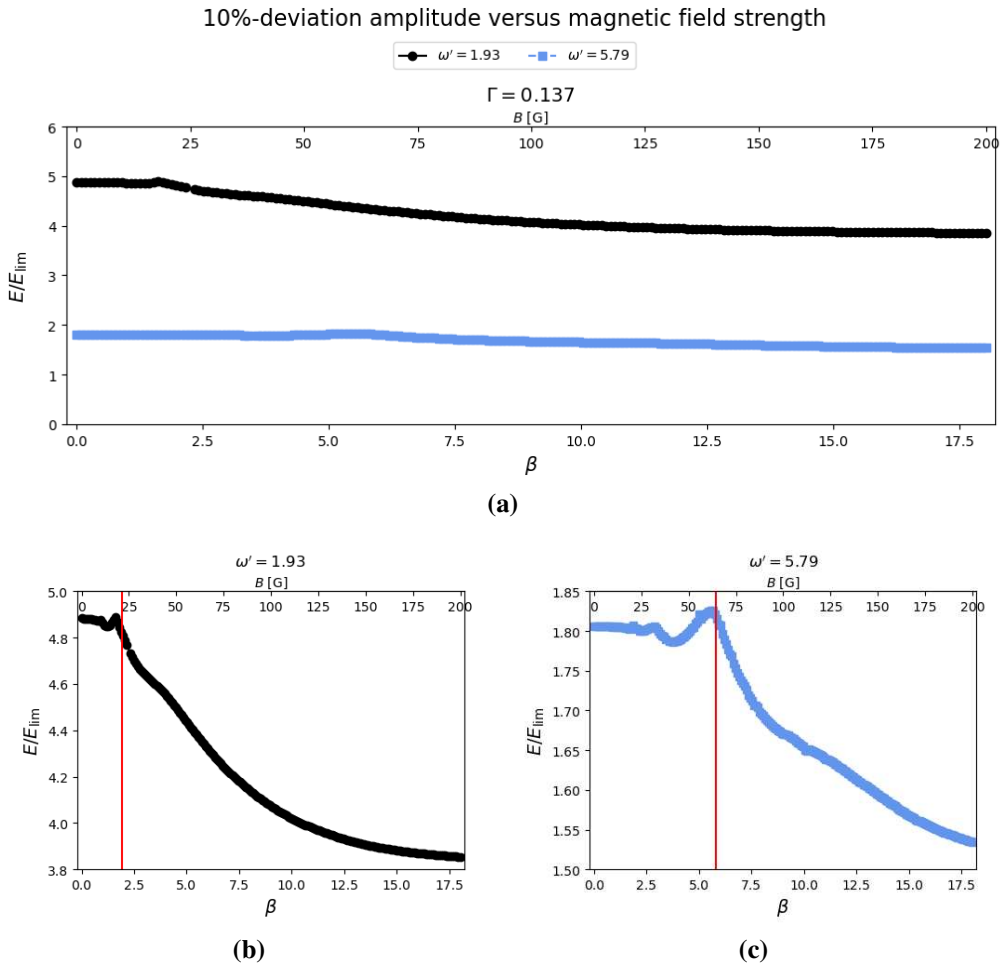

Figure 3.3: (a) Scaled field amplitude characterizing a 10% difference between heating rates H_{SP} and H_{AC} versus magnetic field strength at two RF frequencies $\omega' = \omega_{RF}/\omega_p = 1.93$ and 5.79. In other words, plotted is the solution to $1 - H_{\mathrm{SP}}(E,\beta)/H_{\mathrm{AC}}(\beta) = 0.1$ as a function of β at the $\Gamma = 0.137$, $T_{\mathrm{e}} = 4.5\,\mathrm{K}$ condition for $\omega_{RF} = 2\pi\cdot 60\,\mathrm{MHz}$ and $2\pi\cdot 180\,\mathrm{MHz}$. Lower panels (b), (c) are the same as (a) except split and rescaled to emphasize features associated with cyclotron frequencies near harmonics of the RF frequency. The red vertical lines in the lower panels mark where $\omega_c = \omega_{RF}$.

The variation in H as a function of $\omega' = \omega_{RF}/\omega_p$ is shown in Figure 3.4 for three values of Γ (0.15, 0.05, 0.015) and three degrees of magnetization. The solid, dashed, and dotted lines correspond to evaluations in different Γ–β-dependent magnetization regimes [27]: the solid lines are for $\beta = 0$; the dashed lines are for β representative of strong magnetization when $r_{\min} < r_c < \lambda_{\rm D}$; and likewise, the dotted lines are at extremely magnetized β when $r_c < r_{\min}$. The values of β plotted for each of the non-zero magnetization regimes are $\beta_{r_{\min}<r_c<\lambda_{\rm D}} = 2.5,\ 5.7,\ 14.1$ and $\beta_{r_c<r_{\min}} = 25,\ 130,\ 800$ for couplings $\Gamma = 0.15,\ 0.05,\ 0.015$, respectively.[4] The top row of panels (a,b,c) are evaluations of the low-amplitude AC conductivity predictions (3.59), and the bottom row (d,e) are similar calculations with finite amplitude $E/E_{\rm lim} = 10$ using SPLET (3.56).

The decrease of H with increasing ω' is consistent with previous predictions. [52, 54] For unmagnetized and strongly-magnetized conditions, only mild variations are observed across different values of ω' for the values of Γ investigated. Increasing the magnetization does produce differences, but across all the conditions studied with small enough oscillation amplitudes ($a/r_{\min} \lessapprox 10$) these differences are relatively minor despite order-of-magnitude changes in degree of magnetization.

Whether or not the magnetic field is predicted to enhance or decrease H under conditions of extreme magnetization depends on the coupling strength and oscillation parameters. We see that the dependence of H on ω' is generally steeper in the extremely magnetized regime. This observation is qualitatively similar to the subtle change in dependence of H on $E/E_{\rm lim}$ at the highest β plotted in Figure 3.2. One effect of this is that the sign of the relative change in heating rate with extremely magnetized electrons compared to the lesser-magnetized cases is predicted to depend on a and ω_{RF}. For the range of Γ explored here, the low-amplitude heating rate is enhanced at extreme magnetization for $\omega' \gtrapprox 1$ and decreases with larger ω'. The steeper dependence in this heating rate produces a crossing point where the enhancement at lower ω' generally becomes a reduction for high ω' outside of the $\omega' = \beta$ cyclotron resonance.

[4] E.g. the curves in Figure 3.4(b) and (e) are at $\beta = 0,\ 5.7,\ 130$.

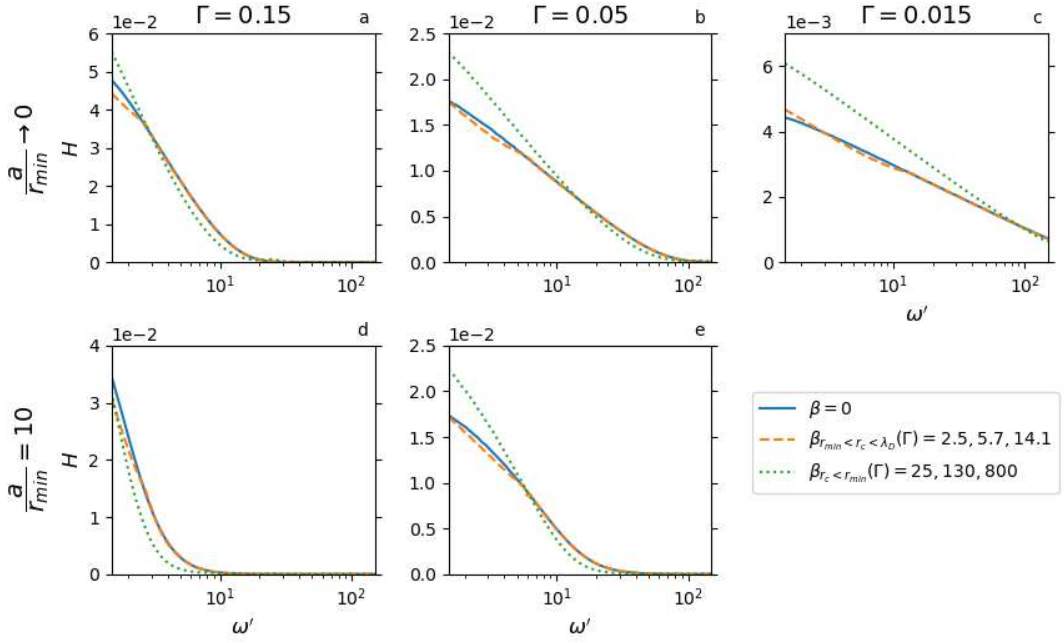

Figure 3.4: Scaled heating rate H versus scaled driving frequency $\omega' = \omega_{RF}/\omega_p$. The solid, dashed, and dotted lines correspond to evaluations in different Γ–β-dependent magnetization regimes [27]: the solid lines are for $\beta = 0$; the dashed lines are for β representative of strong magnetization when $r_{\min} < r_c < \lambda_{\rm D}$; and likewise, the dotted lines are at extremely magnetized β when $r_c < r_{\min}$. The values of β plotted for each of the non-zero magnetization regimes are $\beta_{r_{\min}<r_c<\lambda_{\rm D}} = 2.5,\ 5.7,\ 14.1$ and $\beta_{r_c<r_{\min}} = 25,\ 130,\ 800$ for couplings $\Gamma = 0.15,\ 0.05,\ 0.015$, respectively. The top row of panels (a,b,c) are evaluations of the low-amplitude AC conductivity predictions (3.59), and the bottom row (d,e) are similar calculations with finite amplitude $E/E_{\rm lim} = 10$ using SPLET (3.56).

What is most notable across all of the results plotted in Figs. 3.1 through 3.4 is that consistently there is only a mild dependence on magnetic field for appropriately chosen dimensionless parameters. This is despite the fact that the degree of magnetization of the electrons is changing profoundly over the values of β that have been investigated. This general observation of only mild dependence on electron magnetization in the predictions of this linear response theory with regard to heating arising from finite AC conductivity is the central one obtained as a result of this work as it informs expectations for measurements associated with UCP laboratory-accessible scales.

It is reasonable to question the validity of examining nonlinear effects born from a linear response treatment of RF heating. The authors of Ref. [54] provided results from 2D particle-in-cell (PIC) simulations of unmagnetized RF heating to compare with their nonlinear theory and found agreement when $v' \approx 1$. By $v' = 15$, a factor of ~2 discrepancy between the PIC simulations and theory has developed. The authors suggest correlated collisions could play a role if the driving field causes electrons to collide repeatedly with the same ion(s) over timescales shorter than ω_p^{-1}. Thus, for RF amplitudes and frequencies corresponding to $v' > 10$, the nonlinear heating rate theory presented in this chapter can be expected to breakdown. Still, heating rates in parameter ranges extending beyond these constraints are calculated and plotted in the above figures for the sake of exploration, but the validity of our model's predictions at very large RF amplitude and frequency is very much suspect.

3.4.7 Effects of the electron relaxation term in $\epsilon(\mathbf{k}, \omega)$ on predicted heating

Ref. [36] offers a prescription for including electron relaxation processes by solving the linearized, magnetic Vlasov equation for the dielectric function $\epsilon(\mathbf{k}, \omega)$ with the inclusion of a BGK-type collision term [123]. The resulting formula, transcribed in Section 3.2.1 as (3.9) and succeeding equations, is expressed in terms of the collision frequency γ. The authors relate this parameter to the sum of the electron-electron and electron-ion collision rates,

$$\gamma = \gamma_{\mathrm{ee}} + \gamma_{\mathrm{ei}}. \tag{3.61}$$

The electron collision rate with species ν is given by

$$\gamma_{e\nu} = C_{e\nu}\frac{8\sqrt{2\pi}}{3}\left(\frac{e^2}{4\pi\epsilon_0}\right)^2 \frac{n_\nu}{m_e m_\nu v_{e\nu}^3}\ln\Lambda_{e\nu} \tag{3.62}$$

where $C_{ei} = 1, C_{ee} = \sqrt{2}, v_{e\nu}^2 = \frac{k_B T_e}{m_e} + \frac{k_B T_\nu}{m_\nu}$, and $\ln\Lambda_{e\nu}$ is a generalized Coulomb logarithm [36].

The large ratios between electron/ion temperature and mass lead to simplifying reductions for γ. We see that $v_{ei} \approx \frac{v_{ee}}{2} = \frac{k_B T_e}{m_e}$; similarly $\ln\Lambda_{ei}$ and $\ln\Lambda_{ee}$ are typically within one or two orders of magnitude of each other. Therefore the remaining m_ν factor in the denominator of (3.62) suggests the total collision frequency is well-approximated by solely the electron-electron collision rate.

The authors of Ref. [36] also provided theoretical expressions for and plots of $\ln\Lambda_{e\nu}$ in consideration of both charge species as well as magnetization effects. It is noted that for e-i collisions their expressions are the same as those derived for ionic temperature relaxation rates in the magnetized [32] and unmagnetized [26] cases. Generalizing to e-e interactions can be accounted for by the replacement of ion parameters with those of electrons in addition to a $\sqrt{2}$ factor accounted for in the above formula by C_{ee}.

Rather than using the purely theoretical prediction for γ_{ee} provided by Ref. [36], we may instead wish to find values backed by experimental measurements. This substitution would also serve useful since the form of the expression provided for $\ln\Lambda_{ee}$ is not particularly conducive to straightforward numerical integration and evaluation. Fortunately, magnetized electron collisional equipartition rates—which can be directly related to thermal relaxation rates [32]—have been systematically studied using theoretical treatments in good agreement with measurements [66]. These equipartition rates, τ_{eq}^{-1}, describe the equilibriation of a temperature anisotropy between dimensions parallel and perpendicular to the magnetic field

$$\frac{dT_\perp}{dt} = -\frac{T_\perp - T_\parallel}{\tau_{eq}}. \tag{3.63}$$

In the case of an unmagnetized plasma we find [26, 32]

$$\gamma_{\rm ee} = \frac{5}{\sqrt{2}}\tau_{\rm eq}^{-1}. \tag{3.64}$$

Interpolating Table I in Ref. [66] provides us with predictions for $\tau_{\rm eq}^{-1}$ as a function of the parameter $\bar{\kappa} \sim r_{\rm min}/r_c \sim B/T^{3/2}$ which depends on both magnetic field and temperature. The predicted electron equipartition rate decreases monotonically with increasing $\bar{\kappa}$. If we assume the $\frac{5}{\sqrt{2}}$ conversion factor in (3.64) is constant with respect to the magnetic field then $\tau_{\rm eq}^{-1}(n, \bar{\kappa})$ gives us $\gamma_{\rm ee}(\Gamma, \beta)$. For instance, the predicted collision rate from this method yields $\gamma_{\rm ee} = 1.52 \cdot 10^7\,{\rm s}^{-1}$ at $n = 1.2 \cdot 10^7\,{\rm cm}^{-3}$, $T_{\rm e} = 4.5\,{\rm K}$, $B = 10.6\,{\rm G}$.

The effect on heating rate from including the collisional relaxation term in the dielectric function is explored in Figure 3.5. I evaluated heating rates over two decades of collision rates centered about the rate $\gamma_{\rm ee}(\beta)$ predicted by the method described above for $\Gamma = 0.137$ at the usual three non-zero magnetization strengths. Plotted is the ratio of the heating rates calculated from SPLET at $E/E_{\rm lim} = 1$ using the "collisional" dielectric function $\epsilon(\mathbf{k}, \omega, \gamma)$ from (3.9) compared to rates using the "collisionless" $\epsilon(\mathbf{k}, \omega, 0)$ derived as (3.21). The curves decrease gradually and monotonically with increasing collision frequency. Their intersection with the center vertical gridline shows a modest decrease in predicted heating rate of less than 5%, and the absolute vertical scale suggests that even if the collision rates are underestimated by an order of magnitude the heating rates would decrease by no more than 25%.

3.5 Chapter summary

In this chapter we explored and developed theoretical treatments for RF heating of magnetized ultracold neutral plasma. We identified two separate physical pictures, one in terms of binary collisions and another as a linear response dielectric treatment. The linear response picture can be used to predict Ohmic heating from a magnetic field-dependent AC conductivity, but the theory only applies in the limit of small amplitude oscillations. We developed an alternative model for plasma RF heating using a Vlasov-Poisson-based stopping power-like energy transfer (SPLET) treatment

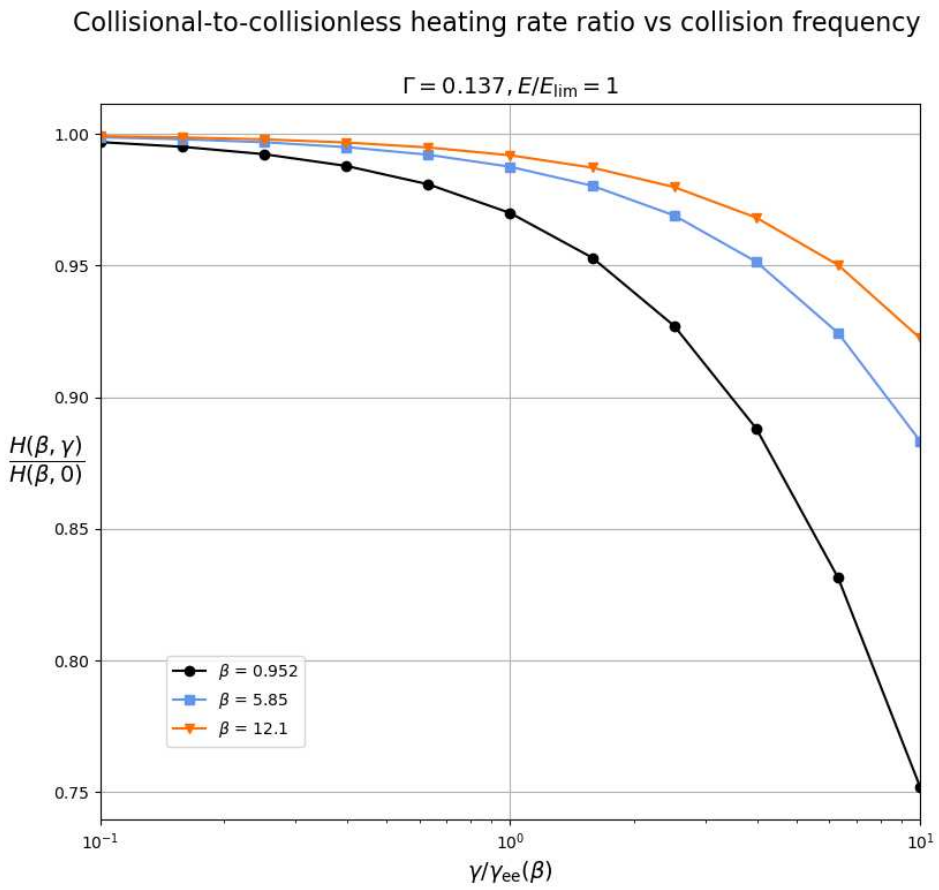

Figure 3.5: The ratio of heating rates calculated using the collisional and collisionless magnetized dielectric functions, (3.9) and (3.21), as a function of collision frequency at $\Gamma = 0.137$ and three magnetic field strengths. The center frequencies $\gamma_{\rm ee}(\beta)$ are determined from (3.64), and at $\beta = 0.952, 5.85, 12.1$ this produces $\gamma_{\rm ee} = 15.2, 6.53, 3.74\,\mu{\rm s}^{-1}$, respectively.

with the goal of finding a prediction applicable to new experimental measurements reported in this dissertation.

We evaluated and compared the predicted scaled, longitudinal RF heating rate from both the AC conductivity and SPLET treatments as functions of applied magnetic field strength, electron temperature, driving field amplitude and frequency, and BGK-type collisional relaxation rate. These calculations teach us several things about expected effects and variations across these parameters. The main result across all of the data presented in this chapter is that variations in the longitudinal RF heating rate are predicted to be mild (of order unity) across a large range of magnetic field strengths—even into the extremely magnetized regime—for plasma and RF parameters accessible to UCP experiments. Nonlinear effects associated with RF amplitudes larger than low-amplitude limits were evaluated and found to not be critical for our experimental conditions. Finally, the potential effect of collisions on the SPLET was evaluated using a BGK relaxation approximation and found to likely be relatively insignificant for our conditions.

The models and evaluations in this chapter establish the theoretical framework for our predictions, and in the next chapter we will develop the experimental framework for our measurements. Looking forward to Chapter 5, there we will combine the results of the theoretical and experimental frameworks established in Chapters 3 and 4 into a systematic measurement paired with reasonable physical predictions.

Chapter 4

Experiment operation

Up to this point in the dissertation we have focused primarily on plasma physics background, theory, and modeling. Now we turn our attention toward experimental aspects. The primary results, experimentally measuring RF heating of magnetized electrons, are presented and discussed in Chapter 5. Understanding where our numbers come from and how to interpret them hinges upon a solid grasp of the machine and techniques used to produce those results. In this chapter we start with a brief overview of key aspects in the experiment apparatus' design and operation with the understanding that most specific details can be found in dissertations from preceding students Truman Wilson [15] and Wei-Ting Chen [17]. What is not covered in those references are the recent modifications made in order to adapt the apparatus to produce and probe strongly magnetized ultracold plasma; I detail these changes and modifications in Section 4.2. In Sections 4.3 through 4.6 I discuss the techniques and results for the calibrations and predicating measurements we needed to ultimately make a systematic experimental determination of RF heating in a magnetized UCP.

4.1 Apparatus design

The experimental apparatus described in this section is of laboratory tabletop scale. The components mainly consist of: an ultrahigh vacuum (UHV) chamber (and related equipment like vacuum pumps); four lasers and associated optics; and combinations of off-the-shelf and student-assembled electronics for electric and magnetic field generation and control. First, I will describe the UHV chamber.

The UHV chamber has a tube-shaped, "stream" design about $1.1\,\mathrm{m}$ long formed by assembling stainless steel sections with inner diameter ~$3.8\,\mathrm{cm}$. We designate two physically separated regions, identified in Figure 4.1 as the Neutral and Plasma regions. The neutral atomic section is on the "upstream" side; the "downstream" end is the photoionization and plasma region. This stream terminology references a typical experiment sequence that transports atoms ~$73\,\mathrm{cm}$ from the neu-

tral region to photoionization region, and the photoelectrons are pulled further downstream toward a detector. This separate-region and transport design was inspired by BEC experiment design [130] and will be discussed in more detail later.

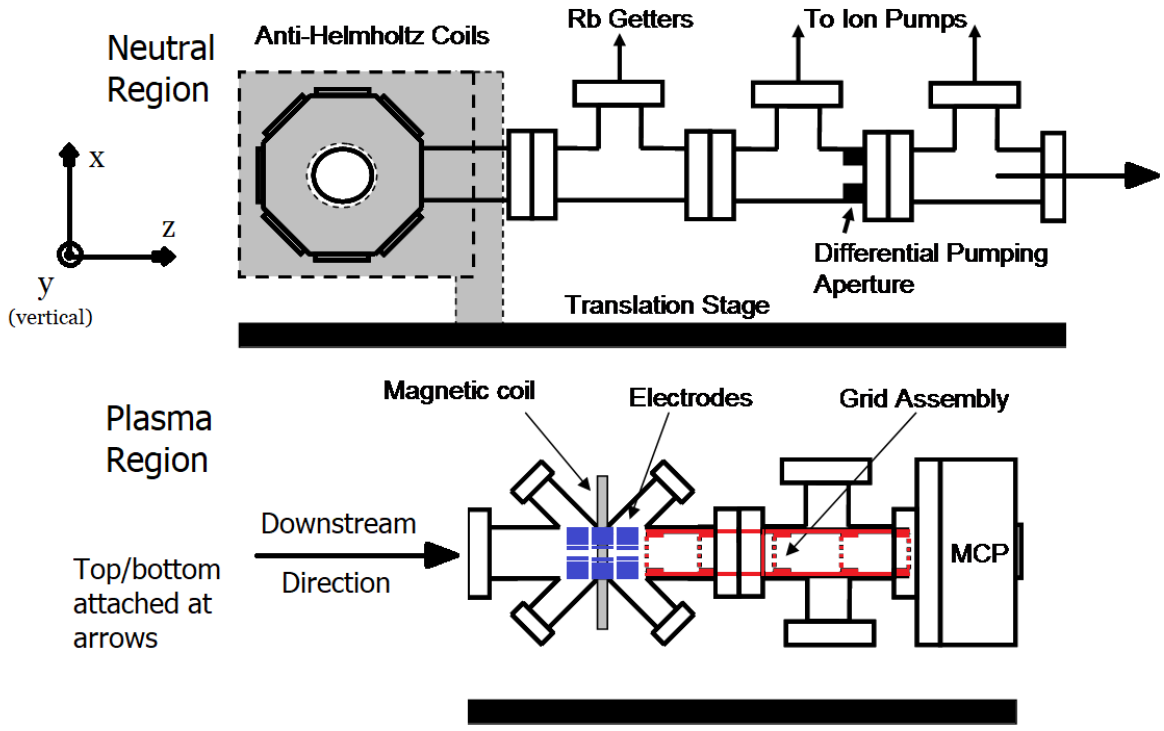

Figure 4.1: Diagram depicting the UHV apparatus and experiment "regions," adapted from Ref. [15]. The top portion includes the upstream neutral preparation region; the bottom portion is the photoionization and plasma region. The top and bottom portions are connected at the black arrow.

I will now provide general descriptions of UHV components going from upstream to downstream before discussing the lasers and electronics. As illustrated in Figure 4.1, the upstream end of the chamber is a glass cell used for neutral Rb laser cooling and trapping. It has a decahedron shape with nine 2" windows for optical access to allow atom fluorescence collection and absorption imaging paths in addition to the laser cooling and trapping. The physically relevant details for the laser cooling and trapping will be summarized in Section 4.1.1. The tenth face of the glass cell is coupled to a stainless steel UHV section. A tee near the glass cell contains Rb atom dispensers, or getters. Two tees downstream are used to attach ion vacuum pumps that maintain the UHV

pressure. A loosely mounted aluminum disk with inner diameter ~$6\,\mathrm{mm}$ separates the two vacuum tees along the stream. This disk acts as a differential pumping aperture to separately pump down the upstream and downstream regions.

The center of the downstream plasma region is defined by the middle of the X-shaped section of the chamber. Within this section is an electrode assembly described in detail in Section 4.2.1. The upstream end of the assembly is capped by a copper disk with a center hole drilled through for atom transport into the region. The downstream end of the assembly has multiple stainless steel wire grids. The four arms of the X shape have windows for optical access for the two-photon photoionization described in Section 4.1.2. A tee and four-way cross provide access for wires to connect the electrode assembly to UHV-compatible electrical feedthroughs. Centered outside the photoionization region is a magnetic wire coil that produces an approximately uniform magnetic field in the middle of the plasma region in a direction coaxial with the chamber stream. This coil and associated current controls are discussed in Section 4.2.2. Electrons from the photoionization region can be pulled downstream by wire grids toward a micro-channel plate (MCP) detector. More information on the MCP and charge detection is provided in Section 4.1.2. Additionally, challenges we discovered in the plasma-to-MCP electron transport process will be described in Section 4.2.3.

The operational sequence for experiments is controlled by LabView on a desktop computer. The program I used was designed by a previous student, Tony Gorges, with adaptations from an undergraduate research assistant, Matt Heine [131]. It sends sequence instructions to a 64-channel National Intrusments Digital I/O (DIO) board from Viewpoint USA. The DIO board generates programmed TTL sequences based on the LabView instructions. More details on the timing and TTL triggering for the measurements presented in this thesis can be found in Section 4.2.4.

4.1.1 Neutral Rb preparation

Now I will go over key operational principles used in the neutral region. I will give basic overviews of the laser cooling and trapping techniques utilized in the neutral Rb preparation. I

have structured my summary of these principles based on the chronological order of a typical experiment sequence.

First, we use a typical Rb magneto-optical trap (MOT) in our experiments [132]. Many more specific details about our MOT beyond what is mentioned in this thesis can be found in Ref. [15]. Here I will review some laser cooling and trapping techniques [130, 132–136] in the context of our experimental parameters.

We can understand many of the basic properties of magneto-optical trapping using a simplified one-dimensional picture. I have supplied an illustration for reference in Figure 4.2, and I will begin by describing Doppler cooling. Consider an atomic system represented by the $J = 0$ and $J = 1$ energy levels, disregarding the specifics of light polarization and Zeeman splitting for the time being. Light tuned away from resonance is scattered by atoms less frequently than near resonance. Momentum can be transferred from laser light to atoms during a scattering event. Since the incoming radiation is directed in a particular direction but the outgoing scattered light has an approximately-uniform random distribution, there can be a non-zero average net momentum transfer over time which results in a force on the atoms. The Doppler effect for atoms moving toward a light source blueshifts the light frequency; conversely, atoms moving away from a light source result in the light being Doppler redshifted. If the frequency of the light is red detuned from the transition, as indicated by the dashed red line in the figure, then the atoms moving toward the light source will experience a greater scattering rate. This velocity-dependent enhancement of scattering creates an average "drag" force. Illuminating the atoms with this red-detuned laser light from both sides, as indicated by the wavy red arrows, creates a cooling effect called optical molasses [132, 136].

This 1D optical molasses, as it has been described thus far, does not have any spatial confinement or trapping qualities. The atoms are free to drift out of the cooling volume. This can be addressed by taking advantage of a spatially-dependent Zeeman splitting and properly chosen light polarizations. Consider the case where an applied magnetic field has a magnitude $B \propto |z|$ such that the $J = 1$ level splits into magnetic m_J sublevels as a function of distance from the origin, as

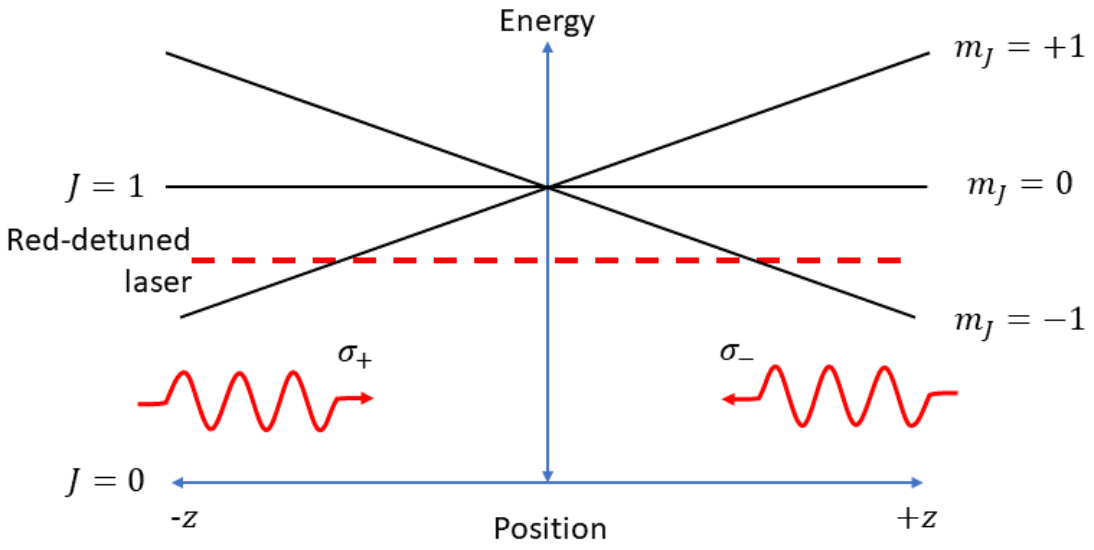

Figure 4.2: Illustration of a one-dimensional magneto-optical trap for a two-level atomic system, with energies indicated by $J = 0$ and $J = 1$ states. Counter-propagating laser light is indicated by the red wavy lines with red-detuned energy depicted with the dashed line. A quadrupole-shaped magnetic field with magnitude $B \propto |z|$ centered at $z = 0$ creates a position-dependent Zeeman splitting for the m_J sublevels. The orientations of the polarizations of the beams that creates a trapping force (see text) is indicated.

indicated by the black lines in Figure 4.2. The polarization of the red-detuned light can be chosen in such a way that an atom drifting away from $z = 0$ is preferentially scattered by the light source it has moved toward. In the figure, this is illustrated by showing that an atom at $z > 0$ has its energy levels shifted closer toward resonance with a $\Delta m_J = -1$ transition, so the σ_- beam will push it toward $z = 0$. A similar argument follows for the $z < 0$ and σ_+ case. Thus, this type of setup would produce both cooling and trapping.

The one-dimensional geometry can be extended into three dimensions. We can implement a beam geometry with laser light intersecting a volume of space from both directions on three orthogonal axes. This six-beam geometry is illustrated in Figure 4.3. We red detune ~12 MHz the laser light to create the optical molasses for cooling. An applied magnetic quadrupole field from Anti-Helmholtz (AH) coils along with appropriately polarized laser beams generate the position-dependent trapping force on the atoms [136]. Adjustable waveplates and retro-reflecting mirrors provide the proper polarizations and alignments for the counter-propagating beams.

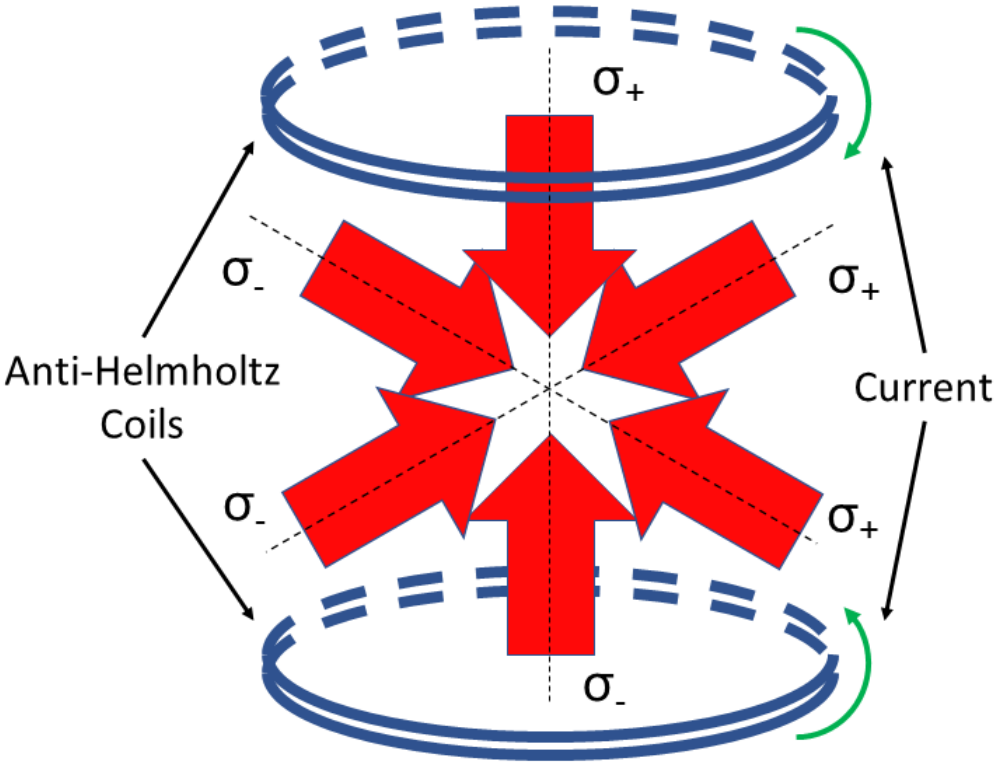

Figure 4.3: Illustration of a magneto-optical trapping configuration. The red arrows indicate laser light directed in both directions along three orthogonal axes; the blue loops represent the anti-Helmholtz (AH) coils that generate the magnetic quadrupole field. Anti-Helmholtz coil current directions and laser polarizations are labeled.

The process described above requires a closed cooling cycle for the atom-light interactions. $^{85}\mathrm{Rb}$ is not a simple two-level system like what was presented earlier in the one-dimensional example. The relevant energy levels are identified in Figure 4.4. The $5S_{1/2}$ ground state has hyperfine levels identified by the F numbers; the $5P_{3/2}$ excited state hyperfine splittings are likewise labeled as F' numbers. The $F = 3 \rightarrow F' = 4$ transition forms a nearly closed cooling cycle. This is because atoms in the $F' = 4$ state will decay back to $F = 3$. However, off-resonant excitations from $F = 3$ to $F' = 3$ and $F' = 2$ are also allowed. Atoms that end up in one of these other excited states have decay channels to the $F = 2$ ground state. The hyperfine splitting of the ground state is such that the cooling beam, indicated in the figure as the red arrow, is no longer resonant for atoms populating the $F = 2$ state. The $F = 2$ atoms are thus dark to the MOT forces, so we apply a repump beam that cycles the $F = 2 \rightarrow F' = 3$ transition as indicated by the magenta arrow. Atoms repumped to the $F' = 3$ state can then decay back to the upper-hyperfine ground state and rejoin the cooling cycle.

The cooling and repump beams used in our experiment are laser diodes mounted in thermally-regulated, student-assembled Littman-Metcalf external cavity housings. The laser diode frequency can scan over ~1–2 GHz without mode hopping. Rubidium Doppler-free saturated absorption spectroscopy [137] configurations calibrate each laser's frequency, and we use dichroic atomic vapor laser locks (DAVLLs) to set and precisely tune laser frequencies over ~$200\,\mathrm{MHz}$ bandwidth [135].

The MOT collects ~10^7–10^8 atoms and reaches a saturation number in about one to two minutes. The loading is monitored in real time by collecting MOT fluorescence on a photodiode. Typical experiment conditions suggest using smaller, colder neutral clouds generally improves operating performance. Hence, experimental sequences starting from the initial MOT begin with a compression stage [134] by red detuning the cooling beam $60\,\mathrm{MHz}$ and attenuating the repump beam for about $20\,\mathrm{ms}$. These changes to the light field cause a reduction in outward radiative pressure within the MOT so it subsequently shrinks. The compressed-MOT—or CMOT—can be observed using laser absorptive imaging. Time-of-flight expansion imaging sequences lets us esti-

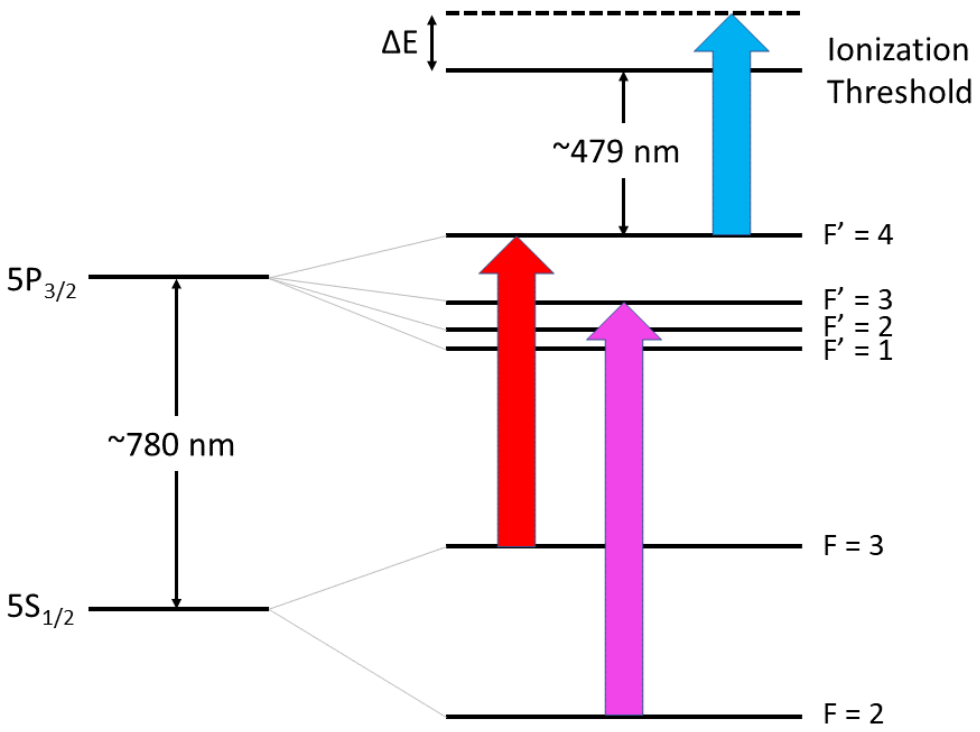

Figure 4.4: Diagram for relevant $^{85}\mathrm{Rb}$ energy levels and laser wavelengths. The red arrow represents the cooling and first-stage photoionization laser, and the magenta arrow is the repump laser. The blue arrow represents the second-stage of photoionization when a ~$479\,\mathrm{nm}$ photon from a tunable pulse dye laser takes the excited Rb electron above the ionization threshold with excess kinetic energy $\Delta\mathrm{E}$.

mate CMOT size and temperature. We observe an approximately spherically-symmetric Gaussian density with $\sigma \sim 300\,\mu\mathrm{m}$, and temperature $T \lessapprox 100\,\mu\mathrm{K}$. This is less than the predicted Rb Doppler cooling limit and can be explained by sub-Doppler cooling mechanisms during the MOT formation and compression stages such as Sisyphus cooling [133]. As the CMOT stage finishes, the repump light is shuttered closed while the cooling beam remains illuminating atoms for $4\mathrm{ms}$. This optically pumps the atoms into the lower hyperfine $F = 2$ ground state in preparation for the next stage.

After the CMOT and optical pumping stage, the atoms need to be transported to the plasma region. We do this by loading the Rb cloud from the CMOT to a magnetic quadrupole trap. This is accomplished by ramping up the MOT AH coil current from 30 to $130\,\mathrm{A}$ and shuttering the laser light. Our radial (horizontal) field gradient is ~$33\,\mathrm{G/cm}$, half the value of the axial (vertical) gradient. The magnetic quadrupole trap (or magnetic trap, for short) uses the linearly increasing field near the AH center and the neutral atom magnetic dipole moment $\boldsymbol{\mu}$ to generate a locally attractive potential for some of the magnetic Zeeman levels, $U = -\boldsymbol{\mu} \cdot \mathbf{B}$. The cloud of trapped atoms distorts into an ellipsoid shape.

The only atoms from the CMOT that can be trapped by the magnetic quadrupole are those in magnetic $m < 0$ sublevels with the correct sign for low-field attraction. The magnetic trap potential is anharmonic in contrast with the approximate MOT potential. This implies the neutral cloud will inevitably heat during the magnetic trap loading process. Absorptive imaging after this stage suggests the size and temperature of the neutral cloud approximately doubles. We have an iterative procedure—that I will soon describe—that attempts to simultaneously optimize the neutral cloud's size, temperature, and spin polarization.

Magnetic shim coils installed along three orthogonal axes provide control over the physical overlap of the center of the $B = 0$ center-point of the magnetic trap (the MOT center is affected by optical forces and is not necessarily at the same $B = 0$ point). Absorptive imaging of the atoms as they are released from either trap let us tune the positions of the MOT and magnetic trap centers to minimize the temperature-increase associated with the loading process. Since the size

of the cloud in the magnetic trap is directly related to the temperature, minimizing the temperature and size go hand-in-hand. We also have a technique to maximize the trappable population of atoms by altering their spin polarization. We use a method we call "recapture" with the following sequence: atoms are loaded from the CMOT to the magnetic trap, the atoms are released from the trap after being held for a number of seconds, then we immediately recover MOT conditions to sense via fluorescence how many atoms were recaptured out of the magnetic trap and back into a MOT. A retro-reflecting mirror geometry creates the anti-propagating MOT beams, which then create wavelength-scale intereference patterns in the trapping volume. Using the collected recapture fluorescence as a proxy for the trappable, properly-spin-polarized atom population, we can crudely adjust polarization patterns in the MOT by realigning these retro-reflecting mirrors to optimize the signal. Performing these slight optical realignments can in turn affect the MOT position and temperature previously optimized by the size-imaging procedure. Since we do not have independent control over each of these parameters, the optimization is imperfect in practice and iterated until the neutral cloud temperature, size, and spin-polarization are as good as we can reasonably achieve.

Once the neutral atoms are successfully loaded into the magnetic trap they can be transported to the photoionization region. This is possible because the atoms will adiabatically follow the magnetic field of the trap so long as the time rate-of-change of the atomic Larmor precession frequency is much smaller than the square of the frequency, $\mathrm{d}\omega_{\mathrm{L}}/\mathrm{d}t \ll \omega_{\mathrm{L}}^2$. The AH coils are attached to a linear translation stage that runs about $1\,\mathrm{m}$ down the length of our chamber. The atoms pass through a differential pumping aperture in addition to the hole in the copper disk. This is accomplished by physically adjusting the chamber alignment with respect to the translation stage; I also installed magnetic shim coils that shift the zero of the AH field near these apertures to optimize atom transfer downstream. Once downstream, absorptive imaging suggests the neutral cloud has roughly doubled in size once again compared to pre-transport magnetic trap images. We attribute this in-trap size increase to Eddy currents in the cylindrical chamber and disk apertures

that cause too-rapid changes in the field of the magnetic trap during the transportation process and heat the atoms.

This summarizes the operational principles used for the neutral atom preparation. I covered—in a brief overview—the key physics associated with magneto-optical trapping, magnetic trapping, and neutral atom transport. The photoionization region is covered next.

4.1.2 Photoionization & plasma region

Once the atoms have been transported to the plasma region they need to be prepped for photoionization. The chamber is designed for two-photon photoionization through the inclusion of a vacuum section with X-shaped arms with windows on the ends for laser access. One arm is used for a red beam excitation to the intermediate $5P_{3/2}$ state, and the other is for our tunable, blue dye-laser pulse beam. The atoms need to be positioned in the intersecting volume of these beams. This is done by finely adjusting the translation stage parameters to position along the stream (z) direction, and shim coils I installed lets us shift the center of the magnetic trap in the (xy) plane perpendicular to the apparatus stream. The atom positioning is observed and verified using absorptive imaging through both arms.

After we position the atoms, a very precisely timed sequence of events must occur in order to generate a photoionized plasma in a uniform magnetic field. I will briefly describe this sequence now; additional details for important steps will be addressed further along in the chapter. The atoms begin positioned in a magnetic trap. Field gradients would create non-uniformities in atom-light interactions across the cloud, so the magnetic trap is turned off before laser light is turned on. At this moment the neutral atom cloud is free to expand and fall due to gravity. We have a time of about five milliseconds to finish photoionization preparations before the atoms start to fall out of the photoionization volume. In this time the atoms need to be optically pumped from the $F = 2$ ground state to the $F = 3$ ground state, the plasma magnetization coil must be ramped up (for appropriate conditions), and then the red photoionization beam can begin cycling Zeeman-

shifted atoms into the excited $5P_{3/2}$ $F' = 4, m_{F'} = -4$ stretched state. The arrival of the blue photoionization pulse marks the time of plasma formation.

As I mentioned, immediately after turning off the magnetic trap field we first need to repump the atoms. The atoms are transported in the $F = 2$ state in the magnetic trap due to an anomalously high trap loss rate we observed for atoms in the $^{85}\mathrm{Rb}$ upper-hyperfine $F = 3$ ground state. We attribute this high loss rate to stray scattered light near the $5P_{3/2}$ $F' = 3$ and $F' = 2$ states, and it effectively prevents us from transporting the atoms downstream in the upper hyperfine state. This problem does not exist for lower-hyperfine $F = 2$ ground state atoms, so we transport the atoms in the lower state and optically pump them with our repump laser into the upper hyperfine state at the plasma region. The repump intensity is relatively weak and is not expected to heat the atoms significantly over millisecond timescales. Therefore we turn the repump light on before the magnetization coil ramp and leave it on throughout the remainder of the experiment.

Since the neutral atoms are freely expanding and falling after release from the magnetic trap, we have a relatively short time to ramp up our magnetization field. We accomplish this with a specialized circuit described in detail in Section 4.2.2. We choose to ramp the magnetic field before photoionization because the Rb Zeeman shift can be taken into account fairly straightforwardly. Otherwise, if the magnetic field were ramped after photoionization, then the EMF generated by a large $\mathrm{d}\mathbf{B}/\mathrm{d}t$ implied by Faraday's Law could heat charges and affect the plasma. Furthermore, switching on a large magnetic field over timescales shorter than the UCP lifetime would require heroic efforts. The field direction is coaxial with the apparatus stream because of the chamber geometry. The coaxial magnetic field also assists with challenges involving electron transport toward the detector. This is addressed further in Section 4.2.3.

We begin the two-photon photoionization by shining the red excitation light on the atoms about $5\,\mu\mathrm{s}$ before the arrival of the blue laser pulse. This duration is more than long enough to saturate the excited population but not so long that it significantly heats the neutral atoms. The red light is tuned to resonance between the $5S_{1/2}$ $F = 3, m_F = -3$ and $5P_{3/2}$ $F' = 4, m_F = -4$ stretched states based on the $1.4\,\mathrm{MHz/G}$ Zeeman shift for each measurement's magnetic field [69].

The blue photoionization pulse is generated by a tunable Sirah dye laser pumped by frequency-tripled Nd:YAG INDI-40-10 QuantaRay laser pulses. The Q-switched YAG laser is pumped by flashlamp with a $10\,\mathrm{Hz}$ repetition rate. The $1064\,\mathrm{nm}$ YAG pulses are frequency-tripled to $355\,\mathrm{nm}$ by a harmonic generator cell in the laser housing. The ultraviolet $355\,\mathrm{nm}$ pulse excites Coumarin-102 dye molecules circulated in the Sirah laser to generate gain tunable over $40\,\mathrm{nm}$ centered around $475\,\mathrm{nm}$. The dye laser produces a beam with ~$6\,\mathrm{ns}$ pulse width and about $2\,\mathrm{mJ}$ of energy per pulse. As mentioned in Section 2.6.1 and illustrated in Figure 4.4, the initial electron temperature of the plasma is determined by the excess energy ($\Delta\mathrm{E}$ in temperature units) of the blue photons over the ionization potential. We use a computer-controlled diffraction grating in the dye laser cavity to tune the wavelength just short of the $479\,\mathrm{nm}$ $5P_{3/2}$-to-continuum threshold. This is how we generate photoelectrons as cold as ~$3\,\mathrm{K}$ in an ultracold neutral $^{85}\mathrm{Rb}^{+}$-e plasma.

During my plasma measurements I observed a gradual decrease in blue pulse power by a factor of about a half over a timescale of two to three weeks of typical experiment operation. The culprit appeared to be rapid degradation of the YAG flash lamps presumably caused by aging equipment. I changed the flashlamps routinely to recover performance and prevent the blue pulse intensity from dropping lower than saturating intensity. The YAG laser has since been replaced after the measurements reported here were taken, and this has solved the power diminishment issue.

The electrodes in the plasma region are configured to guide electrons to the MCP that caps the downstream end of the chamber where they are then detected. Details concerning the electrode assembly are covered in Section 4.2.1. In brief, the plasma region is an open design capped on one end by a copper disk with a center aperture and bounded by a steel wire grid (the "plasma grid") on the other end. Additional grids downstream of the plasma grid guide electrons toward the MCP detector.

The technical specifications and details for the MCP we use can be found in Ref. [15]. To summarize the basic operational principals here, the MCP consists of a millimeter-scale-thick resistive material (wafer) across which is a high-resolution array of micrometer-scale-diameter hollow tubes (channels) through the wafer. The faces of the wafer can be charged by high-voltage supplies to

produce fields that guide electrons that escape the UCP through the channels and generate electron multiplication through dynode effects, i.e. secondary electron emission.

The electron currents escaping the plasma, subsequently amplified by the MCP, are detected as charge current on a phosphor screen. Current from the MCP phosphor screen flows into a $0.5\,\mu\mathrm{F}$ capacitor connected in series that acts as high-pass filter to block the kV DC potential on the MCP phosphor screen from other electronics. Two fast, low distortion RF amplifiers provide a factor of roughly 25 gain in signal sent to a LeCroy WaveSurfer 104MXs-A $1\,\mathrm{GHz}$ digital storage oscilloscope. A fast photodetector senses the blue laser pulse and triggers the oscilloscope to save a voltage trace "shot" where $t = 0$ is synced with photoionization. Example shots demonstrating UCP formation and electron detection can be seen in Figures 4.18a, 4.19a, and 4.21a. The context for those shots will be discussed in their appropriate sections, but for now I will comment on the background noise we observe in our shots.

Example background shot data is presented in Figure 4.5 where we save traces without forming a plasma. The blue trace is an individual shot measuring the MCP background signal; the orange trace is an average of 289 background shots. We can observe relatively high amplitude noise associated with the firing of the YAG laser pulse and lower amplitude noise with a substantial signal around $10\,\mathrm{MHz}$. The low amplitude noise tends to average down, however the pickup from the YAG pulse has a persistent stable structure. I installed a loop of wire around the MCP head to act as an antenna in an attempt to detect the noise and characterize correlations. The green trace in Figure 4.5 is the antenna signal associated with the same shot as the blue MCP trace, offset from the MCP trace for clarity. The red trace is a 289-shot average of the antenna signals measured simultaneously with the MCP signals that produced the orange trace.

I remove DC offsets and variations slow compared to the $\gtrapprox 20\,\mu\mathrm{s}$ observation time using a simple subtraction method. The portions of individual MCP traces where no electrons are detected are fit to smooth quadratic functions to subtract an average background. Most of our relevant metrics are calculated from integration windows that effectively average over high frequency noise.

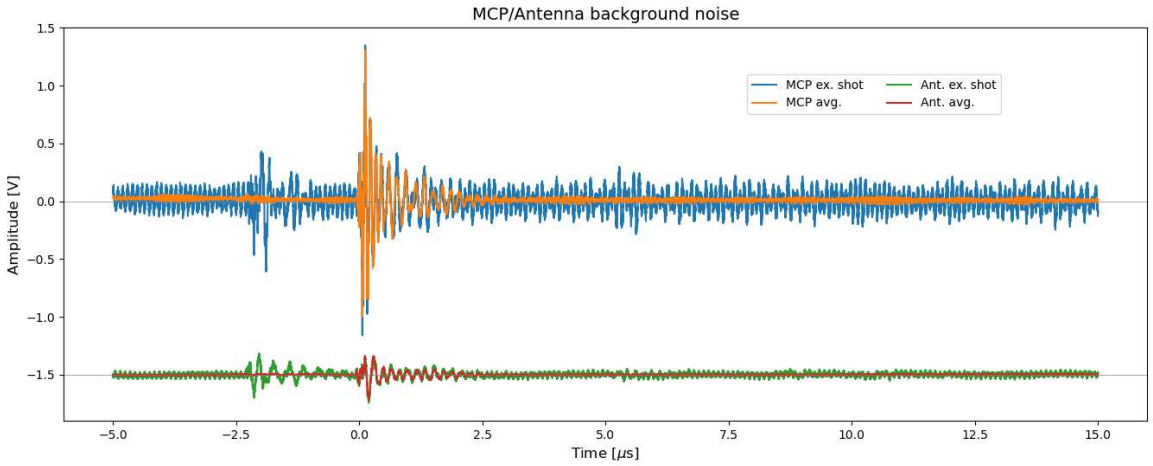

Figure 4.5: MCP background and antenna noise. The blue line is a single example MCP background shot, and the orange line is an average of 289 similar shots. Likewise, the green trace is the antenna signal associated with the MCP example shot, and the red line is an average of the corresponding 289 antenna traces. The antenna traces are offset by $-1.5\,\mathrm{V}$ for clarity.

In theory, the MCP background subtraction can be improved with a clever utilization of correlated information contained in the antenna signal.

We can visualize correlations and common structures between the MCP and antenna time series by plotting the amplitudes of the signals as a parametric curve. Figure 4.6 shows 100×100 histogram heatmaps from 289 curves that plot the MCP signal against the antenna amplitude without any manipulations to the data. The white line in the right panels is the parametric curve associated with the orange and red average traces in Figure 4.5. The results of this fairly straightforward study suggests more advanced single-shot noise filtering is possible with a correlated-antenna technique. However, we chose not pursue an advanced subtraction method for the measurements reported in this dissertation. Current operating conditions suggest our shot-to-shot variations in the number of atoms and their spatial size dominate our statistical uncertainty as opposed to the single-shot noise.

Shot-to-shot fluctuations are most clearly observable in the total detected electron number. We calculate this number using the cumulative integral of the detected electron current. The green and red traces in Figures 4.18a and 4.19a are cumulative integrals of two shots taken in one respective measurement session, and they demonstrate the factor of ~2 variability in shot-to-shot ionization number. Observations suggest the fluctuations come from variability in the neutral atom prepara-

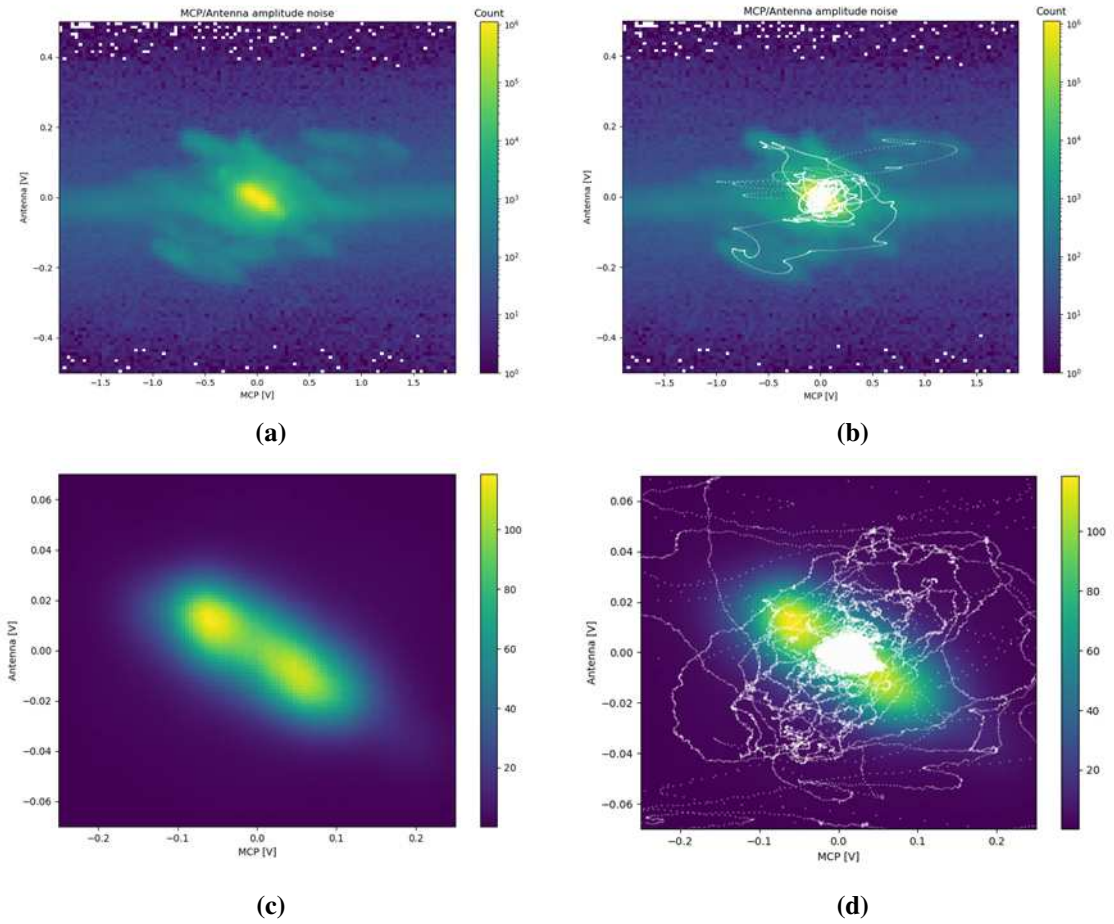

Figure 4.6: (a) Log-scale heat map of MCP-Antenna amplitudes (see text); (b) same as (a) but overlayed with average trace; (c) Linear-scale zoomed in on center; (d) same as (c) but overlayed with average trace.

tion or red beam pre-photoionization excitation. Shot-to-shot variations can be seen in downstream absorptive imaging of the neutral cloud from the same red beam we use for photoionization. The variations in plasma response at a particular number are not as variable as the shot-to-shot total number as is demonstrated by the lower panel plots in Figures 4.18 and 4.19. In general, the fluctuations hurt our signal-to-noise ratio and make data integration times longer, but otherwise they do not appear to be a critical issue.

This concludes my summary of the apparatus and operational principles. Again, additional details can be found in the previous students' dissertations [15] and [17]. In this section I described the process we use to photoionize a prepared ultracold cloud of Rb. The electron detection scheme was given a brief overview, and I discussed background noise and fluctuations we observe in the detected MCP signal. Next I will describe the major modifications to the apparatus we constructed and installed during my time operating the machine that made our reported measurements possible.

4.2 Apparatus modifications

Configuring our apparatus to generate strongly magnetized UCP electrons required making changes from the configuration used in previous experiments. In this section, I describe the key modifications. I will address why each change or addition was made, what specifically was modified, and how we constructed and implemented the modification.

4.2.1 Electrode replacement

One of the first projects I was tasked with before conducting the experiments reported in this thesis was to replace the electrode assembly used to control and enable probing of the plasma. The primary reason for this replacement came from a shift in research direction. The original electrodes were designed with the capability of sculpting an electric potential for a nested Penning-Malmberg trap. A series of seven ring electrodes on the scale of millimeters away from the photoionization volume would in principle allow enough control of the local electric fields to simultaneously confine both charge species of opposite sign [15]. In practice, the electrode configuration produced

complicated and/or steep features in the electric field that made it difficult to characterize the true shape of the potential at the plasma [17]. Furthermore, after evaluating topics of interest available to our UCP experiment, we decided that studying magnetization effects would be more interesting than what our experiment could teach us from trapping the plasma.

The previous electrode configuration could still have been used to generate a UCP with magnetized electrons. Most of the challenges associated with that configuration had to do with the close-scale design of the electrodes relative to the plasma and how to accurately characterize the spatially-complicated electric potentials they generated. The potential was also complicated by time-dependent patch charge effects. By moving the electrodes away from the plasma region we also reduce the effects of variable patch charges. We therefore chose to redesign our plasma region electrodes using a more open, simplified geometry. Rather than using seven rings millimeters from the plasma I constructed and installed a new plasma region consisting of a grounded aluminum tube, inner diameter ~$2.5\,\mathrm{cm}$, capped on both ends by electrodes about $2\,\mathrm{cm}$ centimeters away from the plasma. Figure 4.7 illustrates a not-to-scale cartoon of the different plasma regions. In order to replace the plasma region I had to construct an assembly that included six additional downstream wire grid electrodes for electron extraction toward the detector.

At the upstream end is a disk made from copper, diameter $2.53\,\mathrm{cm}$ and thickness $0.64\,\mathrm{cm}$. We chose this material because it is a good conductor with lower amounts of patch charge. The disk is electrically isolated from the grounded aluminum housing by a thin strip of Kapton. A $6\,\mathrm{mm}$ diameter hole was drilled through the center of the disk to allow the neutral atoms to enter the region as they get transported from the upstream region in the center of the translating magnetic trap.

At the downstream end is a steel wire grid welded to a steel ring. The ring has inner diameter $1.91\,\mathrm{cm}$ and the same outer diameter and axial thickness as the copper disk. The ring is press fit against a copper wire, and insulated from the grounded housing with Kapton. A grid geometry is used so that charges can be pulled downstream through the electrode toward the detector without

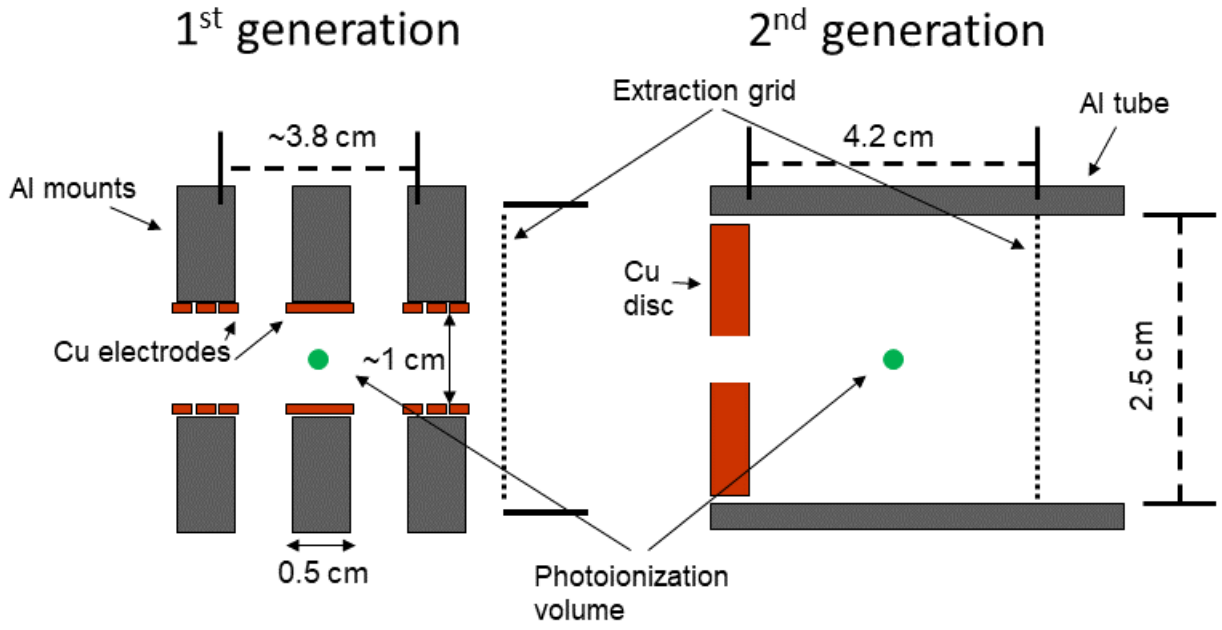

Figure 4.7: Not-to-scale cartoons of the old and new plasma region electrode configurations. The dotted lines indicate wire extraction grids that pull charges further downstream toward the MCP, and the green dot represents the photoionization volume where the plasma is formed.

significant losses from charges impacting conducting surfaces. I call this grid nearest to the plasma region the "plasma grid."

The construction then installation for the plasma region electrodes were such that knowledge of the distances from the copper disk and plasma grid to the plasma volume was not better than the few mm level. Given the way the electric field is structured in the plasma region, this is not sufficient on its own to calculate the electric fields from the applied DC voltages on the electrodes to the necessary precision. Also, the fact that the geometry is not cylindrically symmetric and the presence of patch charges further reduce the possibility of accurately determining the value of the fields solely through calculations.

Between the plasma grid and MCP are additional, identical grids interspaced to transport charges pulled past the plasma grid toward the detector. The plasma grid is connected to an Agilent 33250A 80 MHz Function/Arbitrary Waveform Generator that lets us program DC voltages

and time-dependent ramps, typically between 0 and 4 V. The downstream transfer grids are all connected to steady 135 V DC supplies.

I have provided photographs of the plasma region and full assembly in Figure 4.8 for reference. The copper disk, Kapton insulation, optical access windows, and plasma grid associated with the plasma region are all visible in Figure 4.8a; an axial view of an extraction grid nested within the Al housing is shown in Figure 4.8b. I constructed the assembly using department resources like the machine shop and the invaluable guidance of Bob Adame. It was designed for UHV compatibility and required us to avoid outgassing agents in common adhesives and solder, so I hand-machined everything to press-fit precision. I wove and welded the wire grids by hand in an attempt to minimize the number of electrons impacting conductors on their journey from the plasma to the detector. Figure 4.8c shows a photograph of a custom jig I made to aid in the construction of the grids.

As I mentioned, the primary reason we considered replacing the electrodes was to simplify the structure of the electric potential in the plasma region. I modeled the electrostatic environment of the new assembly using the finite difference method Laplace solver software, SIMION. Contour plots of the potential and fields for typical electrode voltages are shown in Figure 4.9. The model assumes cylindrical symmetry about the z axis, which is only approximately true. The left panels illustrate the electrostatic environment with $1\,\mathrm{V}$ applied to the copper disk and all other conductors grounded; the right panels show a typical UCP electron extraction configuration with a grounded upstream disk, $0.7\,\mathrm{V}$ plasma grid, and $135\,\mathrm{V}$ on the downstream extraction grids. The figures demonstrate the relative smoothness and flatness of the electrostatic environment at and around the photoionization volume near $z = 2, y = 0\,\mathrm{cm}$.

The simplicity of the field in the plasma region, in addition to reduced sensitivity to variable patch charges, opens doors for a number of experiment possibilities. It makes the RF heating measurements reported here much more straightforward. Furthermore, in the future, the new electrode assembly should be well-suited for studying Rydberg formation rates in UCPs using field ionization as a detection method.

(a)

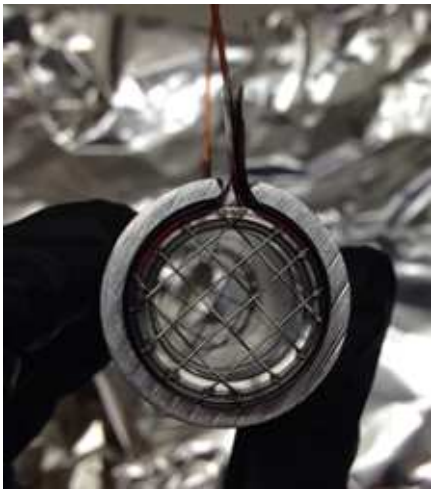

(b)

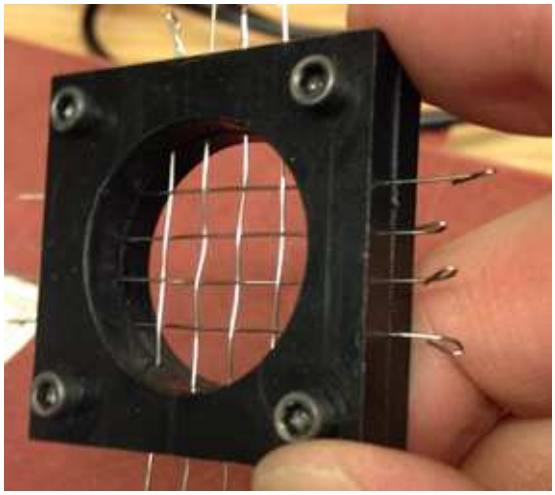

(c)

Figure 4.8: Photographs of the new electrode assembly during construction. (a) Copper disk, optical access, and extraction assembly visible; (b) On-axis view of an extraction grid nested in the Al housing; (c) Student-assembled jig for custom grid weaving and welding.

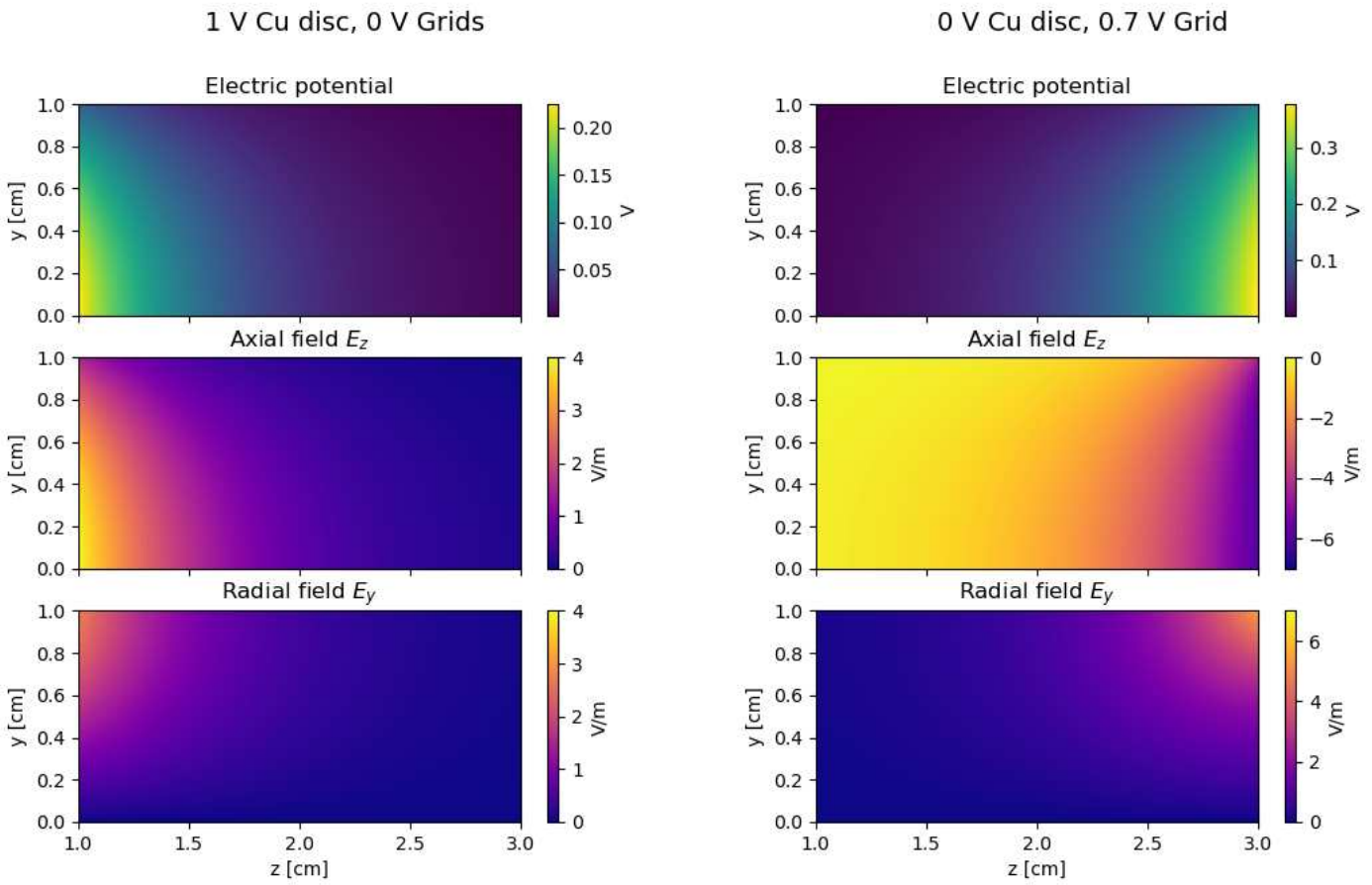

(a) **(b)**

Figure 4.9: SIMION models for two configurations of the electrostatic environment in the plasma region due to voltages applied to the electrodes. (a) Upstream copper disk 1 V, all grids 0 V. (b) Typical extraction configuration: 0 V upstream disk, 0.7 V plasma grid, 135 V downstream extraction grids.

4.2.2 Magnetization coil

The previous iteration of the apparatus used a relatively small ~$10\,\mathrm{G}$ quiescent magnetic field coaxial with the chamber in order to guide electrons leaving the plasma away from the ring electrodes. The associated circuitry for that coil was not rated to produce the >$100\,\mathrm{G}$ fields we sought to use in our study. Therefore, we needed to design circuitry—and while we were at it upgrade hardware—deemed suitable for the planned UCP magnetization experiments. I will first talk about the coil design we chose followed by a discussion on our solution to timing constraints imposed by our UCP formation process.

Our goal was to modify the apparatus to produce a precise, controllable, up to $1000\,\mathrm{G}$ and uniform magnetic field in our photoionization volume. This effectively constrains us to electromagnetic coil geometries. Large B fields can be generated with modest currents if we had a small coil near the plasma, but dissipating heat from a wire coil housed in vacuum poses challenges. In lieu of this we designed a coil external to the chamber. The geometry of the chamber suggested this coil should be coaxial with the apparatus stream like the quiescent coil it replaced.

Using a coil large enough to fit outside the chamber has two issues: a larger coil radius means more current is required to produce the same magnetic field compared to a smaller coil, and a larger coil cross-section means a larger inductance. The problem becomes apparent when considering timing constraints in the photoionization process I described in Section 4.1.2. We need to ramp up the magnetic field in a timescale shorter than $1\,\mathrm{ms}$, and the voltage required to drive this ramp is dominated by the product $L\,\mathrm{d}I/\mathrm{d}t$. Thus we face challenges due to a larger current, inductance, and driving voltage. We solved these issues using a specially-designed circuit to ramp up to stable >$100\,\mathrm{G}$ fields in sub-ms timescales.

Figure 4.10 shows a diagram for the circuit we built to control our plasma magnetization coil. The inductor with the red label represents the 120 turn, ~$4\,\mathrm{cm}$ diameter magnetic field coil (B-coil) wrapped around the chamber. There are four Crydom DC200D60C solid state relays, labeled S1–S4, and two power supplies V1 & V2. These are typically switched between three configurations to vary the magnetic field during an experiment sequence: off, low, and high. The off setting opens

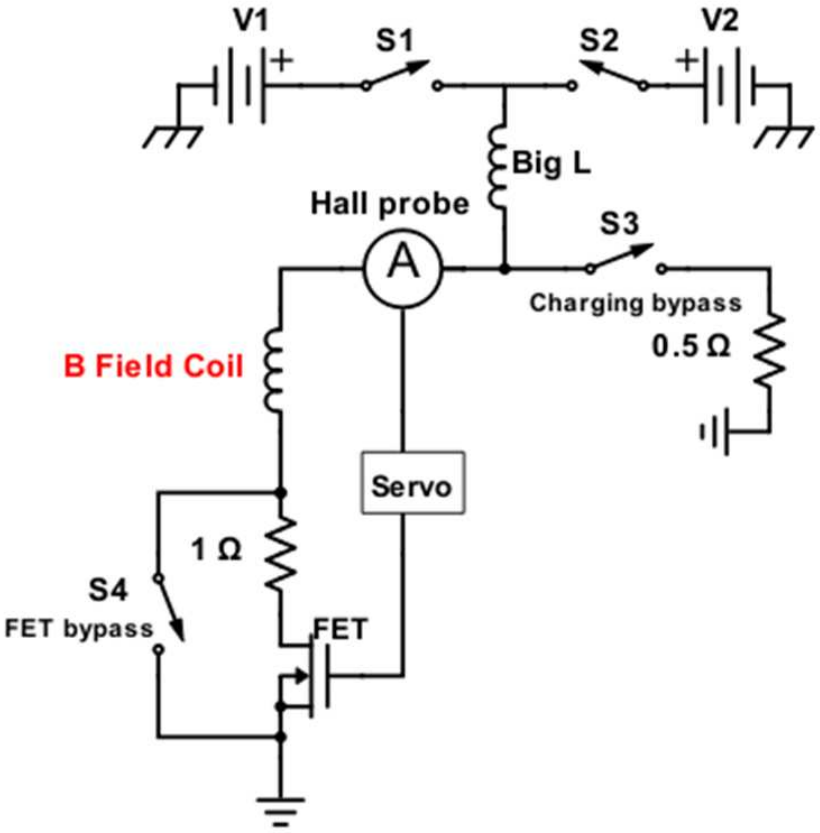

Figure 4.10: Circuit diagram for the system we use to control and switch the applied magnetic field. See text for details on labeled components and sections.

S1 and S2 in order to cutoff current from either supply through the coil. This is done between shots to prevent the steel chamber from acquiring a permanent magnetization.

The "low" field setting refers to S1 & S3 closed and S2 & S4 open. This configuration allows >$8\,\mathrm{A}$ of current to be pulled through a large inductor "Big L" and into a low-resistance ground path labeled "Charging bypass." A servo controls the gate of a FET on the B-coil path so that a fraction of the current coming from V1 is allowed to flow through the B-coil rather than the charging bypass. A Hall probe feeds current information to the servo to stabilize the magnetic field from the coil at a low, quiescent strength. This is the default field configuration for positioning the atoms in the plasma region and for our ~$10\,\mathrm{G}$ measurements where the magnetic field does not ramp to a "high" field setting.

The high field setting refers to the inverse of the low setting described above. Here relays S1 & S3 are opened, and S2 & S4 are closed. The high setting is in general switched from the low setting after Big L has been charged by the current from V1. By opening S3 and closing S4 we are in effect forcing all of the current into the B-coil that was previously flowing into a low resistance bypass. Closing the S4 relay activates a "FET bypass" that circumvents the servo action that stabilizes the field at a quiescent level in the low setting.

Rapidly changing the current through the B-coil in a timescale shorter than its natural L/R time requires a substantial driving potential. This potential is supplied in our circuit by magnetic energy we stored in the Big L inductor before switching out of low-setting operation. The current is supplied by V2. Note that the low-setting and high-setting current paths have different effective resistances, and furthermore the high setting does not incorporate servo stabilization in the current path. It's for these reasons we switch between two power supplies with individualized voltage and current limits we tune for sub-millisecond switching and satisfactory stability at both low and high current settings. In practice, finding these supply limit settings for a particular current is a fairly laborious process because the four knobs we can tune do not independently affect the circuit behavior.

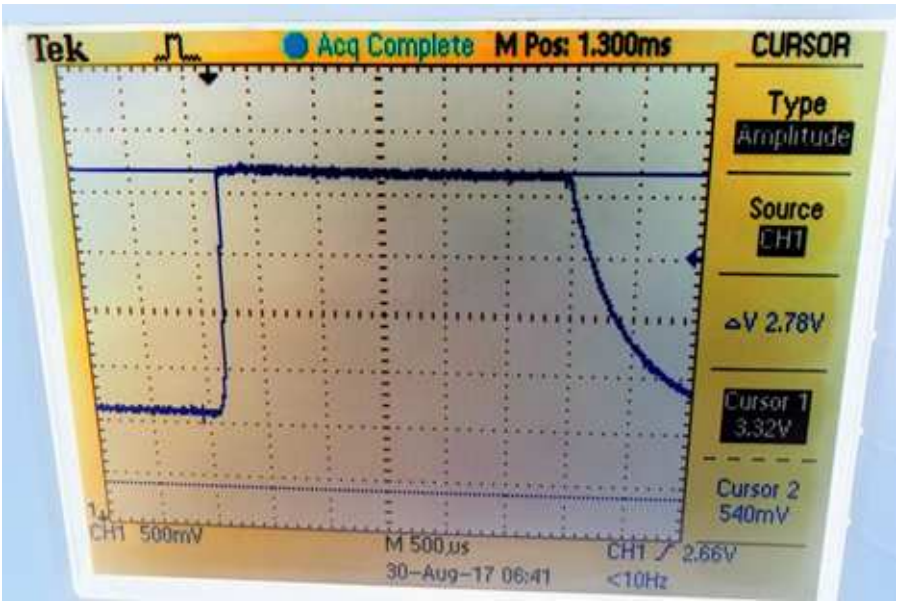

Figure 4.11: Hall probe signal (see Figure 4.10) demonstrating the ~200 μs fast switch-on time for the magnetization coil current. The major horizontal divisions are 500 μs, and the vertical scale shows the current switching from <1 A to ~8 A. The current falls off over its natural inductive timescale at the end of the trace.

Figure 4.11 shows a photograph of a trace measured by a Hall probe that demonstrates the circuit's fast current switching and stability capabilities. The minor divisions along the horizontal axis are 100 μs intervals, and the probe voltage on the vertical axis shows the current switching from a 0.4 A low setting to an ~8 A high setting. We can observe the current switching quickly on the left side of the trace in a time ~200 μs; the gradual slope on the right side of the trace when the power supply is switched off demonstrates the much slower natural inductive timescale of the circuit. I would like to acknowledge the assistance of fellow student Puchang Jiang in characterizing and installing the circuit.

We can model the B field in the plasma region using a geometric, magnetostatic model that accounts for the finite coil dimensions. I calculated the magnetic field from an array of 120 circular current loops arranged in a rectangular-cross-section coil with axial length 1 cm, inner radius 2.07 cm, and outer radius 2.82 cm. We can also determine the magnetic field by measuring the Zeeman effect on the neutral atoms. I recorded the total integrated photoelectron signal as a function of red laser detuning at a ~4 A high current setting. The data from this measurement is plotted

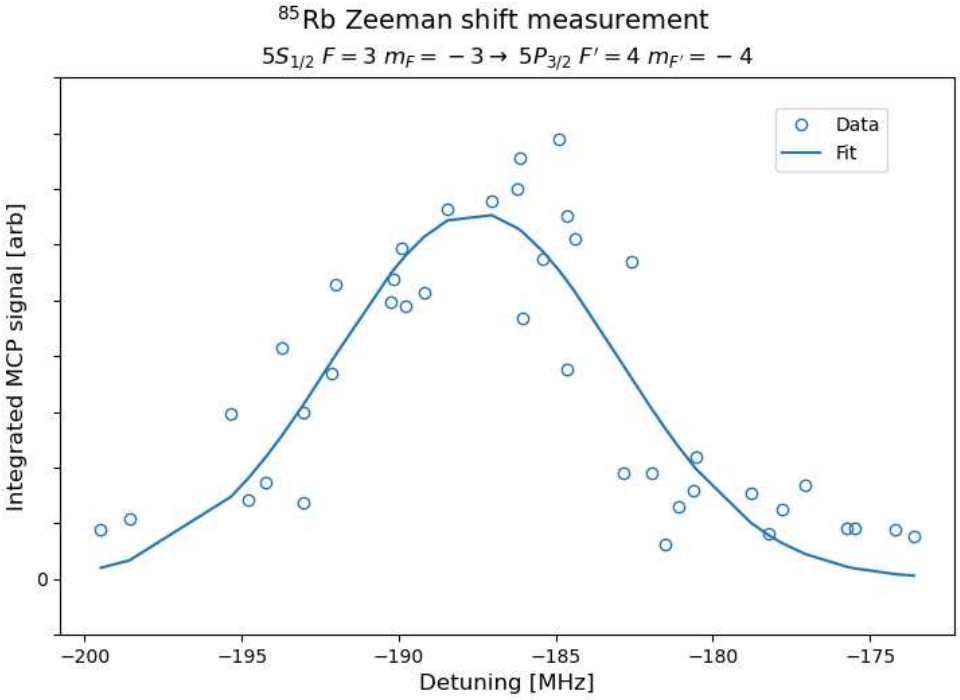

Figure 4.12: Zeeman shift measurement by detuning red laser. Measurement of the $^{85}\mathrm{Rb}$ Zeeman shift for the relevant photoionization transition (see text). The total detected photoionized charge is plotted as dots a function of the first-stage red laser detuning. The line is a Gaussian fit.

in Figure 4.12. The $187\,\mathrm{MHz}$ detuning at the peak of the Gaussian fit function corresponds to a Zeeman shift from a $134\,\mathrm{G}$ magnetic field. The geometric model suggests this field is generated by a current of $4.35\,\mathrm{A}$. This value is within 5% of the current limit settings we used for the power supplies.

4.2.3 Guide solenoid

One of the complications I observed in our experiments was a reduction in electron signal with increasing magnetic field. We should expect our largest photoionization signals near $B = 0$ when Zeeman broadening is small because at larger magnetic fields the red laser is tuned to the $m_F = -3 \rightarrow m_{F'} = -4$ transition and becomes detuned from the $m_F = -1, -2$ atoms. However, this effect is not a sufficient explanation for the reduction in detected signal we observed. The apparatus geometry is also subject to detection inefficiency as the magnetic field alters electron trajectories while they are extracted downstream. A magnetic field-independent detection efficiency is not

critical for our measurements, but signal-to-noise considerations are certainly relevant. In this section I will discuss my implementation of a guide solenoid to improve magnetized photoelectron detectability.

As I mentioned, we expect Zeeman broadening to reduced the number of photoionized neutral atoms when we form our plasma at higher magnetic fields. We do not optically pump the atoms into a particular m_F state so the $5S_{1/2}\,F = 3$ atom population in our magnetic trap will be roughly evenly distributed among the $m_F = -1, -2, -3$ sublevels. We tune our laser to resonance with the Zeeman shifted $m_F = -3$ to $5P_{3/2}\,F' = 4\,, m_{F'} = -4$ stretched-state transition since it has the largest Clebsch-Gordon coefficient of the accessible transitions and because it is a cycling transition in this context. The diminished probability to excite the other trapped atoms accounts for one factor in our photoionization efficiency.

The orientation of the red laser beam with respect to the magnetic field also affects the transition probability. Ideally, we could achieve maximum photoionization probability using circularly polarized σ_- to cycle the $\Delta m = -1$ stretched state transition. However, the magnetic field—which provides the atom quantization axis—is oriented along the chamber axis at a 45° angle to the red beam's optical access. This means the light in the atoms' frame will have both σ_- and σ_0 components. In theory, we can rotate the magnetic field direction with a perpendicular shim coil to align it with the red beam direction and improve the atomic excitation fraction. In practice, the effort required to implement a proper B field rotation is not necessarily worth the gain in photoionization number. Regardless, a nonideal laser polarization will also contribute to photoionization inefficiency.

These effects could account for the reduction in detected photoelectrons I observe when comparing plasmas formed at 10 and $65\,\mathrm{G}$, but they do not explain the reduction I observed going from 65 to $134\,\mathrm{G}$. Our hypothesis was that charge reflection near grounded surfaces was preventing electrons from continuing downstream toward the detector. We form the UCP in a positive potential relative to the grounded conducting chamber, so the electrons are energetically forbidden from

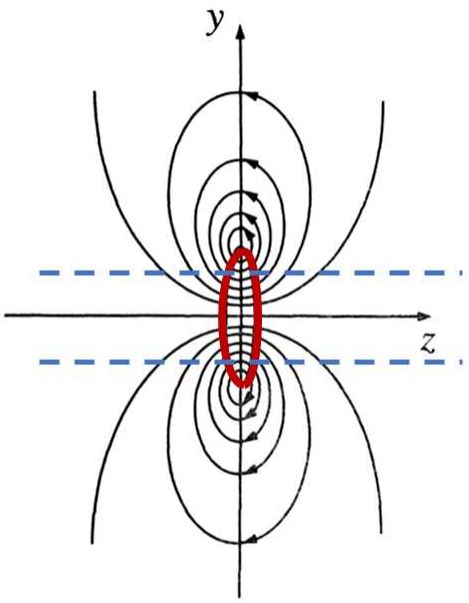

Figure 4.13: Diagram of the magnetic field lines associated with our coil-chamber geometry. The dashed lines symbolize the grounded chamber walls, and the solid red loop represents the magnetization coil. Adapted from [140].

impacting the aluminum housing. In the absence of a magnetic field the electrons are focused in the radial direction and accelerated in the downstream direction toward the positive voltage grids.

In the presence of a magnetic field the electrons gyrate around an axis called the guiding center. This charge gyration is comparable to a loop current with an analogous magnetic dipole moment [138]. This effective moment aligns antiparallel with the external magnetic field lines. Changes in the magnetic field vector will cause the particle trajectory to adjust in such a way that this magnetic moment is an adiabatic invariant [138, 139]. As illustrated in Figure 4.13, the off-axis magnetic field lines that the electrons follow away from the photoionization volume arc radially outward to the grounded walls of the assembly. The magnetic field affects off-axis electron trajectories by bending their momenta from the axial direction to the radial direction. Other effects like $\mathbf{E} \times \mathbf{B}$ and $\mathbf{B} \times \nabla B$ drifts are also present in our system, but their predicted magnitudes are relatively small.[5]

[5]The magnitude of $\mathbf{E} \times \mathbf{B}$ and similar drifts may become large near the wires of the extraction grids, but the interaction time is exceptionally small due to the high electron velocity in those vicinities.

When the magnetic field is weak the radii of curvature of the guiding centers are large. This means the adiabatic rotation of the electron momenta will be small and the parallel kinetic energy $\mathrm{KE}_{\parallel} \propto v_z^2$ remains large compared to $\mathrm{KE}_{\perp} \propto v_x^2 + v_y^2$. This is important because the electric potentials in the spaces between the $135\,\mathrm{V}$ extraction grids form saddle points and therefore act as potential barriers along the axial direction. At stronger magnetic fields, the electron $\mathrm{KE}_{\parallel}$ can become reduced enough that it is reflected in the axial direction before it reaches the detector. The guiding center effect is adiabatic, so the reflected electrons are still energetically allowed to reach the MCP if they eventually acquire an axial trajectory. However, each reflection increases the probability that the electron is lost by impact on a charged conductor before reaching the detector.

This loss mechanism can be demonstrated using the SIMION software to simulate electron trajectories in a model of our electrode and coil configuration. This model, along with certain example electron trajectories, is shown in Figure 4.14. The figure shows five stacked illustrations for identical electrode voltages and different magnetic field configurations; the magnetic field coil (not depicted) is centered between the copper disk and plasma grid. In each panel the electron begins from rest at a distance $y = 0.7\,\mathrm{mm}$ from the z axis of symmetry. The top three panels labeled "No Guide" show that the electron trajectory becomes increasingly off-axis with larger magnetic field and eventually undergoes reflections and loss on a modeled grid wire.

Our solution was to install a guide solenoid wrapped down the length of the chamber from the plasma region to the MCP. This coil provides a weak magnetic field to bend the guiding center field lines downstream. I modeled this solenoid in SIMION using a coil geometry with $1.9\,\mathrm{cm}$ radius, $29\,\mathrm{cm}$ length, and 35 turns. The guide solenoid's ability to counteract losses from the divergence of our magnetization coil is demonstrated in the fourth panel of Figure 4.14 with a guiding field of about $9\,\mathrm{G}$ from a $6\,\mathrm{A}$ current. This is the current I found that roughly optimized the detectable photoelectrons at $134\,\mathrm{G}$, as shown in Figure 4.15. With increasing current, I observe a factor of ~2 increase in number of detected electrons per shot, but this number reaches a maximum and begins to drop off. If the guiding field becomes large enough, then it can produce reflections itself due to field nonuniformities, as demonstrated in the bottom panel of Figure 4.14.

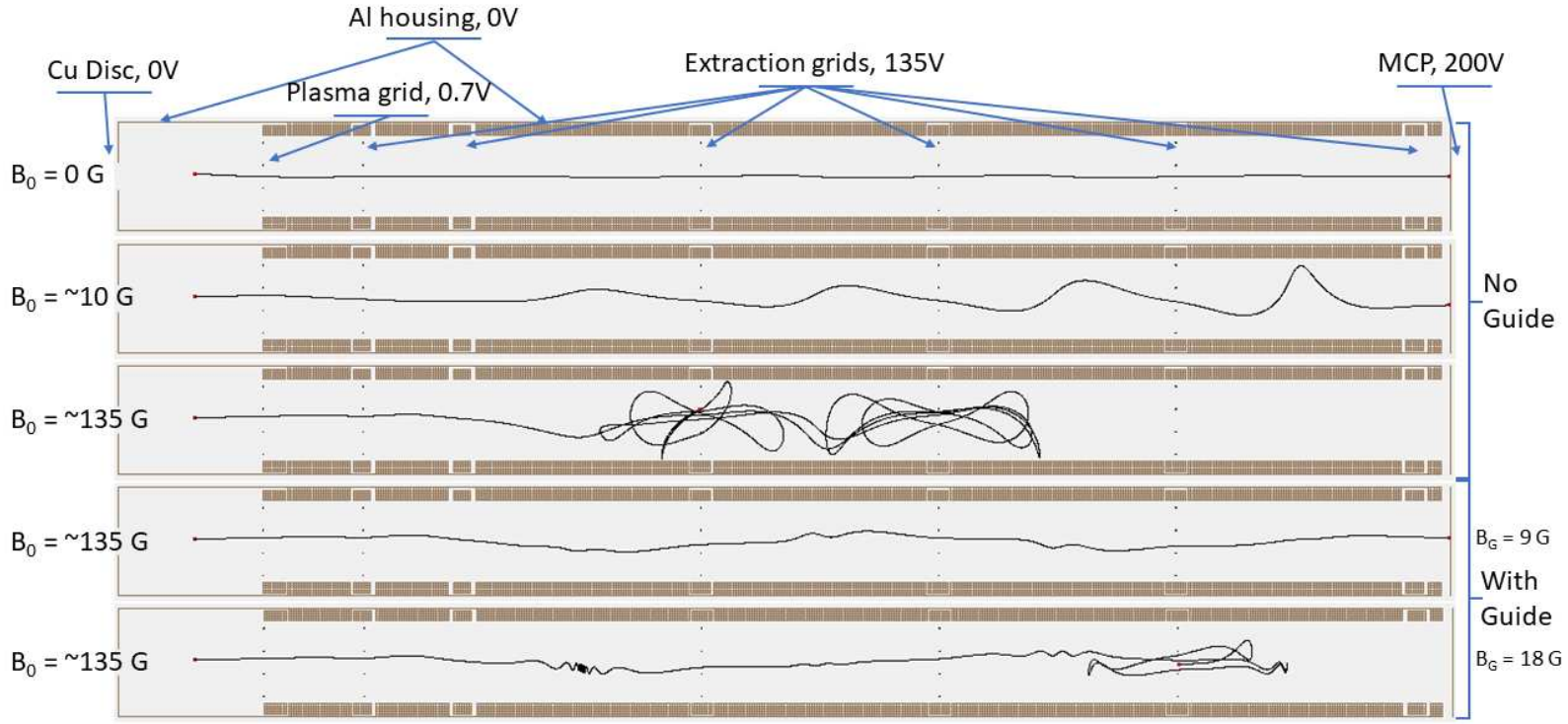

Figure 4.14: Electron trajectories as they are extracted from an off-axis photoionization volume through the electrode assembly, simulated using SIMION. The solid black line is the electron trajectory, and the electrodes are labeled with their corresponding voltages.

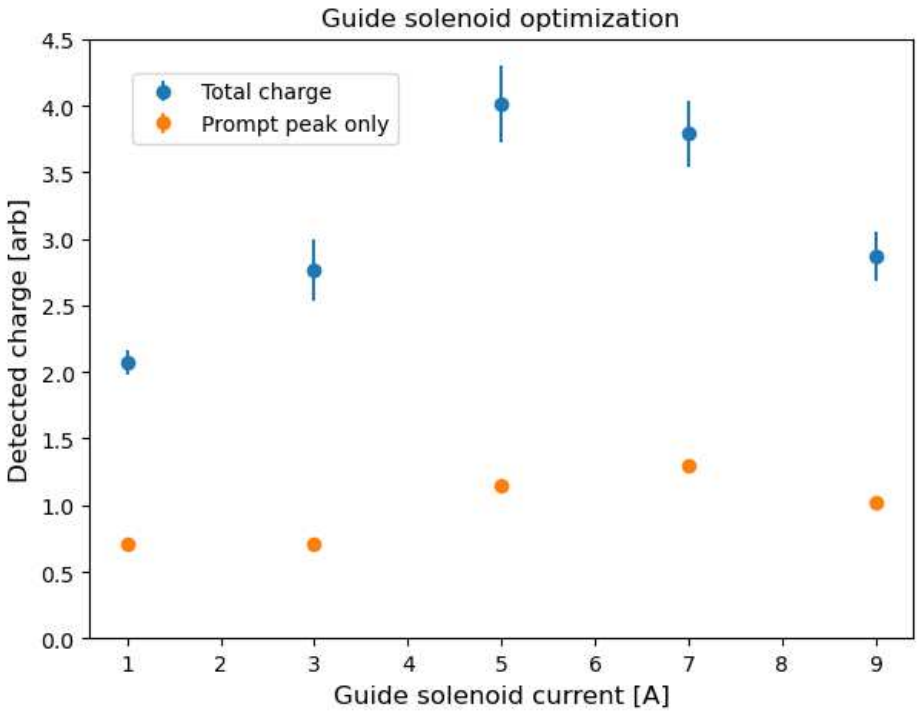

Figure 4.15: Measurement to find the guide solenoid current that optimizes charge detection on the MCP.

4.2.4 Trigger timing

One final modification I will make note of is a change to the triggering process we use for the timing sequence associated with our plasma experiments. The 10 Hz rep rate of the blue photoionization pulses sets the clock the experiment needs to synchronize to. When we "start" an experiment sequence the LabView program sends the timing instructions to the DIO board. The DIO board idles with the loaded instructions until a TTL signal synchronized to the YAG flashlamp supply tells the DIO board to execute the precisely timed sequence. We therefore have two independently cycling, albeit synchronized, clocks: the 40 MHz DIO clock and the 10 Hz YAG clock. In the initial experiment design, the DIO clock effectively controlled the timing of every other part of the experiment besides the YAG pulse.

The synchronization of the clocks at the beginning of the DIO-controlled sequence is temporally separated from when the photoionization occurs by a relatively large number of cycles. This is illustrated in a timeline diagram, Figure 4.16. There is a fairly short early sequence for neutral

preparation; followed by a relatively long, several-second wait for the motorized translation stage; then finally a short, precise sequence programmed to form and probe UCPs. I observed up to ~100 ns timing jitter in DIO triggers relative to blue light generation at time of plasma formation. To remove this jitter, we installed hardware to effectively decouple the plasma sequence TTL signals from the DIO clock. Now, we can instead trigger off of the YAG-synchronized TTL signal associated with the blue photoionization pulse.

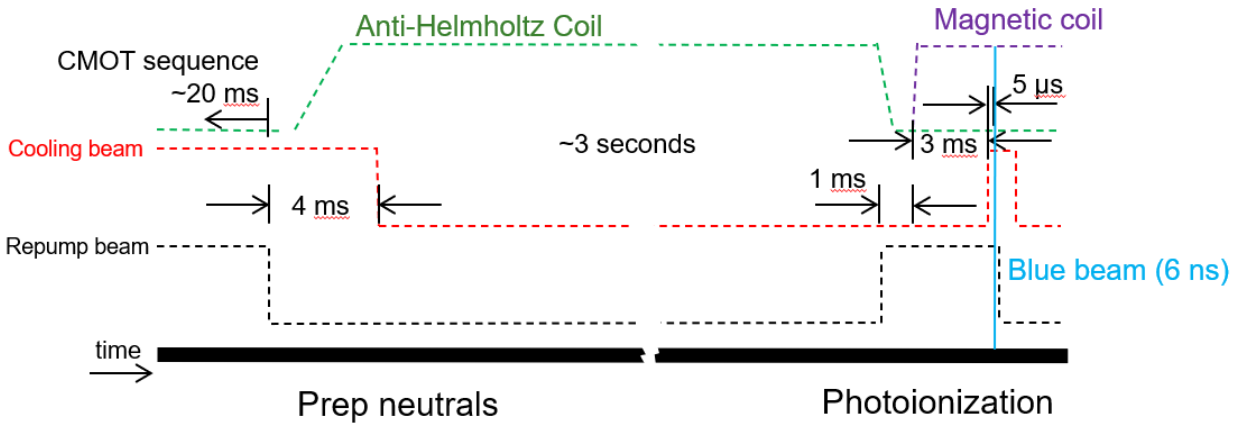

Figure 4.16: Diagram illustrating key sequences in a timeline format for preparing the neutral atom sample and performing the photoionization.

I installed a TTL-driven wideband switch[6] (RF switch) with connections illustrated in a diagram format in Figure 4.17. The black-bordered boxes correspond to the labeled equipment and electronics, and the blue arrows are the TTL trains and sequences. The input of the RF switch is connected to the TTL signals synchronized from the power supply for the YAG laser flashlamp. The output of the switch is connected to a Berkeley Nucleonics 525-6C delay/pulse generator. This switch prevents the delay/pulse generator's trigger-sync port (green circle) from receiving every pulse in the 10 Hz train coming from the YAG power supply. The gate of the switch is closed by the DIO board during an interval such that the only signal from the YAG pulse train that is transmitted by the switch is the one immediately preceding the ionization pulse.

[6]Mini-Circuits ZASWA2-50DR-FA+, DC–5 GHz

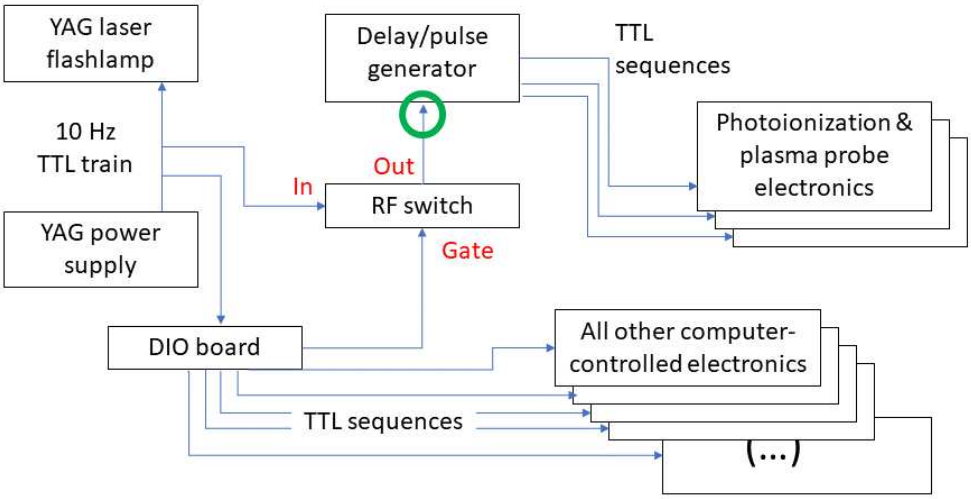

Figure 4.17: Diagram showing connections for improved trigger timing. The black-bordered boxes correspond to the labeled equipment and miscellaneous electronics; the blue lines with arrows are the TTL trains and sequences; the ports of the wideband RF switch are labeled in red text; and the trigger-sync port for the delay/pulse generator is circled in green.

The delay between the YAG TTL signal and the generation of the blue light is ~$200\,\mu$s which is long enough that the pulse generator can trigger the appropriate plasma-region hardware. This includes a $280\,\mathrm{MHz}$ AOM that switches on the red excitation (not repump) photoionization light as well as two arbitrary function generators that apply DC, AC, and/or ramping voltages to the copper disk and plasma grid. The DIO board continues to control the magnetic field switching because that occurs milliseconds before ionization and would not be affected by the sub-microsecond jitter I observed in plasma formation timing. The applications of the photoionization light and electric fields, on the other hand, benefit from the $< 1\,\mathrm{ns}$ jitter in synchronization with plasma formation afforded by the improved trigger timing.

This concludes the section's discussion of major apparatus modifications. I covered the following key additions: a new, open-design plasma region electrode assembly; a sub-ms-switchable magnetization coil and control circuit; a guide solenoid for increased electron detection efficiency; and an adjustment to experiment sequence triggering to reduce timing jitter. We will now turn toward the predicating calibrations and measurements made in the process of our RF heating ex-

periments. In the remaining sections of this chapter, I will discuss the purpose and relevant principles for each calibration and measurement. The general procedures used and key results are also reported.

4.3 Charge and DC field calibration

After replacing the electrode assembly and magnetic coil we chose to recalibrate the MCP using the method described in Ref. [15]. This technique correlates the total ion plasma number with the electron signal measured at the oscilloscope and simultaneously determines the approximate DC electric field in the photoionization volume. The overall accuracy of our number calibration is unimportant for us, as we mainly need to know the plasma density rather than the plasma number. Similarly for the electric field, an approximate measure of the DC field at the plasma is sufficient, but the AC amplitude from the applied RF fields needs to be calibrated with precision. Regardless of precision, the number-field calibration measurements reported in this section provide us with a model that self-consistently incorporates the plasma's total charge number, it's size, and the axial electric field in the region.

4.3.1 Principle

The primary goal of the measurement is to calibrate the voltage measured on the oscilloscope from the MCP-amplifier configuration with the true number of charges formed during photoionization. The technique is described in detail by Truman Wilson in his PhD dissertation [15]. The primary concept relies on the UCP property of electron confinement in a finite ion potential. The total confining potential $U(\mathbf{r})$ depends on the electron and ion spatial distributions and the external electric field. In order for an electron to be completely confined to the ions there must exist a potential barrier ΔU greater than the electron kinetic energy.

The calibration technique, in essence, seeks to determine the shape of the confining potential that traps a single electron as influenced by only the ions and external electric field. When a UCP is formed, the most energetic electrons will leave the plasma in the "prompt peak" until a large

potential barrier has developed for confinement. If there does not exist enough charge to produce this barrier then practically *all* of the electron population will escape in the prompt peak. The goal is to determine the MCP signal that corresponds to this threshold between no confinement and confinement. The threshold value corresponds to the total ion number required to trap a single $\mathrm{KE} < \Delta U$ electron. Tabulating the threshold values as a function of electron temperature and electrode voltages lets us fit to models that determine the charge number and DC field calibration factors self-consistently.

4.3.2 Procedure & Results

We wish to find the threshold signal corresponding to electron confinement at a variety of kinetic energies and DC field configurations. The kinetic energy gets set by the blue laser wavelength since nearly all of the excess photon energy above the ionization potential, ΔE, is imparted to the electrons. The electric field can be set by independently adjusting the voltages on the upstream copper disk and the downstream plasma grid. The confinement threshold signal is determined by varying the ion number and evaluating the resulting electron escape trace.

The ion numbers tend to vary shot-to-shot presumably due to fluctuations in the neutral preparation process before photoionization. We can also systematically adjust the photoionization number by attenuating the red light intensity. Uniformly reducing the first-stage excitation beam intensity should preserve the shape of the initial ion distribution and only vary the total number.

The plasma is formed in the electric field determined by the chosen electrode configuration. We give the charges $3\,\mu\mathrm{s}$ of evolution time after photoionization during which the prompt peak electrons escape. We apply an extraction field after this evolution time by ramping the plasma grid voltage. The field will pull any electrons that remain in the plasma region at the time toward the MCP. If the ion number is below the electron confinement threshold and all of the electrons escaped in the initial prompt peak then this extraction field will not produce a signal.

Figure 4.18a shows two example MCP traces that use this technique. We can see in both the blue and orange traces the initial prompt peak near $t = 0$. The ~$400\,\mathrm{ns}$ delay between $t = 0$

when the laser pulse arrives and the electron arrival time is due to the time-of-flight from the plasma region to the MCP. The green and red traces in the figure are the cumulative integrals of the respective blue and orange traces, scaled to fit on the same axis. The spike in the blue trace, corresponding to the step in the green trace, is the post-prompt-peak electron extraction signal. The orange/red traces are also subject to the same extraction ramp but do not show a similar electron detection signature.

We can integrate the trace in a window associated with the post-prompt extraction signal. This is equivalent to taking the difference in the cumulative integral trace at the window edges. Plotting the integrated signal in the post-prompt extraction window against the total integrated signal produces the data shown in Figure 4.18b. This figure shows three example conditions I used in part to determine the number calibration and plasma grid field calibration. The blue and orange points were taken with a grounded upstream disk and $0.5\,\mathrm{V}$ plasma grid, but at different electron energies $\Delta \mathrm{E}/k_{\mathrm{B}} = 25$ and $200\,\mathrm{K}$. The orange and green points were recorded with the same $200\,\mathrm{K}$ excess ionization energy but at different plasma grid voltages. The solid curves are functions generated from fitting the data to x-intercept and slope parameters for a line that flattens to zero. The best-fit x-intercepts for each configuration are taken to be the confinement threshold signals. I took data at $\Delta \mathrm{E}/k_{\mathrm{B}} = 10, 25, 50, 100, 200\,\mathrm{K}$ and combinations of upstream & downstream electrode voltages at $0, 0.25,$ and $0.5\,\mathrm{V}$.

We ultimately determine the calibration factors from the measured threshold signals by fitting their temperature and field dependence to an approximate model. We treat the ion distribution as a spherically symmetric Gaussian with size σ. The size parameter for the model can be determined by absorptive imaging of the neutral atoms at the time when they would be ionized. The magnitudes and gradients of the applied electric fields in the model are roughly informed by the SIMION predictions, but with enough data they too can be allowed to float as fit parameters. We use this approximate ion potential and electric field structure to calculate the electric potential $U(\mathbf{r})$.

We want to find the depth of the confining potential for the electrons ΔU. The cylindrical symmetry means the saddle point in the potential will exist on the z axis, and for our conditions

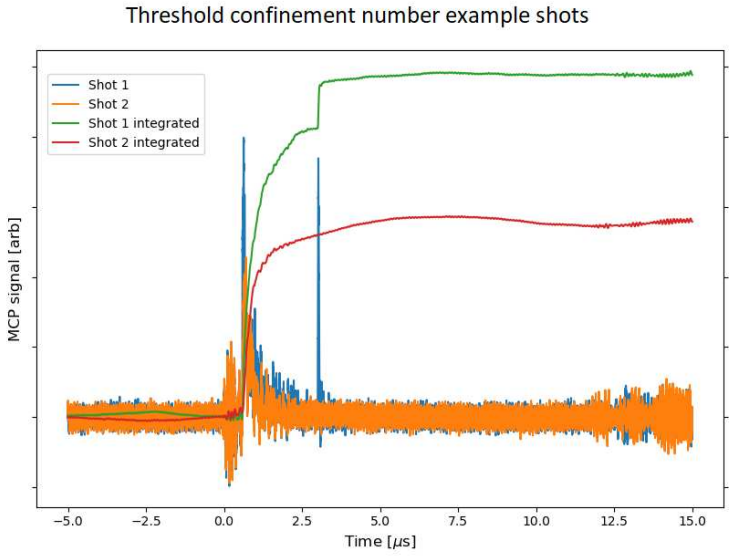

(a)

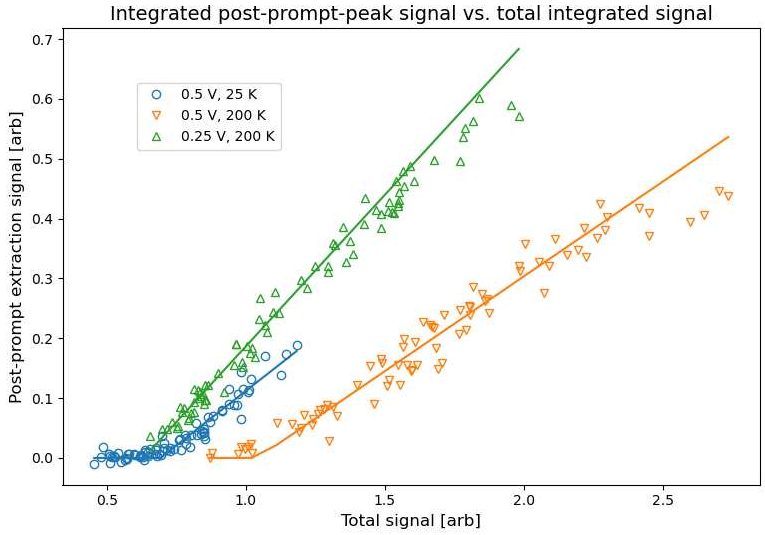

(b)

Figure 4.18: (a) Example time series of post-prompt extraction taken from two shots. The blue and orange lines are the MCP traces, and the green and red lines are the cumulative integrals of the respective MCP traces. The integrals have been rescaled to fit on the same axis as the escape current traces. The detected escape signal from an extraction ramp applied shortly after detection of the prompt peak is identified as the "post-prompt extraction signal" associated with electron confinement to the ions (b) Example data demonstrating how we measure the confinement number threshold for various electrostatic configurations and electron temperatures. The markers are data at different conditions (see legend), and the lines are best-fit functions we use to determine the intercept associated with threshold confinement.

it can typically be found around ~$3\,\sigma$ downstream from the center of the ion distribution. The confining depth is taken to be the potential difference between the minimum near the ion cloud center and the maximum along the axis at the saddle point. Any electrons with kinetic energies KE strictly less than ΔU experience total confinement. We can now find the calibration factors that self consistently fit our measured threshold-vs-$\Delta\mathrm{E}$ data against the model's predicted ion-number-vs-ΔU behavior.

This technique produces satisfactory fits around $4.8 \cdot 10^4\ \mathrm{electrons}/(\mu\mathrm{V}\cdot\mathrm{s})$ for our number calibration factor. Any data referred to in terms of detected charge or electron number reported in this thesis uses this conversion ratio. The measurement also predicts a $1\,\mathrm{V}$ plasma grid produces an axial field with a magnitude about 7–$8\,\mathrm{V/m}$. The fits also predict a background field from the $135\,\mathrm{V}$ downstream extraction grids of about $1\,\mathrm{V/m}$ when the copper disk and plasma grid are both grounded. I applied a plasma grid bias voltage of $100\,\mathrm{mV}$ during most of the other measurements reported in this thesis; the total DC axial field in that case should be approximately $2\,\mathrm{V/m}$ according to the model and measurements.

To reiterate a point I made at the beginning of this section, the accuracy of this calibration is relatively unimportant for us. Still, it is helpful because it provides us with a self-consistent picture that incorporates the absolute charge number, distribution size, and electric field environment with evidence backed by data. The number-field calibration parameters determined by my measurement-model fits are accurate within a factor of two, and they generally agree with supportive observations and models. However, the plasma density, a key parameter directly related to the number and size, does need to be known with precision. In the next section I introduce the resonant response technique I used to determine our UCP density.

4.4 Density measurements

The charge density is an important parameter for characterizing our UCP and plasma in general. It appears in scales discussed in Chapter 2 like the coupling strength, plasma frequency, Debye screening length, and average interparticle spacing, for example. The previous section discussed

techniques we use to determine the number of charges in and size of our UCP. In theory, this is enough information to determine an appropriate average density, however those methods rely on a fair number of approximations and, in our case, imprecise measurements. Instead, we used a resonant response technique to probe the plasma density directly using its relationship to the plasma frequency $n \propto \omega_p^2$.

4.4.1 Principle

The guiding principle for our density measurements is the proportionality between the plasma center-of-mass resonant frequency ω_{CM} and the plasma frequency ω_p. Truman Wilson derived a relationship between ω_{CM} and the average density $\langle n \rangle$ using a spherical harmonic-dipole approximation [15]. Approximating the UCP electron distribution as a zero-temperature, spatially-spherically-symmetric Gaussian with equivalent peak and size parameters as the ion distribution necessitates a cutoff at some radius to account for the lower number of electrons as compared to the ions, thereby producing a charge imbalance-dependent average density. Wilson showed that his model predicts, as a function of charge imbalance, $\omega_{CM} = 0.34\text{–}0.58\,\omega_{peak}$, where ω_{peak} is the plasma frequency associated with the peak density $\sqrt{e^2 n_{peak}/m_e \epsilon_0}$.

We are able to adjust the peak plasma density in our UCP by attenuating the red photoionization light. In the previous section, I discussed how this technique should reduce the charge number without substantially affecting the size. In reality, a complicated number-size correlation may very well exist for our UCP owing to radiation trapping effects of the applied light at sufficiently large light intensities. One of the advantages of measuring the density directly is that we can determine the condition *at a particular charge number* without having to know the precise number-size relationship.

Using these principles, we can determine our UCP density if we can measure a detectable resonant response to a driving RF field. Generating an observable response means we cannot in practice use an infinitesimal amplitude. However, we can use molecular dynamics simulations

[141] to both correct for finite amplitude effects and convert the center-of-mass frequency to an electron density.

4.4.2 Procedure & Results

Our goal is to find the resonance associated with plasma conditions where we make our systematic measurements. The reasons we chose these conditions will be explained in Chapter 5, but I sought the $16\,\mathrm{MHz}$ resonant response as a function of plasma number for $T_\mathrm{e} = 3.5\,\mathrm{K}$ at each of the magnetic fields of interest. We also adiabatically ramp an extraction field in the first $2\,\mu\mathrm{s}$ after formation to remove electrons to create a ~35% charge imbalance. This generates a confining depth of $\Delta U/k_\mathrm{B} \approx 200\text{–}300\,\mathrm{K}$. The rationale for applying this ramp will be made clear in the section following this one. After this ramp, $2\,\mu\mathrm{s}$ after formation, we apply $16\,\mathrm{MHz}$ RF for $1.2\,\mu\mathrm{s}$. We can then look for a resonance signature in the electron escape measurement.

I have plotted example MCP traces in Figure 4.19a from one of the $16\,\mathrm{MHz}$ RF measurements I performed. The blue and orange curves are the MCP time series and the green and red lines are the respective cumulative integrals, like how the data in Figure 4.18a was displayed. The electron signal from $t = 0$ to $2\,\mu\mathrm{s}$ is the prompt peak enhanced by the adiabatic ramp, and the electrons detected at $t > 8\,\mu\mathrm{s}$ come from an extraction ramp. The electron escape we observe between about $t = 3$ and $5\,\mu\mathrm{s}$ is the response to the applied $16\,\mathrm{MHz}$ RF.

We see that the orange trace, shot 2, was generated by a plasma with a larger total charge number than shot 1, but the resonant response was smaller. This behavior creates a peak structure in the measured RF response versus the existing charge number in the plasma, as illustrated in Figure 4.19b. This figure plots the integrated MCP signal in a window around $t = 2.5\text{–}5\,\mu\mathrm{s}$ as the RF response. The number of electrons in the plasma at the time the RF is applied is given by the total detected number at $t = 11\text{–}13\,\mu\mathrm{s}$ minus the electrons that escaped in the prompt peak around $t < 2.5\,\mu\mathrm{s}$, so I call this the post-prompt integrated charge.

This technique requires choosing a driving RF amplitude that induces electron escape near resonance. This amplitude is relatively high for our conditions because the electrons are formed

with a temperature around $3.5\,\mathrm{K}$ and confined to a potential depth around $\Delta U/k_\mathrm{B} \approx 200$–$300\,\mathrm{K}$. Peak-to-peak amplitudes of about $8\,\mathrm{V/m}$ were used to generate a measurable response at $B = 10.6\,\mathrm{G}$ and $134\,\mathrm{G}$. At $65\,\mathrm{G}$, we needed to roughly double this amplitude to generate a response still lower than the comparable responses at the other two fields, as we can see in Figure 4.19b. This hints at and provides qualitative supporting evidence for the quantitative off-resonant RF heating results ultimately presented in Chapter 5.

We use scaled molecular dynamics (MD) simulations to inform us of the plasma density based on the $16\,\mathrm{MHz}$ resonant response frequency [141]. We determine the peak electron temperature rise predicted by the MD by fixing the spatial size, varying the modeled charge number, and simulating the driving RF field. We associate the peak temperature increase from the RF as a function of modeled electron number with the resonant response signal observed in the experimental data. Then we calculate[7] and record the density predicted by the MD simulation that corresponds with the associated peak temperature rise. We also adjust the simulated RF amplitude to estimate finite-amplitude corrections. Table 4.1 lists the corresponding electron densities for the $16\,\mathrm{MHz}$ resonant responses I measured at three magnetic fields.

Table 4.1: Table of simulation-corrected average electron densities measured with $16\,\mathrm{MHz}$ center-of-mass responses at three applied magnetic field strengths.

$B\,[\mathrm{G}]$	$\langle n \rangle\ [\mathrm{cm}^{-3}]$	$\omega_p/2\pi\,[\mathrm{MHz}]$
10.6	$11.29 \cdot 10^6$	30.1
65.0	$12.73 \cdot 10^6$	32.0
136	$10.85 \cdot 10^6$	29.5

We can conceive of the effects of using a finite amplitude with this technique with a thought experiment: Assume we apply a $16\,\mathrm{MHz}$ field to a plasma with a true center-of-mass resonant frequency slightly higher than $16\,\mathrm{MHz}$. The slightly-off-resonant field will still cause the electrons to oscillate and acquire kinetic energy, albeit not as much as if it were on resonance. If the RF

[7] We find an average density—or density-weighted-density—from $\langle n(r) \rangle = \int n(r)^2 \mathrm{d}V/N$ where $n(r)$ is a spherically symmetric Gaussian distribution of total number N.

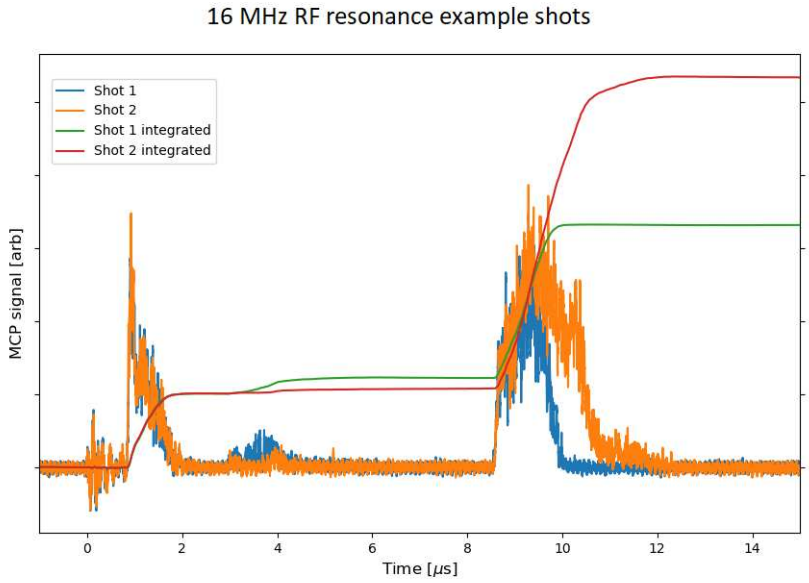

(a)

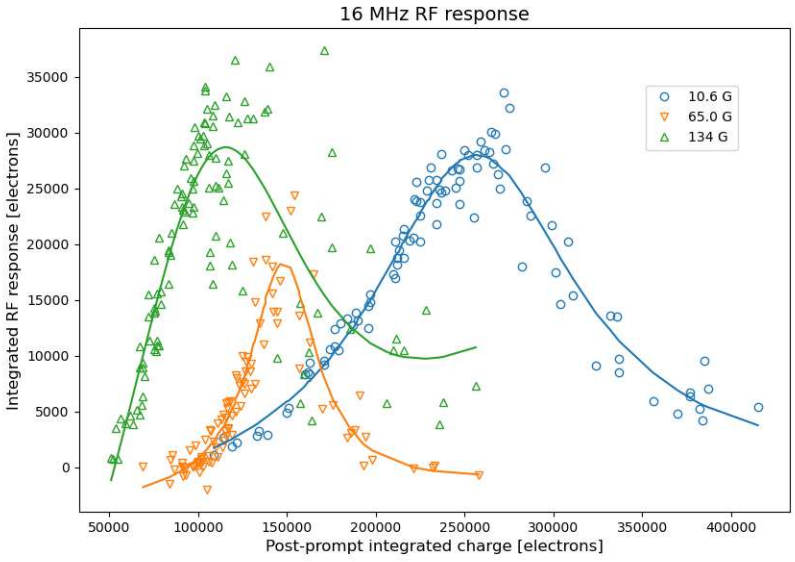

(b)

Figure 4.19: (a) 16 MHz resonant escape example time series, similar to how Figure 4.18a was plotted. The electron escape signal observed shortly after the prompt peak escape is identified as the RF response. (b) The integrated RF response plotted as a function of the post-prompt integrated number. The markers are measurements made at different magnetic fields (see legend), and the lines are fit functions constructed from a Lorentzian distribution modified by a linear polynomial.

field is applied for a finite time with a large enough amplitude, the oscillating electrons can acquire heat from, e.g., collisions with ions and raise the plasma temperature. A higher plasma temperature means faster expansion, and, in principle, an enhanced expansion can reduce the density from slightly-above-resonance to on-resonance during the finite time the RF is applied. We can expect that this effect would lead to a broadened resonant RF response particularly on the higher-frequency, higher-density side where the plasma has the opportunity to expand "into resonance". A similar argument can be applied for the expected effects of a spatial non-uniformity in the density distribution.

In principle, we could use a smaller amplitude that would not require as large of a correction to find the resonant response. The downside is at some point we no longer detect a substantial enough number of electrons directly escaping the plasma to quantify a peak signal. In that case we can use what I call a "partial extraction ramp" to obtain a detectable RF response. The number of electrons that escape during a partial extraction process depends on the plasma temperature. I can still observe a peak response structure with the lower-amplitude partial extraction technique, but the signal-to-noise and data integration time are much worse compared to the direct escape method presented here. I ultimately used the "partial extraction ramp" method for the remaining calibrations and measurements reported in this dissertation. This will be addressed in additional detail in the next section where I introduce a calibration technique to precisely measure average temperature differences in our UCP experiments.

4.5 Kick-temperature rise calibration

In Chapter 3, I showed how we can calculate a scaled RF heating rate $H \equiv \eta/\omega_p$ from information about the applied field amplitude and the electron temperature rise ΔT, (see (3.50)). To determine these values experimentally, we needed a procedure that quantifies plasma heating effects due to the applied RF fields. To accomplish this, we developed a series of calibration measurements using sequences of extraction ramps, electric field impulses, and arbitrary RF waveforms that in-

form us of the electron temperature. The first of these measurements I will discuss, what I call the "kick-temperature rise calibration", provides us with necessary information for determining ΔT.

In this section, I present a method we developed that combines partial extraction ramps with our ability to precisely alter the initial electron temperature. We also use electric field impulses, or "kicks", to deliver a precise amount of energy that heats the electrons across our measurement parameter space. The final goal of this calibration measurement is to determine what impulse or kick amplitude corresponds to a given temperature difference ΔT_{e}. These calibrated kicks will be used in measuring RF heating rates as described in the remainder of this thesis.

4.5.1 Principle

If the plasma temperature is fixed and the electric field environment changes in a way that produces a different confining depth ΔU, then the number of electrons that escape the plasma will change. This statement is also true with negated conditionals; if the plasma temperature changes and the electric field environment is fixed, then the number of electrons that escape the plasma will also change. These principles were demonstrated in the number-field calibration in Section 4.3. Along the same lines, a ramp designed to partially extract the electrons will produce a temperature-dependent escape response. This is the idea behind the partial extraction ramp technique presented in this section.

We require not only a temperature-correlated response signal, but also precise, systematic ways of characterizing the electron temperatures associated with the signals. We chose electric field impulses (kicks) and adjustments to the excess photoionization energy $\Delta\mathrm{E}$ for this calibration technique. Bear in mind that we ultimately want to measure the heat from applied AC electric fields. A potentially killer issue for systematically measuring the heat imparted by kicks and RF is if electrons escape and carry away kinetic energy before it thermalizes with the plasma. This is the reason why we apply a triangular extraction field ramp during the prompt peak. If we change the field adiabatically with respect to the plasma period ω_p^{-1}, then the electrons will remain near their initial $3.5\,\mathrm{K}$ temperature while confined to a much deeper ionic potential.

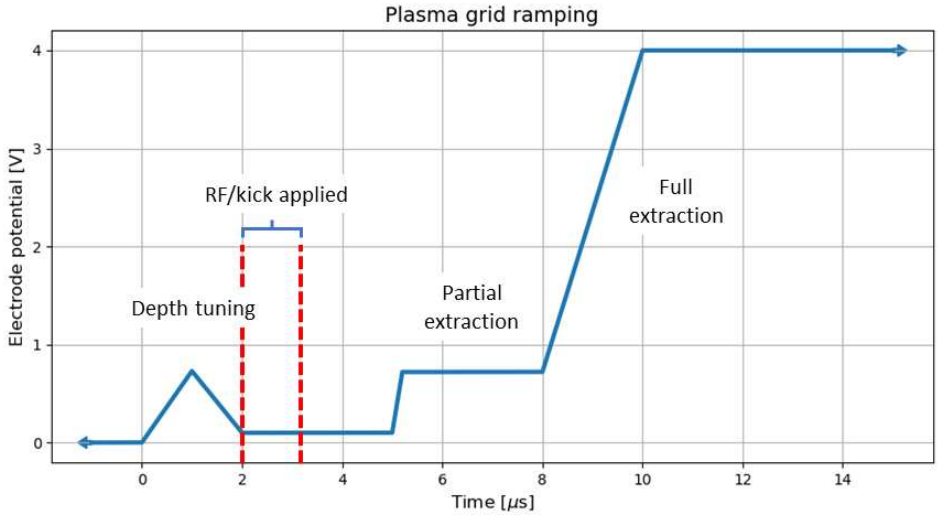

Figure 4.20: Diagram illustrating the voltage ramps applied to the plasma grid for the partial extraction technique. The three ramps are labeled: Depth tuning, Partial extraction, and Full extraction. The $1.2\,\mu$s window demarcated immediately after the depth tuning ramp is when external RF signals may be applied to the plasma.

An example sketch of the voltage ramp extraction sequence applied to the plasma grid is labeled in Figure 4.20. The plasma grid begins grounded at $t < 0$. At $t = 0$—the moment of photoionization—the voltage ramps with a triangle shape over a time of $2\,\mu\text{s} \gg \omega_p^{-1}$. This sets the charge imbalance by modifying the prompt peak escape during formation. The triangle ramp comes down to a low positive bias voltage so that electron escape is detectable. After the ramp is a window of time when RF or kicks may be applied. We want this window to be relatively short and early in the lifetime of the plasma so that effects due to ion expansion can be neglected. Following the RF application window is a delay of about $2\,\mu$s before the beginning of the partial extraction ramp. This delay gives the plasma time to thermalize changes in kinetic energy from applied RF and will be covered in more detail at the end of this subsection.

The partial extraction technique begins after this thermalization time using a ramp from a low bias to a larger bias over $200\,\text{ns}$. Electrons are allowed to spill out of the plasma for ~$3\,\mu$s before a larger "full extraction" ramp is finally applied to collect the remainder of electrons from the plasma. The amplitude of the partial extraction ramp was chosen to spill ~10% of the post-prompt electron

number. This fraction should be large enough for us to sample the bulk of the electron energy distribution—not just the high energy tail—while remaining sensitive to the electron temperature. In the limit of too large of an extraction ramp all the electrons will be pulled out independent of their temperature. If the ramp is too small then the signal-to-noise suffers, and the measurement may only be sensitive to the hard-to-characterize, high-energy tail of the distribution.

For the calibration method described in this section, we use monopolar field pulses, or "kicks," to heat the plasma in contrast with AC methods with vanishing time-averaged RF fields. The impulse duration is short compared to the plasma period, so screening is not expected to play a role. As demonstrated in Section 4.2.1, the spatial variation of the field in the plasma volume is mild, so finite size effects should not play a role in the plasma electron response to the kick. These simplifying principles give a straightforward $\Delta T \propto E^2$ amplitude scaling. The kick causes center-of-mass motion in the electron distribution which over time damps into heat. Electrons heated enough, roughly on the order of their initial thermal energy, produce a measurably larger partial extraction response.

The left panel of Figure 4.21a shows MCP current and integrated charge signals for two conditions, with a kick and without a kick, each averaged over about 72 shots. The right panel displays conditions without kicks but with different initial electron temperatures. We can identify three prominent non-zero features in the electron signals from the three ramps depicted in Figure 4.20. Figure 4.21b is a zoomed in view of the partial extraction response window for the traces. In the left panel we see the enhanced escape in the partial extraction response in the with-kick average trace compared to without.

The right panels of Figure 4.21 show similar data we collected comparing electron response at two initial temperatures. We adjust the blue laser wavelength to produce 3.5 and $5.5\,\mathrm{K}$ photoelectrons. I will comment more on this in the following procedure subsection. Right now, I turn attention back to the timing of our heating fields and extraction ramps.

The energy from the electric field kicks does not instantaneously thermalize into an increased electron temperature. The momentum imparted to the electrons in the axial direction by the im-

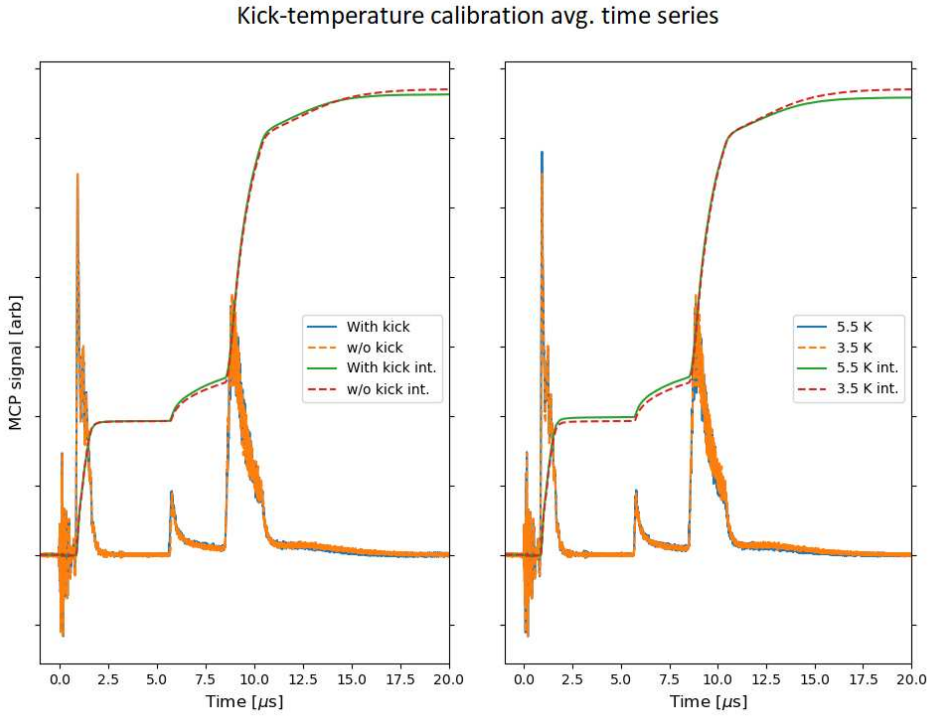

(a)

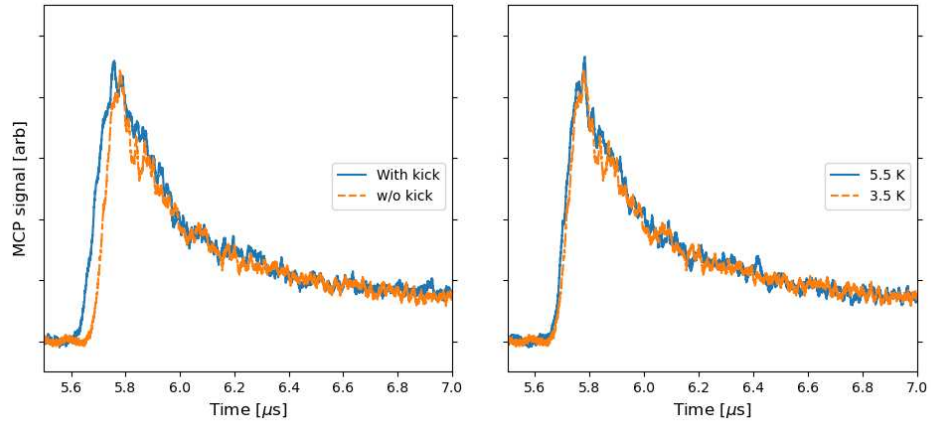

(b)

Figure 4.21: 72-shot averages of MCP traces using the partial extraction technique to do the kick-temperature rise calibration. (a) The blue, orange, green, and red lines are data plotted in a fashion similar to Figure 4.18a and Figure 4.19a. The left panel compares the escape response if the plasma is subjected to a kick or not; the right panel compares escape responses for plasmas created with different initial electron temperatures (see legends). (b) Zoomed in view of partial extraction response for the respective signals in (a).

pulse needs time to thermalize from collisions with other plasma particles, for example. Otherwise, the escape response to the partial extraction ramp will not be a true representation of the electron temperature, and a key assumption in the calibration procedure will be violated.

Figure 4.22 shows data from a study I did of the apparent thermalization of the kick energy. I varied the time between the application of the kick and the beginning of the partial extraction ramp and measured the response. The dots are responses with kicks, the lines are the baseline partial extraction responses without a kick. The primary observation here is the reduced variability in response for the "$2\,\mu$s delay" blue points compared to the "$1\,\mu$s delay" orange points. The elongated delay between the kick and ramp in the blue data allows more time for the electron velocity distribution to thermalize and produces a response that, relative to the orange data, is much less sensitive to the timing. We performed our heating and calibration measurements using a long enough delay that the response becomes flat.

4.5.2 Procedure & Results

I will now describe the procedure we use to combine the kick response illustrated in the left panels of Figure 4.21 with $\Delta\mathrm{E}$ information contained in the right panel data. Our goal was to find the kick amplitude that corresponds with $\Delta T = 2\,\mathrm{K}$. We chose to measure a $2\,\mathrm{K}$ effect because it is not excessive in comparison with the initial temperature, and it is large enough to produce a measurable signal with tolerable signal-to-noise ratio.

We can make precise changes to the electron initial temperature by varying the $\Delta\mathrm{E}$ energy above the ionization threshold. However, forming the plasma with different initial temperatures also means different prompt peak escapes and charge imbalances. This effect is visible in Figure 4.21a in the integrated signal traces; the left panel with equal initial temperature conditions have equivalent prompt peaks, but the right panel shows additional prompt peak escape in the $5.5\,\mathrm{K}$ electrons. This additional prompt peak escape generates a different charge imbalance. Thus, there is a different confining depth and therefore different partial extraction response. This is implied by the right panel in Figure 4.21b, where we see that despite the higher electron temperature

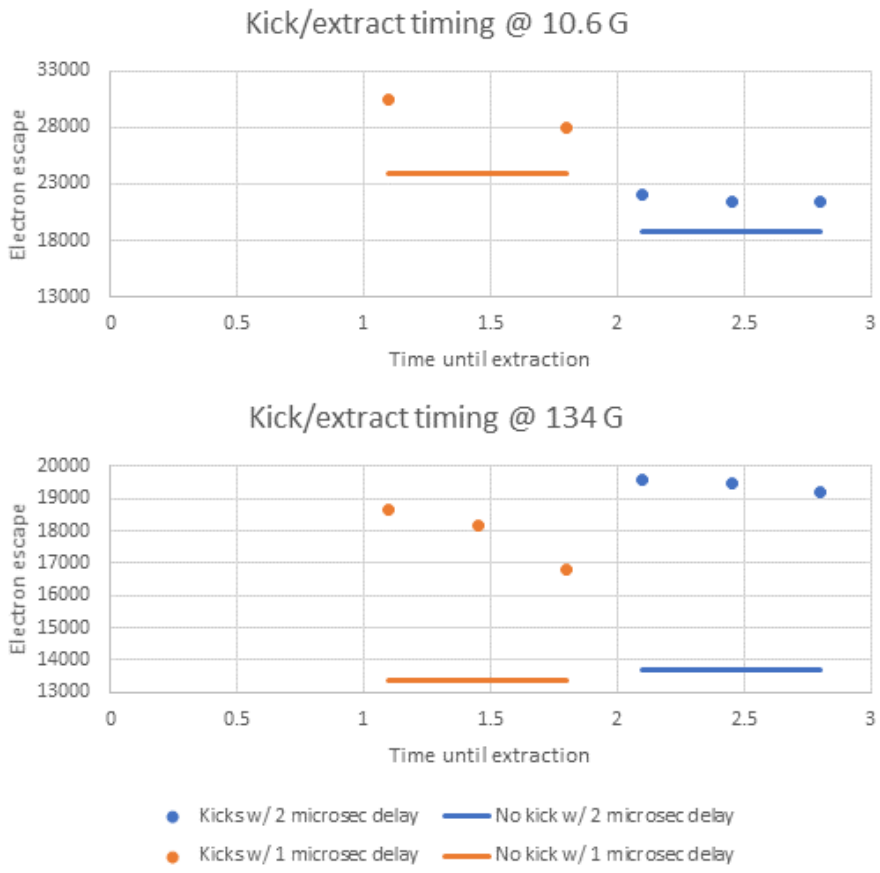

Figure 4.22: Data from a measurement used to characterize the thermalization of energy deposited into the plasma using the "kick" technique. The window of time between the application of the kick and the beginning of the partial extraction ramp was varied; this is the "Time until extraction." The markers are integration partial extraction responses with kicks, and the lines are responses without any kick. The orange and blue data correspond to different measurement sets where an additional 1 μs delay was added.

we get a comparable partial extraction response. We need to correct the ΔE response measurement for the charge imbalance.

The charge imbalance can be precisely controlled using the amplitude of the adiabatic triangle ramp. We can bracket the prompt peak number at $5.5\,\mathrm{K}$ around the prompt peak number measured at $3.5\,\mathrm{K}$ by changing the triangle ramp amplitude. A plot of the resulting data is presented in Figure 4.23a. Here I show the charge integrated in the prompt peak versus the post-prompt charge. Plotting and fitting the data in this manner lets me correct for shot-to-shot total number variations and determine the relevant signal at the post-prompt charge numbers I associated with peak $16\,\mathrm{MHz}$ resonance. I use a quadratic fit function so the curve has some flexibility to minimize error at the edges without compromising the interior fit of interest.

We use this imbalance-bracketing data to interpolate the partial extraction response as a function of charge imbalance at $5.5\,\mathrm{K}$. This lets us determine the $5.5\,\mathrm{K}$ electron response at the charge imbalance associated with the nominal $T_0 = 3.5\,\mathrm{K}$ initial temperature. The only piece left is to find the electric field amplitude that recreates this $\Delta T = 2\,\mathrm{K}$ partial extraction response. We can similarly find this with an interpolation method much like the charge imbalance bracketing. I have plotted the kick response data at $T_0 = 3.5\,\mathrm{K}$ as a function of post-prompt charge in Figure 4.23b.

This yields the information we need to pair the partial extraction response from a $2\,\mathrm{K}$ temperature rise to a kick amplitude. Figure 4.24 shows our final result from this calibration method where we interpolate[8] the kick responses at $T_0 = 3.5\,\mathrm{K}$ to find the amplitude that matches the imbalance-corrected $5.5\,\mathrm{K}$ response. Using this tool, we can now compare partial extraction signals across conditions by referencing them relative to a condition-insensitive $\Delta T = 2\,\mathrm{K}$ heating effect.

4.6 RF amplitude calibration Part I

I described in Section 4.3 a methodology for calibrating the DC fields from our electrode configuration. Now we want to know the electric field amplitude from an applied AC RF wave. The

[8]The interpolation function used here is a quadratic with non-zero linear dependence on the kick amplitude. Even though we reasonably expect the true temperature rise to scale as E^2, the partial extraction response to the temperature rise may not necessarily have the same simple dependence.

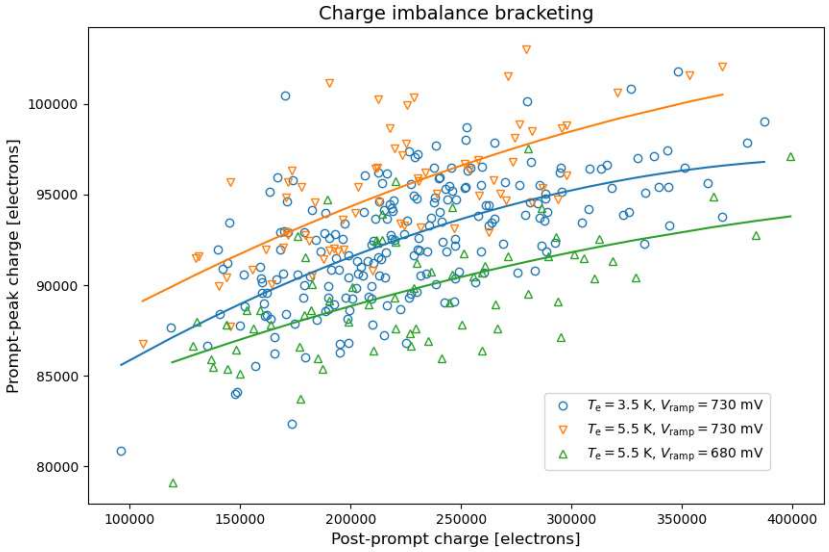

(a)

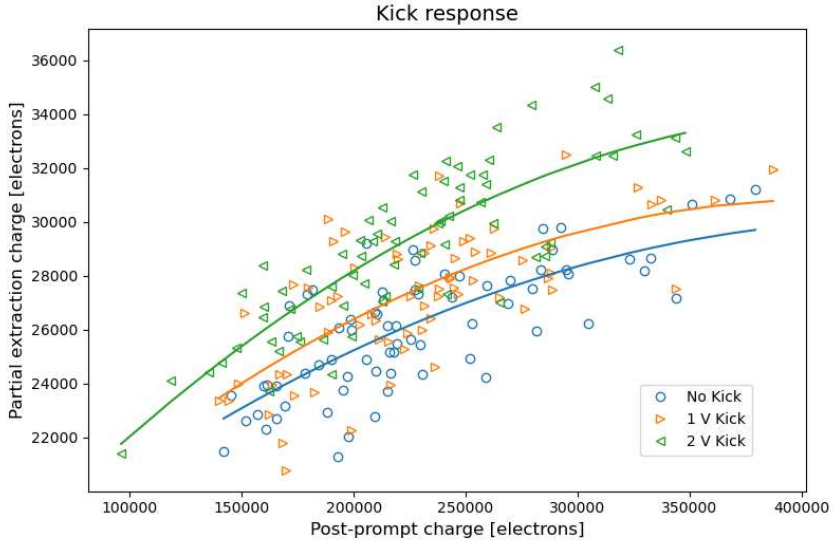

(b)

Figure 4.23: Data taken in order to calibrate a kick amplitude to a known temperature increase. (a) Plot showing data (markers) and quadratic fit functions (lines) evaluating the charge imbalance for different plasma temperatures and depth tuning ramp amplitudes (see legend). The vertical axis is the integrated prompt peak charge, and the horizontal axis is the remaining detected post-prompt charge. (b) Data plotted similarly to (a) except the vertical axis is now the integrated partial extraction response. Also, the three conditions (see legend) compare responses with applications of a kick at two amplitudes (triangles) and a baseline no kick response (circle).

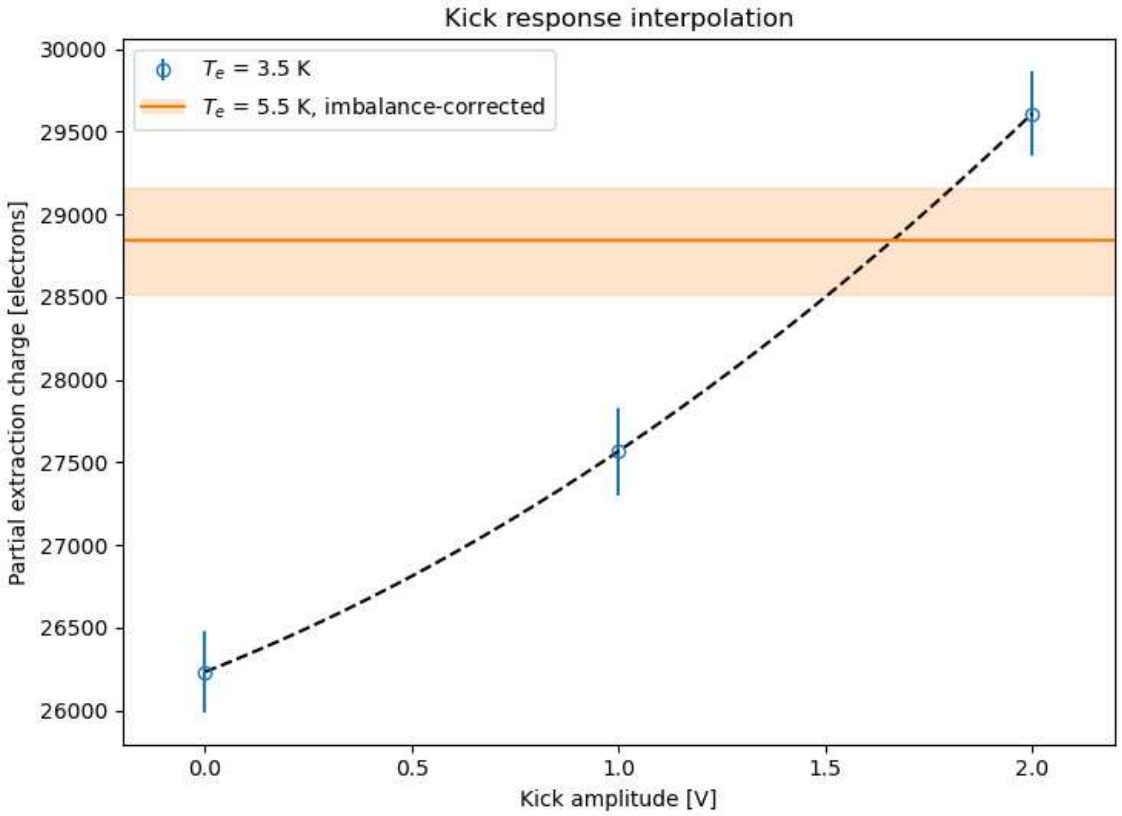

Figure 4.24: Plot showing the final result of our kick-temperature rise calibration method where we interpolate kick responses at $T = 3.5\,\mathrm{K}$ to find the amplitude that matches the imbalance-corrected $5.5\,\mathrm{K}$ response. The dashed line is a quadratic best fit.

frequency-dependent response for the upstream copper disk needs to be accounted for in order to accurately determine the electric field at the plasma when a function generator drives the electrode with an alternating current. In this section I introduce a technique we developed for calibrating the electric field amplitude at the plasma with the amplitude of a driving waveform at a particular frequency. We use our ability to determine a fixed amount of heating from Section 4.5 in conjunction with applications of different RF waveforms to self-consistently determine the electric field from measurements of the plasma itself.

In fact, the end result of these measurements qualify as RF heating data we ultimately seek to analyze in Chapter 5. In this section, I limit the discussion to the broad principles and finer corrections behind the technique we use to calibrate the RF field amplitude. The results from this technique will be discussed in the following chapter.

4.6.1 Principle

The general idea behind using different RF waveforms to drive heating as a calibration technique works as follows. We can model the electron response to an off-resonant, sinusoidal RF driving field, $\mathbf{E}(t) = E(t)\hat{z}$ with amplitude E_0 and frequency ω_0, as the solution to a driven-damped oscillator equation

$$\ddot{z} + \xi\dot{z} + \omega_{CM}^2 z = -\frac{eE(t)}{m_\mathrm{e}}. \tag{4.1}$$

For this to be accurate, the applied RF frequency needs to be much greater than the electron center-of-mass resonant frequency, $\omega_0 \gg \omega_{CM}$. Otherwise, the electric field may cause changes in the relative electron distribution across space and the center-of-mass equations no longer serve as a good approximation. The off-resonant solution for the position under these conditions is sinusoidal with amplitude

$$a = \frac{eE_0/m_\mathrm{e}}{\sqrt{(\omega_0^2 - \omega_{CM}^2)^2 + (\xi\omega_0)^2}} \tag{4.2}$$

as was identified in (3.52) in Section 3.4.3. Here, ξ is an oscillation damping rate related to—not necessarily equivalent to—the electron-ion collision rate. Solving (4.1) for the quiver velocity $\dot{z}(t)$

lets us calculate the work done by the driving field on the electron,

$$W = \int_{-\infty}^{\infty} \mathrm{d}t \, [-eE(t)] \, \dot{z}(t). \tag{4.3}$$

We can relate this work to the change in electron temperature under the assumption the energy completely thermalizes into heat, $W = \frac{3}{2} k_{\mathrm{B}} \Delta T$. Therefore, if we measure the electron temperature rise associated with known waveform $\varepsilon(t) = E(t)/E_0$ for two independent conditions, then we can calculate the two unknown parameters ξ and E_0.

The two waveforms we chose for our independent conditions were $\omega_{RF} = 2\pi \cdot 60\,\mathrm{MHz}$ sine waves with different amplitude modulations. The first condition, what I named the "slow turnoff," has Heaviside steps $\theta(t - t')$ from 0 to 1 at $t = 0$ and from 1 to 0 at time $t_f = 1.2\,\mu\mathrm{s}$. The amplitude of the wave is further modulated by an exponential rise-to-maximum function starting from $t = 0$ and a similar reflected function with zero-crossing at $t = t_f$ both with time constant $\tau_{\mathrm{slow}} = 200/(2\pi)\,\mathrm{ns}$. This functional form is expressed in (4.4) and plotted in Figure 4.25. The second condition we used is called the "sudden turnoff." It begins identically to the slow turnoff condition with a switch and exponential rise from $t = 0$ with time constant τ_{slow}. However, we suddenly switch off the driving field when it is at a zero-crossing at $t = t_f/3 = 400\,\mathrm{ns}$ as seen in Figure 4.25.

$$\begin{aligned}
\varepsilon_{\mathrm{slow}}(t) &= \overbrace{\theta(t)\left[1 - \exp\left(-\frac{t}{\tau_{\mathrm{slow}}}\right)\right]}^{\text{turn on}} \sin(\omega_{RF} t) \overbrace{\left[1 - \exp\left(\frac{t - t_f}{\tau_{\mathrm{slow}}}\right)\right][1 - \theta(t - t_f)]}^{\text{turn off}} \\
\varepsilon_{\mathrm{sudden}}(t) &= \theta(t)\left[1 - \exp\left(-\frac{t}{\tau_{\mathrm{slow}}}\right)\right] \sin(\omega_{RF} t) \left[1 - \theta(t - \frac{t_f}{3})\right]
\end{aligned} \tag{4.4}$$

We chose these particular waveforms, modulations, and parameters for the following multitude of reasons. The off-resonant driving condition $\omega_{RF} \gg \omega_{CM}$ means the velocities of electrons relative to each other across the spatial distribution should remain consistent in the presence of the field and allows a center-of-mass approximation. Plasma simulations of appropriate conditions in the context of our groups measurements show no discernible signs of non-collisional heating due

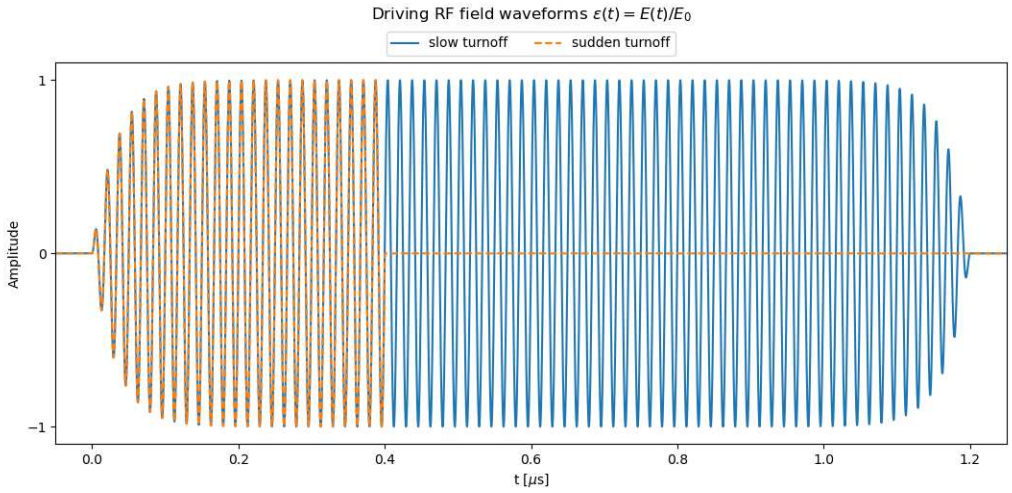

Figure 4.25: Waveforms in (4.4) used for RF field calibration and plasma heating measurements.

to the off-resonant RF. The duration $t_f = 1.2\,\mu$s was chosen because it contains enough integer RF cycles to justify comparisons with time-averaged continuous AC heating treatments, but it is also short enough to avoid significant complicating factors from longer timescale effects like ion expansion. The exponential parts of the turn on were included so that the electrons in the plasma would have time to adiabatically respond to the presence of a continuous RF field. The particular value of the time constant τ_{slow} was picked because it creates a smooth rise in amplitude to within 20% percent of the maximum in roughly three to four cycles; this lets us compromise on adiabatically switching the field without sacrificing many cycles for the time-averaged continuous approximation. A symmetric term is used to adiabatically turn off the field in the slow turnoff configuration.

We decided to suddenly turn off the driving field at $t = t_f/3$ without an adiabatic term to produce our second heating measurement with a waveform independent from the first. The reasoning here is that by suddenly turning off the driving field at a zero crossing then the 90° out-of-phase electron velocity will be at an extremum, and the associated kinetic energy will be transformed into heat as the center-of-mass oscillations damp freely. This contrasts with the slow turnoff where the center of mass is driven to equilibrium by adiabatically slowing the electron quiver velocity back to zero. This implies the two independent waveforms contribute to the overall temperature

increase through different physical mechanisms. The total heat from the slow turnoff depends on the amplitude E_0 and the damping rate ξ associated with the $60\,\mathrm{MHz}$ oscillations; the total heat from the sudden turnoff depends strongly on E_0 but weakly on ξ. The time it takes for the center of mass oscillations induced by the sudden turnoff to thermalize into heat depends on ξ, but the total amount of heat is fixed from conservation of energy considerations.

We found that having knowledge of the true structures of the $\varepsilon(t)$ waveforms is imperative in order for this technique to produce an accurate calibration. As expected, differences between the ideal waveform and physical current were observed to be most apparent in the sharp turnoff in the sudden configuration. The non-ideal function generator behavior and "RLC behavior" in the copper electrode circuit were found to be particularly troublesome systematic uncertainties. In theory, the drive abruptly stops and the field drops to zero. In practice, the function generator has a nonzero transient response, and the charged copper electrode producing the field has finite RLC characteristics. Since this non-ideal response does not necessarily generate a field amplitude with a vanishing time-average, it can contribute a significant amount of electron kinetic energy and therefore heat the plasma. The procedure and eventual result described by the actual plasma heating measurements will be addressed at the beginning of the next chapter, but first I will discuss the measurements we made to characterize our RF circuit's transient response and quantify the correction to our amplitude calibration factor.

4.6.2 Correction

As mentioned previously, we need to find the true form of the electric field at the plasma due to charge on the copper disk. The disparity between the true and ideal RF waveforms was observed to be most apparent in the abrupt zeroing of the sudden turnoff configuration at $t_f/3$. We characterized the electrode's transient response by modeling our RF connections as a composite RLC circuit. The circuit diagram is illustrated in Figure 4.26. This configuration lets us model RLC ringing in the electrode and chamber coupling, non-ideal shutoff of the function generator wave-

form, and the effects of adding a probe cable. Next, I will describe what each circuit component represents and how we identified the RLC parameters.

The current waveform is produced by a Tektronix AFG3102 100 MHz arbitrary function generator (AFG). I programmed the waveforms externally using ArbExpress software and uploaded them to the AFG. The waveform begins with an external trigger supplied by a pulse generator synced to the photoionization light (see Section 4.2.4). A BNC cable connects the AFG to the AC terminal of a wideband bias tee (Mini-Circuits ZFBT-4R2GW+, 0.1–4200 MHz) in conjunction with a voltage supply on the DC terminal so that both DC and AC signals can be sent to the copper disk. The signal from the combined port of the bias tee is sent to the chamber by a coaxial BNC cable and is represented in Figure 4.26 by current I_0. The physical junction where I_0 splits through tee adapters into I_1, I_2, I_3 is at the apparatus's UHV connectors. At this junction, the signal from the AFG is coupled to a $50\,\Omega$ terminator as indicated by current I_2. Connected in parallel with this path is the copper electrode represented by capacitor C_v. The current I_1 that charges C_v is carried through a thinly insulated wire with press-fit UHV connections on both ends; we model this coupling configuration through the resistance and induction parameters R_v and L_v.

Our goal is to find the charge on the electrode capacitor, $Q_v(t)$, that corresponds to our observations of the waveform physically produced by the AFG. We can observe the waveform by measuring voltage on a parallel $20'$-long probe cable connected to an oscilloscope. However, doing so requires adjustments to our model in order to account for this additional cable and connection. We treat the effect of a probe cable with the inclusion of resistance, induction, and capacitance parameters R_p, L_p, C_p. These are illustrated within the orange-dotted box in Figure 4.26. The probe voltage measured on the oscilloscope is proportional to the charge Q_p on capacitor C_p in this picture.

For the RF heating measurements reported in this work, *a probe cable was not used during the data collection process.* This implies that we are challenged with deducing what waveform was produced *without* a probe cable by making observations of waveforms produced *with* a probe cable. Our approach for solving this challenge was to make measurements of waveforms using extra

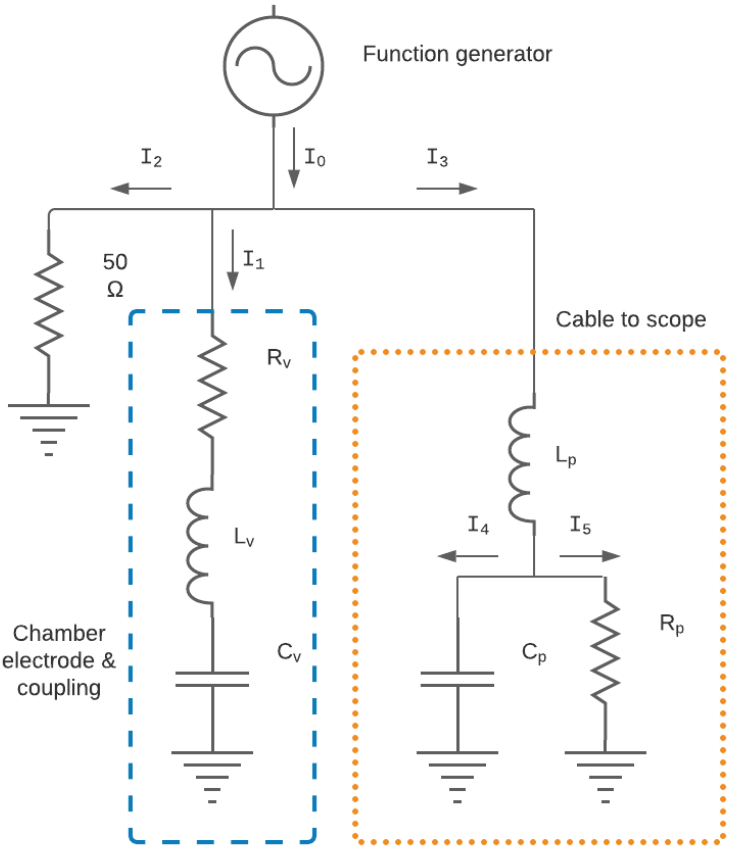

Figure 4.26: Circuit model diagram for the electrode transient response we can use to characterize and correct a systematic calibration error. The blue-dashed section indicates components modeling the copper disk electrode and associated couplings at the chamber; the orange-dotted section models a cable attached in parallel between the chamber connections and an oscilloscope.

proxy probe cables followed by an extrapolation of our analysis to a case with zero probe cables. In terms of our circuit diagram, these proxy cables would look like additional dotted-orange sections connected in parallel with the one depicted. The proxy cables used in our measurements have specifications identical to the probe cable. In the future, experiment procedure will be corrected to perform measurements with an attached probe cable that can record the exact waveforms associated with individual shots. This change would make the proxy cable-extrapolation analysis obsolete and reduce the experiment's systematic uncertainty.

We return now to our effort for determining the disk charge $Q_v(t)$ by applying Kirchoff's Rules to our circuit model. Simplifying terms yields the following system of coupled second-order differential equations

$$\begin{aligned} L_p\ddot{Q}_p(t) &= R_{50}I_0(t) - \left(\frac{L_p}{R_pC_p} + R_{50}\right)\dot{Q}_p(t) - \left(\frac{R_{50}}{R_p} + 1\right)\frac{Q_p(t)}{C_p} - R_{50}\dot{Q}_v(t) \\ L_v\ddot{Q}_v(t) &= R_{50}I_0(t) - (R_v + R_{50})\,\dot{Q}_v(t) - \frac{Q_v(t)}{C_v} - R_{50}\dot{Q}_p(t) - \frac{R_{50}}{R_pC_p}Q_p(t) \end{aligned} \tag{4.5}$$

where $\dot{Q}_v = I_1(t)$ and $\dot{Q}_p = I_4(t)$. Ultimately, we wish to correct our RF field calibration by quantifying effects like LC ringing and non-ideal AFG shutoff in the sudden turnoff waveform. We chose to model the non-ideal shutoff to first order as a DC current I_δ that exists for a duration δt after the ideal $I_0(t) \propto \epsilon_{\text{sudden}}(t)$ shuts off at $t_f/3$.

How we chose the values used for I_δ, δt, and the pair of RLC model parameters—R_v, L_v, C_v, R_p, L_p and C_p—will be addressed shortly, but first I will describe the measurements we made to compare our apparatus response with our model. We can treat the charge on the probe capacitor Q_p as proportional to the voltage measured by an oscilloscope. We recorded the average response to sudden-turnoff AFG waveforms using the probe-proxy cable configuration described earlier. Plotted in Figure 4.27 with solid lines are the probe measurements with different numbers of proxy cables when the current is programmed to shut off at $t \approx 400\,\text{ns}$; the behavior predicted by the model is shown as the dashed line. The model parameters for the "0 cable" curve come from extrapolating the relevant parameters that adequately fit the three, two and one cable curves. The

$20'$ length of the probe cables creates a delay in the reflected response that can be observed in the measured traces around $t > 450\,\mathrm{ns}$.

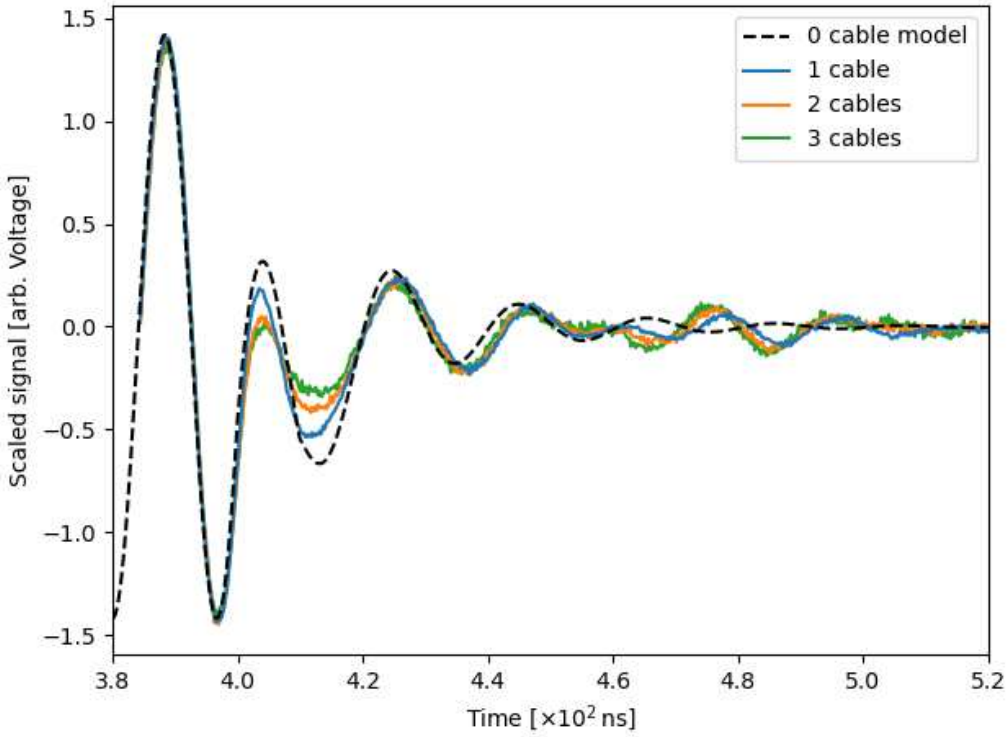

Figure 4.27: Plot comparing the scaled responses of the sudden turnoff measured by probes to the model prediction. The solid lines show the traces when 1, 2, or 3 probe + proxy cables are attached. The dashed line is the curve associated with extrapolating fitted probe RLC parameters to find the predicted 0 cable behavior.

Now I will describe how we identified the circuit parameters R_v, L_v, C_v, R_p, L_p and C_p. The copper disk/chamber capacitance C_v was measured by detecting the current drawn when a ~$1\,\mathrm{MHz}$ signal is sent directly into the chamber. The idea is the overall impedance without any parallel connections or $50\,\Omega$ terminators is dominated by the capacitance. We found that $C_v = 85\,\mathrm{pF}$. The resonant frequency of the disk/chamber section tells us about the product $L_v C_v$. We measured the frequency of transient ringing in the circuit and saw $42\,\mathrm{MHz}$ oscillations; this yields $L_v = 0.17\,\mu\mathrm{H}$. The series resistance R_v is necessarily included to account for the real damping of energy in the LC circuit, and we assume that the predominant source of this resistance is in the press-fit contact

interfaces. We therefore estimated $R_v = 0.2\,\Omega$ as a physically reasonable value. Furthermore, the qualitative agreement observed was insensitive to the exact value of R_v. The probe cable resistance R_p is approximately equal to the $50\,\Omega$ oscilloscope coupling. The probe inductance L_p was found to have little effect on our model for reasonable physical values and thus subsequently set to zero. The value of the capacitance C_p is adjusted to match the RC damping rate of the ringing. Finally, the magnitude and duration of the non-ideal current correction, $I_\delta \sim 0.225 \times \max\, I_0$ and $\delta t = 10\,\mathrm{ns}$, were determined by qualitatively matching the results of our model with the measurements as shown in Figure 4.27.

We use the corrected waveforms predicted by our RLC circuit model in conjunction with the damped-driven oscillator approximation to calculate the work done on the electrons by the waveforms. We can then match these predictions with experimental plasma heating measurements using the kick-temperature calibration described earlier in Figure 4.5. The procedure and results for these measurements will be discussed in the following chapter.

4.7 Chapter summary

The focus of this chapter is to provide foundational context for the RF heating measurements I present in Chapter 5. I discuss basic details covering the design and operational principles of our apparatus in Section 4.1. In Section 4.2, I highlight important apparatus modifications we implemented that made the measurements presented in this dissertation possible. In particular, I assess new electrostatic and magnetostatic environments within which we can generate and probe UCPs. Sections 4.3 and 4.4 explore techniques and measurements we utilized to characterize the number, size, density, and DC field parameters for our plasma. I present a calibration procedure we developed to measure precise electron temperature differences in Section 4.5, and finally, in Section 4.6, I introduce a method for calibrating programmable AC fields generated at the plasma by our upstream electrode.

In the next chapter, I combine the key concepts and results we have so far established into a coherent, systematic study of UCP off-resonant RF heating rates. I use the methodologies presented

in this chapter to produce quantitative measurements backed by experimental data. I compare these measurements to the theoretical predictions for RF heating we developed in Chapter 3. I follow this with a discussion on what we have learned from this previously unreported information and what we hope to learn using these techniques in the future.

Chapter 5

Measurements of off-resonant RF heating

The goal of this chapter is to combine the theory treatment for RF heating we developed in Chapter 3 with the experimental tools described in Chapter 4 to present a study of off-resonant RF heating rates in UCPs at various magnetic fields.

In the first section, we complete our discussion of the RF amplitude calibration technique. I address the data collection and analysis procedures and explain how it ultimately gives us a determination of the absolute heating rate at $B \approx 11\,\mathrm{G}$. I show how the calibration factor is burdened by fairly large uncertainties, so I also derive a heating rate ratio that compares the relative heating rate across conditions and does not depend on this uncertain factor. This information is provided by comparisons of the peak-to-peak voltage settings on the arbitrary function generator (AFG) that produces our RF waveforms. Taking the ratio of the voltage settings that produce an associated ΔT response for different experimental conditions produces a determination of relative heating rate comparisons with unprecedented precision. This methodology is discussed in additional detail in this chapter.

The primary results for the experimental measurement and theory predictions are tabulated in Section 5.2. This is followed by a discussion on the mixed agreement observed in comparisons between observations and predictions. We find that the absolute heating rate at $11\,\mathrm{G}$ and the relative heating rate at $134\,\mathrm{G}$ as compared to $11\,\mathrm{G}$—using the ratio method described above—are within uncertainty for agreement with theory. However, we also find a factor of ~3 disagreement with a high degree of confidence between the observation and prediction for the 65-compared-to-$11\,\mathrm{G}$ heating rate ratio.

We conclude the body of this chapter with an overview of potential research directions that may be pursued in the future. The work presented in this dissertation produced experimental data points that can be used to evaluate theory while simultaneously laying a foundation for several different future lines of investigation.

5.1 RF amplitude calibration Part II

We now return to our discussion on RF amplitude calibration. In the previous section I covered the basic idea of using "slow" and "sudden" RF waveforms to heat the plasma by an amount W (Eq. (4.3)). If we know how much the plasma heated from the RF using these two types of waveforms then we can calibrate the parameters that determine the oscillation amplitude, E_0 and ξ. We are able to determine this using the kick-ΔT calibration described in Section 4.5. In this section I describe the procedure we use to do the RF/kick matching that associates the amplitude of the applied RF with the temperature rise detected in the plasma. The results of this measurement also generates our first data point for our evaluation of heating as a function of electron magnetization, which is presented in the next section.

5.1.1 Procedure & results

The goal of this section is to explain how we find E_0 and ξ, which will let us calibrate the amplitude of an applied waveform with the amplitude of the electron center-of-mass motion. As mentioned previously, ξ is a damping rate associated with the $60\,\mathrm{MHz}$ oscillations. In principal, it is effectively a heating rate dependent on electron-ion collisions like the one we're ultimately interested in. Without these values we can make relative measurements of heating rates by comparing uncalibrated AFG driving voltages. With the RF amplitude calibrated, we can determine absolute measures of the heating rate, as well.

The amplitude calibration measurements are based on our ability to associate the plasma response to a fixed amount of heat through partial extraction measurements as demonstrated in Section 4.5. In order to do the kick-ΔT calibration, we compared the partial extraction response of a known $\Delta T_\mathrm{e} = 2\,\mathrm{K}$ signal determined precisely by the photoionization laser wavelength to the partial extraction response when different amplitude kicks heat the plasma. Then, for our RF amplitude calibration, we compared the partial extraction responses from RF as a function of AFG driving voltage to the response from kicks corresponding to $\Delta T_\mathrm{e} = 2\,\mathrm{K}$. Generally, I looked at partial extraction response measurements under the following conditions: a baseline response with no

RF or kick applied, the response with the ΔT kick, and the responses when at least three different RF amplitudes are applied.

Once the data is collected, it is analyzed in a way similar to what is depicted in Figure 4.23b. I evaluate the measured partial extraction responses versus post-prompt number and apply quadratic fit functions for each condition. These fits allow me to determine the central value and uncertainty for the partial extraction response at a particular post-prompt number. This lets me evaluate the partial extraction response at the conditions associated with the $16\,\mathrm{MHz}$ resonance response I measured. For example, if the $16\,\mathrm{MHz}$ resonance condition at $11\,\mathrm{G}$ was observed in plasma with around 250,000 post-prompt charges, then I can use the method described above to find the partial extraction responses associated with those conditions.

The central values and uncertainties from these partial extraction responses can be plotted and compared in terms of the AFG peak-to-peak voltage V_{pp} used to set the RF amplitude, as illustrated for one set of magnetization conditions as an example in Figure 5.1. This plot shows the partial extraction response for five heating conditions: baseline (no RF/kick), three non-zero applied RF amplitudes, and the response from the ΔT kick. This data can be fit, as demonstrated by the dashed curve, in order to find the AFG amplitude associated with a $\Delta T = 2\,\mathrm{K}$ response.

This analysis procedure was applied in all of our RF heating measurements across magnetization strengths, including the RF amplitude calibration comparing "slow" and "sudden" turnoff responses at $11\,\mathrm{G}$. The electric field RF amplitude at the plasma is related to the peak-to-peak voltage of the function generator with a calibration factor $\kappa \equiv E_0/V_{pp}$. This factor ultimately comes from matching the "sudden" turnoff measurement to the $\Delta T = 2\,\mathrm{K}$ response, and the damping coefficient ξ is determined by matching the slow turnoff response to the sudden turnoff response.

To get a sense of how this works, one can consider comparisons between the slow and sudden turnoff in an idealized limit. We can imagine an idealization where there RF amplitude modulation in the sudden turnoff case is simply an adiabatic ramp up to a maximum amplitude E_0 followed by an ideal shutoff without any significant full-amplitude RF heating. In other words, all of the heating in the sudden turnoff case is approximated as coming from damping of the electron center-of-mass

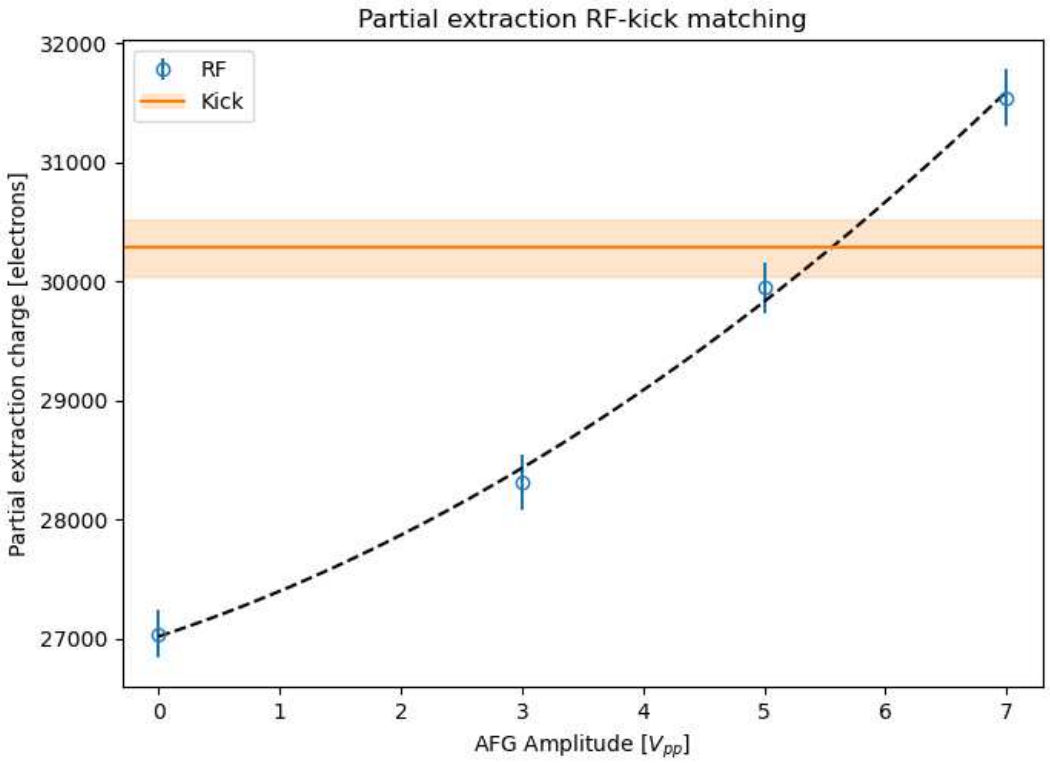

Figure 5.1: Plot of "slow turnoff" data evaluating the partial extraction response as a function of applied RF amplitude in order to find the amplitude corresponding to a $\Delta T_\mathrm{e} = 2\,\mathrm{K}$ response determined by the calibrated kick. The blue points are responses for RF amplitudes in terms of the peak-to-peak voltage programmed into the arbitrary function generator (AFG). The orange line is the response and uncertainty associated with a $\Delta T_\mathrm{e} = 2\,\mathrm{K}$ temperature rise from the calibrated kick. The dashed line is a quadratic fit through the data.

oscillations after the RF is shut off. ΔT is determined solely by E_0 without any dependence on ξ in that case. The length of time it takes for the oscillations to completely damp into heat depends in some way on ξ, but the total amount of energy transferred does not. The slow turnoff heating, in contrast, depends on both E_0 and ξ. Once the heating in the sudden and slow turnoff cases is measured, the sudden turnoff fixes E_0 given ΔT, and the ratio between the sudden and slow turnoff heating sets the value of ξ.[9] This is important because once κ has been determined by the sudden turnoff heating it is a known for all other conditions where RF heating measurements are taken.

[9]Interestingly, this means the value of ξ does not depend on ΔT, only the ratio of heating between the sudden and slow cases.

For actual data rather than this idealized case, the heating in the sudden turnoff depends not only on E_0 but on ξ as well. The general dependence is different than the slow turnoff case, for the reasons explained above, so E_0 and ξ can still be determined through comparing the sudden and slow turnoff heating amounts. However, the real sudden turnoff waveform also has the non-ideal AFG and RLC electrode behavior that was discussed in Section 4.6.2. These corrections are also applied in our determination of the RF amplitude calibration factor.

The RF calibration was conducted with conditions $T_0 = 3.5\,\mathrm{K}$, $B = 10.6\,\mathrm{G}$, $n = 11.3 \cdot 10^6\,\mathrm{cm}^{-3} \rightarrow \beta = 0.98$ which puts it right by the boundary of the weakly-strongly magnetized electron regime. As demonstrated in Figure 5.1, I found that a $\Delta T = 2.00 \pm 0.44\,\mathrm{K}$ response associated with a $1.66\,\mathrm{V}$ kick is matched by a $5.55 \pm 0.33\,\mathrm{V}_{pp}$ $60\,\mathrm{MHz}$ RF signal. Combining this data with the amplitude calibration factor κ lets us determine a heating rate. Next, I will describe the uncertainties associated with these techniques and how they combine in our analysis of the final results.

5.1.2 Uncertainty considerations

The purpose of this section is to lay out the statistical and systematic uncertainties associated with the combination of methods we have developed thus far. By the end, we will have developed assumptions and expressions we can use to represent our data in a way that lets us compare the experiment to a prediction. This includes formulas to calculate the absolute heating rate from our measurements in addition to a relative heating number that compares rates by a ratio across different magnetic field conditions.

The amplitude calibration factor κ plays a significant role in our determination of the absolute measure of the heating rate. We require it to relate ΔT to V_r (the applied RF amplitude), $\Delta T \propto E_0^2 = \kappa^2 V_r^2$. As described above, it comes from a process of finding ξ through matching sudden and slow RF responses followed by matching the sudden response to $\Delta T = 2\,\mathrm{K}$. The uncertainty on κ^2 is determined by the combined statistical and systematic uncertainties accumulated during the analysis.

The RLC correction to the sudden turnoff discussed in Section 4.6.2 produces an uncertainty in the amplitude calibration due to an uncertainty in the fitting of the i_δ parameter in the RLC response. This creates a 21% systematic uncertainty in κ^2. We also need to take into account the uncertainty in the measured RF amplitude of the matched slow and sudden turnoff responses. The slow and sudden amplitude uncertainties are 6.0% and 7.2%, respectively. These combine in quadrature to 9.4%, and propagating this uncertainty through the amplitude calibration analysis yields a 32% variation in κ^2. This 32% uncertainty and the 21% RLC-correction uncertainty add in quadrature to a total 38% systematic uncertainty in κ^2.

To see how the uncertainty in κ^2 affects our measurements of the absolute heating rate, η, we can start from our expression for the one-cycle heating Eq. (3.30),

$$\Delta \mathrm{E}^{(1)} = \frac{\pi e^2 \omega_{RF}}{m\left[\left(\omega_{RF}^2 - \omega_{CM}^2\right)^2 + \xi^2 \omega_{RF}^2\right]} \eta E_0^2. \tag{5.1}$$

Now, I will make the following assumptions accompanied by their rationale:

1. I assume no *a priori* knowledge of the temperature scaling of η. In principle, we could assume a T^α temperature scaling and use $\alpha \approx -2/3$ from the theory presented in Chapter 3 for our conditions. However, that would then directly tie our presentation of experimental results to the theory. If the theory is invalid, then a representation of our measurements dependent on that theory may also be invalid.

2. The above argument does not apply for assuming density scaling. I can safely assume the heating rate scales linearly with density based on first principles for weakly coupled plasma. In theory, at our coupling parameter, the linear scaling is modified very weakly by an order-unity Coulomb logarithm factor [19].

3. I also assume the total heat $\Delta \mathrm{E} = \frac{3}{2} k_\mathrm{B} \Delta T$ is related to the single cycle heat $\Delta \mathrm{E}^{(1)}$ by the effective number of cycles in the slow turnoff waveform, $N_\mathrm{cyc} = \Delta t_\mathrm{eff} \cdot 2\pi\omega_{RF} = 66.27$. Furthermore, for $T_0 = 3.5\,\mathrm{K}$ and $\Delta T = 2\,\mathrm{K}$, the heating rate we calculate is associated

with the "average temperature" $T = T_0 + \Delta T/2 = 4.5\,\mathrm{K}$. These statements are effectively corollaries of Assumption 1.

From (5.1) and the above assumptions, we can write

$$\begin{aligned} \Delta T &= \frac{2}{3k_{\mathrm{B}}} \frac{\pi e^2 N_{\mathrm{cyc}} \omega_{RF}}{m\left[\left(\omega_{RF}^2 - \omega_{CM}^2\right)^2 + \xi^2 \omega_{RF}^2\right]} \eta E_0^2 \\ &= \zeta \eta_{4.5} \left(\frac{n}{n_{4.5}}\right) \kappa^2 V_r^2, \end{aligned} \tag{5.2}$$

where the ζ term contains the parameters ω_{RF}, ω_{CM}, and ξ, in addition to constants. The density dependence on η has been made explicit in terms of the heating rate and density at the "average temperature" $T = 4.5\,\mathrm{K}$. Solving for $\eta_{4.5}$ gives us

$$\eta_{4.5} = \frac{\Delta T}{\zeta \kappa^2 V_r^2} \left(\frac{n_{4.5}}{n}\right). \tag{5.3}$$

This is the expression I use to determine the central value and uncertainty for $\eta_{4.5}$.

The sub-5% uncertainties associated with the ζ and density terms are dwarfed in comparison to the 38% uncertainty in κ^2. The uncertainty in the slow turnoff RF amplitude V_r has already been worked into the uncertainty of the calibration factor. I also want to note that ΔT and κ^2 are correlated based on the amplitude calibration technique, so their uncertainties are not independent. Analysis of this aspect showed that variations in ΔT would also be captured in κ^2 in such a way that the overall effect of the variations on $\eta_{4.5}$ mostly cancel out. This means that the uncertainty in our absolute measure of the heating rate is entirely dominated by the 38% systematic uncertainty from the amplitude calibration.

However, we can make much more precise relative comparisons of heating rates measured under different conditions. This comes from the fact that the calibration factor divides out when taking the ratio, so the only contributions to the uncertainty left over are mostly in the density and uncalibrated amplitudes. Let us define $g_B \equiv \eta_{4.5}^{(B)}/\eta_{4.5}^{(11)}$, which is the ratio of the heating rate at magnetic field B to the heating rate determined at ~$11\,\mathrm{G}$. From Eq. (5.3),

$$g_B = \left(\frac{\zeta_{11}}{\zeta_B}\right)\left(\frac{n_{11}}{n_B}\right)\left(\frac{V_{11}}{V_B}\right)^2, \tag{5.4}$$

where we have taken advantage of the fact that ΔT is equal for both measurements of $\eta_{4.5}$ at different B fields. The values of ω_{RF} and ω_{CM} were fixed with sub-1% uncertainty for all of the heating rate measurements reported in this thesis. The off-resonance condition $\omega_{RF} \gg \omega_{CM}$ makes the ζ factor fairly insensitive to variations in ξ. Therefore, across the relevant conditions, $\zeta_{11}/\zeta_B = 1.00(1)$.

In the next section, I will use these relationships to report central values and uncertainties for $\eta_{4.5}^{(11)}$, g_{65}, and g_{134} based on my measurements. I will also provide complementary predictions based on the theoretical treatment from Chapter 3 using the central values I measured.

5.2 RF heating measurement results

We have arrived at the crux of my thesis: the results from measuring the off-resonant RF heating rate for magnetized electrons in ultracold plasma. I will start with a very brief overview of how the methods discussed throughout this work combine into our ultimate results. Then I will present the combined results of our measurement and theory predictions for the heating rate across magnetization strengths.

First, I needed to establish the temperature, magnetic field and density conditions. I used temperature calibration data reported by the previous student, Wei-ting Chen, to set the initial UCP electron temperature to $T_0 = 3.5\,\mathrm{K}$ [17]. This temperature was chosen for several reasons. At higher temperatures the electron-ion collision rate reduces [19], which has multiple effects relevant for our measurement: a lower collision rate means a lower heating rate and may require larger RF amplitudes to produce detectable temperature differences, and the kinetic energy deposited in electrons by kicks or sudden RF turnoff would take longer to thermalize in the plasma. At lower temperatures, and stronger coupling, we face issues associated with the rapidly growing three-body recombination rate [142]. The three-body recombination of two cold electrons and a Rb^+ ion into a neutral Rydberg atom and an energetic free electron not only heats the plasma but can

also contaminate our signal. If a significant number of weakly-bound Rydberg atoms form and get re-ionized by our applied fields [17], then the electrons can show up in the partial extraction signal even though they do not characterize RF heating. We chose $T_0 = 3.5\,\mathrm{K}$ to mitigate each of these undesired effects.

I used the magnetic field calibration measurement presented in Section 4.2.2 to generate UCPs at three magnetic fields, $B = 10.6$, 65.0, and $134\,\mathrm{G}$. These fields were chosen because at our $\Gamma \approx 0.14$ they span the electron weakly-strongly magnetized boundary to the strongly-extremely magnetized boundary as defined by Ref. [27] (see Figure 2.4). Then I found the plasma number conditions associated with a $16\,\mathrm{MHz}$ center-of-mass resonance at each of the magnetic field values. This resonant RF data also informs us of the plasma density with the help of simulations, as described in Section 4.4.

To measure the off-resonant RF heating rate at the different magnetizations, I applied the $60\,\mathrm{MHz}$ "slow" turnoff waveform and varied the amplitude to match the RF partial extraction response to that from the $1.66\,\mathrm{V}$ kick. Data from this technique is presented for $B = 10.6\,\mathrm{G}$ in Figure 5.1. Using a consistent kick amplitude gave me a consistent $\Delta T \approx 2\,\mathrm{K}$ for relative comparisons. This let me use equation (5.4) to determine relative ratios of heating rates across magnetic fields with ~20% precision. Combining the slow turnoff data at $10.6\,\mathrm{G}$ with corresponding sudden turnoff measurements, as described in Section 5.1, determined a systematic-error-prone RF field calibration factor. We used this factor to produce a measurement of the absolute heating rate at $10.6\,\mathrm{G}$ with ~40% precision. We are presently capable of collecting one RF heating data point in roughly one calendar month using these steps. This rate may possibly be improved by up to a factor of two if laborious tasks—like finding proper power supply settings for the magnetization coil—can be done more efficiently.

The central values determined by the measurements can be used to generate predicted heating rates from theory. I used Eq. (3.51) to find the predicted single-cycle heat at $T = 4.5\,\mathrm{K}$ that is

associated with the experimentally determined RF amplitude at each magnetic field.[10] Then I used the assumptions and equations enumerated in the previous section to calculate theory predictions with a representation consistent with the way the measured values are reported. These values and associated uncertainties are tabulated in Table 5.1.

Table 5.1: Tabulation of our primary RF heating rate versus applied magnetic field results. The top part lists the β, Γ, and v' for the three magnetic fields where I performed my measurements (see text). The bottom part contains the results of our $60\,\mathrm{MHz}$ heating rate experiments (exp) and predictions (pred) in terms of the absolute heating rate $\eta_{4.5}$ (see Eq. (5.3)) at $10.6\,\mathrm{G}$ and g, the rates at higher magnetization measured relative to that at $10.6\,\mathrm{G}$ (see Eq. (5.4)).

$B\,[\mathrm{G}]$	β	Γ	v'
10.58 ± 0.21	0.985 ± 0.053	0.134 ± 0.015	0.465 ± 0.091
65.0 ± 2.6	5.69 ± 0.36	0.140 ± 0.015	0.825 ± 0.162
134.0 ± 2.7	12.7 ± 0.7	0.133 ± 0.014	0.452 ± 0.089

$B\,[\mathrm{G}]$	$\eta_{\mathrm{exp}} \pm$ (stat) $\pm$ (sys) $[\times 10^6 s^{-1}]$	$\eta_{\mathrm{pred}}\,[\times 10^6 s^{-1}]$	g_{exp}	g_{pred}
10.58 ± 0.21	$5.57 \pm 0.71 \pm 2.12$	7.24	-	-
65.0 ± 2.6	-	-	0.282 ± 0.053	0.852
134.0 ± 2.7	-	-	1.11 ± 0.24	1.03

Table 5.1 is split into a top and bottom part. The top part lists the dimensionless magnetization strength, $\beta \equiv \omega_c/\omega_p$, and Coulomb coupling, $\Gamma \propto n^{1/3}/T$, for the three magnetic fields where I performed my measurements. The $\pm$ uncertainty numbers are the 1σ values from the combined statistical and systematic uncertainties in the magnetic field, density, and temperature determinations. The scaled oscillation velocity $v' = a\omega_{RF}/v_{\mathrm{th}}$ corresponding to the RF amplitude that matches the $\Delta T = 2\,\mathrm{K}$ response is also listed alongside its uncertainty, which is dominated by the systematic uncertainty in the amplitude calibration factor κ.

The bottom part of Table 5.1 contains our heating rate results for the three magnetic fields. It is formatted such that the absolute rate for $10.6\,\mathrm{G}$ is listed in the first entry, and the rates at 65 and $134\,\mathrm{G}$ are presented in terms of g, relative to the $10.6\,\mathrm{G}$ rate. The results from the experiment

[10] I will note that the uncertainties on $T_0 = 3.5\,\mathrm{K}$ and $\Delta T = 2\,\mathrm{K}$ produce a ~10% uncertainty on $T = 4.5\,\mathrm{K}$. However, propagating this into the predicted heating rate produces an uncertainty in the theory value of about 7%. This is much smaller than the ~40% precision in the measured value so we can effectively ignore it.

are listed with exp subscripts. The uncertainty in the η_{exp} has been decomposed into its statistical and systematic parts in order to emphasize the dominant source. The uncertainty in the g_{exp} observations is much less because it does not depend on an amplitude calibration factor and therefore is predominantly statistical. The corresponding predicted values calculated from the theoretical treatment are presented as η_{pred} and g_{pred}. Next, I will discuss key observations concerning these results.

5.3 Discussion

To avoid burying the lede, I will begin the discussion with the most remarkable result: the relative heating rate comparing 65 to $10.6\,\mathrm{G}$ in our measurements is a factor of ~3 lower than the theory prediction. The precision in our relative measurements shows that this disagreement is on the order of 10σ. Aside from the disagreement at this individual point, the fact that there is structure in the heating rate as a function of magnetic field as large as what we observed is also in contrast to the theory predictions shown in Figure 3.1a.

It naturally follows to ask, "if the $65:11\,\mathrm{G}$ ratio disagrees between the experiment and theory, then is it the behavior at $11\,\mathrm{G}$, $65\,\mathrm{G}$, or some combination causing the discrepancy?" The data I have presented does not answer this question in full, but it suggests the disagreement may be associated with the predicted $65\,\mathrm{G}$ behavior. There is agreement-within-uncertainty for the $11\,\mathrm{G}$ absolute determination of the heating rate, and an equivalent comparison between experiment and predictions for the absolute rate at $65\,\mathrm{G}$ disagrees by over $6\,\sigma$ in terms of the measurement uncertainty. Our data is not precise enough to totally answer the question posed, as it could very well be some combination of disagreement in both the $11\,\mathrm{G}$ and $65\,\mathrm{G}$ rates that causes the disagreement in the relative comparison. However, it does say with great certainty that the physics contained in the measurements across these conditions is not represented well in the theory.

Looking at the v' column in the top part of Table 5.1, we see that our measurement of the $\Delta T = 2\,\mathrm{K}$ heating rate required much larger scaled oscillation velocities at $65\,\mathrm{G}$ than for the other magnetizations. The fact that we used larger fields in the $65\,\mathrm{G}$ measurement leads to con-

cerns about nonlinear driving effects. The SPLET treatment we developed in Chapter 3 sought to capture nonlinear effects not present in the low-amplitude approximation for magnetized AC conductivity. The orange (downward triangle) curve in Figure 3.2a shows that SPLET predicts about a 15% decrease in the heating rate compared to the low-amplitude limit for our $65\,\mathrm{G}$ condition at $E/E_{lim} = 5$ (the scaled amplitude corresponding to $v' = .83$).

We decided to perform an experimental check to see if nonlinearity effects could account for the disagreement between g_{exp} and g_{pred} at $65\,\mathrm{G}$. For this check, instead of applying a $1.66\,\mathrm{V}$ kick and finding the RF that matched, we applied a $5.55\,\mathrm{Vpp}$ RF signal ($v' \approx 0.45$) and varied the kick amplitude to match. This method does not preserve the $\Delta T = 2\,\mathrm{K}$ heat amount, and thus the heating rate measured is associated with a different "average temperature" than the reported $T = 4.5\,\mathrm{K}$ values. Therefore, this "nonlinearity check" cannot be compared directly to our other measurements, but it can still inform us in some sense about the scale of nonlinear driving effects. We found that the $65\,\mathrm{G}$ heating rate measured with $v' \approx 0.45$—compared to the $11\,\mathrm{G}$ rate—was consistent with what we found using $v' \approx 0.83$. Like the $v' \approx 0.83$ data point, we observed a factor of ~3 reduction compared to theory with a measurement uncertainty around 20%. This check strongly suggests that the factor of ~3 disagreement between observations and predictions at $65\,\mathrm{G}$ is not due to nonlinear amplitude effects.

In addition to the nonlinearity check, I also applied my measurement technique at $11\,\mathrm{G}$ with ultracold plasmas approximately resonant with $11\,\mathrm{MHz}$ center-of-mass oscillations (as opposed to $16\,\mathrm{MHz}$ in our primary result) to check the scaling of the heating rate with density. While this "scaling check" data requires further analysis before it can be reported with accuracy, preliminary observations show that the measured heating rate with reduced density is also reduced by roughly the magnitude predicted. Producing $\Delta T = 2\,\mathrm{K}$ with about half the UCP density required about double the RF power.

The measured and predicted relative heating rates between $11\,\mathrm{G}$ and $134\,\mathrm{G}$, g_{134}, do not show the same disagreement displayed in the g_{65} comparison. The experiment detected little to no variation in the heating rate between 11 and $134\,\mathrm{G}$, unlike the $65\,\mathrm{G}$ case, so the observed heating rate

across these magnetizations does not vary monotonically with increasing field. Given the context of effectively having two points in agreement and a third in disagreement lying between the other two, it is hard to say anything definitive with regard to comparisons between measurement and prediction with respect to the $134\,\mathrm{G}$ point that lies on the border of strong and extreme magnetization regimes. Given the unexpected variation observed in the heating rate versus magnetic field, we do not yet know if the unpredicted variation extends through $134\,\mathrm{G}$ and the observations just coincidentally agree or if the unexpected structure only exists near the $65\,\mathrm{G}$ point.

Prior to this work, systematic measurements of electron-ion interactions across magnetization regimes have not been reported.[11] In this sense, the results reported here demonstrate a proof of principle. In demonstrating this proof, we have also learned of realistic expectations for the level of precision the techniques we developed are capable of. It is clear that uncertainties in the RF amplitude calibration pose large challenges when it comes to determining absolute heating rates with precision. On the other hand, assuming finite-amplitude nonlinearity is not an issue, we see that the ΔT-kick-RF method produces fairly precise determinations of heating rate ratios.

It is not known what is causing the disagreement between measurements and theory we observe associated with the $65\,\mathrm{G}$ data. One possibility is the weakness in the dielectric theory's treatment of hard-angle collisions made apparent through its inclusion of an unphysical hard cutoff in the k-space integral. There are plasma simulations results that suggest the $k_{\max} = 1/r_{\min}$ cutoff is consistent across magnetization strengths. But given the irregular, chaotic behavior of magnetized binary scattering explored in Section 2.5.2, it is hard to believe such magnetized binary collision effects would not play a substantial role in RF heating. If the effects of chaotic binary collisions do play a substantial role in magnetized RF heating, then an accurate theory should properly capture that physics, and standard linear response dielectric theory does not seem to do so. Performing additional measurements could help determine whether or not this explanation of the discrepancy is reasonable.

[11] Which is not to discount observations of electron cooling in ion beam storage rings [33, 34]. However, in those studies the magnetic field cannot be easily varied and the large temperature anisotropies limit the general applicability to other plasma systems.

The sum of the work and results presented in this thesis has taught us several important things about the study of RF heating of magnetized ultracold plasma. However, in order to make stronger, bolder claims about the variation of the heating rate across electron magnetization strengths, we need to take additional data. In the next section I look toward the future and discuss potential avenues that we can learn from based on the foundation we have established.

5.4 Future outlook

The results presented above constitute a complete work in the sense that (1) we tested the RF heating rates under weakly to strongly to extremely magnetized conditions at unprecedented precision with a new technique, (2) we have enough data to demonstrate that modifications of the theory are necessary, as we observe neither a mild nor monotonic dependence of the heating rate on magnetization, and (3) the final data points were measured just before the lab was shut down for COVID-19.

To expand on point (3), the apparatus does not handle long periods of downtime without upkeep if drifts in hardware like lasers go uncorrected. Efforts are currently underway to bring the magnetized RF heating experiment back into operation. Additionally, with the foundation established in this work, we have opened up multiple paths to take in the future to acquire further knowledge. In this section I will discuss some of these paths, such as improvement and expanded utilization of the techniques developed for this work in addition to other potential experiment directions.

We have identified several improvements to the measurements presented. Perhaps the most obvious example of this was our failure to probe and record the RF waveforms throughout standard operation. One consequence of this produced a fairly large ~20% systematic uncertainty that factored into our RF amplitude calibration. It is worth noting that this was not a major contribution to the systematic uncertainty in the end, though.

This calibration uncertainty can also be addressed by modifying the properties of the electrode RLC model. For example, an impedance-matched resistor could be installed to dampen the non-ideal RF turnoff, but a low-distortion amplifier would also be required to produce satisfac-

tory power at the electrode. A somewhat curious—and potentially clever—solution could exist by exploiting causality. If the arbitrary function generator (AFG) is connected to a nearby $50\,\Omega$ terminator coupled in parallel to the chamber but separated by a long enough wire, then the AFG could produce a complete "ideal" waveform before reflections and non-ideal effects have time to affect the AFG behavior.

There are several ideas we may pursue for future surveys that would reduce the RLC model uncertainty, but resolving that particular systematic source will only slightly improve the overall absolute calibration. Estimates of realistic uncertainties in our uncalibrated amplitude determinations suggest the systematic uncertainty for this calibration method may only get as low as ~30%. It is important to emphasize these problems are only associated with the absolute heating rate determinations and are essentially irrelevant in well-planned relative measurements. Estimates indicate 10–15% precision in relative measurements simply by taking more data should be achievable. For this reason, it would be fairly justified to predominantly focus future efforts on improving and expanding the relative heating rate measurements.

Even with the ~20% uncertainty we have demonstrated in our relative measurements, there is a promising well of knowledge presently within reach simply by applying this technique at more magnetic field strengths. With only three effective data points we already have learned that the physics contained in the theory predictions for our conditions between 11 and $65\,\mathrm{G}$ is inadequate. So, "filling out the curve" by taking additional measurements at points between the 11 and $134\,\mathrm{G}$ conditions could illuminate what physics is manifesting in our observations. Furthermore, the equipment used for these measurements is rated with the capability to produce and probe higher electron magnetization strengths. This would allow us to explore electron-ion interactions deeper in the extremely magnetized regime. [27]

We can also consider how to compare our results to some other forms of theory predictions outside the linear response treatment presented in this work. In principle, it should be possible to use molecular dynamics or Monte Carlo-type simulations to generate predictions for magnetized electron AC conductivity with today's computational performance capabilities [38,110]. However,

simultaneously conserving energy and proper physical trajectories for strong magnetic fields [110] or close binary collisions [38] is extraordinarily computationally expensive. Furthermore, the simulation would have to be suited for a finite-size (i.e. no periodic boundary conditions), quasi-neutral (i.e. attractive, two-component) Coulomb system. As of now, there are simulation platforms with the computational performance capabilities required to achieve convergence on physics of interest, but they are not adapted to match our experiment [27, 110]. On the other hand, we have a simulation platform in our group that is adapted to match our experiment, however we do not presently have the computational capabilities to achieve convergence with strong magnetization in reasonable runtimes. In order to use our current MD platform to simulate magnetized RF heating we first need to update it to compute with double-precision and validate appropriate convergence with checks. Then the main challenge will be long run times with estimates indicating ~1000 hours of computation time may be required to simulate 10^4 electrons and ions over an appropriate duration to evaluate magnetized RF heating.

Taking a step back from RF heating versus magnetization, we can also identify several more physical effects we are sensitive to and could potentially systematically measure. This includes RF heating rates versus coupling strength by appropriately repeating our measurements at different densities or temperatures. The "nonlinearity check" data that I described in the above Discussion section suggests we may be able to evaluate large electric field amplitude effects relevant in inverse Bremsstrahlung physics [53, 54]. Likewise, the sensitivity to energy thermalization in the partial extraction method (see Figure 4.22) could also possibly be exploited in some way to measure thermalization rates. However, it is not yet clear how to turn the equilibration of the upper tail of the Maxwell-Boltzmann distribution into a useful measurement to compare to a theory prediction.

As mentioned in Section 4.2.1, the electric field environment in the new electrode assembly should also be well-suited for surveys of Rydberg populations via field ionization. Measurements like this would not necessarily require the partial extraction method, but data integration times could be considerable due to shot-to-shot variations in the total ionization number. Evaluations of Rydberg atom populations in our UCP have been made previously by our group [17], which

includes a rate equation model [73] I helped to adapt to compare with the measurements. However, we have not yet characterized Rydberg atom populations using the second generation electrode assembly.

Lastly, on a semi-related note, the question of "how cold (or strongly coupled) can electrons in a UCP get?" does not yet have a definitive answer [17, 19]. Perhaps additional knowledge of magnetized electron-ion interactions could be exploited to generate colder UCPs with reduced three-body recombination heating, as predicted by theory [143], if we can observe how magnetic fields at these scales affect Rydberg atom formation.

5.5 Summary

In this chapter, we began by completing the discussion of the RF amplitude calibration started in Section 4.6. I explained the measurements we made using a technique that matches partial extraction responses due to ΔT-calibrated impulses, or kicks, to the response due to RF heating. Varying the RF amplitude to match responses due to "slow" and "sudden" turnoff waveforms, then matching those to a $2\,\mathrm{K}$ response using an RLC-corrected, harmonic oscillator model gave us an amplitude calibration factor. I described considerations in the propagation of uncertainty using this technique and how it generates a value for the absolute heating rate at $B \approx 11\,\mathrm{G}$ with ~40% uncertainty due to systematics. I showed how our technique instead can make much more precise determinations of relative heating rates on the order of ~$15 - 20\%$ uncertainty.

I tabulated the primary results from RF heating measurements made at three magnetic field values that span the strongly magnetized electron regime [27]. These are presented in Table 5.1 in terms of the absolute heating rate at $10.6\,\mathrm{G}$ and relative heating rates at 65 and $134\,\mathrm{G}$ as compared to that at $10.6\,\mathrm{G}$. The corresponding values predicted by the theory treatment developed in Chapter 3 are listed alongside the observed rates.

We presented a result that showed the measured absolute rate at $10.6\,\mathrm{G}$ and ratio between rates comparing 134 to $10.6\,\mathrm{G}$ are consistent with predictions within their uncertainties, but that is not true for the ratio between rates comparing $65\,\mathrm{G}$. We observe a factor of ~3 reduction in the relative

heating rate between 10.6 and $65\,\mathrm{G}$ with a level of certainty on the order of a 10σ difference. This clear contradiction between observation and theory strongly suggests the magnetized electron linear response RF heating treatment is not accurately capturing the relevant physics. A check we performed at $65\,\mathrm{G}$ ruled out nonlinear amplitude effects as the source of the disagreement.

We wrapped up this chapter with an overview of potential future work. Additional surveys across magnetization using the techniques we developed in Chapters 4 and 5 are prescribed as a promising direction to further understand magnetic field effects on electron-ion collisions. These techniques may also be adapted to probe nonlinearity effects and thermalization rates. Furthermore, Rydberg population observations could also be utilized in future experiments to teach us even more about fundamental electron-ion interaction processes.

Chapter 6

A scalable theoretical mean-field model for the electron component of an ultracold neutral plasma[12]

Chapter 6 is for the most part a duplication of Ref. [67]. It can be considered supplemental to the primary UCP research presented in this thesis, as it is not directly related to the measurements of magnetized RF heating.

The peer-reviewed article Ref. [67], republished here, details work we did developing a scalable model to simulate the electron component of a UCP. The details and results demonstrated for the model are presented in the chapter overview immediately below, so here I will add additional historical context not present in the article. The work presented in this chapter was effectively my first ultracold plasma research project after joining Prof. Roberts' group. We faced challenges with accurately simulating a finite-size Coulomb system with proper representation of charges due to the impossibility of maintaining relevant parameter ratios while directly scaling down the total particle number. This inconsistent scaling problem is addressed in the penultimate section of this chapter, and it is in large part what motivated the scalable mean-field project.

However, the scalable mean-field model we developed was not used in the work presented in Chapters 1 through 5 of this dissertation. This is mainly for two reasons: A full N^2 molecular dynamics (MD) code was adapted for our UCP parameters by Craig Witte, a previous student [91, 141]; and the UCP experiment has been running with intentionally lower densities and charge numbers to facilitate our ability to achieve higher magnetization, lower three-body recombination heating, and better MD modeling feasibility. Furthermore, the model presented in this chapter accounts for DC electric fields, but additional work is required to implement magnetic fields. However, the additional accuracy provided by MD simulations over the mean-field model

[12] J. Guthrie and J. Roberts, *J. Phys. B: At. Mol. Opt. Phys.* **49** 045701 (2016). DOI: 10.1088/0953-4075/49/4/045701 (© IOP Publishing. Reproduced with permission. All rights reserved)

presented in this chapter comes at a cost of additional computational complexity and hardware requirements. Thus, the scalable mean-field model we developed stands as a useful tool, especially for finite-size plasma with higher particle numbers than full-N^2 MD can reasonably handle.

6.1 Chapter overview

The electron component of an ultracold neutral plasma (UCP) is modeled based on a scalable method using a self-consistently determined mean-field approximation. Representative sampling of discrete electrons within the UCP are used to project the electron spatial distribution onto an expansion of orthogonal basis functions. A collision operator acting on the sample electrons is employed in order to drive the distribution toward thermal equilibrium. These equilibrium distributions can be determined for non-zero electron temperatures even in the presence of spherical symmetry-breaking applied electric fields. This is useful for predicting key macroscopic UCP parameters, such as the depth of the electrons' confining potential. Dynamics such as electron oscillations in UCPs with non-uniform density distributions can also be treated by this model.

6.2 Introduction to UCP modeling

Since their creation ultracold neutral plasmas (UCPs) [14, 81, 144] have provided a rich system of studying plasma physics in a unique parameter space, including influences of strong coupling [16, 94, 96, 145–147]. Determining UCP properties such as electron temperature and internal electric fields *in situ* is typically a difficult task due to the fact that physical probes (e.g. Langmuir probes [148]) placed inside the plasma would destroy the UCP. Many UCP experiments, especially those focused on the electron component, utilize detection schemes that rely on particle escape and extraction with the assistance of applied external fields in order to address these problems [149, 150]. In most cases extrapolating information about the plasma from this extraction process depends on accurately knowing properties such as the depth of the confining potential. In addition, it is useful to calculate electron dynamics such as electron plasma frequencies in order to determine parameters like the UCP density, for example [82]. Fortunately, UCPs also provide a

relatively clean environment apt for computational modeling. However, the long-range nature of the Coulomb forces that dominate UCP dynamics makes simulation a nontrivial task.

A number of different simulation schemes have been previously utilized for modeling ultracold plasmas using few approximations [73, 151–157]. The most complete models are molecular dynamics (MD) simulations that treat the plasma as a collection of N individual particles interacting via Coulomb forces [151–155]. These methods face difficulties due to the long-range nature of the Coulomb force in addition to other effects such as disparate timescales between short orbit electrons bound to an ion and unbounded electrons. The long-range Coulomb forces that drive the dynamics of the individual particles make for $\mathcal{O}(N^2)$ calculations in the most natural implementation of a numerical model. This makes MD simulations computationally expensive thereby limiting their usefulness when studying large numbers of particles or long time scale effects [153].

Other methods have been developed that are designed to reduce the $\mathcal{O}(N^2)$ complexity of these simulations by making various approximations. Methods that adaptively subdivide the space around each particle, such as the TREE model [157], are able to reduce the scaling to $\mathcal{O}(N \log N)$ [158]. The state of the art Fast Multipole Method [73] that approximates batches of distant charges as multipoles rather than individual sources can be shown to reduce the calculations to $\mathcal{O}(N)$ [159]. While these approximations can provide increased efficiency for sufficiently large N there is nontrivial computational overhead in implementing these methods, and so simulations can still often be computationally expensive. While these methods can provide a fairly complete description of the plasma, less computationally intensive techniques are still useful.

In principle, one way of reducing the complexity would be to decrease the number of particles that require calculations below the total N in the system being modeled. However, this reduction cannot be as simple as reducing the number of particles by some factor and increasing their charge and/or mass by an appropriate factor as this leads to inconsistent scaling of characteristic plasma parameters. That is, if the number of particles is changed there is no way to simultaneously preserve relationships between, for instance, the spatial electron distribution and the electron-electron

collision rate through adjusting charge and mass values. We have included an additional section at the end of this chapter that details these scaling problems.

Instead, the model we developed details a scalable simulation suitable for extracting macroscopic UCP parameters based on assumed parameters like electron temperature, charge imbalance, and spatial extent. This is accomplished by averaging the electric field inside the plasma using a mean-field approximation. The mean field is calculated self-consistently using Monte Carlo sampling of individual electrons that move under the influence of the mean field. The use of point particles makes our approach different from other mean-field models that describe plasmas using Vlasov equations, for instance [92, 160]. There are similarities between the treatment described in this work and such other mean-field models, however instead of solving PDEs for phase space distributions we utilize point-particle sample electrons. These S_{e} sample electrons can be used as a representation of the distribution of the total N_{e} electrons being modeled in the system by scaling their statistical weight while still maintaining their standard electron charge and mass. By constructing a suitable set of basis functions, the sample electrons can be projected onto a series of these functions in order to generate a smoothed approximation of the discrete distribution. This lets us compute forces on the sample electrons with complexity $\mathcal{O}(S_{\mathrm{e}})$ that gives us a scalable way of determining individual electron trajectories. Momenta and energy exchange events can be applied to these sample electrons to drive them to a thermal equilibrium distribution. The smooth equilibrium distributions can model sufficiently long-wavelength oscillations through variations in the electron density; short-wavelength oscillations will not be captured, however convergence in the measured quantities of interest with increasing basis function number indicates such short-wavelength oscillations do not contribute significantly for those measured quantities.

Macroscopic parameters can be extracted from both the discrete sample electrons as well as the smooth, approximate distribution. As an example and test of the technique, we examine the convergence of the potential depth as a function of the number of basis expansion terms used in the calculation. Additionally, we will present simulation results for the potential depth of the plasma as a function of applied DC electric field strength. For thermal equilibrium static properties the

model should be accurate in the limit that correlations are not significant (i.e. weak-coupling). In addition, some dynamic processes can be calculated using this model, too. As long as the electron collision time is significantly slower than the dynamical quantity of interest or not relevant to it, this model is applicable. For instance, electron center of mass plasma oscillation frequencies can be predicted using this model.

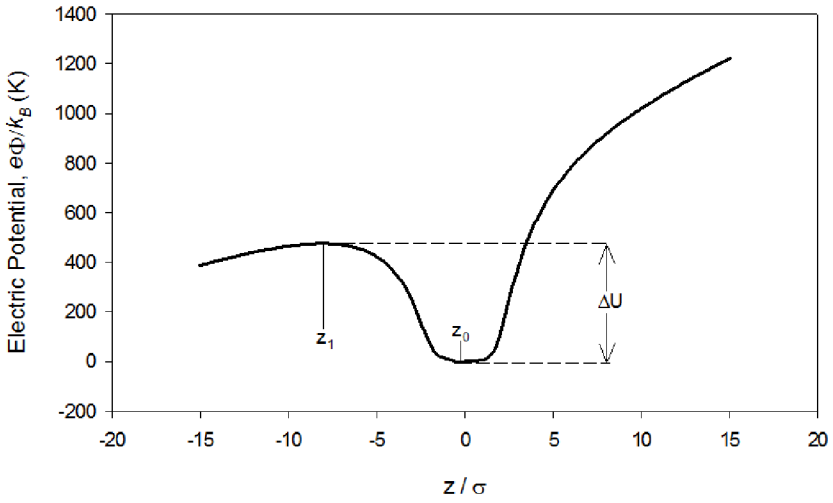

Figure 6.1: A typical electric potential curve, in scaled temperature units, along the z axis for an ultracold plasma under the influence of a DC electric field pointed along the z axis. The ion density distribution is assumed to be a spherically symmetric Gaussian $\propto \exp\left(-r^2/2\sigma^2\right)$. The positions of the local extrema in the curve are marked by z_0 and z_1. The potential depth of the plasma, ΔU, is also illustrated. This was taken from data using σ = 800 μm; $T = 20$ K; $E_{\mathrm{DC}} = 3$ V/m; ion number N_{i} = 200,000; and electron number N_{e} = 110,000.

As mentioned, one purpose of the calculations presented in this chapter is to extract the predicted potential depth of a UCP from a fast, approximate computational model. Various experiments focused on studying the electron component of UCPs have looked toward electron evaporation and escape as measurable quantities from which additional information about the plasma may be extracted. For instance, the depth parameter is useful for determining a predicted electron evaporation rate that can be compared to experimentally measured rates [102]. The parameter is also relevant for certain electron temperature measurement techniques that rely on electron extraction from the plasma using applied electric fields [149]. The plasma potential can be calculated

with much less difficulty by using systems with simplifying assumptions such as spherical symmetry [101, 161] or zero temperature electron distributions [162]. However, in many experiments a spherical symmetry-breaking external electric field is an integral part of the system as a means for guiding electrons for detection. Figure 6.1 shows a typical potential energy curve for an electron, computed by our model, along the z axis of a UCP under the influence of a DC electric field. Breaking spherical symmetry will often increase the complexity of modeling certain systems by changing calculations from solving ordinary differential equations to partial differential equations, for example. Finite temperature effects will also play a role in shaping the electron thermal distribution and ultimately affect the depth parameter. Factors such as these have motivated us to find a more complete computational model for efficiently calculating plasma parameters such as potential depth.

In addition to equilibrium parameters such as the potential depth, we are also interested in characterizing some dynamics of the electrons. From the classical plasma definitions for the two-body collision rate $\nu_{ee} \sim \sqrt{n}\,\Gamma^{3/2}\ln\left(\alpha\Gamma^{-1}\right)$ [26] and electron plasma oscillation frequency $\omega_p \sim \sqrt{n}$ we find that the dimensionless ratio ν_{ee}/ω_p scales as $\Gamma^{3/2}\ln\left(\alpha\Gamma^{-1}\right)$, where n is the electron density, α is a constant, and Γ is the Coulomb coupling parameter [145]. For $\Gamma \ll 1$ when the plasma is weakly coupled, as is the case for the UCPs modeled in this chapter, the collision rate is much less than the oscillation frequency. Therefore limited electron dynamics can be treated using a mean-field approximation to a reasonable degree of accuracy.

The evolution of the plasma with regard to temperature changes, expansion, or particle escape are not treated by this model as currently implemented, however certain dynamics such as electron oscillation frequencies can be simulated. Incorporating three-body effects is possible, if desired, by including in the model the three-body recombination rate to different Rydberg states [161]. For the extracted quantities and dynamics of interest here, estimates show that such three-body recombination should not contribute significantly given the temperature and electron density as inputs.

In this chapter we make a number of assumptions about the structure of the UCP. In typical experiments, the UCP is formed by laser ionizing a cloud of neutral atoms [14]. We assume the atoms have a radially symmetric Gaussian spatial density distribution, $n(r) \propto \exp(-r^2/2\sigma^2)$ where r is the radial distance from the origin and σ is the typical spatial extent parameter, and after ionization the ions retain the same structure. We note that this assumed spatial charge distribution is appropriate for conditions without significant (i.e. $<10\%$) conversion of ions back to atoms via three-body recombination. The specified ion charge distribution is flexible, however, and so in the presence of higher rates of three-body recombination the ion distribution can be modeled appropriately. The frequency of the photoionizing laser can be tuned above the ionization threshold and therefore provides control over the initial kinetic energy of the electrons. The resulting cloud of ions and electrons is initially neutral and allows a fraction of electrons to escape; we assume this escape fraction can be controlled experimentally, e.g. through the use of an applied electric field. The electrons that remain inside the plasma will then experience space charge confinement due to the resulting charge imbalance. At this point the confined electrons will exert a thermal pressure on the ions and drive expansion of the ion cloud [16]. While this expansion is not included in the model detailed in this chapter, it could be included by extension. For practical purposes, UCP experiments focused on measuring the electron component use electric fields as a means of controlling and guiding electron escape [84, 149, 162]. Our model includes an applied DC electric field, and this is indeed one of the motivating factors for developing these models. It does not incorporate an applied magnetic field at this time, but could be modified to do so.

6.3 Basis function expansion

The crux of the method presented in this chapter is the approximation of the electron density, $n_{\mathrm{e}}(\mathbf{x})$, using an expansion of suitable basis functions. The model presented here incorporates a DC electric field along the z-axis which breaks the spherical symmetry but maintains axial symmetry. We therefore assume a separable, axially symmetric form for the electron density given by

$$n_{\rm e}(r,\theta,\phi) = N_{\rm e}\sum_{l,n} a_{l,n} R_{l,n}(r)\, Y_l^0(\theta,\phi) \tag{6.1}$$

where the angular part is specified by the spherical harmonics, $Y_l^m(\theta,\phi)$ with $m = 0$ due to symmetry, and the $a_{l,n}$'s are the expansion coefficients. The radial functions $R_{l,n}(r)$ are constructed from polynomials modified by a Gaussian:

$$R_{l,n}(r) = f_{l,n}(r)\exp\left(-\frac{r^2}{2\sigma^2}\right). \tag{6.2}$$

The $f_{l,n}(r)$ functions are dimensionless polynomials in powers of r/σ calculated using Gram-Schmidt orthogonalization, where σ is a parameter that characterizes the size of the plasma and is fixed in this treatment. These polynomials are chosen so that the radial functions satisfy the orthogonality relation

$$\int_0^\infty R_{l,n}(r)\, R_{l,n'}(r)\, r^2\, {\rm d}r = \sigma^3 q_{l,n}\delta_{nn'}. \tag{6.3}$$

The $q_{l,n}$ factor on the right hand side is a numerical constant determined by enforcing two different normalization conditions. For $l \neq 0$ the constant is equal to 1, but for all $l = 0$ terms—which we recognize as the monopole part of the distribution—it is a numerical factor that results from each individual function being normalized over all space to unity. In order to avoid singularities at the origin when calculating the electric potential from these functions we construct a different basis set for each l that begins with the term $(r/\sigma)^l$, as is typical. For example, the $l = 0$ set comes from orthogonalizing the terms $\{1, \frac{r}{\sigma}, \left(\frac{r}{\sigma}\right)^2, ...\}$ whereas the $l = 1$ set is derived from $\{\frac{r}{\sigma}, \left(\frac{r}{\sigma}\right)^2, \left(\frac{r}{\sigma}\right)^3, ...\}$.

We can now use (6.3) to project the electron density, (6.1), onto each basis function and retrieve the corresponding $a_{l,n}$ coefficient:

$$a_{l,n} = \frac{1}{N_{\rm e}\,\sigma^3\, q_{l,n}} \int {\rm d}\Omega \int_0^\infty r^2\, {\rm d}r\, n_{\rm e}(r,\theta,\phi)\, R_{l,n}(r)\, Y_l^0(\theta,\phi). \tag{6.4}$$

Once each of these coefficients is known it is possible to construct the approximated, smoothed electron density function.

If we wish to keep the number of basis functions required to accurately approximate the electron distribution reasonably low then we must address the issue of projecting smooth functions on a finite spatial size distribution. The finite nature of the distribution will lead to a boundary at which the electron density will become exactly zero outside, and without enough basis functions the smoothed distribution will have difficulties accurately representing this boundary. In most cases we found that the basis functions produced a distribution that would go negative or have a local minimum at this boundary. We observed that the unphysical non-zero portions of the distribution outside of the boundary could generate anomalous electric fields inside of the plasma large enough to affect the electrons' dynamics.

Our solution to this issue is to approximate the boundary as a sphere around the electron center of mass and redefine the basis functions to be piecewise with a cut-off radius beyond which they are exactly zero. This cut-off radius is found by searching the projected distribution for the zeros and local minima mentioned above. It is these cut-off, piecewise basis functions that are used to calculate the electric field and potential for the electron component of the plasma. Fortunately, this piecewise cut-off did not prevent us from analytically determining the functions for the electric potential and fields.

Using cut-off distributions to calculate the electric fields implies that electrons that cross the boundary and escape the plasma do not have an effect on the remaining electrons. This is a limitation of this model, but we don't expect it to play a significant role for the conditions that we treat in this chapter which correspond to realistic UCP experimental parameters well after formation. The plasmas we studied here have a small escape fraction. Furthermore the applied DC electric field quickly carries the escaped electrons away, and they therefore have a negligible impact on the UCP.

The electric potential $\Phi_{\mathrm{e}}(\mathbf{x})$ generated from each basis function can be calculated by inserting the series approximation (6.1)—with $R_{l,n}(r)$ now being the piecewise cut-off functions—into the

integral form of Poisson's equation with $\rho_{\mathrm{e}}(\mathbf{x}) = -e\, n_{\mathrm{e}}(\mathbf{x})$, where e is the elementary charge. We can take advantage of the fact that the angular part of ρ_{e} can be expressed in spherical harmonics by replacing the Green's function $1/|\mathbf{x} - \mathbf{x}'|$ in Poisson's equation with its Laplace expansion [163]. This allows the angular part of the integral to be computed using the orthogonality condition for $Y_l^m(\theta, \phi)$. The potential can now be expressed as the following series of radial integrals:

$$\Phi_{\mathrm{e}}(\mathbf{x}) = -\frac{eN_{\mathrm{e}}}{\epsilon_0} \sum_{n=0}^{\infty} \sum_{l=0}^{\infty} \frac{a_{l,n}}{2l+1} \left[r^{-(l+1)} A_{l,n}(r) + r^l B_{l,n}(r) \right] Y_l^0(\theta, \phi) \tag{6.5}$$

where

$$A_{l,n}(r) = \int_0^r R_{l,n}(r')\, r'^{l+2}\, \mathrm{d}r' \quad \text{and} \quad B_{l,n}(r) = \int_r^{\infty} R_{l,n}(r')\, r'^{1-l}\, \mathrm{d}r',$$

and ϵ_0 is the vacuum permittivity. Since each $R_{l,n}(r')$ is simply a series of polynomial-Gaussian products inside the cut-off and constant zero outside we can analytically compute every above term. The resulting expressions for the $A_{l,n}$ and $B_{l,n}$ terms consist of sums of error functions and polynomial-Gaussian products.

The objective of this method is to have the ability to calculate the trajectories of electrons in the plasma using a mean-field approximation. The electrons' contribution to the net electric field $\mathbf{E}_{\mathrm{net}}$ can be calculated from (6.5) using $\mathbf{E} = -\vec{\nabla}\Phi$:

$$\begin{aligned}
\mathbf{E}_{\mathrm{e}} \cdot \hat{r} &= \frac{eN_{\mathrm{e}}}{\epsilon_0} \sum_{n=0}^{\infty} \sum_{l=0}^{\infty} \frac{a_{l,n}}{2l+1} \left[\frac{-(l+1)}{r^{l+2}} A_{l,n}(r) + l\, r^{l-1} B_{l,n}(r) \right] Y_l^0(\theta, \phi) \\
\mathbf{E}_{\mathrm{e}} \cdot \hat{\theta} &= \frac{eN_{\mathrm{e}}}{\epsilon_0} \sum_{n=0}^{\infty} \sum_{l=0}^{\infty} \frac{a_{l,n}}{2l+1} \left[r^{-(l+2)} A_{l,n}(r) + r^{l-1} B_{l,n}(r) \right] \left[\sqrt{l(l+1)}\, \mathrm{e}^{-\mathrm{i}\phi}\, Y_l^1(\theta, \phi) \right]
\end{aligned} \tag{6.6}$$

An identical treatment can be performed for the ion density $n_{\mathrm{i}}(\mathbf{x})$. The ions are not expected to evolve as rapidly as the electrons since they are much more massive. In this chapter, we focus on short timescale electron motion such that the ion component of the UCP does not change significantly and could thus be treated as constant. Our method of the mean-field treatment of the electrons could be extended to the ions to capture their dynamics, if desired. We make the approximation that shortly after ionization the ions remain as a spherically symmetric Gaussian

distribution fixed at the origin,

$$n_{\mathrm{i}}(r) = \frac{N_{\mathrm{i}}}{(2\pi\sigma^2)^{3/2}} \exp\left(-\frac{r^2}{2\sigma^2}\right),$$

with the corresponding electric potential and field

$$\begin{aligned} \Phi_{\mathrm{i}}(r) &= \frac{e}{4\pi\epsilon_0}\frac{N_{\mathrm{i}}}{r}\operatorname{erf}\left(\frac{r}{\sqrt{2}\sigma}\right) \\ \mathbf{E}_{\mathrm{i}}(r) &= \frac{e}{4\pi\epsilon_0}\frac{N_{\mathrm{i}}}{r^2}\left[\operatorname{erf}\left(\frac{r}{\sqrt{2}\sigma}\right) - \sqrt{\frac{2}{\pi}}\frac{r}{\sigma}\exp\left(-\frac{r^2}{2\sigma^2}\right)\right]\hat{r}. \end{aligned} \tag{6.7}$$

With the total mean electric field we calculated trajectories of individual electrons within the plasma using Newtonian mechanics. Starting from some spatial distribution of discrete electrons we projected that distribution onto each density basis function to determine the $a_{l,n}$ coefficients. Once the coefficients were found they could be used to determine the mean electric field from the electron component of the plasma by utilizing (6.6). Combining the field from the electrons with the ion component's field in (6.7) and the applied DC field let us compute the force on each electron, $\mathbf{F} = -e\left(\mathbf{E}_{\mathrm{e}} + \mathbf{E}_{\mathrm{i}} + \mathbf{E}_{\mathrm{DC}}\right)$. Calculating individual electron trajectories from these forces allows the system to evolve self-consistently.

Since the discrete electrons are free to move independently under the influence of the calculable mean-field forces we do not need to make any assumptions about the velocity distribution of the particles. Additionally, if a mechanism is present that can mediate exchanges of energy and momentum between the particles then the distribution will approach thermal equilibrium. To create thermal equilibrium distributions easily and efficiently, a non-physical collision operator that randomizes the velocities of nearest-neighbour pairs of electrons is included in our model. These random collisions guarantee that microstates of the system will be effectively sampled and approach an equilibrium distribution. The same thermal equilibrium state will be achieved regardless of the details of the collision operator as long as certain usual assumptions (e.g. detailed balance) are observed [164]. Thus a thermal distribution for the electron component under the influence of a DC electric field can ultimately be found.

6.4 Simulation details

One of the advantages of this mean field approximation is that we are not required to account for every individual particle in the plasma. Instead it is possible to find the basis expansion coefficients and evaluate certain macroscopic parameters using only a statistical sampling of electrons. We do *not* scale the charge nor mass of these sample electrons as they are not single particle representations of multi-electron bunches. When the forces from the mean-field approximation act on the sample electrons they are treated as having the standard electron charge and mass. What is being scaled here instead is a statistical weighting parameter that accounts for the fact that we're describing the distribution of the total N_e electrons using a fewer number of sample particles. We choose some sample electron number, $S_\mathrm{e} < N_\mathrm{e}$, and use their positions as a representation of the entire electron density,

$$n_\mathrm{e}(\mathbf{x}) \approx \frac{N_\mathrm{e}}{S_\mathrm{e}} \sum_{i=1}^{S_\mathrm{e}} \delta(\mathbf{x} - \mathbf{x}_i). \tag{6.8}$$

Inserting (6.8) into (6.4) gives us an expression for determining the expansion coefficients from our representative sample,

$$a_{l,n} = \frac{1}{S_\mathrm{e}\, \sigma^3\, q_{l,n}} \sum_{i=1}^{S_\mathrm{e}} R_{l,n}(r_i)\, Y_l^0(\theta_i, \phi_i). \tag{6.9}$$

Using these coefficients and our expansion for the mean electric field we found the trajectories of our sample electrons by numerically integrating the second order ODE $\ddot{\mathbf{x}} = -e\,\mathbf{E}(\mathbf{x})/m_\mathrm{e}$ where m_e is the electron mass. We would typically calculate trajectories over durations on the order of 300 ω^{-1} and recalculate the coefficients every 0.3 ω^{-1} or so, where $\omega^{-1} = \left(n_\mathrm{i,peak} e^2/m_\mathrm{e}\epsilon_0\right)^{-1/2}$ is the natural timescale for our system and $n_\mathrm{i,peak} = N_\mathrm{i}/\left(2\pi\sigma^2\right)^{3/2}$. As the electrons move the spatial distribution changes and thus the $a_{l,n}$ coefficients change as well. In our implementation of the calculations we use a predictor-corrector method with self-consistency checks so that the coefficients may evolve continuously throughout the integration of the trajectories.

The sample electrons are initialized to a Maxwell-Boltzmann velocity distribution and a truncated Gaussian spatial distribution to match electron and ion densities out to a radius determined

by the selected electron-to-ion number ratio. The spatial distribution approximates an equilibrium thermal distribution but is not identical to one and so after initialization the plasma electrons' spatial distribution evolves and in turn this impacts the velocity distribution. Most often, a thermal equilibrium distribution is desired for the simulation.

In order to produce such a thermal distribution, as the plasma evolves pseudo-collisions are used to bring the electrons to thermal equilibrium. A togglable elastic collision operator acts on the electron cloud between integration time steps in such a way that velocities of pairs of electrons are randomized while preserving the kinetic energy and center of mass momentum. At selected time intervals, the ODE integration is halted and a number of random electrons are chosen. A scan is done to find their nearest neighbors in order to ensure that the difference in potential energy of each selected electron and its pair is small compared to their kinetic energy. Transforming to the center of mass frame of the electron pair allows us to rotate their relative velocity vector to a random direction while preserving its magnitude. This allows the electrons to change velocity while conserving the total momenta and energy of the pair. Iterating this collision process over many time steps is what ultimately determines our electron equilibrium distribution for our assumed parameters (temperature, charge imbalance, etc.) before we begin calculating the macroscopic parameters of interest.

With the sample electron trajectories and expansion coefficients at our disposal we are able to calculate a number of macroscopic parameters that describe the electron cloud and the plasma as a whole. The positions of the electrons can be used to track the center of mass motion of the electron component as well as its rms size. Using the velocities we are able to characterize the total kinetic energy of the electrons, K_{total} , and determine an approximate temperature from $K_{total} \approx \frac{3}{2} N_{\mathrm{e}}\, k_B\, T$, where k_B is the Boltzmann constant. As mentioned, one plasma parameter that we are interested in extracting is the total potential depth of the plasma. Using the notation in figure 6.1, we define the potential depth in "temperature" units $\Delta U = e\left[\Phi\left(z_1\right) - \Phi\left(z_0\right)\right]/k_B$. From (6.5) and (6.7) it is possible to determine the net electric potential once the $a_{l,n}$ coefficients

are known. Using these tools we can determine the plasma potential depth along the symmetry axis in the presence of an external electric field by locating and evaluating the net potential's extrema.

6.5 Simulation results for typical UCP parameters

6.5.1 Convergence and equilibrium characteristics

Our first objective after developing the model was to verify self-consistency between the smoothed basis functions and discrete sample electrons. Figure 6.2 illustrates the good agreement that we found between the spatial distribution calculated from the basis expansion and the distribution of individual sample electrons. The data presented in figure 6.2 is taken from a typical simulation and represents a thermal distribution for the electron component in the presence of an applied DC electric field. For each simulation we are able to tune a number of parameters including the sample electron number S_{e}, the applied DC field strength E_{DC}, the electron temperature T, the charge imbalance $\delta = (N_{\mathrm{i}} - N_{\mathrm{e}})/N_{\mathrm{i}}$, and the plasma size scale factor σ. For all of the data presented in this chapter we chose σ = 800 μm and N_{i} = 200,000 in correspondence with measurements made for UCPs formed in a typical experiment in our apparatus.

We monitored energy conservation as a check on the validity of the model. For our conditions energy conservation held at a fraction of a percent variation over the time of the simulation with no detectable average variation. To evaluate any quantity of interest, multiple simulations were performed to average over variations intrinsic to the Monte Carlo method. Typically, percent-level convergence was obtained with twelve runs.

Next we investigated how many terms we needed to calculate in our basis expansion in order for the distribution to converge. This was accomplished by examining macroscopic parameters, in particular the potential depth, extracted from the simulations as a function of the number of terms used. We looked at this by varying the maximum l terms calculated as well as the maximum number of n terms calculated for each l in the expansion. Figure 6.3 shows the convergence of the potential depth in temperature units, ΔU, as we increase the number of n terms for each l in simulations that utilized $l = \{0, 1\}$ (max l = 1) or $l = \{0, 1, 2\}$ (max l = 2). We see that by max n

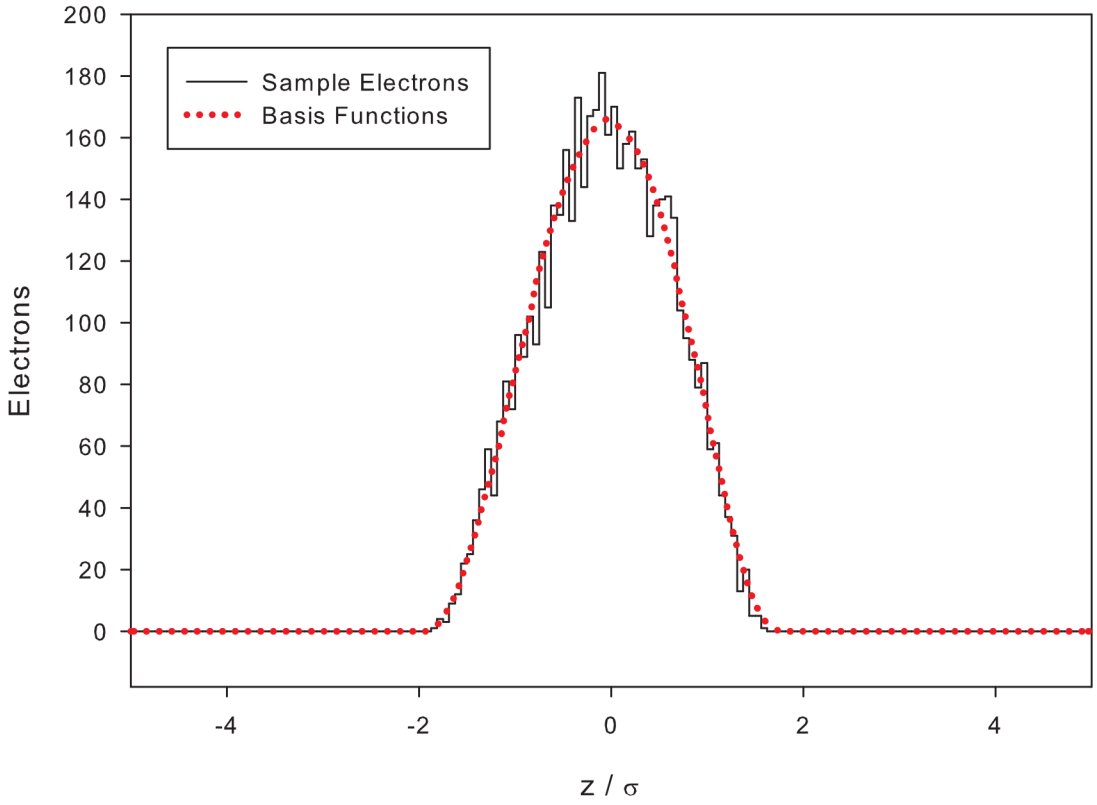

Figure 6.2: A typical distribution of the electrons' z coordinates showing good agreement between the discrete electrons and the basis function approximation. The solid black line is a histogram of the individual sample electrons; the dotted red line is the result calculated from the basis functions. This was taken from data with S_e = 5,000; T = 5 K; E_{DC} = 3 V/m; δ = 0.45.

= 6 for max l = 1 the potential depth appears to have converged to within a few percent of the final value. Including $l = 2$ terms in our model adds only small corrections to the data which indicates that higher order terms are not required to get an accurate description. The data was taken by time averaging the potential depth after equilibrium had been established for 12 different simulations each using S_e = 5,000; T = 20 K; E_{DC} = 3 V/m; δ = 0.45. The sample electron number of 5,000 was chosen as it produced consistent results between runs while maintaining acceptable simulation runtimes; the twelve trials were used to reduce the ~5% statistical uncertainty due to fluctuations in a single trial. Figure 6.4 shows data taken using the same method and parameters except at T = 5 K. We see that even at a lower temperature the depth converges with about as many basis functions,

and higher l corrections are small as before. On figure 6.4, this is shown with the max $n = 9$, max $l = 2$ point. With the self-consistency and convergence established we were able to extract plasma characteristics such as the potential depth and examine how they scale with various parameters.

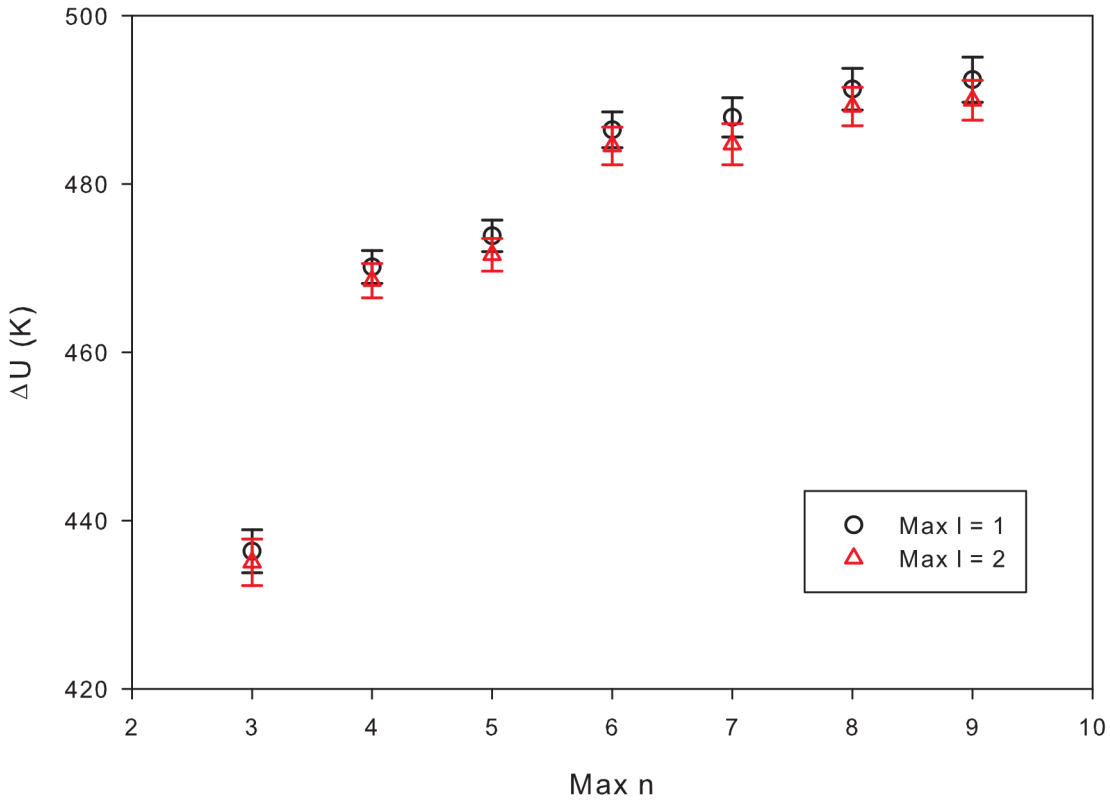

Figure 6.3: Demonstration of convergence of the potential depth in temperature units, ΔU, as we increase the number of n terms for each l calculated during a simulation. The black circles are from simulations that utilized $l = \{0, 1\}$ (max l = 1); the red triangles are from $l = \{0, 1, 2\}$ (max l = 2) simulations. This data was taken from simulations at T = 20 K, E_{DC} = 3 V/m, $\delta = 0.45$.

Typically UCP experiments focused on measuring the electron component utilize electric fields for guiding electrons toward a detector or to tip the confining potential for electron extraction. The strength of the field can be tuned to reduce the depth of the confining potential which in turn can provide information about the electron temperature by detecting the fraction spilled [84, 149, 162]. Additionally, there is work currently being done examining the possibility of applying forced evaporation in order to cool the electrons [91]. Quantifying the dependence of the depth on the

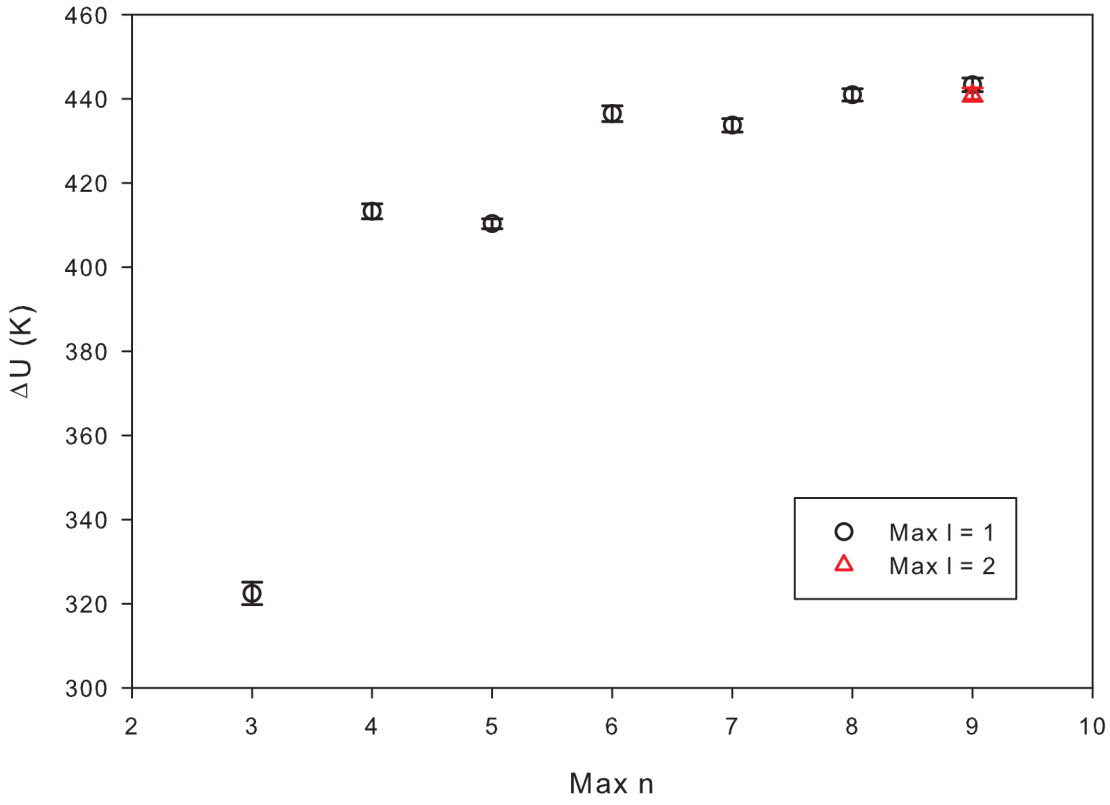

Figure 6.4: The same as figure 6.3 except for T = 5 K.

field strength is important for calibrating these effects precisely. Figure 6.5 shows our model's prediction for the dependence of the potential depth on the strength of an applied DC electric field with conditions T = 20 K and δ = 0.45.

6.5.2 Electron dynamics after an applied impulse

In addition to static properties, this model can be used to study some nonequilibrium electron dynamics. Loosely following the experimental design used in reference [102], we applied an instantaneous impulse to the electrons in the z direction by an amount equal to half of the thermal velocity ($\sqrt{k_B T/m_e}$). Before the impulse the electrons are initialized to equilibrium using the electron-electron collisions discussed in Section 4. Once equilibrium is established and the impulse is applied the collisions are toggled off, and the electrons undergo oscillations within the confining

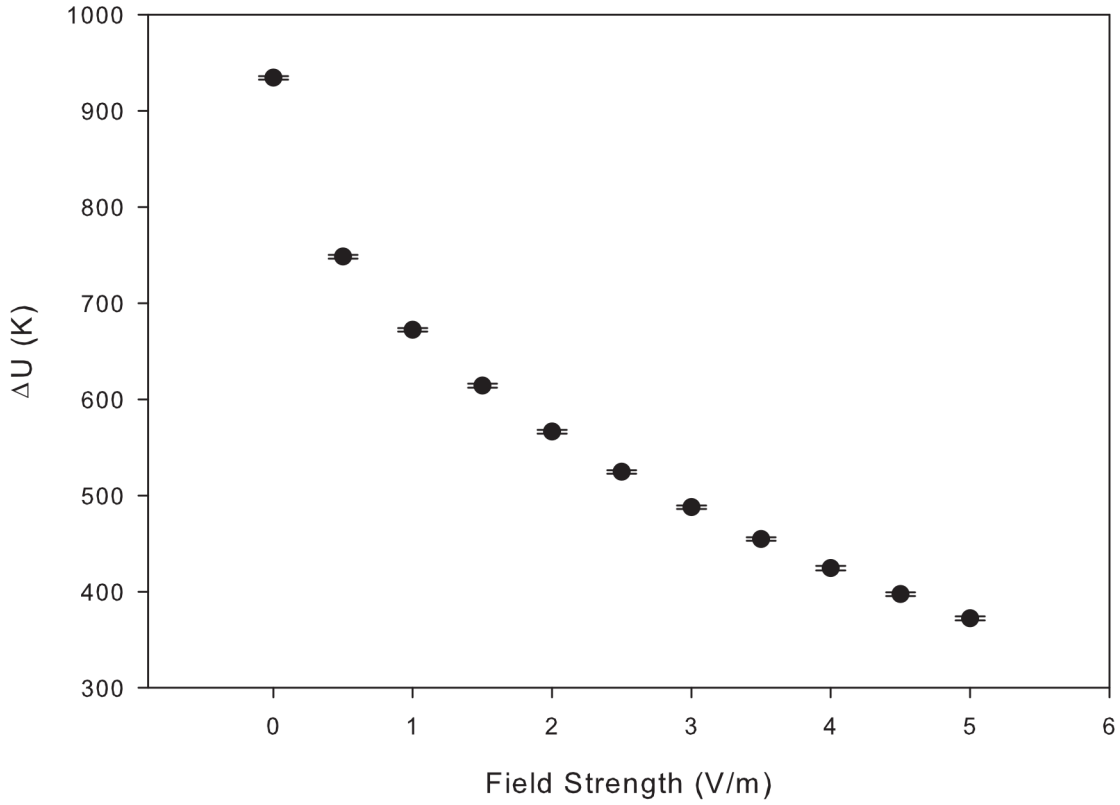

Figure 6.5: Plasma potential depth in temperature units as a function of applied DC electric field strength. Taken with parameters T = 20 K, δ = 0.45.

potential. The center of mass motion of the electrons was fit to a sinusoidal function modified by a decaying exponential as shown in figure 6.6. From the fit parameters we were able to extract the oscillation frequency of the center of mass. This was modeled for a range of charge imbalances at T = 20 K and E_{DC} = 0 V/m, the results for which are presented in figure 6.7. We found that the frequency scales fairly linearly in the δ range explored roughly agreeing with the results presented in reference [102]. There are differences in the calculated oscillation frequency due to the fact that the simplified model of the earlier reference is not strictly correct, and an improved determination of density from our technique is obtained.

As shown in figure 6.6, our model predicted center of mass damping that fits well with an exponential decay even in the absence of collisions. From the fit we were able to extract the decay time. This non-collisional damping is also observed experimentally. The damping occurs

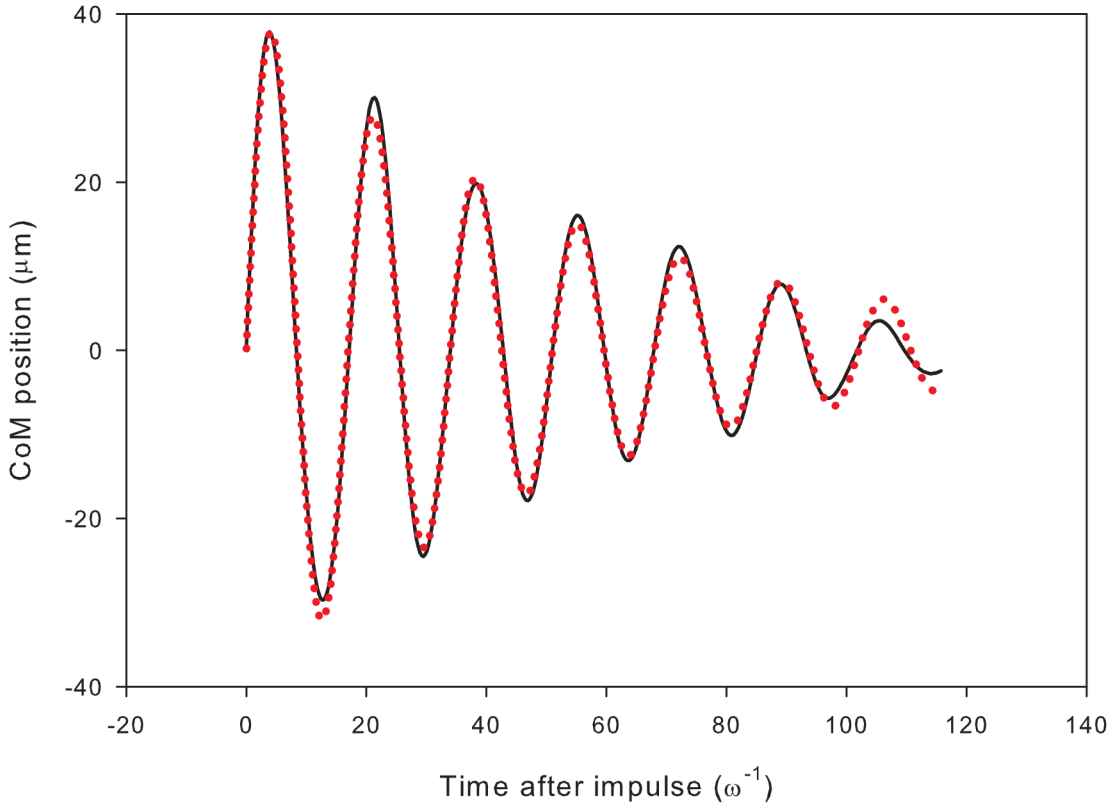

Figure 6.6: A typical center of mass trajectory showing electron oscillations and damping after receiving an instantaneous impulse at t = 0. The solid black line is the result from our model; the dotted red line is a fit. Taken with parameters T = 5 K, E_{DC} = 0 V/m, δ = 0.45.

in this case due to the non-uniformity of the density distribution of the ions. This non-uniformity creates anharmonicity in the potential and therefore causes the individual electrons' oscillations to dephase.

6.6 Plasma number scaling

An attractive possibility for modeling UCPs is to run a simulation with a smaller number of electrons than an experimental situation and then scale physical parameters such as charge, spatial extent, mass, etc. in order to maintain the appropriate ratios of e.g. collision rate to plasma oscillation frequency or screening length to plasma spatial extent. In this section, we show that such a scaling cannot be done in a way that preserves relevant UCP physical parameter ratios.

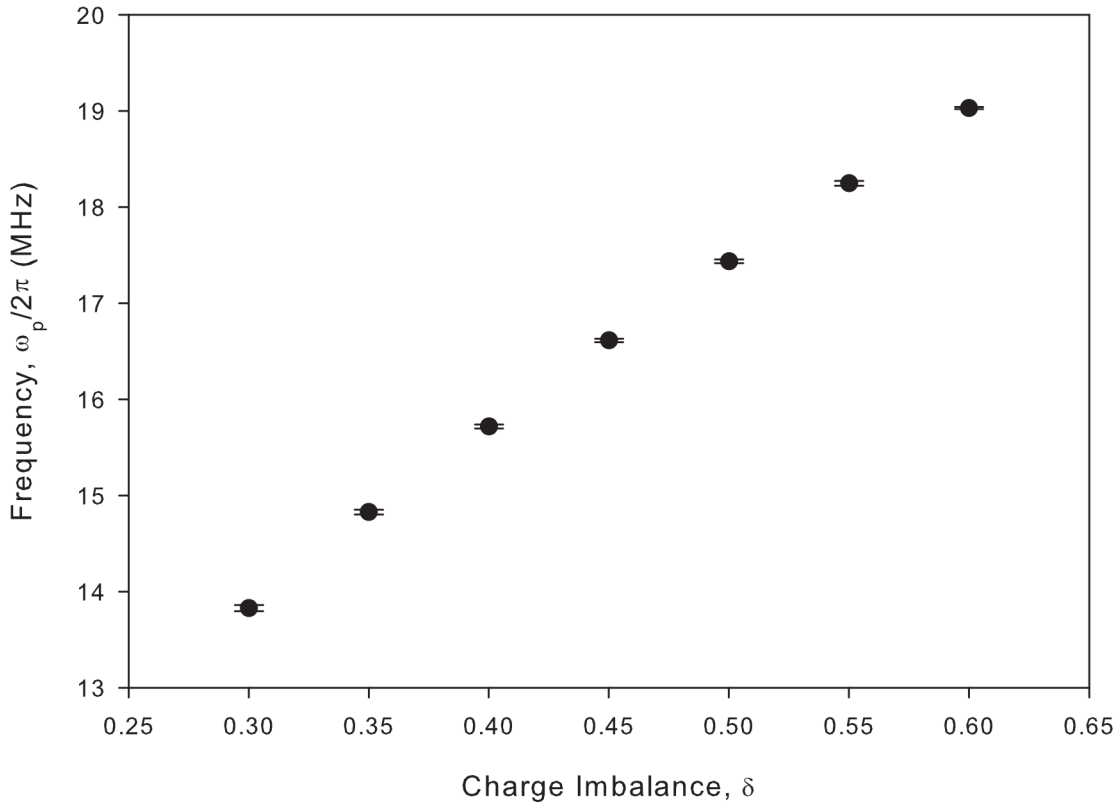

Figure 6.7: Electron oscillation frequency calculated from fitting the center of mass motion as a function of charge imbalance. Taken with parameters T = 20 K, E_{DC} = 0 V/m, δ = 0.45.

For instance, one of the defining characteristics of a plasma is its strong coupling parameter $\Gamma = e^2/4\pi\epsilon_0 a k_B T_{\mathrm{e}}$, where $a = (3/4\pi n)^{1/3}$ and n is the density. In this section we assume a Gaussian ion density distribution with spatial size parameter σ thus $n \sim N/\sigma^3$. Other defining plasma characteristics are, for example, the two-body collision rate ν_{ee}, the three-body collision rate K, the screening-to-size ratio $\kappa = \lambda_D/\sigma$, and the UCP expansion timescale t_{exp}. We can define the above characteristic parameters using the classical plasma definitions and demonstrate inconsistent scaling by writing them in terms of the following plasma parameters: N, Γ, the ion mass m_{i}, and the plasma frequency ω_p.

Now consider a plasma where Γ is fixed. From table 6.1 we see that this will preserve the ratios $\nu_{\mathrm{ee}}/\omega_p$ and K/ω_p. Since t_{exp} depends on m_{i} the quantity $t_{\mathrm{exp}}\omega_p$ can be held constant regardless by adjusting the ion mass. Nevertheless, κ depends explicitly on N so a reduction in particle number

Table 6.1: Table showing the scaling of the two-body collision rate $\nu_{\rm ee}$, three-body collision rate K, screening-to-size parameter κ, and expansion timescale $t_{\rm exp}$.

Parameter	Scaling	
$\nu_{\rm ee}$	$\omega_p \Gamma^{3/2} \ln\left(\alpha \Gamma^{-1}\right)$	[26]
K	$\omega_p \Gamma^{9/2}$	[96]
κ	$N^{-1/3} \Gamma^{-1/2}$	[26]
$t_{\rm exp}$	$\sqrt{m_{\rm i}}/\omega_p \kappa$	[16]

means that κ cannot stay constant. Thus it is impossible to preserve κ and Γ simultaneously. Furthermore, if κ was fixed while scaling the particle number then Γ must be adjusted thereby disrupting the scaling of the above collision rate to plasma frequency ratios. Therefore there is no way to create a scaling that keeps κ, Γ, $\nu_{\rm ee}/\omega_p$, and K/ω_p all fixed.

6.7 Chapter summary

To summarize, we have developed a scalable method for numerically modeling the electron component of UCPs using a mean-field approximation constructed by projecting a basis function expansion on discrete sample electrons. Our model includes features such as spherical symmetry-breaking DC electric fields and electron-electron thermalizing collisions. Using these tools we have developed a means for determining key UCP characteristics such as the potential depth. This allows us to quantify the effects of an applied electric field on the electrons' confining potential which in turn is useful when studying electron extraction and evaporation from the plasma. We also explored an extension of this model in order to study center of mass dynamics of the electrons after receiving an impulse. This technique allowed us a better determination of UCP density. Future work will include expanding this model to simulate and predict electron escape rates to be compared to experiment and adding the effects of an externally applied magnetic field.

We acknowledge funding support for this work from the Air Force Office of Scientific Research, grant number FA9550-12-1-0222.

Bibliography

[1] R. C. Mancini, J. E. Bailey, J. F. Hawley, T. Kallman, M. Witthoeft, S. J. Rose, and H. Takabe. Accretion disk dynamics, photoionized plasmas, and stellar opacities. *Physics of Plasmas*, 16(4):041001, 2009.

[2] J. E. Bailey, G. A. Rochau, R. C. Mancini, C. A. Iglesias, J. J. MacFarlane, I. E. Golovkin, C. Blancard, Ph. Cosse, and G. Faussurier. Experimental investigation of opacity models for stellar interior, inertial fusion, and high energy density plasmas. *Physics of Plasmas*, 16(5):058101, 2009.

[3] Daniel Verscharen, Kristopher G. Klein, and Bennett A. Maruca. The multi-scale nature of the solar wind. *Living Reviews in Solar Physics*, 16(1):5, Dec 2019.

[4] A. B. Zylstra, A. L. Kritcher, O. A. Hurricane, D. A. Callahan, K. Baker, T. Braun, D. T. Casey, D. Clark, K. Clark, T. Döppner, L. Divol, D. E. Hinkel, M. Hohenberger, C. Kong, O. L. Landen, A. Nikroo, A. Pak, P. Patel, J. E. Ralph, N. Rice, R. Tommasini, M. Schoff, M. Stadermann, D. Strozzi, C. Weber, C. Young, C. Wild, R. P. J. Town, and M. J. Edwards. Record energetics for an inertial fusion implosion at nif. *Phys. Rev. Lett.*, 126:025001, Jan 2021.

[5] B. Bigot. Progress toward ITER's first plasma. *Nuclear Fusion*, 59(11):112001, jun 2019.

[6] M. E. Cuneo, M. C. Herrmann, D. B. Sinars, S. A. Slutz, W. A. Stygar, R. A. Vesey, A. B. Sefkow, G. A. Rochau, G. A. Chandler, J. E. Bailey, J. L. Porter, R. D. McBride, D. C. Rovang, M. G. Mazarakis, E. P. Yu, D. C. Lamppa, K. J. Peterson, C. Nakhleh, S. B. Hansen, A. J. Lopez, M. E. Savage, C. A. Jennings, M. R. Martin, R. W. Lemke, B. W. Atherton, I. C. Smith, P. K. Rambo, M. Jones, M. R. Lopez, P. J. Christenson, M. A. Sweeney, B. Jones, L. A. McPherson, E. Harding, M. R. Gomez, P. F. Knapp, T. J. Awe, R. J. Leeper, C. L. Ruiz, G. W. Cooper, K. D. Hahn, J. McKenney, A. C. Owen, G. R. McKee, G. T. Leifeste, D. J. Ampleford, E. M. Waisman, A. Harvey-Thompson, R. J. Kaye, M. H. Hess, S. E. Rosenthal,

and M. K. Matzen. Magnetically driven implosions for inertial confinement fusion at sandia national laboratories. *IEEE Transactions on Plasma Science*, 40(12):3222–3245, 2012.

[7] Scott D. Bergeson, Scott D. Baalrud, C. Leland Ellison, Edward Grant, Frank R. Graziani, Thomas C. Killian, Michael S. Murillo, Jacob L. Roberts, and Liam G. Stanton. Exploring the crossover between high-energy-density plasma and ultracold neutral plasma physics. *Physics of Plasmas*, 26(10):100501, 2019.

[8] V. Malka. Laser plasma accelerators. *Physics of Plasmas*, 19(5):055501, 2012.

[9] John H. Booske. Plasma physics and related challenges of millimeter-wave-to-terahertz and high power microwave generation. *Physics of Plasmas*, 15(5):055502, 2008.

[10] Chris G N Lee, Keren J Kanarik, and Richard A Gottscho. The grand challenges of plasma etching: a manufacturing perspective. *Journal of Physics D: Applied Physics*, 47(27):273001, jun 2014.

[11] John E. Foster. Plasma-based water purification: Challenges and prospects for the future. *Physics of Plasmas*, 24(5):055501, 2017.

[12] Mounir Laroussi. Cold plasma in medicine and healthcare: The new frontier in low temperature plasma applications. *Frontiers in Physics*, 8:74, 2020.

[13] Thomas C. Killian. Ultracold neutral plasmas. *Science*, 316(5825):705–708, 2007.

[14] T. C. Killian, S. Kulin, S. D. Bergeson, L. A. Orozco, C. Orzel, and S. L. Rolston. Creation of an ultracold neutral plasma. *Phys. Rev. Lett.*, 83:4776–4779, Dec 1999.

[15] Truman Wilson. *Dynamics of low-density ultracold plasmas in externally applied electric and magnetic fields*. PhD dissertation, Colorado State University, 2013.

[16] S. Kulin, T. C. Killian, S. D. Bergeson, and S. L. Rolston. Plasma oscillations and expansion of an ultracold neutral plasma. *Phys. Rev. Lett.*, 85:318–321, Jul 2000.

[17] Wei-Ting Chen. *Measurements of electron-ion collision rates and Rydberg atom populations in ultracold plasmas by using short electric field pulses*. PhD dissertation, Colorado State University, 2017.

[18] Thomas K. Langin, Grant M. Gorman, and Thomas C. Killian. Laser cooling of ions in a neutral plasma. *Science*, 363(6422):61–64, 2019.

[19] Wei-Ting Chen, Craig Witte, and Jacob L. Roberts. Observation of a strong-coupling effect on electron-ion collisions in ultracold plasmas. *Phys. Rev. E*, 96:013203, Jul 2017.

[20] X. L. Zhang, R. S. Fletcher, S. L. Rolston, P. N. Guzdar, and M. Swisdak. Ultracold plasma expansion in a magnetic field. *Phys. Rev. Lett.*, 100:235002, Jun 2008.

[21] ITER Physics Basis Editors, ITER Physics Expert Group Chairs an Co-Chairs, ITER Joint Central Team, and Physics Unit. Chapter 1: Overview and summary. *Nuclear Fusion*, 39(12):2137–2174, dec 1999.

[22] R Aymar, P Barabaschi, and Y Shimomura. The ITER design. *Plasma Physics and Controlled Fusion*, 44(5):519–565, apr 2002.

[23] Ross E. Falcon, G. A. Rochau, J. E. Bailey, T. A. Gomez, M. H. Montgomery, D. E. Winget, and T. Nagayama. LABORATORY MEASUREMENTS OF WHITE DWARF PHOTOSPHERIC SPECTRAL LINES: Hβ. *The Astrophysical Journal*, 806(2):214, jun 2015.

[24] Lilia Ferrario, Domitilla de Martino, and Boris T. Gänsicke. Magnetic white dwarfs. *Space Science Reviews*, 191(1):111–169, Oct 2015.

[25] Vyacheslav E Zavlin and GG Pavlov. Modeling neutron star atmospheres. *Arxiv preprint astro-ph/0206025*, 2002.

[26] Lyman Spitzer, Jr. *Physics of Fully Ionized Gases*. John Wiley and Sons, Inc., New York, 2nd rev. edition, 1956.

[27] Scott D. Baalrud and Jérôme Daligault. Transport regimes spanning magnetization-coupling phase space. *Phys. Rev. E*, 96:043202, Oct 2017.

[28] A.I. Akhiezer, I.A. Akhiezer, R.V. Polovin, and D.T. Haar. *Plasma Electrodynamics: Linear Theory*. Elsevier Science, 1975.

[29] Scott D. Baalrud. Transport coefficients in strongly coupled plasmas. *Physics of Plasmas*, 19(3):030701, 2012.

[30] Daniel H. E. Dubin. Parallel velocity diffusion and slowing-down rate from long-range collisions in a magnetized plasma. *Physics of Plasmas*, 21(5):052108, 2014.

[31] Nathaniel R. Shaffer and Scott D. Baalrud. The barkas effect in plasma transport. *Physics of Plasmas*, 26(3):032110, 2019.

[32] Setsuo Ichimaru and Marshall N. Rosenbluth. Relaxation processes in plasmas with magnetic field. temperature relaxations. *The Physics of Fluids*, 13(11):2778–2789, 1970.

[33] M. Steck, G. Bisoffi, M. Blum, A. Friedrich, C. Geyer, M. Grieser, B. Holzer, E. Jaeschke, M. Jung, D. Krämer, K. Matl, W. Ott, and R. Repnow. Electron cooling of heavy ions. *Nucl. Instrum. Methods Phys. Res. A*, 287(1):324 – 327, 1990.

[34] M. Beutelspacher, H. Fadil, T. Furukawa, M. Grieser, A. Noda, K. Noda, D. Schwalm, T. Shirai, and A. Wolf. Electron cooling experiments at the heavy ion storage ring TSR. *Nucl. Instrum. Methods Phys. Res. A*, 532(1):123 – 128, 2004. International Workshop on Beam Cooling and Related Topics.

[35] Guy Dimonte and Jerome Daligault. Molecular-dynamics simulations of electron-ion temperature relaxation in a classical coulomb plasma. *Phys. Rev. Lett.*, 101:135001, Sep 2008.

[36] Hrachya B. Nersisyan, Claude Deutsch, and Amal K. Das. Number-conserving linear-response study of low-velocity ion stopping in a collisional magnetized classical plasma. *Phys. Rev. E*, 83:036403, Mar 2011.

[37] Wei-Ting Chen, Craig Witte, and Jacob L. Roberts. Damping of electron center-of-mass oscillation in ultracold plasmas. *Physics of Plasmas*, 23(5):052101, 2016.

[38] Puchang Jiang, John Guthrie, and Jacob L. Roberts. Many-body collision contributions to electron momentum damping rates in a plasma influenced by electron strong coupling. *Physics of Plasmas*, 27(1):012109, 2020.

[39] Naobumi Honda, Osamu Aono, and Taro Kihara. Fluctuations in a plasma iii: Effect of the magnetic field on the stopping power. *Journal of the Physical Society of Japan*, 18(2):256–260, 1963.

[40] Robert M. May and N. F. Cramer. Test ion energy loss in a plasma with a magnetic field. *The Physics of Fluids*, 13(7):1766–1770, 1970.

[41] Thomas Peter and Jürgen Meyer-ter Vehn. Energy loss of heavy ions in dense plasma. I. linear and nonlinear vlasov theory for the stopping power. *Phys. Rev. A*, 43:1998–2014, Feb 1991.

[42] Hrachya Nersisyan, Christian Toepffer, and Günter Zwicknagel. *Interactions between charged particles in a magnetic field: A theoretical approach to ion stopping in magnetized plasmas*. Springer-Verlag Berlin Heidelberg, Jan 2007.

[43] Hrachya B. Nersisyan and Claude Deutsch. Energy loss of ions by electric-field fluctuations in a magnetized plasma. *Phys. Rev. E*, 83:066409, Jun 2011.

[44] H.B. Nersisyan and C. Deutsch. Stopping of ions in a plasma irradiated by an intense laser field. *Laser and Particle Beams*, 29(4):389–397, 2011.

[45] Haikel Jelassi, Djamel Benredjem, Hrachya B Nersisyan, Günter Zwicknagel, and Claude Deutsch. *Stopping Power of Ions in a Magnetized Plasma: Binary Collision Formulatio*. IntechOpen, Feb 2019.

[46] Zhang-Hu Hu, Yuan-Hong Song, and You-Nian Wang. Dynamic polarization and energy dissipation for charged particles moving in magnetized two-component plasmas. *Phys. Rev. E*, 79:016405, Jan 2009.

[47] Zhang-Hu Hu, Yuan-Hong Song, and You-Nian Wang. Wake effect and stopping power for a charged ion moving in magnetized two-component plasmas: Two-dimensional particle-in-cell simulation. *Phys. Rev. E*, 82:026404, Aug 2010.

[48] Paul E. Grabowski, Michael P. Surh, David F. Richards, Frank R. Graziani, and Michael S. Murillo. Molecular dynamics simulations of classical stopping power. *Phys. Rev. Lett.*, 111:215002, Nov 2013.

[49] Trevor Lafleur and Scott D Baalrud. Transverse force induced by a magnetized wake. *Plasma Physics and Controlled Fusion*, 61(12):125004, oct 2019.

[50] Carl Oberman, Amiram Ron, and John Dawson. High-frequency conductivity of a fully ionized plasma. *The Physics of Fluids*, 5(12):1514–1522, 1962.

[51] Carl Oberman and Fred Shure. High-frequency plasma conductivity in a magnetic field. *The Physics of Fluids*, 6(6):834–838, 1963.

[52] Kyoko Matsuda. Classical anomalous absorption in strongly magnetized plasmas and effective shielding length. *Phys. Rev. Lett.*, 46:481–485, Feb 1981.

[53] A. Bruce Langdon. Nonlinear inverse bremsstrahlung and heated-electron distributions. *Phys. Rev. Lett.*, 44:575–579, Mar 1980.

[54] C. D. Decker, W. B. Mori, J. M. Dawson, and T. Katsouleas. Nonlinear collisional absorption in laser-driven plasmas. *Physics of Plasmas*, 1(12):4043–4049, 1994.

[55] J. M. Liu, J. S. De Groot, J. P. Matte, T. W. Johnston, and R. P. Drake. Measurements of inverse bremsstrahlung absorption and non-maxwellian electron velocity distributions. *Phys. Rev. Lett.*, 72:2717–2720, Apr 1994.

[56] Susanne Pfalzner and Paul Gibbon. Direct calculation of inverse-bremsstrahlung absorption in strongly coupled, nonlinearly driven laser plasmas. *Phys. Rev. E*, 57:4698–4705, Apr 1998.

[57] M. Kundu. Anomalous collisional absorption of laser pulses in underdense plasma at low temperature. *Phys. Rev. E*, 91:043102, Apr 2015.

[58] M. Sedaghat, M. Ettehadi-Abari, B. Shokri, and M. Ghorbanalilu. The effect of external magnetic field on the bremsstrahlung nonlinear absorption mechanism in the interaction of high intensity short laser pulse with collisional underdense plasma. *Physics of Plasmas*, 22(3):033114, 2015.

[59] Narges Firouzi Farrashbandi, Mohammad Eslami-Kalantari, and Abdelaziz Sid. Inverse bremsstrahlung absorption in magnetized plasmas. *EPL (Europhysics Letters)*, 130(2):25001, may 2020.

[60] P. B. Radha, R. Betti, Thomas Boehly, J. Delettrez, Dana Edgell, Valeri Goncharov, I.V. Igumenshchev, J.P. Knauer, J.A. Marozas, Frederic Marshall, Robert Mccrory, David Meyerhofer, Steve Regan, Thomas Sangster, Wolf Seka, S. Skupsky, A. Solodov, C. Stoeckl, W. Theobald, and Richard Petrasso. Inertial confinement fusion using the omega laser system. *Plasma Science, IEEE Transactions on*, 39:1007 – 1014, 05 2011.

[61] Y. Lu, P. Tzeferacos, E. Liang, R. K. Follett, L. Gao, A. Birkel, D. H. Froula, W. Fu, H. Ji, D. Lamb, C. K. Li, H. Sio, R. Petrasso, and M. S. Wei. Numerical simulation of magnetized jet creation using a hollow ring of laser beams. *Physics of Plasmas*, 26(2):022902, 2019.

[62] K D Hahn, G A Chandler, C L Ruiz, G W Cooper, M R Gomez, S Slutz, A B Sefkow, D B Sinars, S B Hansen, P F Knapp, P F Schmit, E Harding, C A Jennings, T J Awe, M Geissel, D C Rovang, J A Torres, J A Bur, M E Cuneo, V Yu Glebov, A J Harvey-Thompson, M C Herrman, M H Hess, O Johns, B Jones, D C Lamppa, J S Lash, M R Martin, R D McBride, K J Peterson, J L Porter, J Reneker, G K Robertson, G A Rochau, M E Savage, I C Smith, J D

Styron, and R A Vesey. Fusion-neutron measurements for magnetized liner inertial fusion experiments on the z accelerator. *Journal of Physics: Conference Series*, 717:012020, may 2016.

[63] Zsolt Lécz and Alexander Andreev. Laser-induced extreme magnetic field in nanorod targets. *New Journal of Physics*, 20(3):033010, mar 2018.

[64] Tulasi N. Parashar, William H. Matthaeus, Michael A. Shay, and Minping Wan. Transition from kinetic to MHD behavior in a collisionless plasma. *The Astrophysical Journal*, 811(2):112, Sep 2015.

[65] A Ishizawa, Y Kishimoto, and Y Nakamura. Multi-scale interactions between turbulence and magnetic islands and parity mixture—a review. *Plasma Physics and Controlled Fusion*, 61(5):054006, mar 2019.

[66] Michael E. Glinsky, Thomas M. O'Neil, Marshall N. Rosenbluth, Kenji Tsuruta, and Setsuo Ichimaru. Collisional equipartition rate for a magnetized pure electron plasma. *Physics of Fluids B: Plasma Physics*, 4(5):1156–1166, 1992.

[67] John Guthrie and Jacob Roberts. A scalable theoretical mean-field model for the electron component of an ultracold neutral plasma. *Journal of Physics B: Atomic, Molecular and Optical Physics*, 49(4):045701, jan 2016.

[68] S. Ichimaru. *Basic Principles of Plasma Physics: A Statistical Approach*. W. A. Benjamin, 1973.

[69] Daniel A. Steck. *Rubidium 85 D Line Data*. available online at `http://steck.us/alkalidata` (revision 2.2.1, 21 November 2019).

[70] Scott D. Baalrud and Jérôme Daligault. Effective potential theory for transport coefficients across coupling regimes. *Phys. Rev. Lett.*, 110:235001, Jun 2013.

[71] Sanat Kumar Tiwari and Scott D. Baalrud. Reduction of electron heating by magnetizing ultracold neutral plasma. *Physics of Plasmas*, 25(1):013511, 2018.

[72] Liam G. Stanton and Michael S. Murillo. Ionic transport in high-energy-density matter. *Phys. Rev. E*, 93:043203, Apr 2016.

[73] G. Bannasch and T. Pohl. Rydberg-atom formation in strongly correlated ultracold plasmas. *Phys. Rev. A*, 84:052710, Nov 2011.

[74] Michael Bonitz. *Quantum Kinetic Theory*. Springer eBook collection. Springer International Publishing, Cham, 2nd edition, 2016.

[75] George Schmidt, Erich E. Kunhardt, and Joseph L. Godino. Intermittent chaos in electron scattering. *Phys. Rev. E*, 62:7512–7515, Nov 2000.

[76] B. Hu, W. Horton, and T. Petrosky. Chaotic scattering and the magneto-coulomb map. *Phys. Rev. E*, 65:056212, May 2002.

[77] B. Hu, W. Horton, C. Chiu, and T. Petrosky. Coulomb scattering in a strong magnetic field. *Physics of Plasmas*, 9(4):1116–1124, 2002.

[78] J. B. Delos, S. K. Knudson, and D. W. Noid. Trajectories of an atomic electron in a magnetic field. *Phys. Rev. A*, 30:1208–1218, Sep 1984.

[79] Hiroshi Hasegawa, Marko Robnik, and Günter Wunner. Classical and Quantal Chaos in the Diamagnetic Kepler Problem. *Progress of Theoretical Physics Supplement*, 98:198–286, 05 1989.

[80] M. C. Gutzwiller. *Chaos in classical and quantum mechanics*. F. John, L. Kadanoff, J. E. Marsden, L. Sirovich, and S. Wiggins, eds. Springer-Verlag, New York, 1990.

[81] M. P. Robinson, B. Laburthe Tolra, Michael W. Noel, T. F. Gallagher, and P. Pillet. Spontaneous evolution of rydberg atoms into an ultracold plasma. *Phys. Rev. Lett.*, 85:4466–4469, Nov 2000.

[82] Truman M. Wilson, Wei-Ting Chen, and Jacob L. Roberts. Density-dependent response of an ultracold plasma to few-cycle radio-frequency pulses. *Phys. Rev. A*, 87:013410, Jan 2013.

[83] Tucker Sprenkle, Adam Dodson, Quinton McKnight, Ross Spencer, Scott Bergeson, Abdourahmane Diaw, and Michael S. Murillo. Ion friction at small values of the coulomb logarithm. *Phys. Rev. E*, 99:053206, May 2019.

[84] J.-H. Choi, B. Knuffman, X. H. Zhang, A. P. Povilus, and G. Raithel. Trapping and evolution dynamics of ultracold two-component plasmas. *Phys. Rev. Lett.*, 100:175002, Apr 2008.

[85] Tobias Kroker, Mario Großmann, Klaus Sengstock, Markus Drescher, Philipp Wessels-Staarmann, and Juliette Simonet. Ultrafast Electron Cooling in an Expanding Ultracold Plasma. *arXiv e-prints*, page arXiv:2005.14009, May 2020.

[86] J. P. Morrison, C. J. Rennick, J. S. Keller, and E. R. Grant. Evolution from a molecular rydberg gas to an ultracold plasma in a seeded supersonic expansion of NO. *Phys. Rev. Lett.*, 101:205005, Nov 2008.

[87] J Hung, H Sadeghi, M Schulz-Weiling, and E R Grant. Evolution from rydberg gas to ultracold plasma in a supersonic atomic beam of Xe. *Journal of Physics B: Atomic, Molecular and Optical Physics*, 47(15):155301, jul 2014.

[88] Ludwig C. Balling. Phase-shift calculation for low-energy electron-rb scattering. *Phys. Rev.*, 179:78–84, Mar 1969.

[89] Paul J. Visconti, James A. Slevin, and Kenneth Rubin. Absolute total cross sections for the scattering of low-energy electrons by rubidium, cesium, and potassium. *Phys. Rev. A*, 3:1310–1317, Apr 1971.

[90] C. E. Simien, Y. C. Chen, P. Gupta, S. Laha, Y. N. Martinez, P. G. Mickelson, S. B. Nagel, and T. C. Killian. Using absorption imaging to study ion dynamics in an ultracold neutral plasma. *Phys. Rev. Lett.*, 92:143001, Apr 2004.

[91] Craig Witte and Jacob L. Roberts. Ultracold plasma expansion as a function of charge neutrality. *Physics of Plasmas*, 21(10):103513, 2014.

[92] S. Laha, P. Gupta, C. E. Simien, H. Gao, J. Castro, T. Pohl, and T. C. Killian. Experimental realization of an exact solution to the vlasov equations for an expanding plasma. *Phys. Rev. Lett.*, 99:155001, Oct 2007.

[93] F. Reif. *Fundamentals of Statistical and Thermal Physics*. Fundamentals of Physics Series. McGraw-Hill, 1965.

[94] M. S. Murillo. Using fermi statistics to create strongly coupled ion plasmas in atom traps. *Phys. Rev. Lett.*, 87:115003, Aug 2001.

[95] S. D. Bergeson, A. Denning, M. Lyon, and F. Robicheaux. Density and temperature scaling of disorder-induced heating in ultracold plasmas. *Phys. Rev. A*, 83:023409, Feb 2011.

[96] T. C. Killian, M. J. Lim, S. Kulin, R. Dumke, S. D. Bergeson, and S. L. Rolston. Formation of rydberg atoms in an expanding ultracold neutral plasma. *Phys. Rev. Lett.*, 86:3759–3762, Apr 2001.

[97] Peter Mansbach and James Keck. Monte carlo trajectory calculations of atomic excitation and ionization by thermal electrons. *Phys. Rev.*, 181:275–289, May 1969.

[98] J. Stevefelt, J. Boulmer, and J F. Delpech. Collisional-radiative recombination in cold plasmas. *Phys. Rev. A*, 12:1246–1251, Oct 1975.

[99] Puchang Jiang and Jacob L. Roberts. Electric field influences on the initial electron temperature of ultracold plasmas. *Physics of Plasmas*, 26(4):043513, 2019.

[100] P. McQuillen, T. Strickler, T. Langin, and T. C. Killian. Ion temperature evolution in an ultracold neutral plasma. *Physics of Plasmas*, 22(3):033513, 2015.

[101] D Vrinceanu, G S Balaraman, and L A Collins. The king model for electrons in a finite-size ultracold plasma. *Journal of Physics A: Mathematical and Theoretical*, 41(42):425501, sep 2008.

[102] Truman Wilson, Wei-Ting Chen, and Jacob Roberts. Influence of electron evaporative cooling on ultracold plasma expansion. *Physics of Plasmas*, 20(7):073503, 2013.

[103] S. H. Kim. Heating of and force acting on the electrons of the magnetic plasma by the electromagnetic wave. *Phys. Rev. A*, 26:567–577, Jul 1982.

[104] V Erckmann and U Gasparino. Electron cyclotron resonance heating and current drive in toroidal fusion plasmas. *Plasma Physics and Controlled Fusion*, 36(12):1869–1962, dec 1994.

[105] R. S. Craxton, K. S. Anderson, T. R. Boehly, V. N. Goncharov, D. R. Harding, J. P. Knauer, R. L. McCrory, P. W. McKenty, D. D. Meyerhofer, J. F. Myatt, A. J. Schmitt, J. D. Sethian, R. W. Short, S. Skupsky, W. Theobald, W. L. Kruer, K. Tanaka, R. Betti, T. J. B. Collins, J. A. Delettrez, S. X. Hu, J. A. Marozas, A. V. Maximov, D. T. Michel, P. B. Radha, S. P. Regan, T. C. Sangster, W. Seka, A. A. Solodov, J. M. Soures, C. Stoeckl, and J. D. Zuegel. Direct-drive inertial confinement fusion: A review. *Physics of Plasmas*, 22(11):110501, 2015.

[106] H. B. Nersisyan, G. Zwicknagel, and C. Toepffer. Energy loss of ions in a magnetized plasma: Conformity between linear response and binary collision treatments. *Phys. Rev. E*, 67:026411, Feb 2003.

[107] H. B. Nersisyan and G. Zwicknagel. Binary collisions of charged particles in a magnetic field. *Phys. Rev. E*, 79:066405, Jun 2009.

[108] H. B. Nersisyan and G. Zwicknagel. Energy transfer in binary collisions of two gyrating charged particles in a magnetic field. *Physics of Plasmas*, 17(8):082314, 2010.

[109] Hrachya B. Nersisyan and Günter Zwicknagel. Cooling force on ions in a magnetized electron plasma. *Phys. Rev. ST Accel. Beams*, 16:074201, Jul 2013.

[110] Louis Jose and Scott D. Baalrud. A generalized boltzmann kinetic theory for strongly magnetized plasmas with application to friction. *Physics of Plasmas*, 27(11):112101, 2020.

[111] Lorin X. Benedict, Michael P. Surh, Liam G. Stanton, Christian R. Scullard, Alfredo A. Correa, John I. Castor, Frank R. Graziani, Lee A. Collins, Ond řej Čertík, Joel D. Kress, and Michael S. Murillo. Molecular dynamics studies of electron-ion temperature equilibration in hydrogen plasmas within the coupled-mode regime. *Phys. Rev. E*, 95:043202, Apr 2017.

[112] I L Isaev and A P Gavriliuk. Interaction of ultracold non-ideal ion–electron plasma with a uniform magnetic field. *Journal of Physics B: Atomic, Molecular and Optical Physics*, 51(2):025701, Dec 2017.

[113] N. N. Bogolyubov. Kinetic equations. *Journal of Physics USSR*, 10(3):265–274, 1946.

[114] Max Born and H. S. Green. A general kinetic theory of liquids i. the molecular distribution functions. *Proceedings of the Royal Society of London. Series A. Mathematical and Physical Sciences*, 188(1012):10–18, 1946.

[115] John G. Kirkwood. The statistical mechanical theory of transport processes i. general theory. *The Journal of Chemical Physics*, 14(3):180–201, 1946.

[116] J. Yvon. *La théorie statistique des fluides et l'équation d'état*. Actualités scientifiques et industrielles. Hermann & cie, 1935.

[117] A. A. Vlasov. The vibrational properties of an electron gas. *Usp. Fiz. Nauk*, 93(11):444–470, 1967.

[118] Andrew Lenard. On bogoliubov's kinetic equation for a spatially homogeneous plasma. *Annals of Physics*, 10(3):390 – 400, 1960.

[119] R. Balescu. Irreversible processes in ionized gases. *The Physics of Fluids*, 3(1):52–63, 1960.

[120] R.L. Liboff. *Kinetic Theory: Classical, Quantum, and Relativistic Descriptions*. Graduate Texts in Contemporary Physics. Springer New York, 2006.

[121] John David Jackson. *Classical electrodynamics*. Wiley, New York, NY, 3rd edition, 1999.

[122] G. Ecker. *Theory of Fully Ionized Plasmas*. Academic Press, 1972.

[123] P. L. Bhatnagar, E. P. Gross, and M. Krook. A model for collision processes in gases. i. small amplitude processes in charged and neutral one-component systems. *Phys. Rev.*, 94:511–525, May 1954.

[124] *NIST Digital Library of Mathematical Functions*. http://dlmf.nist.gov/ (Release 1.0.27 as of 2020-06-15). F. W. J. Olver, A. B. Olde Daalhuis, D. W. Lozier, B. I. Schneider, R. F. Boisvert, C. W. Clark, B. R. Miller, B. V. Saunders, H. S. Cohl, and M. A. McClain, eds.

[125] S. Johnson. *Faddeeva Package*. http://ab-initio.mit.edu/wiki/index.php/Faddeeva_Package (Revision as of 00:41, 17 April 2017).

[126] B.D. Fried and S.D. Conte. *The Plasma Dispersion Function*. Academic Press, 1961.

[127] Sergey Bochkanov. *ALGLIB*. www.alglib.net (ALGLIB 3.16.0 for C++).

[128] S. Johnson. *Cubature (Multi-dimensional integration)*. http://ab-initio.mit.edu/wiki/index.php/Cubature_(Multi-dimensional_integration) (Revision as of 21:06, 19 July 2017).

[129] John M. Guthrie and Jacob. L Roberts. Nonlinear RF heating model for magnetized electrons in neutral plasma. (manuscript in preparation).

[130] H. J. Lewandowski, D. M. Harber, D. L. Whitaker, and E. A. Cornell. Simplified system for creating a bose–einstein condensate. *Journal of Low Temperature Physics*, 132(5):309–367, Sep 2003.

[131] Anthony Gorges. *Simultaneous trapping of 85Rb & 87Rb in a far off resonant trap*. PhD dissertation, Colorado State University, 2010.

[132] H Ludvigsen, A Äijälä, A Pietiläinen, H Talvitie, and E Ikonen. Laser cooling of rubidium atoms in a vapor cell. *Physica Scripta*, 49(4):424–428, apr 1994.

[133] J. Werner, H. Wallis, and W. Ertmer. Atoms with anomalous zeeman effect in a 1d-magneto-optical molasses. *Optics Communications*, 94(6):525 – 529, 1992.

[134] Wolfgang Petrich, Michael H. Anderson, Jason R. Ensher, and Eric A. Cornell. Behavior of atoms in a compressed magneto-optical trap. *J. Opt. Soc. Am. B*, 11(8):1332–1335, Aug 1994.

[135] Kristan L. Corwin, Zheng-Tian Lu, Carter F. Hand, Ryan J. Epstein, and Carl E. Wieman. Frequency-stabilized diode laser with the zeeman shift in an atomic vapor. *Appl. Opt.*, 37(15):3295–3298, May 1998.

[136] H.J. Metcalf and P. van der Straten. *Laser Cooling and Trapping*. Graduate Texts in Contemporary Physics. Springer New York, 2001.

[137] Daryl W. Preston. Doppler-free saturated absorption: Laser spectroscopy. *American Journal of Physics*, 64(11):1432–1436, 1996.

[138] R. Fitzpatrick. *Plasma Physics: An Introduction*. Taylor & Francis, 2014.

[139] Martin Kruskal. Asymptotic theory of hamiltonian and other systems with all solutions nearly periodic. *Journal of Mathematical Physics*, 3(4):806–828, 1962.

[140] D.J. Griffiths, P.D.J. Griffiths, and R. College. *Introduction to Electrodynamics*. Prentice Hall, 1999.

[141] Craig Witte. *Computational Modeling of Low-Density Ultracold Plasmas*. PhD dissertation, Colorado State University, 2017.

[142] R. S. Fletcher, X. L. Zhang, and S. L. Rolston. Using three-body recombination to extract electron temperatures of ultracold plasmas. *Phys. Rev. Lett.*, 99:145001, Oct 2007.

[143] Sanat Kumar Tiwari and Scott D. Baalrud. Reduction of electron heating by magnetizing ultracold neutral plasma. *Physics of Plasmas*, 25(1):013511, 2018.

[144] S. K. Dutta, D. Feldbaum, A. Walz-Flannigan, J. R. Guest, and G. Raithel. High-angular-momentum states in cold rydberg gases. *Phys. Rev. Lett.*, 86:3993–3996, Apr 2001.

[145] Setsuo Ichimaru. Strongly coupled plasmas: high-density classical plasmas and degenerate electron liquids. *Rev. Mod. Phys.*, 54:1017–1059, Oct 1982.

[146] G. Bannasch, J. Castro, P. McQuillen, T. Pohl, and T. C. Killian. Velocity relaxation in a strongly coupled plasma. *Phys. Rev. Lett.*, 109:185008, Nov 2012.

[147] M. Lyon, S. D. Bergeson, and M. S. Murillo. Limit of strong ion coupling due to electron shielding. *Phys. Rev. E*, 87:033101, Mar 2013.

[148] S. H. Lam. Unified theory for the langmuir probe in a collisionless plasma. *The Physics of Fluids*, 8(1):73–87, 1965.

[149] J. L. Roberts, C. D. Fertig, M. J. Lim, and S. L. Rolston. Electron temperature of ultracold plasmas. *Phys. Rev. Lett.*, 92:253003, Jun 2004.

[150] D. Comparat, T. Vogt, N. Zahzam, M. Mudrich, and P. Pillet. Star cluster dynamics in a laboratory: electrons in an ultracold plasma. *Monthly Notices of the Royal Astronomical Society*, 361(4):1227–1242, 08 2005.

[151] F. Robicheaux and James D. Hanson. Simulation of the expansion of an ultracold neutral plasma. *Phys. Rev. Lett.*, 88:055002, Jan 2002.

[152] S. G. Kuzmin and T. M. O'Neil. Numerical simulation of ultracold plasmas: How rapid intrinsic heating limits the development of correlation. *Phys. Rev. Lett.*, 88:065003, Jan 2002.

[153] S. G. Kuzmin and T. M. O'Neil. Numerical simulation of ultracold plasmas. *Physics of Plasmas*, 9(9):3743–3751, 2002.

[154] T. Pohl, T. Pattard, and J. M. Rost. Kinetic modeling and molecular dynamics simulation of ultracold neutral plasmas including ionic correlations. *Phys. Rev. A*, 70:033416, Sep 2004.

[155] Michael S. Murillo. Ultrafast dynamics of strongly coupled plasmas. *Phys. Rev. Lett.*, 96:165001, Apr 2006.

[156] A. J. Christlieb, R. Krasny, J. P. Verboncoeur, J. W. Emhoff, and I. D. Boyd. Grid-free plasma simulation techniques. *IEEE Transactions on Plasma Science*, 34(2):149–165, 2006.

[157] B. Jeon, J. D. Kress, L. Collins, and N. Grønbech-Jensen. Parallel tree code for two-component ultracold plasma analysis. *Comput. Phys. Commun.*, 178:272–279, 2008.

[158] Josh Barnes and Piet Hut. A hierarchical o(n log n) force-calculation algorithm. *Nature*, 324(6096):446–449, Dec 1986.

[159] L Greengard and V Rokhlin. A fast algorithm for particle simulations. *Journal of Computational Physics*, 73(2):325–348, 1987.

[160] D. S. Dorozhkina and V. E. Semenov. Exact solution of vlasov equations for quasineutral expansion of plasma bunch into vacuum. *Phys. Rev. Lett.*, 81:2691–2694, Sep 1998.

[161] F. Robicheaux and James D. Hanson. Simulated expansion of an ultra-cold, neutral plasma. *Physics of Plasmas*, 10(6):2217–2229, 2003.

[162] K. A. Twedt and S. L. Rolston. Electron evaporation from an ultracold plasma in a uniform electric field. *Physics of Plasmas*, 17(8):082101, 2010.

[163] G.B. Arfken, H.J. Weber, and F.E. Harris. *Mathematical Methods for Physicists: A Comprehensive Guide*. Elsevier Science, 2011.

[164] R. Kubo, H. Ichimura, T. Usui, and N. Hashitsume. *Statistical Mechanics*. North-Holland Personal Library. Elsevier Science, 1990.